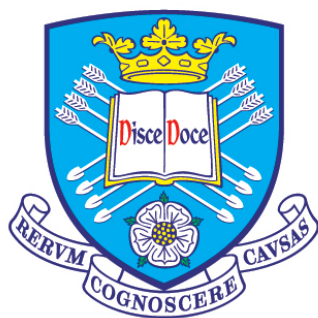


Fabrication of artificial light-harvesting systems for energy transfer studies



**The
University
Of
Sheffield.**

Xia Huang

A thesis submitted for the degree of Doctor of Philosophy

The University of Sheffield

Faculty of Science

Department of Molecular Biology and Biotechnology

June 2018

Summary

Photosynthesis is the process by which solar energy is converted into chemical energy. Solar energy is captured by light-harvesting (LH) antenna complexes, and then transferred to a specialized, membrane-bound complex called the reaction centre (RC) where this energy is trapped as a charge separated state. The development of lithographic techniques has allowed patterning of photosynthetic complexes on surfaces, creating the possibility of studying their light-harvesting and energy transfer properties. Reconstitution techniques enable the assembly of membrane vesicles containing LH and RC complexes for measuring the processes of energy harvesting and excitation transfer.

LH2 and RCLH1 complexes purified from the phototrophic bacterium *Rhodobacter (Rba.) sphaeroides* have been patterned on glass surfaces. Fluorescence lifetime imaging microscopy (FLIM) results show that both complexes retained their native functions, and energy transfer from LH2 to RCLH1 was observed. Repeated FLIM measurements show that the patterned complexes can last for 60 days with their fluorescence properties and energy transfer capability retained.

Methods were developed for nanoscale patterning of purified LH2, RCLH1 and LHCII complexes on semiconductive silicon surfaces. AFM images and FLIM results show that these complexes had retained their structural properties and energy transfer functions.

LH2 and $\Delta crtB$ RCLH1 purified from *Rba. sphaeroides* have been reconstituted with lipids to form artificial proteoliposomes. Five different LH2/ $\Delta crtB$ RCLH1 ratios were used for the reconstitution process. AFM images show the distribution of the complexes in the proteoliposomes and FLIM results show varying energy transfer efficiencies according to the different LH2/ $\Delta crtB$ RCLH1 ratios used in reconstitutions.

LHCII from spinach and $\Delta crtB$ RCLH1 from *Rba. sphaeroides* have been cross-patterned on glass surfaces, to form a hybrid plant/bacterial photosynthetic system. FLIM results show evidence for energy transfer from LHCII to $\Delta crtB$ RCLH1, and assembly of a biohybrid photosynthetic unit.

Acknowledgements

First, I would like to thank my supervisor Professor Neil Hunter for his continued support, care and advice through the years that I have worked in his research group. I would also like to thank The Photosynthetic Antenna Research Center (PARC), an Energy Frontier Research Center funded by the U.S. Department of Energy, Office of Science, and Office of Basic Energy Sciences under Award Number DE-SC0001035. PARC funded my PhD project, and I am grateful for their support.

I would like to thank all the people in the Hunter laboratory, past and present, who have helped me with their expertise and wise advice over the course of my PhD. In particular I would like to thank Dr Cvetelin Vasilev for guiding me through all the surface patterning experiments, and for providing lots of help on AFM and FLIM, and with scientific suggestions every now and then; Dr David Swainsbury for teaching me about cell culturing, protein purification and providing much other biological knowledge; Dr Pu Qian and Dr Craig MacGregor-Chatwin for helping with the EM imaging and protein purifications; Dr Matt Johnson and Guy Mayneord for providing purified proteins; Dr Samuel Barnett for teaching me all he knows about super-resolution imaging and STORM; Elizabeth Martin and Dr Katie Grayson for making mutants; Dr Michaël Cartron for helping me with the liposome work; Dr Andy Hitchcock, Dr Paul A Davison, and Dr Guangyu Chen for offering help in the lab; and Dr Amanda Brindley for all her constant help and care through my four years in the lab.

Thank you to all my friends. I thank all those back home: Lei Li, Zhiyue Liu, Sipeng Yuan, Jianshan Wang, Ying Zhang, for getting me through my PhD with support and cheering me on all the way. Thank you to my friends in Sheffield: Tingyu Luo, Jie Yang, Fei Mo, Zhen Ma, Alix Boulouis, Helen, Jonathon for accompany and listening; Thank you to the lovely girls from the Sheffield Cricket Club for all the joy and fun you have brought to me. Thank you to Yuan Pan for your company and things you have taught me.

Finally, I would like to say a special thank you to my family for their love, belief and support. My mom, who always loves me so much and supports me unconditionally since I was born, I love you! My dad, who talks little but does a lot and supports me in

his own way; I love you too. My Aunty, Zhiying, who cheers me up when I feel blue. And my Grandma, Shubin, who has no degree but generously supported me to see the world since I was young and to start this PhD study. Without their love, I would not have the courage to finish this PhD.

Table of Contents

Chapter 1: Introduction

1.1 Photosynthesis	1
1.2 Photosynthetic organisms	2
1.2.1 Classification of photosynthetic organisms	2
1.2.2 Distinct groups of photosynthetic organisms	3
1.2.2.1 Plants and algae	3
1.2.2.2 Cyanobacteria	4
1.2.2.3 Purple bacteria.....	4
1.2.2.4 Green sulphur bacteria	4
1.2.2.5 Green non-sulphur bacteria.....	5
1.2.2.6 Heliobacteria.....	5
1.2.2.7 Acidobacteria	5
1.2.3 <i>Rhodobacter sphaeroides</i>	5
1.2.4 <i>Synechocystis</i>	6
1.2.5 <i>Arabidopsis</i> and spinach	6
1.3 Light harvesting and energy trapping in <i>Rhodobacter sphaeroides</i>	7
1.3.1 The photosynthetic unit of <i>Rhodobacter sphaeroides</i>	7
1.3.2 The peripheral light-harvesting complex LH2.....	8
1.3.3 The light-harvesting LH1 complex.....	9
1.3.4 The reaction centre.....	10
1.3.5 The core complex.....	11
1.3.6 Excitation transfer to the reaction centre	13
1.3.7 Membrane structure of <i>Rhodobacter sphaeroides</i>	13
1.3.8 A three-dimensional model of a <i>Rba. sphaeroides</i> chromatophore	15
1.4 Light harvesting and energy trapping in plants	18
1.4.1 The photosynthetic unit in plants.....	18
1.4.2 Chlorophyll.....	19

1.4.3 LHCII	20
1.4.4 PSII.....	21
1.4.5 PSI-LHCI	22
1.4.6 Thylakoid membrane structure	23
1.4.7 Excitation energy and electron transfer chain.....	26
1.5 Immobilisation of functional proteins molecules on surfaces	28
1.5.1 Protein-resistant surfaces.....	28
1.5.2 Functional groups for covalent immobilisation of proteins	28
1.6 Techniques for fabricating patterns of proteins on surfaces	31
1.6.1 Soft lithography.....	31
1.6.2 Nanoimprinting lithography	35
1.6.3 Photolithography	38
1.6.4 AFM scanning probe lithography.....	42
1.6.5 Outlook for surface patterning of proteins.....	44
1.7 Förster resonance energy transfer	46
1.8 Sample imaging by atomic force microscopy	49
1.8.1. Instrumentation	49
1.8.2 Imaging modes.....	51
1.8.3 Advantages and limitations	52
1.9 Aims of this work	53

Chapter 2: Materials and Methods

2.1 Standard buffers, reagents and media	55
2. 2 <i>Rhodobacter sphaeroides</i> strains and growth	55
2.2.1 <i>Rhodobacter sphaeroides</i> strains.....	55
2.2.2 Growth on agar plates	55
2.2.3 Semi-aerobic growth.....	56
2.2.4 Photosynthetic growth	56
2. 3 Purification of protein complexes from <i>Rba. sphaeroides</i>.....	57

2.3.1 Cell harvesting and breakage	57
2.3.2 Preparation of intracytoplasmic membranes (ICM)	57
2.3.3 Solubilisation of ICM by detergent	57
2.3.4 Purification of His-tagged proteins	58
2.3.5 Purification of proteins using ion-exchange chromatography	58
2.4 Purification of LHCII from spinach	59
2.4.1 Spinach sources.....	59
2.4.2 Thylakoid preparation.....	59
2.4.3 Thylakoid digestion	59
2.4.4 Purification of LHCII trimers.....	59
2.5 Room temperature absorption spectra	60
2.6 Room temperature fluorescence emission spectra in solution	60
2.7 Fluorescence life-time imaging microscopy (FLIM)	60
2.7.1 Home-built fluorescence microscope	60
2.7.2 Fluorescence images.....	61
2.7.3 Measurement of fluorescence emission spectra.....	61
2.7.4 Measurement of fluorescence lifetimes.....	61
2.7.5 Analysis of fluorescence data	62
2.8 Atomic force microscope (AFM) imaging	62
2.8.1 Instrumentation	62
2.8.2 Buffer and sample adsorption	63
2.8.3 Imaging patterned samples created by PDMS soft-patterning lithography.....	63
2.8.4 Imaging nanopatterned samples created by local oxidation lithography	63
2.8.5 Imaging liposome-protein samples.....	64
2.9 PDMS soft-patterning	64
2.9.1 Stamp preparation	64
2.9.2 Active cross-linking of substrates	64
2.9.3 Immobilising light-harvesting complexes by soft-patterning	65
2.10 Local oxidation nanopatterning	65

2.10.1 Preparation of mPEO-terminated silane monolayers on silicon substrate	65
2.10.2 Creation of nanopatterns on mPEO-SAM silicon by local oxidation lithography	65
2.10.3 Activation of the –COOH group to an NHS ester	66
2.10.4 Protein immobilisation	66
2. 11 Proteoliposome reconstitution	66
2.11.1 Liposome preparation.....	66
2.11.2 Reconstitution of light-harvesting complexes into the liposome.....	67
2.11.3 Purification of proteoliposome suspensions	67
2. 12 Calculation of protein concentration in proteoliposomes	67

Chapter 3: Excitation energy transfer and trapping in fabricated microarrays constructed from photosynthetic antenna and reaction centre complexes

3.1 Summary	69
3.2 Introduction.....	70
3.3 Results.....	72
3.3.1 Directed formation of crossed-patterned LH2 and RCLH1 complexes on glass and silicon	72
3.3.2 Excitation energy transfer between LH2 and RCLH1 under physiological conditions.	73
3.3.3 Energy transfer from LH2 to $\Delta crtB$ RCLH1 under physiological conditions	76
3.3.4 Energy transfer from LH2 to $\Delta crtB$ RCLH1 in an argon protective environment	78
3.3.5 Long-term stability of cross-patterened LH2 and $\Delta crtB$ RCLH1 complexes on glass surfaces	80
3.3.6 Visualising the arrangement of patterned protein complexes on a glass substrate ...	83
3.4 Discussion.....	85

Chapter 4: Nanoscale patterning of photosynthetic complexes on silicon by local oxidation lithography

4.1 Summary	87
4.2 Introduction.....	88
4.3 Results.....	90

4.3.1 Nanopatterning photosynthetic complexes on silicon using local oxidation lithography	90
4.3.2 AFM imaging of surface oxidation and protein immobilisation	91
4.3.3 Improvements in local oxidation scanning for high quality protein nanolines	95
4.3.4 Bias duration over 100 ms/pixel shows no further improvement on the local oxidation	97
4.3.5 Determination of the most efficient incubation time for photosynthetic complexes on oxidised mPEO	98
4.3.6 Immobilisation of LH2 complexes on mPEO-SAM coated silicon surface by local oxidation	99
4.3.7 Immobilisation of LHCII complexes on mPEO-SAM coated silicon surface by local oxidation	102
4.3.8 Co-patterning two types of photosynthetic complex on mPEO-SAM coated silicon surface by local oxidation	105
4.3.9 Energy transfer between LH2 and RCLH1 complexes immobilised on a silicon surface	111
4.4 Discussion	116
4.4.1 Over long bias duration will not contribute to further oxidation of mPEO molecules on the silicon surface	116
4.4.2 Photosynthetic complexes retained their structural and fluorescence properties after immobilisation on the silicon surface	117
4.4.3 Fluorescence quenching caused by the silicon substrate	117
4.4.4 Energy transfer between immobilised LH2 and RCLH1 on the silicon surface	118
4.4.5 Additional work	119
4.4.6 Conclusion	119
 Chapter 5: Energy transfer in reconstituted LH2/ $\Delta crtB$ RCLH1 proteoliposomes	
5.1 Summary	120
5.2 Introduction	121
5.3 Results	124

5.3.1 Reconstitution of LH2 and $\Delta crtB$ RCLH1 complexes into liposomes.....	124
5.3.2 Sucrose gradient fractionation of reconstituted LH2/ $\Delta crtB$ RCLH1 proteoliposomes	125
5.3.3 Size of the reconstituted proteoliposomes	126
5.3.4 Absorption spectra of LH2/ $\Delta crtB$ RCLH1 proteoliposomes	128
5.3.4 AFM observation of the assembled LH2/ $\Delta crtB$ RCLH1 in the proteoliposomes.....	131
5.3.5 Fluorescence emission spectra of the LH2/ $\Delta crtB$ RCLH1 proteoliposomes.....	135
5.3.6 Fluorescence lifetime decay of LH2 complexes in proteoliposomes.....	138
5.4 Discussion.....	142
5.4.1 LH2 and $\Delta crtB$ RCLH1 complexes have been reconstituted into proteoliposomes at the expected ratio with their functional properties retained.....	142
5.4.2 LH2 and $\Delta crtB$ RCLH1 complexes retain their light-harvesting and energy transfer properties when reconstituted in proteoliposomes.....	143
5.4.3 Decreasing LH2/ $\Delta crtB$ RCLH1 ratios progressively increase energy transfer efficiency in the reconstituted proteoliposomes.....	144
5.4.5 Conclusion.....	145

Chapter 6: Excitation energy transfer from LHCII to RCLH1 in fabricated microarrays of bacterial/plant photosynthetic complexes

6.1 Summary	146
6.2 Introduction.....	146
6.3 Results.....	148
6.3.1 Directed formation of crossed-patterned LHCII and $\Delta crtB$ RCLH1 complexes on glass	148
6.3.2 Absorption spectra of purified LH2CII and $\Delta crtB$ RCLH1 complexes in detergent	149
6.3.3 LH complexes retain their optical properties following immobilisation on glass.....	149
6.3.4 Energy transfer from LHCII to $\Delta crtB$ RCLH1 in a biohybrid plant/bacterial artificial photosystem	151
6.4 Discussion.....	154

Chapter 7: Conclusion

7.1 Concluding remarks	156
Appendix: Growth medium for <i>Rhodobacter sphaeroides</i> M22+ medium (10× stock)	159
References	160

List of Figures

Page #	Figure
2	Figure 1.1 Classification of photosynthetic organisms
3	Figure 1.2 Types of photosynthetic organism
8	Figure 1.3 Schematic of energy transfer from pigmented light-harvesting complexes to reaction centres in <i>Rba. sphaeroides</i>
9	Figure 1.4 The LH2 complex of <i>Rhodopseudomonas acidophila</i>
11	Figure 1.5 The <i>Rhodobacter sphaeroides</i> reaction centre
12	Figure 1.6 The <i>Rhodobacter sphaeroides</i> core complex dimer
15	Figure 1.7 Tapping mode AFM showing the organisation of <i>Rhodobacter sphaeroides</i> photosynthetic membranes
16	Figure 1.8 An in silico model of an entire photosynthetic membrane vesicle
17	Figure 1.9 Atomic structural model of a photosynthetic membrane vesicle
18	Figure 1.10 Location of the photosynthetic machinery
20	Figure 1.11 The structure and electrodynamics of chlorophyll
21	Figure 1.12 The structure of LHCII
22	Figure 1.13 Basic structure of the PSII–LHCII supercomplex from spinach
23	Figure 1.14 Basic structure of the PSI–LHCI supercomplex from pea
24	Figure 1.15 Lateral heterogeneity in thylakoid membrane organization
25	Figure 1.16 AFM topographs of grana membranes from spinach
26	Figure 1.17 Macromolecular organization of grana thylakoids
27	Figure 1.18 The photosynthetic electron and proton transfer chain
33	Figure 1.19 Schematic illustration of the procedure for casting PDMS replicas from a master having relief structures on its surface
34	Figure 1.20 Schematic illustration of μ CP protein patterns using PDMS replicas

35	Figure 1.21 Schematic of the NIL process and SEM images of NIL fabrications
36	Figure 1.22 Schematic of thermal NIL and UV NIL processes
37	Figure 1.23 Schematic representation of the lithographic process
39	Figure 1.24 Schematic of fabricating three SAMs by exposing photosensitive SAM through mask to 365 nm and 220 nm UV light
40	Figure 1.25 Interferometric lithography
41	Figure 1.26 Scanning near-field photolithography
42	Figure 1.27 Schematic diagram of different AFM scanning probe lithography approaches
44	Figure 1.28 Schematics of constructive nanolithography and the generated patterns
46	Figure 1.29 Jablonski diagram of FRET
47	Figure 1.30 Spectral overlap of absorption and emission of CFP/YFP
50	Figure 1.31 Schematic for AFM
72	Figure 3.1 Schematic diagram of the micro-contact printing method used to fabricate the cross-patterned LH2 and RCLH1 protein arrays
73	Figure 3.2 Absorption spectra of purified complexes
75	Figure 3.3 Fluorescence spectrum and lifetime data from a cross-patterned LH2 and RCLH1 complexes under physiological conditions (in imaging buffer) on a functionalised glass substrate
77	Figure 3.4 Fluorescence spectrum and lifetime from cross-patterned LH2 and $\Delta crtB$ RCLH1 complexes imaged under physiological conditions
80	Figure 3.5 Fluorescence spectrum and lifetime from cross-patterned LH2 and $\Delta crtB$ RCLH1 complexes on a functionalised glass substrate imaged in protective atmosphere of argon
82	Figure 3.6 Fluorescence spectrum and life-time data obtained 60 days after the sample preparation showing long-term stability of the cross-patterned LH2 and $\Delta crtB$ RCLH1 complexes

- 84 **Figure 3.7** Topography of the cross-patterned LH2 / $\Delta crtB$ RCLH1 complexes on a Si substrate
- 91 **Figure 4.1** Schematic for protein immobilisation by local oxidation lithography
- 93 **Figure 4.2** AFM images of the mPEO/COOH lines formed by local probe oxidation on a silicon surface
- 94 **Figure 4.3** AFM images of the RCLH1 complexes immobilisation on NHS ester activated COOH pattern
- 96 **Figure 4.4** Fluorescence emission from the immobilised RCLH1 complexes on local probe oxidised nanolines
- 97 **Figure 4.5** Normalised fluorescence intensity from RCLH1 nanolines created by local oxidation for bias duration from 80 ms/pixel to 240 ms/pixel
- 98 **Figure 4.6** Fluorescence intensity from RCLH1 nanolines created by increasing cross-linking incubation time from 40 minutes to 20 hours
- 99 **Figure 4.7** AFM images of mPEO/COOH lines formed by local probe oxidation on a silicon surface
- 101 **Figure 4.8** AFM images of LH2 complexes immobilised on an NHS ester activated COOH pattern
- 102 **Figure 4.9** Fluorescence emission from nanolines of LH2 complexes
- 103 **Figure 4.10** AFM images of mPEO/COOH lines formed by local probe oxidation on a silicon surface
- 104 **Figure 4.11** AFM images of the LHCII complex immobilisation on the NHS ester activated COOH pattern
- 105 **Figure 4.12** Fluorescence emission from nanolines of LHCII complexes
- 106 **Figure 4.13** Schematic for multiple protein immobilisation by local oxidation lithography
- 107 **Figure 4.14** AFM images of mPEO/COOH lines made by the first local oxidation on a silicon surface

- 108 **Figure 4.15** AFM images of RCLH1 complexes immobilised on an NHS ester
activated COOH pattern following the first local oxidation
- 109 **Figure 4.16** AFM images of the RCLH1 pattern from the first local oxidation and
the mPEO/COOH pattern from the second local oxidation
- 110 **Figure 4.17** AFM images of the intersecting RCLH1 and LH2 nanolines created
by successive local oxidations on a silicon surface
- 112 **Figure 4.18** AFM images of two local oxidations
- 113 **Figure 4.19** AFM images of co-patterned LH2 square and RCLH1 lines
- 114 **Figure 4.20** Zoomed-in AFM images of co-patterned LH2 square and RCLH1
lines
- 115 **Figure 4.21** Fluorescence images of co-patterned LH2 square and RCLH1 lines
- 121 **Figure 5.1** Model of an antenna-energy trapping system
- 125 **Figure 5.2** Schematic diagram of reconstituting membrane proteins into
proteoliposome
- 126 **Figure 5.3** Sucrose gradient fractionation of LH2/ $\Delta crtB$ RCLH1
proteoliposomes
- 127 **Figure 5.4** Size distribution of LH2 proteoliposomes
- 129 **Figure 5.5** Normalised absorption spectra from native *Rba. sphaeroides*
membranes, purified LH2 and the $\Delta crtB$ RCLH1 complexes, and the five LH2/
 $\Delta crtB$ RCLH1 reconstituted proteoliposome samples
- 131 **Figure 5.6** Normalised absorption spectra showing the absorption intensity of
the carotenoid at 485 nm
- 132 **Figure 5.7** AFM image of sample #1 LH2 only proteoliposome and the height
profile
- 132 **Figure 5.8** AFM image of sample #1 LH2 only proteoliposome
- 133 **Figure 5.9** AFM image of sample #2 $\Delta crtB$ RCLH1 only proteoliposome and the
height profile

- 133 **Figure 5.10** AFM image of sample #3 2LH2/1 Δ *crtB* RCLH1 proteoliposome
- 134 **Figure 5.11** AFM image of sample #4 1LH2/1 Δ *crtB* RCLH1 proteoliposome
- 134 **Figure 5.12** AFM image of sample #5 1LH2/2 Δ *crtB* RCLH1 proteoliposome
- 136 **Figure 5.13** Fluorescence emission spectra of purified protein complexes and the five LH2/ Δ *crtB* RCLH1 proteoliposome samples
- 137 **Figure 5.14** Fluorescence emission spectra of the five LH2/ Δ *crtB* RCLH1 proteoliposome samples, following addition of 2% β -DDM
- 139 **Figure 5.15** Fluorescence emission spectra from each LH2/ Δ *crtB* RCLH1 proteoliposome sample before and after solubilisation by 2% β -DDM
- 140 **Figure 5.16** Fluorescence lifetime of LH2 in proteoliposomes compared with the LH2 lifetime when the proteoliposomes are solubilised by 2% of β -DDM
- 141 **Figure 5.17** Fluorescence lifetime decay curves of the LH2 complexes
- 148 **Figure 6.1** Schematic diagram of the micro-contact printing method used to fabricate cross-patterned LHCII and Δ *crtB* RCLH1 protein arrays
- 149 **Figure 6.2** Spectra of purified LHCII and Δ *crtB* RCLH1 complexes
- 151 **Figure 6.3** False colour fluorescence image of crossed-patterns of LHCII and Δ *crtB* RCLH1, and fluorescence emission spectra of the LHCII complexes
- 152 **Figure 6.4** Fluorescence intensity images and fluorescence spectra from cross-patterned LHCII and Δ *crtB* RCLH1 complexes on a functionalised glass substrate
- 153 **Figure 6.5** Fluorescence lifetime data from cross-patterned LHCII and Δ *crtB* RCLH1 complexes on a functionalised glass substrate

List of Tables

Page #	Table
29	Table 1.1 Commonly available functional groups in proteins and functionalities of the required surfaces
48	Table 1.2 Förster radius (R_0) values for photosynthetic pigments
56	Table 2.1 <i>Rhodobacter sphaeroides</i> strains
59	Table 2.2 Absorbance ratios for collection of purified complexes
81	Table 3.1 Fluorescence lifetime of LH2 at 860 nm.
125	Table 5.1 Ratio between lipid and protein complexes for proteoliposome reconstitutions
126	Table 5.2 Sucrose concentrations of purified LH2/ $\Delta crtB$ RCLH1 proteoliposomes samples
127	Table 5.3 Size distribution of LH2 proteoliposomes
130	Table 5.4 LH2 / $\Delta crtB$ RCLH1 ratios in reconstituted proteoliposomes calculated from absorption spectrum fitting results, and compared with protein ratios used during incubation
140	Table 5.5 LH2 lifetime measured at 857 nm when proteins are in proteoliposomes and when the proteoliposomes are solubilised by 2% β -DDM

Abbreviations

2-D	two dimensional
3-D	three dimensional
β -DDM	n-dodecyl- β -D-maltopyranoside
Å	Ångstrom(s)
AFM	atomic force microscopy
Ar	argon
ATP	adenosine triphosphate
B800	bacteriochlorophyll in LH2 with an absorbance maximum of 800 nm
B850	bacteriochlorophyll in LH2 with an absorbance maximum of 850 nm
B875	bacteriochlorophyll in LH1 with an absorbance maximum of 875 nm
BChl(s)	bacteriochlorophyll(s)
Chl(s)	chlorophyll(s)
Crt	carotenoid
cyt	cytochrome
DMS	dimethyl sulfoxide
DOPC	1,2-dioleoyl- <i>sn</i> -glycero-3-phosphocholine
EDC	1-ethyl-3-[3-dimethylaminopropyl]carbodiimide hydrochloride
EET	excitation energy transfer
EM	electron microscopy
EMCCD	electron multiplying charge coupled device
FLIM	fluorescent lifetime imaging microscopy
FRET	Förster resonance energy transfer
FWHM	full width at half maximum
g/ μ g/ ng	gram(s)/microgram(s)/nanogram(s)
GFP	green fluorescent protein
HEPES	N-2-hydroxyethylpiperazine-N'-2-ethanesulphonic acid
HPLC	high performance liquid chromatography
hr	hour(s)
ICM	intracytoplasmic membrane

(N)IR	(near)infrared
LH1	light-harvesting complex 1
LH2	light-harvesting complex 2
LHCI	light-harvesting complex I
LHCII	light-harvesting complex II
LMV	large multi-lamellar vesicles
min	minute(s)
ml/ μ l/ L	millilitre(s)/ microlitre(s)/ litre(s)
M/ mM	molar/ millimolar
mPEO	2-[methoxy (polyethyleneoxy) 6-9propyl] trichlorosilane
NA	numerical aperture
NHS	N-hydroxysuccinimide
NIL	Nanoimprint lithography
nm/ μ m	nanometre(s)/ micrometres(s)
OD _x	optical density (at "x" nm)
PDMS	polydimethylsiloxane
PLL	poly-L-lysine
PSI	photosystem I
PSII	photosystem II
Q (UQ)	quinone (ubiquinone)
QH ₂ O	distilled water purified using the Milli-Q system
<i>Rba.</i>	<i>Rhodobacter</i>
RC	reaction centre
rpm	revolutions per minute
s/ns/ps	second(s)/nanosecond(s)/picosecond(s)
SAM	self-assembled monolayer
TCSPC	time-correlated single photon counting
TIRF	total internal reflection fluorescence
τ	Fluorescence lifetime
μ CP	microcontact printing

UV	ultraviolet
V	volts
WT	wild-type
YFP	yellow fluorescent protein

Introduction

1.1 Photosynthesis

Photosynthesis is the biological process by which light energy is captured and converted into biochemical energy, and it is the primary energy source for the majority of life on Earth. Photosynthetic organisms, including plants, algae and specialised bacteria, contain light-harvesting pigment-protein complexes that absorb solar energy. This energy is used to drive a series of electron transfers, which are coupled to the translocation of protons and generation of a proton gradient across a membrane. The transmembrane proton-motive force is utilised for the synthesis of ATP, which is then used to drive the metabolism of the cell, including fixation of carbon dioxide.

Although the pigment-protein complexes for photosynthesis vary significantly in different types of organism, the overall process for photosynthesis is a redox reaction and can be represented by the equation:



H₂A represents electron and hydrogen ion donors, such as H₂O and H₂S, for the reductive assimilation of CO₂ to form CH₂O (carbohydrate). Photosynthesis can be divided into two main types, depending on the oxidation product of this reaction: oxygenic photosynthesis (oxygen-evolving) and anoxygenic photosynthesis (non-oxygen-evolving). Oxygenic photosynthesis occurs in plants, algae and cyanobacteria, using H₂O as the electron donor and with O₂ as the oxidation product. Thus, oxygenic photosynthesis is imperative for aerobic life, as it was responsible for and maintains atmospheric oxygen levels. Anoxygenic photosynthesis occurs in other photosynthetic bacteria, excluding cyanobacteria, using a number of different compounds, including inorganic acids such as succinate and acetate.

1.2 Photosynthetic organisms

1.2.1 Classification of photosynthetic organisms

Organisms can be phylogenetically classified into three domains by their evolutionary relationships, based on the sequence of their small subunit ribosomal RNA in a 'tree of life'. According to the classification method, photosynthetic organisms are found within the 'eukarya' and 'bacteria' domains. No 'archaeal' photosynthetic organisms have been found. The photosynthetic phyla are: cyanobacteria, purple bacteria, green sulphur bacteria, Gram positive bacteria, acidobacteria, green non-sulphur bacteria and plants (including algae). Groups containing photosynthetic organisms are shown in Figure 1.1.

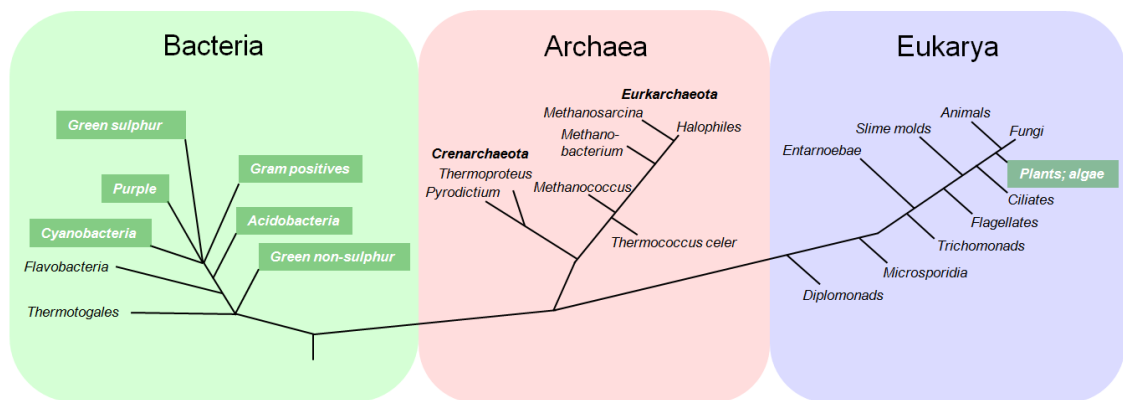


Figure 1.1. Classification of photosynthetic organisms

Phylogenetic classification is based on the sequences of the small rRNA subunit. Phyla with photosynthetic organisms present are highlighted in green.

(Mothersole 2013)

Another method to classify photosynthetic organisms is by metabolic properties:

(a) Carbon source: autotrophs derive their cellular carbon from CO₂, whilst heterotrophs derive cellular carbon from pre-formed organic compounds. Most photosynthetic organisms are autotrophs; some may grow by either method.

(b) Energy source: phototrophs utilise sunlight as the source of energy, whilst chemotrophs use various complex chemical compounds as the energy source. Photosynthetic organisms are phototrophs.

(c) Oxygen usage: An aerobe requires oxygen to grow, whereas an anaerobe grows in without oxygen, by anaerobic respiration or fermentation.

1.2.2 Distinct groups of photosynthetic organisms

Types of photosynthetic organism

Eukaryotic oxygenic photosynthesis (chloroplasts)



Plants

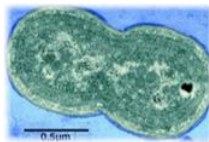
Mosses

Green algae

Red algae

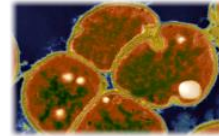
Brown algae

Prokaryotic oxygenic photosynthesis



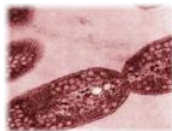
Cyanobacteria (-)

Archaeal photosynthesis



Halobacteria

Prokaryotic anoxygenic photosynthesis



Purple bacteria (-)



Green sulphur
bacteria (-)



Green nonsulfur
bacteria (-)



Heliobacteria (+)

Figure 1.2. Types of photosynthetic organism.

The (-/+) refers to the Gram-negative classification, which is based on the type of cell wall.

1.2.2.1 Plants and algae

One distinct phylum of the “eukarya” domain is the photosynthetic eukaryotes, such as plants, mosses, green algae, red algae, and brown algae. These photosynthetic eukaryotes all contain chloroplasts, in which thylakoid membranes house the apparatus for oxygenic photosynthesis. Although algae and plants are complex, the same basic principles of eukaryotic photosynthesis are found in oxygenic cyanobacteria.

1.2.2.2 Cyanobacteria

Apart from the eukaryotes some prokaryotes are also capable of photosynthesis, and they can be classified into five distinct major groups, only one of which is oxygenic, the cyanobacteria. The other four groups are anoxygenic, known as the purple bacteria, the green sulphur bacteria, the green non-sulphur bacteria and the heliobacteria.

The cyanobacteria are a large and diverse oxygenic photosynthetic group, and they occupy a wide range of habitats across the Earth, including some extreme environments such as hypersaline bays and hot springs. Cyanobacteria are often referred to as “blue-green algae” because they have a molecular mechanism of photosynthesis similar to the eukaryotic phototrophs. Many species of cyanobacteria can fix N_2 and some can use H_2S as an electron donor (Padan 1979). According to the endosymbiotic theory, chloroplasts found in plants and eukaryotic algae evolved from cyanobacterial ancestors (Zimorski et al 2014).

1.2.2.3 Purple bacteria

Purple phototrophic bacteria, as one of the anoxygenic photosynthetic prokaryotes, can metabolise in versatile ways. They can grow photoautotrophically, photoheterotrophically, aerobically, anaerobically and fermentatively (Imhoff 1995). Purple phototrophic bacteria are subdivided into ‘purple non-sulphur’ (the Rhodospirillaceae family) and ‘purple sulphur’ (the Chromatiaceae family) groups, based on their sulphide tolerance (van Niel 1944). Only the purple sulphur bacteria can use sulphur containing compounds such as H_2S as an electron donor (Brune 1995). Most purple bacteria can fix molecular nitrogen and the Calvin cycle fixes CO_2 in all purple bacteria (Tabita 1995).

1.2.2.4 Green sulphur bacteria

The photosynthetic green bacteria can be divided to two types: the green sulphur bacteria and the green non-sulphur bacteria. The green sulphur bacteria primarily use H_2S as an electron donor, whilst the others do not. The green sulphur bacteria are obligate anoxygenic phototrophs and are strict anaerobes. They are found in oxygen-free environments with very low light, for example at the bottom of lakes. They are

capable of nitrogen fixation and can fix CO₂ through a reverse tricarboxylic acid cycle (Sirevåg 1995).

1.2.2.5 Green non-sulphur bacteria

Green non-sulphur bacteria are significantly more versatile than green sulphur bacteria. They are facultative anaerobes that grow aerobically by autotrophy or heterotrophy with reduced carbon compounds as electron donors.

1.2.2.6 Heliobacteria

Photosynthetic heliobacteria are strictly anaerobic photoheterotrophs. They are the only group of Gram-positive or spore-forming phototrophs, often found in soils and rice paddies. Photosynthetic heliobacteria are active nitrogen fixers but their CO₂ fixation is not well understood. The primary pigment involved in the photosynthesis of the heliobacteria is chlorophyll *g*, which is unique to this group.

1.2.2.7 Acidobacteria

The species *Candidatus Chloracidobacterium thermophilum*, recently discovered in a hot spring in Yellowstone National Park (Bryant et al 2007), has been assigned to a newly devised phylum, the physiologically diverse and ubiquitous Acidobacteria.

1.2.3 *Rhodobacter sphaeroides*

Rhodobacter (Rba.) sphaeroides is a Gram-negative, rod-shaped, and metabolically diverse purple non-sulphur bacterium. It can perform anoxygenic photosynthesis under anaerobic conditions in the light and can grow by chemoheterotrophy under semi-aerobic or aerobic conditions in the dark (Madigan & Gest 1979). It is also capable of diazotrophic growth and fermentation (Blankenship et al 1995). *Rba. sphaeroides* is typically found in anoxic zones at the bottom of deep lakes and in sediments (Madigan 1988, Pfennig 1978), sewage (Siefert et al 1978), and waste lagoons (Cooper et al 1975).

Rba. sphaeroides is an excellent model organism for many reasons: it can be easily cultured in liquid medium in the laboratory under the light or in the dark; its small genome has been fully sequenced and well annotated, allowing for rapid genomic manipulation; since it can grow by chemotrophy, the genes essential for anoxygenic photosynthesis can be removed, allowing for in-depth genetic and biochemical

studies. A wealth of structural information is available for the *Rba. sphaeroides* photosynthetic membrane protein complexes, including the light harvesting complexes, LH2 and LH1, the reaction centre (RC), the cytochrome *bc*₁ complex and ATP synthase.

1.2.4 *Synechocystis*

Synechocystis is a unicellular, Gram-negative cyanobacterium. It performs oxygenic photosynthesis reducing CO₂ with H₂O and can grow phototrophically under the light or heterotrophically when supplied with a carbon source (Anderson & McIntosh 1991).

Synechocystis is a useful photosynthetic model organism for several reasons. Significantly, the photosynthetic mechanism of *Synechocystis* is similar to that of plants and algae, showing a high level of homology among many of the photosynthetic protein complexes. Its genome is fully sequenced (Kaneko & Tabata 1997). *Synechocystis* is naturally competent, its genome can uptake and incorporate foreign DNA by homologous recombination (Grigorieva & Shestakov 1982). Since it can grow photoheterotrophically, genetic manipulation of essential photosynthetic protein complexes is more straightforward than for eukaryotic counterparts, and there are many useful mutants available in the genes encoding proteins for biosynthesis, assembly and photosynthetic function.

1.2.5 *Arabidopsis* and spinach

Arabidopsis is a genus in the family Brassicaceae, small flowering plants related to cabbage and mustard. *Arabidopsis* is the first plant whose genome has been fully sequenced and one of the model organisms for plant biology studies. Spinach is also a flowering plant but in the family Amaranthaceae native to central and western Asia. It is also widely used as a model organism for photosynthesis studies in plants.

1.3 Light harvesting and energy trapping in *Rhodobacter sphaeroides*

1.3.1 The photosynthetic unit of *Rhodobacter sphaeroides*

The photosynthetic unit (PSU) of *Rhodobacter sphaeroides* consists of pigment–protein complexes that absorb solar energy as electronic excitation energy (Şener et al 2007a). PSUs are embedded in intracytoplasmic membranes (ICM) (Schachman et al 1952, Sener et al 2016). The PSU contains three types of pigment-protein complexes: the reaction centre (RC), and the light-harvesting (LH) complexes LH1 and LH2. The LH complexes form an interconnected antenna system for absorbing solar energy and funnelling the excitation energy to the RC where excitation energy is trapped and converted to a charge separation (Figure 1.3). In wild-type *Rba. sphaeroides*, the LH1 complex encircles the RC at a stoichiometrically fixed ratio of 1:1 (Aagaard & Sistrom 1972) and forms the ‘core complex’. The amount of LH2, however, varies with light intensity (Aagaard & Sistrom 1972, Adams & Hunter 2012). Both LH complexes comprise α and β polypeptides, which occur in a 1:1 ratio and form a scaffold for the light-harvesting pigments. Energy migration is directed by the spatial organisation and energetic order of the pigments binding within the LH complexes, which are bacteriochlorophylls (BChls) and carotenoids. Carotenoids are found in all photosynthetic organisms and have two major functions in photosynthesis. First, they act as accessory antenna pigments, absorbing light between 450 nm and 600 nm and transferring the energy to BChls, thus augmenting BChl absorption. Second, they protect the photosynthetic organism from photo-oxidative damage (Guiraud & Foote 1976). The BChls will be introduced with their specific LH complexes.

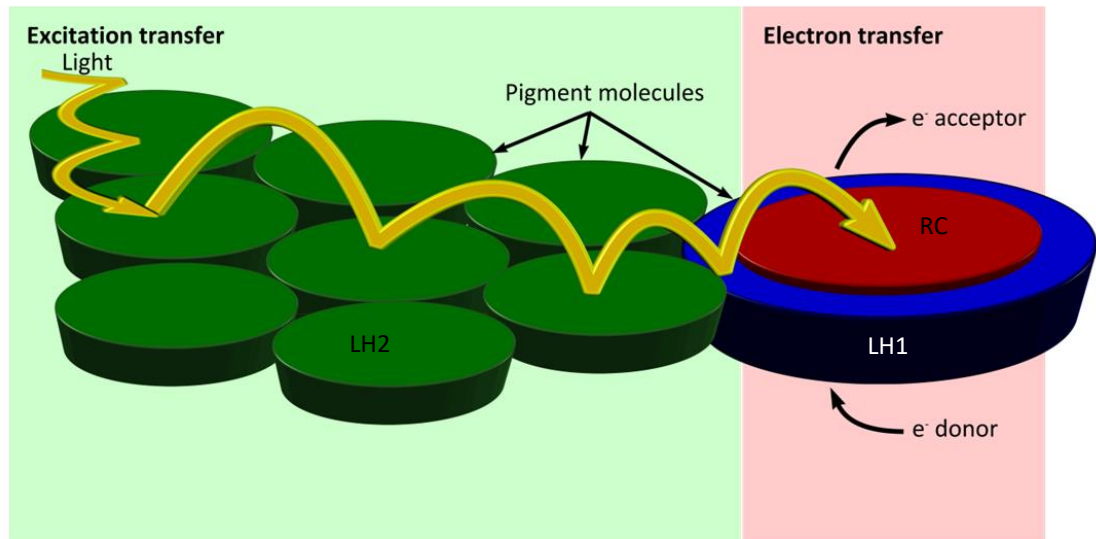


Figure 1.3. Schematic of energy transfer from pigmented light-harvesting complexes to reaction centres in *Rba. sphaeroides*

Photons of light are absorbed by the peripheral light-harvesting LH2 complexes (green) and create excited states. This electronic excitation energy is transferred via light-harvesting LH1 complexes (blue) to the reaction centre (red). At the reaction centre, the excitation energy is trapped and transduced to a photochemical charge separation, then ultimately as a quinol.

(From Mothersole, 2013)

1.3.2 The peripheral light-harvesting complex LH2

LH2 complexes are commonly found in purple bacteria. X-ray crystal structures were obtained for the nonameric LH2 from *Rhodospseudomonas (Rps.) acidophila* and the octameric LH2 from *Phaeospirillum (Ph.) molischianum* (Koepke et al 1996, McDermott et al 1995). A 6 Å electron microscopy (EM) projection map showed that the *Rba. sphaeroides* LH2 is nonameric (Walz et al 1998) and atomic force microscopy (AFM) analysis of 2-D crystals later confirmed this (Scheuring et al 2003).

As of May 2018, no high-resolution 3D crystal structure of *Rba. sphaeroides* LH2 has been obtained. Therefore, the LH2 structure discussed here is that of *Rhodospseudomonas acidophila*, as it has similar structure to that of *Rba. sphaeroides* (Figure 1.4) (Papiz et al 2003).

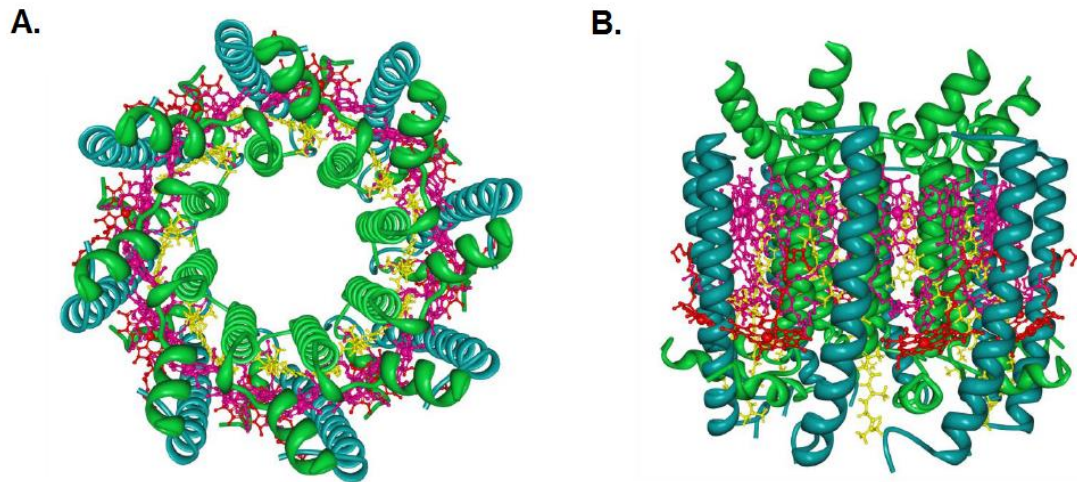


Figure 1.4. The LH2 complex of *Rhodospseudomonas acidophila*

Components have been coloured as follows: LH2 α -polypeptides in green, LH2 β -polypeptides in cyan, B850 BChl in pink, B800 BChl in red and carotenoids in yellow.

- A. Projection view from the periplasmic side of the complex.
- B. Side view with the periplasmic side uppermost.

(Modified from Mothersole, 2013)

The LH2 complex has two absorbance maxima at 800 nm and 850 nm, arising from bound BChls, which are known as B800 and B850 (Cogdell 1985). These BChls are non-covalently attached to α and β polypeptides, which associate in a 1:1 ratio forming a heterodimer (Brunisholz & Zuber 1992). Each LH2 complex consists of nine $\alpha\beta$ helices with the β helical subunits forming the outer ring, while the α helical subunits form the inner ring. Nine B800 BChl α molecules are positioned perpendicular to the transmembrane helix axis between the outer β helices, and eighteen B850 BChl molecules form an overlapping ring sandwiched between the $\alpha\beta$ helices; there are also 13-14 carotenoid molecules, 9 of which are closely associated with the phytyl tails of the BChl α molecules (Freer et al 1996, McDermott et al 1995, Papiz et al 2003). In terms of energy transfer, excitation energy from carotenoid molecules and B800 is first passed to the B850 ring and then via the B875 ring in the LH1 complex to the RC.

1.3.3 The light-harvesting LH1 complex

The LH1 complex has a single BChl absorbance band at 875 nm in *Rba. sphaeroides* (B875). In *Rba. sphaeroides* an S-shaped LH1 complex of 28 $\alpha\beta$ heterodimers and 56

BChls intertwines two reaction centres (Qian et al 2013). In some other bacteria, such as *Thermochromatium tepidum*, LH1 complexes consist of 32 B875 BChl molecules and form a complete circular array surrounding a single RC (Yu et al 2018); and the 2.9 Å structure of the RC-LH1 complex from *Blastochloris viridis* (Qian et al 2018) has a ring of 34 BChls. Models of the RC-LH1 'core complex' are presented in section 1.3.5.

1.3.4 The reaction centre

The reaction centre (RC) is the membrane protein-pigment complex that carries out primary photochemical charge separation using excitation energy from the surrounding LH1 complex. The RC reduces quinone to quinol, which leaves the RC and diffuses to the cytochrome *bc*₁ complex. Here, a proton-motive force is generated that powers ATP synthesis. The *Rba. sphaeroides* RC was first purified from a carotenoid-less LH2-deficient mutant called R-26 (Feher 1971). Subsequent studies show the RC from *Rba. sphaeroides* is composed of three protein subunits: L (light), M (medium) and H (heavy), according to their apparent molecular weights (Clayton & Haselkorn 1972). The first structure of the *Rba. sphaeroides* RC shows that each L and M subunit comprises five transmembrane α -helices and these subunits are related by pseudo-twofold symmetry, whilst the H subunit has a single transmembrane helix with the bulk of its mass forming a globular domain containing two β -sheets at the cytoplasmic side of the membrane (Figure 1.5).

Multiple cofactors bounding to the L and M subunits are arranged in two pseudo-symmetric branches, designated A and B (Figure 1.5 B). Two BChl *a* molecules form a strongly interacting dimer known as the 'special pair' ($P_A P_B$, or P870, from their Q_y maximal absorbance). Other bound cofactors are two accessory BChl *a* molecules, two bacteriopheophytins (H_A and H_B), two ubiquinones (Q_A and Q_B), a non-haem Fe^{2+} , and a carotenoid molecule. Only branch A, which is more closely associated with L-subunit, is used in the light-driven electron transfer process and is therefore termed the 'active' branch (Yeates et al 1987). The carotenoid molecule is within van der Waals contact with the accessory BChl of branch B and it has two roles: transferring excitation to the special pair and prevention of photo-oxidative damage by quenching the triplet excited state of the special pair (Cogdell et al 2000).

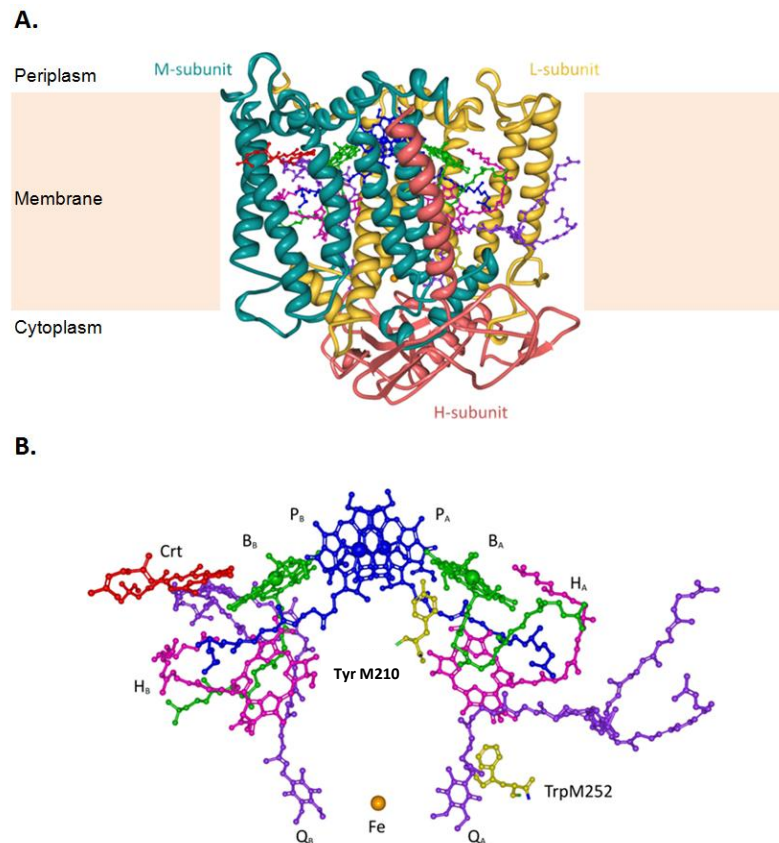


Figure 1.5. The *Rhodospirillum rubrum* reaction centre

- A. Model of the reaction centre showing the L (orange), M (cyan) and H (red) subunits. Pigment molecules are in the same colours as in B.
- B. The reaction centre pigment cofactors including the two molecules of BChl *a* (P_A and P_B) known as the “special pair” (blue), two accessory molecules of BChl (B_A and B_B) (green), two molecules of bacteriopheophytin (H_A and H_B) (pink), and the carotenoid (spheroidene) (red). Also shown are two quinones (Q_A and Q_B) (purple), the Fe atom (orange) and two important aromatic amino acid side chains (yellow).

(From Mothersole, 2013)

1.3.5 The core complex

The LH1 complex encircles the RC and together these complexes are known as the photosynthetic core complex (or RC-LH1). In *Rba. sphaeroides* there is an S-shaped dimeric RC-LH1 complex, with the small transmembrane polypeptide PufX acting as a channel to allow the mobilization of quinol and quinone between RC and cytochrome *bc*₁ complexes (Figure 1.6) (Qian et al 2013).

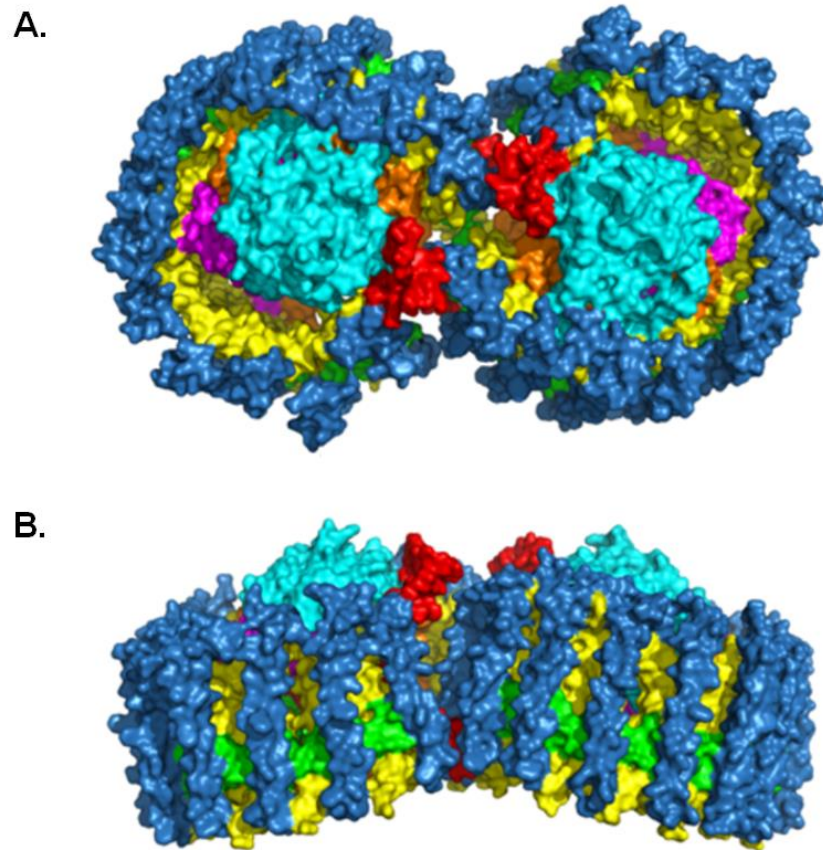


Figure 1.6. The *Rhodospirillum rubrum* core complex dimer

LH1 β in blue, LH1 α in yellow, RC-H in cyan, RC-L in orange, RC-M in magenta, and PufX in red.

- A. Cytoplasmic face of the complex viewed perpendicular to the membrane.
- B. Complex viewed in the plane of the membrane

(From Qian *et al.*, 2013)

The 3D crystal structure of the *Rba. sphaeroides* core complex has been defined at a resolution of 8 Å (Qian *et al* 2013). Each monomer contains 14 LH1 subunits around one RC forming a C-shaped assembly (Qian *et al* 2005, Qian *et al* 2013). The two halves of the dimer incline towards each other at an angle of about 168°, forming a V-shaped structure that imposes curvature on the membrane (Hsin *et al* 2009, Qian *et al* 2008). PufX is essential for the dimeric complex structure and mutants lacking PufX only form monomeric RC-LH1 complexes (Francia *et al* 1999, Ratcliffe *et al* 2011). Monomeric PufX-minus RC-LH1 core complexes are hexagonally packed and the curvature of the membrane is significantly reduced (Adams *et al* 2011, Frese *et al* 2008, Siebert *et al* 2004).

Membranes of *Rba. sphaeroides* contain a mixture of monomeric and dimeric core complexes; the monomeric form predominates when grown under chemoheterotrophic conditions and the dimeric form predominates under anaerobic heterotrophic growth (Crouch & Jones 2012, Ratcliffe et al 2011). Some other species of photosynthetic bacteria, such as *Rhodopseudomonas (Rsp.) palustris*, possess only monomeric core complexes (Roszak et al 2003).

1.3.6 Excitation transfer to the reaction centre

After photon absorption by a pigment molecule, a series of ultrafast energy transfers takes place within LH2 and between RC-LH1 complexes. There are several pathways for excitation energy to arrive at the RC. In the case of *Rba. sphaeroides*, excitation energy transfer generally begins with photon absorption by B800 Bchl then follows the following route to the RC: B800 (LH2) → B850 (LH2) → B875 (LH1) → RC (Dahlberg et al 2017). Ultrafast energy transfer also occurs from carotenoids to nearby BChls.

Within the LH2 complex, B800 to B850 excitation transfer takes approximately 650-800 fs at room temperature (Jimenez et al 1996, Joo et al 1996, Ma et al 1997). As the B850 BChls are very well coupled, energy transfer time between B850 molecules within the LH2 ring is about 110 fs (Jimenez et al 1996, Monshouwer et al 1995). Excitation transfer from LH2 B850 to an adjacent LH1 B875 takes 3.3-4.6 ps (Hess et al 1995a, Hess et al 1995b, Nagarajan & Parson 1997). As the B875 BChls are also very well coupled, energy transfer within the LH1 B875 ring is on the 80-100 fs timescale (Bradforth et al 1995). Excitation transfer from B875 to RC is the rate-limiting step, requiring 35-50 ps because of the approximately 4.5 nm separation between the LH1 and the RC special pair. This longer transfer time also has the benefit of a low (10-20%) probability of back transfer from RC to the LH1 (Beekman et al 1994, Otte et al 1993, Visscher et al 1989).

1.3.7 Membrane structure of *Rhodobacter sphaeroides*

Light harvesting and energy transfer are related to the arrangement and stoichiometry of the light harvesting and reaction centre complexes in the photosynthetic membrane. Using atomic force microscopy (AFM) to image the organisation of protein complexes in native cellular membranes provides insights

into how photosynthetic membranes funnel energy to reaction centres so efficient charge separation can take place (Şener et al 2007a). As many of the crystal structures of pigment containing membrane proteins have been revealed, photosynthetic membrane topology can be investigated by AFM and membrane proteins can be identified from their membrane protrusions (Sturgis et al 2009).

Photosynthetic membrane architecture in *Rba. sphaeroides* (see Figure 1.7) was first revealed using AFM by Bahatyrova and co-workers (Bahatyrova et al 2004a), and more recently using whole chromatophore vesicles (Kumar et al 2016). The RC-LH1 core complexes formed rows of up to six (RC-LH1-PufX) dimers and LH2 complexes formed 'sandwich regions' of 10–20 LH2s clustered between the RC-LH1 rows and LH2-only domains of variable size. The authors proposed that the functional significance of core clustering may be to increase the probability of trapping energy at an RC by allowing excitation energy transfer between adjacent dimers. When excitation energy arrives at an occupied RC (undertaking photochemistry), LH1-LH1 transfer between B875 rings is most favourable. It was proposed that the energy could migrate along a succession of dimers until an open RC was found (Bahatyrova et al 2004a, Cartron et al 2014, Qian et al 2013). AFM of membranes from *Rba. blasticus* found that the core complex dimers are randomly distributed amongst LH2 and formed no rows of core complex dimers (Scheuring et al 2005).

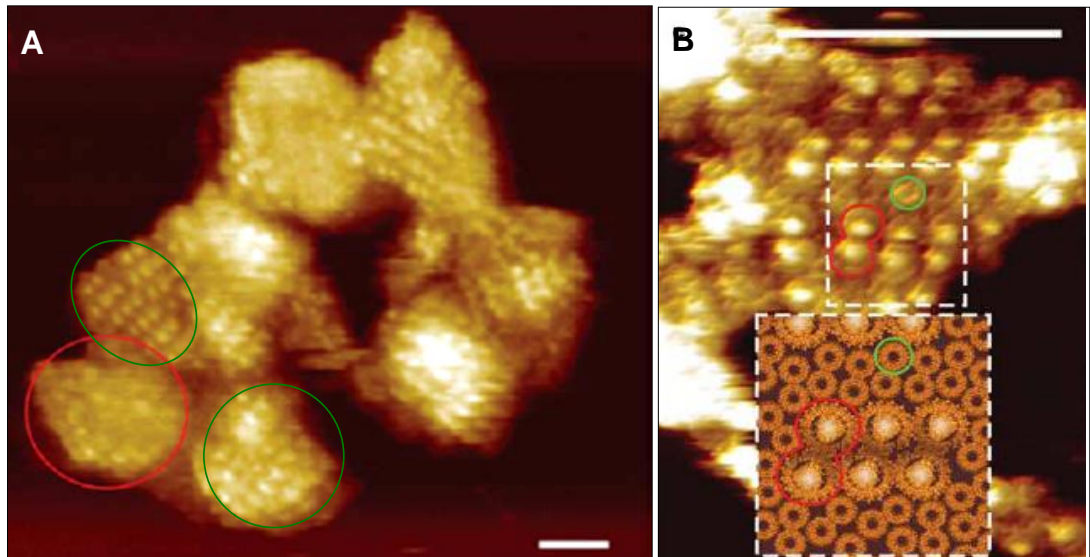


Figure 1.7. Tapping mode AFM showing the organisation of *Rhodospira rubra* photosynthetic membranes

- A. Membrane patches showing two types of domain: LH2-only regions (*red circle*) and regions containing a mixture of core complexes and LH2s (*ringed green*).
- B. Magnified, three-dimensional view of a mixed region. Rows of RC-LH1-PufX core complex dimers are shown, interspersed with LH2 complexes. A single core complex dimer is delineated (*red outline*). The strongly protruding RC-H, appears as a bright spot at the centre of the LH1 ring. LH2 is observed as the smaller hollow rings (*green circle*). The *inset* shows a model of the mixed region: a row of three RC-LH1-PufX dimers is separated from another by LH2s sandwiched two-deep between them.

(Adapted from Bahatyrova et al. 2004a)

1.3.8 A three-dimensional model of a *Rba. sphaeroides* chromatophore

A model for the *Rba. sphaeroides* membrane vesicle was proposed based on combination of AFM and linear dichroism data on the organisation of core complexes and LH2, and atomic models of the complexes (Bahatyrova et al 2004a, Frese et al 2004). The semi-spherical shaped ICM vesicles are densely packed with light-harvesting complexes: rows of RC-LH1 dimer complexes and interspersed LH2 complexes.

By combination of multiple AFM topographs, a computer-based 3D model of ICM vesicle in photosynthetic membrane was reconstructed, regardless of the position of the cyt bc_1 and the ATPase (Figure 1.8) (Şener et al 2007a). Complex algorithms were

used to map the excitation migration over the entire vesicle according to the B800, B850, B875 and RC-BChl energy couplings. For a vesicle with 18 core complex dimers and 101 LH2 complexes, the calculated average excitation lifetime was 50 ps, which is a 95% quantum yield, showing a high energy transfer efficiency.

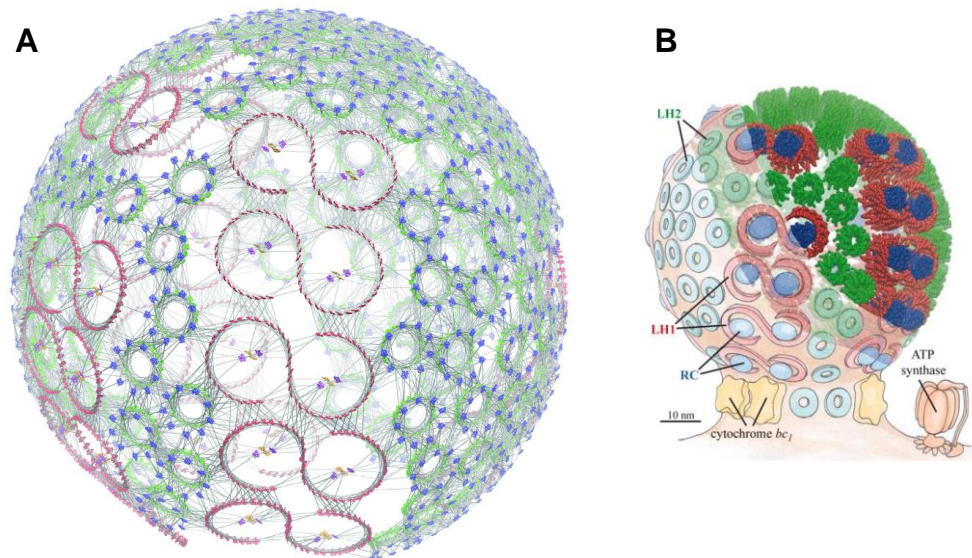


Figure 1.8. An in silico model of an entire photosynthetic membrane vesicle

- A.** Electronic interactions across an ICM vesicle depicting the potential routes of excitation energy transfer. BChls are represented by their porphyrin rings, LH2 B800 (*blue*), B850 (*green*), LH1 B875 (*red*), RC accessory (*purple*), RC special pair (*orange*). Electronic couplings between BChls are shown as grey connecting lines.
- B.** Organisation of the photosynthetic complexes within a vesicle, depicted as space-filling atomic structures (top-right) or cartoon representations (bottom-left): LH2 (*green*), LH1 (*red*), RC (*blue*). The location of *cyt bc₁* (*yellow*) and ATP synthase (*orange*) is not established and they are depicted schematically as peripheral to the light harvesting complexes, at the 'neck' of the vesicle.

(From Sener et al 2007)

More recently, the model was refined using more data; mass spectrometry was used to quantify all major components, and the location of the *cyt bc₁* complex was established using EM and AFM (Cartron et al 2014) (Figure 1.9). This 1.9 million atom structural and functional model comprised 67 LH2 complexes, 22 dimer and 2 monomer RC-LH1-PufX complexes, 4 *cyt bc₁* complexes and 2 ATP synthases. It was used to simulate all processes, from photon absorption to ATP production. It showed that the whole process is limited by the number of *cytbc₁* complexes. Also, under low

light conditions (~3% or less of bright sunlight) ATP turnover can still run at 50% of the maximum rate. The quantitative aspects of the model were expanded more recently (Sener et al 2016).

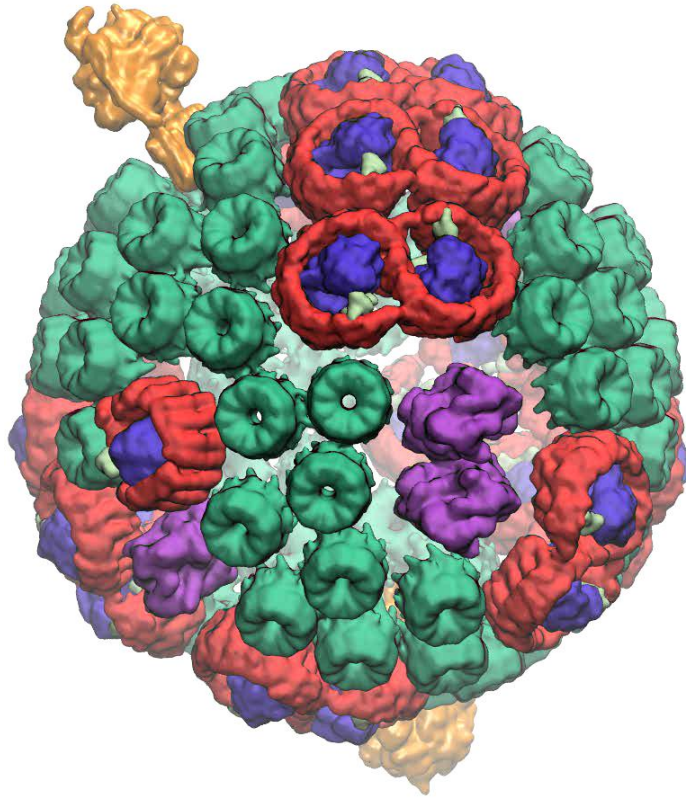


Figure 1.9. Atomic structural model of a photosynthetic membrane vesicle

The vesicle comprises 67 LH2 complexes (green), 11 LH1-RC-PufX dimers & 2 RC-LH1-PufX monomers (blue/red), 4 cytb_c1 dimers (magenta), and 2 ATP synthases (orange).

(from Cartron *et al.*, 2014)

1.4 Light harvesting and energy trapping in plants

1.4.1 The photosynthetic unit in plants

Photosynthesis in plants occurs in the leaf cells and more specifically in chloroplasts. The chloroplast encloses an aqueous space (the stroma) wherein sits stacks of thylakoid membranes (Johnson 2016) (Figure 1.10).

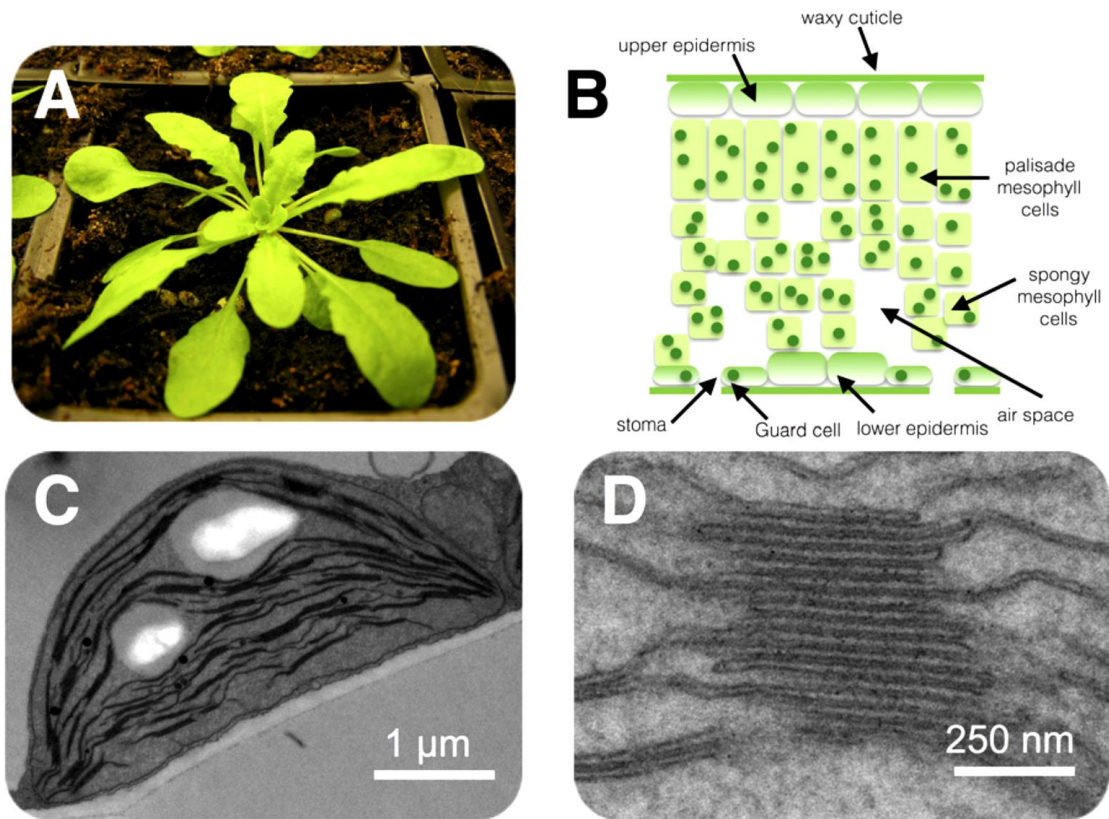


Figure 1.10. Location of the photosynthetic machinery

- A. The model plant *Arabidopsis thaliana*.
- B. Basic structure of a leaf shown in cross-section. Chloroplasts are shown as green dots within the cells.
- C. An electron micrograph of an *Arabidopsis* chloroplast within the leaf.
- D. Close-up region of the chloroplast showing the stacked structure of the thylakoid membrane.

(From Johnson, 2016)

The whole photosynthetic process can be split into the 'light' and 'dark' reactions. In the light reactions, solar energy is harvested and water is split, whilst in the dark reaction, CO₂ is reduced to carbohydrate and energy is stored. The light actions occur in the thylakoid membrane and the dark reactions take place in the stroma. The light reactions begin with the light absorption by pigment molecules, such as chlorophylls and the carotenoids, which are attached to thylakoid membrane-embedded protein

complexes known as light-harvesting complexes (LHCs) and photosystems (PSs). LHCII and LHCI are antenna systems, which collect and concentrate excitation energy and transfer it towards the PSII and the PSI complexes respectively. PSII and PSI are reaction centres, where there is a charge separation, electron donors are oxidized, and acceptors are reduced.

1.4.2 Chlorophyll

Chlorophyll pigments in the thylakoid membranes have alternating series of carbon single and double bonds (Figure 1.11A). Plants contain two types of chlorophyll, chlorophyll *a* and chlorophyll *b*. When a red photon (~650 nm) is absorbed, an electron in the chlorophyll molecule is excited from the ground state (S_0) to the first excited state (S_1), corresponding to the Q_y peak in the absorption spectrum. When absorbs a blue photon (~450 nm), the electron is excited from S_0 to the second excited state (S_2), but quickly drops back to S_1 through internal conversion (Figure 1.11B). The excited electron in the S_1 state can either return to the S_0 by fluorescence emission or heat radiation, or transfer the excitation energy to a nearby chlorophyll under certain conditions (Figure 1.11C).

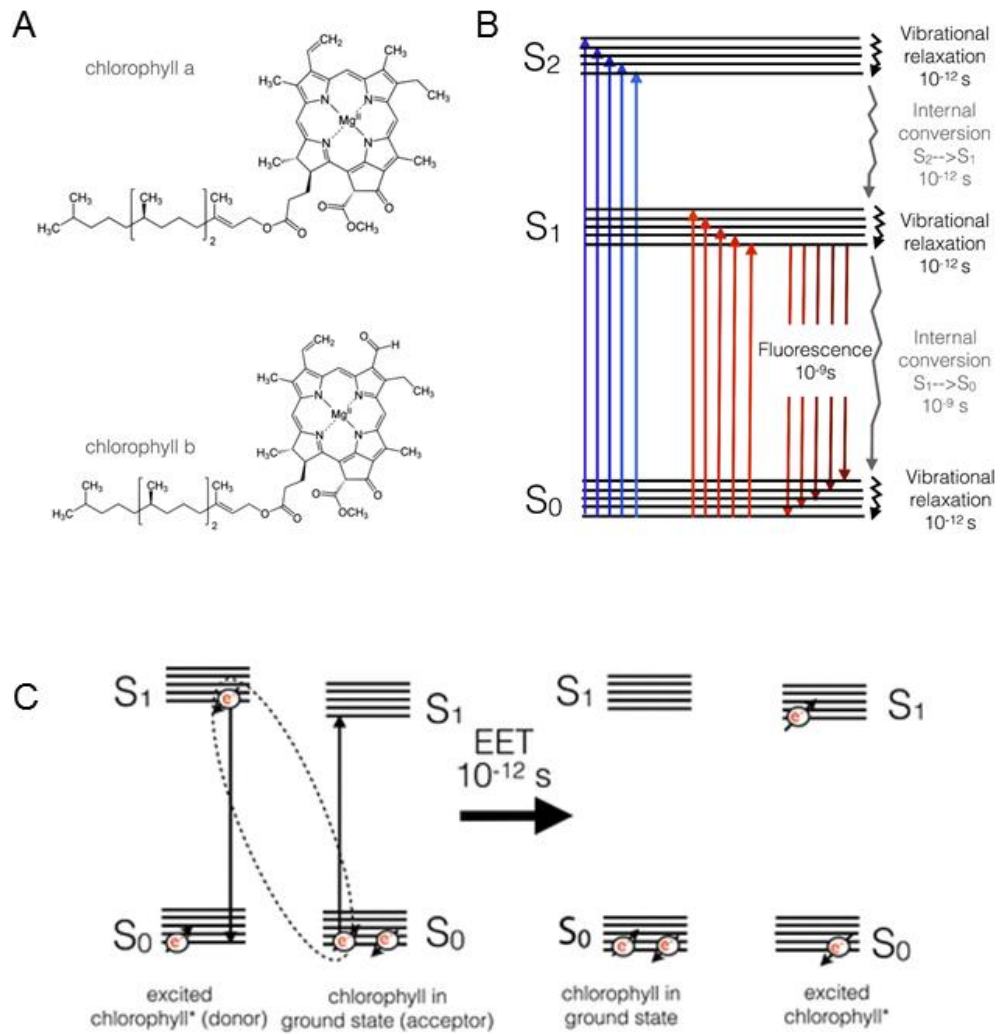


Figure 1.11. The structure and electrodynamics of chlorophyll

- A. The structures of chlorophylls *a* and *b*.
- B. Jablonski diagram of the excitation of an electron by a photon.
- C. Excitation energy transfer between two chlorophylls.

(From Johnson, 2016)

1.4.3 LHCII

The LHCII complex serves as an antenna for the PSII in light harvesting and excitation energy transfer. The number of LHCII in the thylakoid varies with light conditions, allowing adaption to the environment. The number is increased in low-light, whilst in high-light the LHCII dissipates energy through non-photochemical quenching (NPQ).

The LHCII monomer consists of 3 transmembrane α -helices which bind to 8 chlorophyll *a* and 6 chlorophyll *b* molecules (Liu et al 2004, Standfuss et al 2005) (Figure 1.12A). The chlorophylls are arranged in a circular geometry with an average

10 Å centre-to-centre distances (Fig. 1.12B), facilitating excitation transfer within the same molecule and to neighbouring LHCIIs (Liu et al 2004).

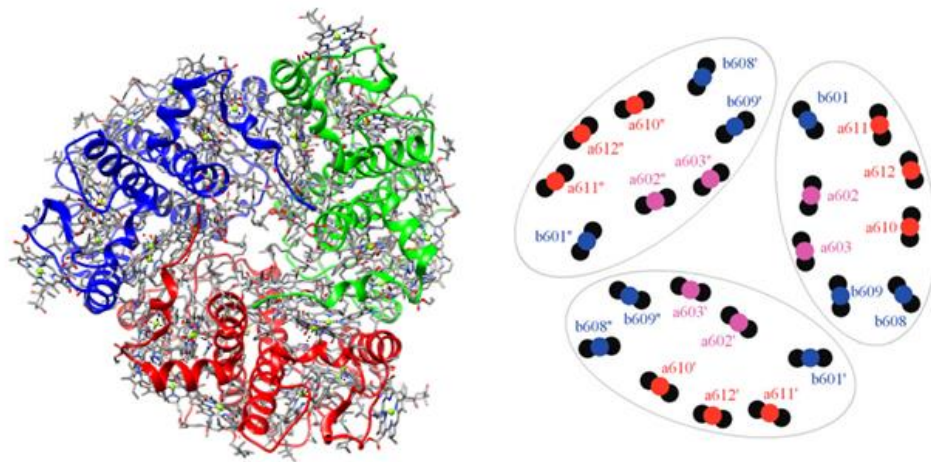


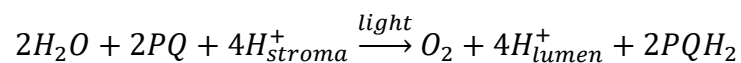
Figure 1.12. The structure of LHCII

- A. The crystal structures of the LHCII trimer from pea.
- B. The organisation of chlorophylls *a* (red and pink) and *b* (blue).

(Novoderezhkin et al 2011)

1.4.4 PSII

PSII is a unique photochemical water-plastoquinone (PQ) oxidoreductase, able to split water into protons, electrons and oxygen. It uses light energy to excite a special pair of chlorophylls the P680 to form a radical pair $P680^+Q_A^-$ with quinone Q_A , which has a sufficient redox potential to oxidize water. The overall H_2O -PQ process generates proton translocation into the thylakoid lumen, contributing to the proton gradient used for ATP synthesis, and the by-product O_2 (McEvoy & Brudvig 2006):



PSII is found within the thylakoid membrane as a dimeric RC complex surrounded by a six minor monomeric antenna LHCII and two to eight trimeric LHCII, forming a PSII-LHCII supercomplex (Figure 1.13) (Johnson 2016, Wei et al 2016). The PSII-LHCII supercomplex is mainly located in the stacked regions, known as the grana, in the thylakoid membrane (Wood et al 2018).

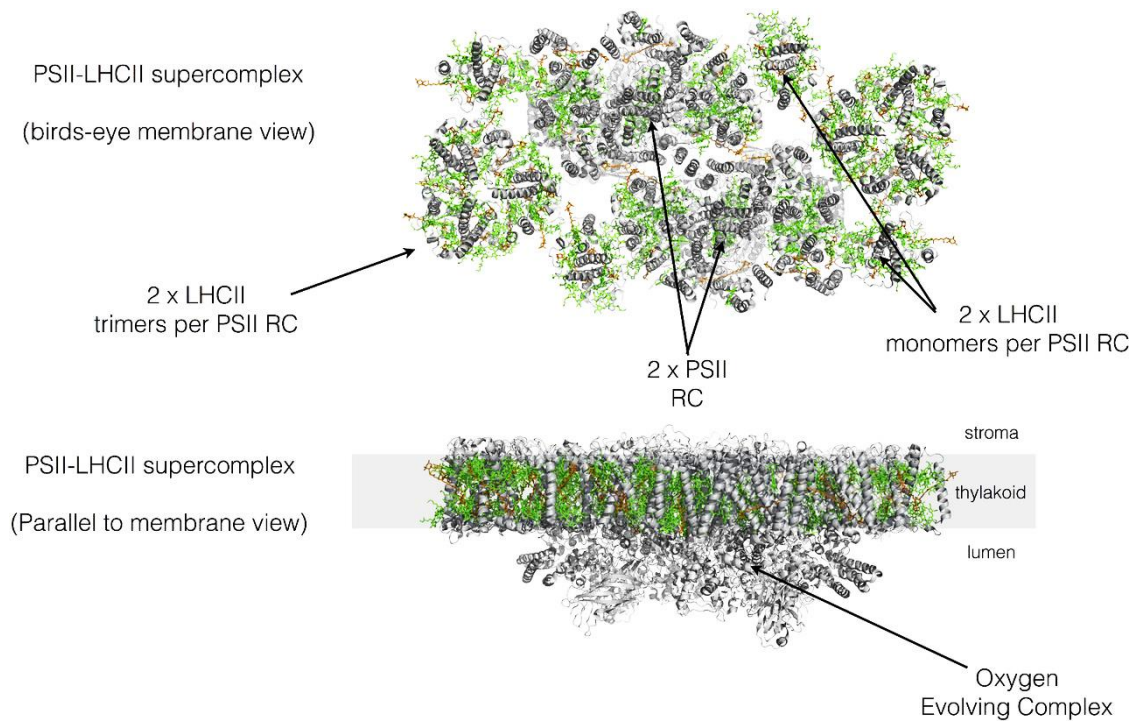


Figure 1.13. Basic structure of the PSII–LHCII supercomplex from spinach

The organization of PSII and its light-harvesting antenna. Protein is shown in grey, with chlorophylls in green and carotenoids in orange.

(From Johnson, 2016)

1.4.5 PSI-LHCI

PSI is a light-driven plastocyanin-ferredoxin oxidoreductase. It uses light energy to excite a special pair of P700 chlorophylls to form the extremely strong reductant P700* which is capable of reducing ferredoxin. The reduced ferredoxin is then utilized for the generation of NADPH as an energy source for subsequent dark, carbon-fixing reactions.

PSI is found within the thylakoid membrane as a monomeric RC complex surrounded by four antenna LHCI on one side only, forming a PSI-LHCI supercomplex (Figure 1.14) (Amunts et al 2007, Ben-Shem et al 2003, Johnson 2016). PSI-LHI is mainly located in the unstacked regions, known as the stromal lamellae, in the thylakoid membrane (Wood et al 2018).

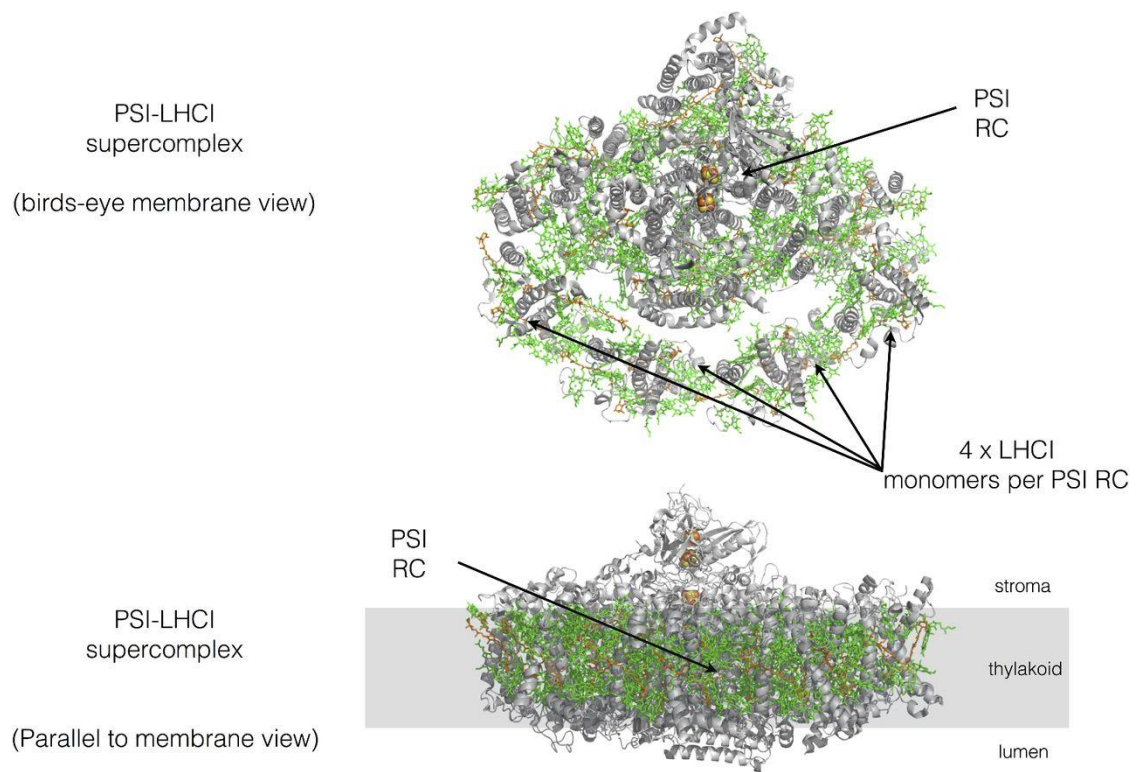


Figure 1.14. Basic structure of the PSI–LHCI supercomplex from pea

The organization of PSI and its light-harvesting antenna. Protein is shown in grey, with chlorophylls in green and carotenoids in orange.

(From Johnson, 2016)

1.4.6 Thylakoid membrane structure

The major components of the light reactions, LHCII, PSII, *cytb₆f*, PSI, and ATP synthase are all embedded in the thylakoid membrane. The two domains in thylakoid membrane are the grana and the stromal lamellae. The grana associate with one another to form cylindrical stacks about 500 nm in diameter and more than 500 nm in height; the stromal lamellae wrap helically around the grana stacks forming contacts with grana layers (Austin & Staehelin 2011) (Figure 1.15A). The PSII-LHCII complexes distribute almost entirely within the grana, whereas the PSI and the ATP synthase are located in the stromal lamellae (Andersson & Anderson 1980). *Cytb₆f*, however, is evenly found in the thylakoid (Johnson et al 2014) (Figure 1.15B).

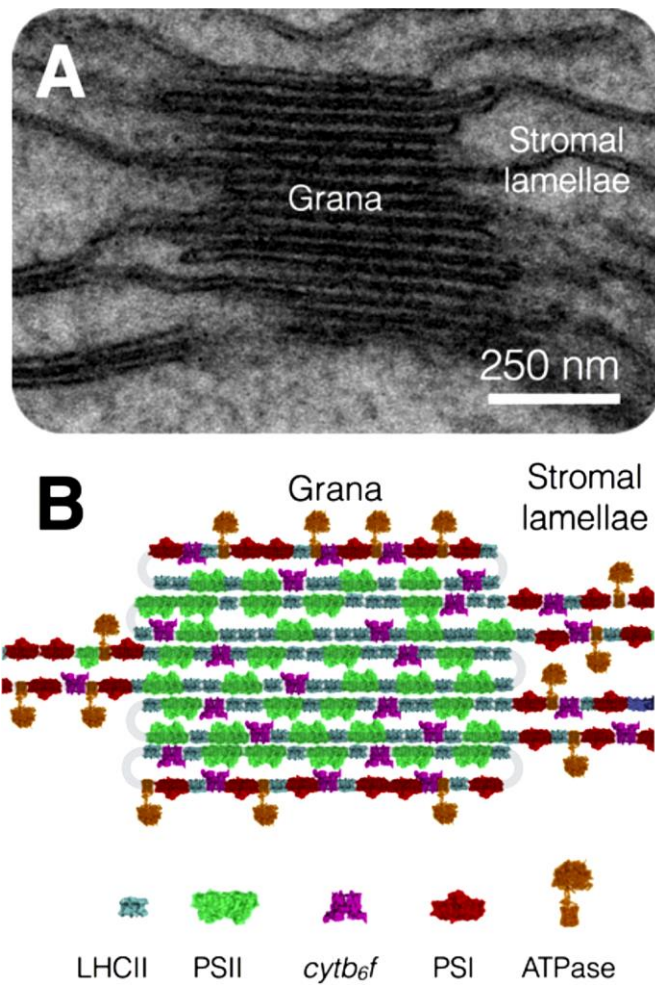


Figure 1.15. Lateral heterogeneity in thylakoid membrane organization

- A. Electron micrograph of the thylakoid membrane showing stacked grana and unstacked stromal lamellae regions.
- B. Model showing the distribution of the major complexes of photosynthetic electron and proton transfer between the stacked grana and unstacked stromal lamellae regions.

(From Johnson, 2016)

Sznee *et al.* showed by AFM the PSII arrangement in the grana stack and the presence of PSI in the ends of the grana stack (Sznee et al 2011) (Figure 1.16).

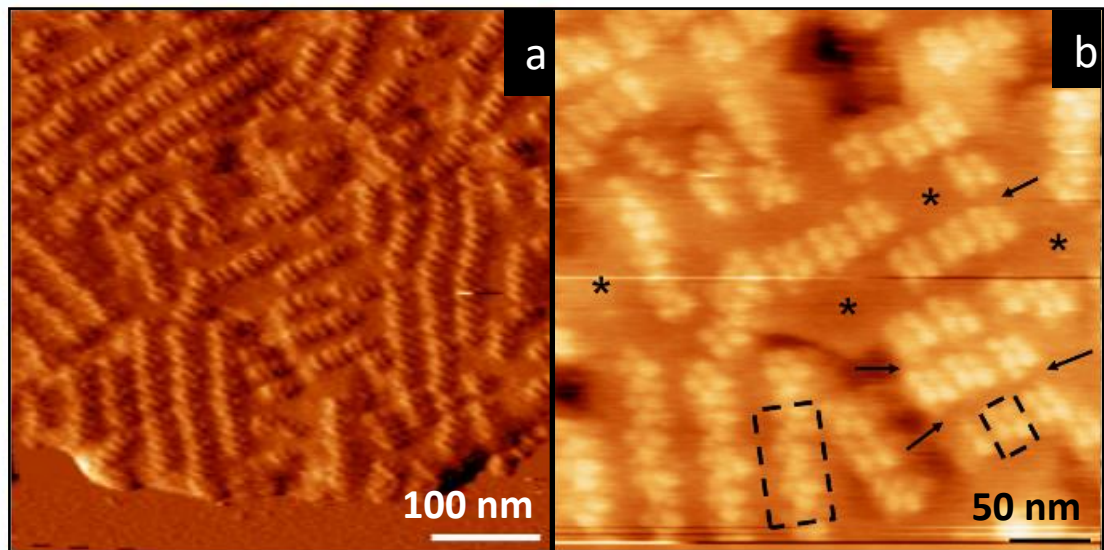


Figure 1.16. AFM topographs of grana membranes from spinach.

- A. A lower resolution AFM topograph showing PSII complexes forming ordered arrays within the granal membrane.
- B. A higher resolution AFM topograph in which individual PSII complexes can be identified from their protruding subunits.

(From Sznee et al., 2011)

Later on, Johnson *et al.* used affinity-mapping AFM and showed the arrangement of cytochrome b_6f and PSII complexes in spinach grana thylakoid membrane (Johnson et al 2014). The constructed map revealed the co-localisation between the cytochrome b_6f and PSII, and suggested that their close proximity optimized photosynthetic efficiency by integrating solar energy conversion and electron transfer through fostering short-range diffusion of PQ in the protein-crowded thylakoid membrane. Wood *et al.* imaged the thylakoid stacks from spinach grown in light and dark surroundings (Wood et al 2018). Spinach grown in light synthesised grana with smaller average diameter, fewer membrane layers but more grana per chloroplast, creating a larger contact area of contact with the stromal lamellae (Figure 1.17). These changes in thylakoid stacking were proposed to regulate the balance between linear electron transfer (LET) and cyclic electron transfer (CET), enabling smaller grana to promote more efficient LET and larger grana enhance the efficiency of CET.

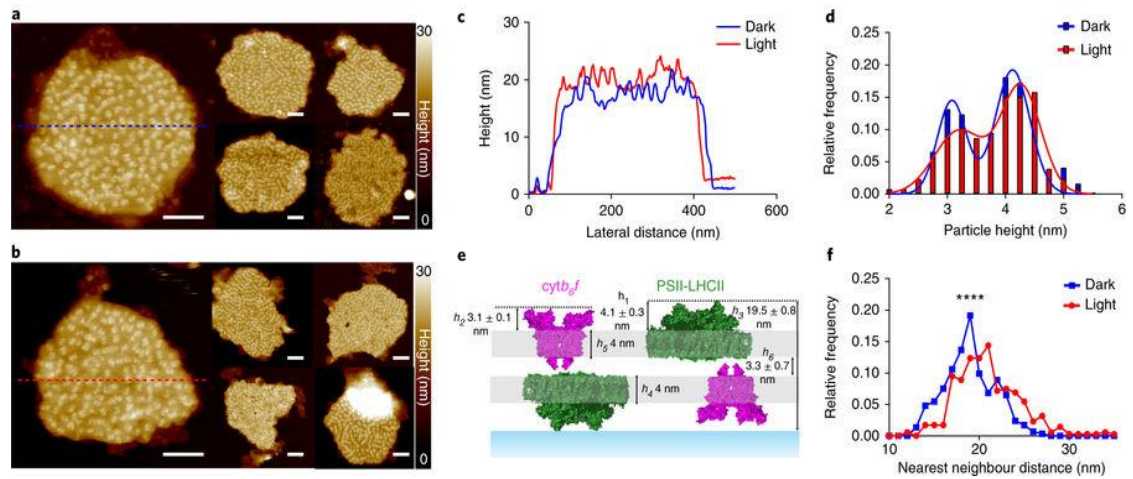


Figure 1.17. Macromolecular organization of grana thylakoids.

- A. AFM topographs of dark-adapted grana thylakoids (scale bars: 100 nm).
- B. AFM topographs of light-adapted grana thylakoids (scale bars: 100 nm).
- C. Height cross-sections of the grana thylakoids in the main panels of A and B as indicated by the dashed lines.
- D. Histogram of the protein protrusion heights above the grana membrane surface with two-Gaussian fit in dark-adapted grana (blue line, N = 121) and light-adapted grana (red line, N = 126).
- E. Schematic model of measured protrusion heights in comparison with the atomic structures (Protein DataBank (PDB) accession numbers: 1Q90 and 3JCU).
- F. Nearest neighbour analysis of the protein protrusions in dark-adapted grana (blue line, N = 292) and light-adapted grana (red line, N = 347) (Unpaired Student's t-test. ****P < 0.0001).

(From Wood, 2018)

1.4.7 Excitation energy and electron transfer chain

The light reactions are the processes that harvest solar energy and temporarily store it in form of ATP and NADPH (Figure 1.18). These processes start with utilizing light energy to excite electrons within chlorophyll molecules residing in PSII-LHCII or PSI-LHCI to a higher energy level. The LHCII and LHCI behave like antennas, transferring excitation energy to the reaction centres, PSII and PSI respectively. The excited chlorophyll in the reaction centre is then used to reduce the subsequent acceptors, followed by the oxidized chlorophyll being reduced by water in the case of PSII and plastocyanin in the case of PSI. The water oxidation at PSII results in the migration of protons into the lumen, forming a proton gradient against the stroma. The proton gradient is then utilized for ATP synthesis. Plastocyanin reduced by the cytochrome *b₆f* complex diffuses to the PSI complex, replacing electrons used by PSI to reduce ferredoxin, and to contribute to the formation of NADPH.

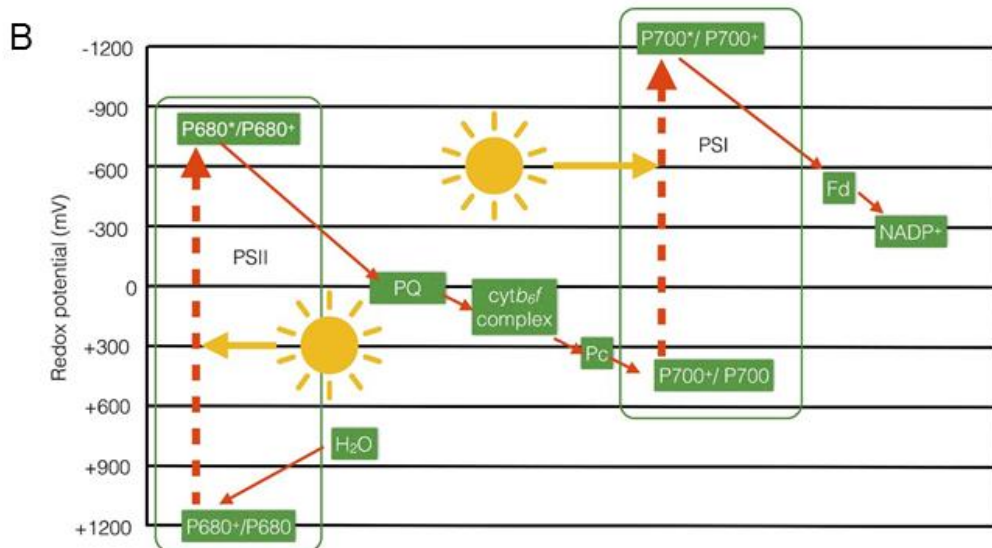
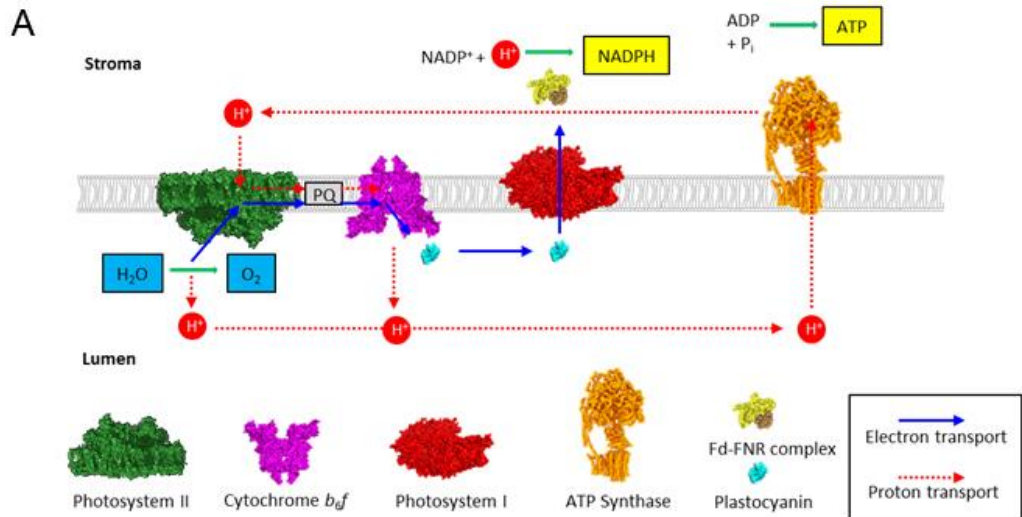


Figure 1.18. The photosynthetic electron and proton transfer chain

- A.** The linear electron transfer pathway from water to $NADP^+$ to form NADPH results in the formation of a proton gradient across the thylakoid membrane that is used by the ATP synthase enzyme to make ATP.
- B.** Redox potentials of the steps of linear electron flow in the thylakoid membrane.
(Adapted from Johnson, 2016)

1.5 Immobilisation of functional proteins molecules on surfaces

1.5.1 Protein-resistant surfaces

Microscience and nanoscience are two important areas in biology as their scales match the size of the cells or the functional components (proteins, lipid bilayers, nucleic acids, etc). Proteins, as one of the most important cellular components, have been widely studied in terms of microscience and nanoscience, and immobilising proteins on surfaces has been a useful method for both fundamental studies of proteins and for the design of novel protein-based hybrid devices. It is important to be able to fabricate specific micro- and nanoscale arrangements of proteins on surfaces, but there is a challenge to overcome; non-specific adsorption is an enormous problem caused by strong and irreversible adhesion between proteins and most surfaces. Thus, protein resistant surfaces are required to effectively reduce the non-specific adsorption and precisely direct the deposition of proteins.

Various surface-chemicals have been used for generating protein resistant surfaces. Naturally occurring compounds such as bovine serum albumin (BSA) (Bernard et al 2000), elastin-like polypeptides (Nath et al 2004), sarcosine (Ostuni et al 2001) and polysaccharides (Luk et al 2000) have been used. Synthetic compounds such as fluorocarbon polymers (Ko et al 2005), polyvinyl alcohol (Sugawara & Matsuda 1995) and polyethylene glycol (PEG) (Harris 2013) or the PEG-related oligo ethylene glycol (OGE) have been thoroughly studied (Lopez et al 1993a, Lopez et al 1993b, Ostuni et al 2001, Pale-Grosdemange et al 1991, Prime & Whitesides 1991).

1.5.2 Functional groups for covalent immobilisation of proteins

Various interactions can be used to immobilize protein on surfaces and they differ in binding strength, binding dynamics, packing density and arrangement, and reversibility of the assembly process. The simplest process is physical adsorption where proteins are attached to surfaces through attractive forces such as ionic, hydrophobic, or van der Waals forces. However, this physical adsorption is weak in binding force, low in surface occupancy and poor in binding stability, even though the binding shows some reversibility.

By contrast, covalent interactions more stably link proteins to surfaces through chemical bonds. Various surface-chemicals are capable of coupling with proteins and derivative surfaces through different functional groups (Table 1.1).

Table 1.1 Commonly available functional groups in proteins and functionalities of the required surfaces (Rusmini et al 2007).

Side groups	Amino acids	Surface group
-NH ₂	Lys, hydroxyl-Lys	carboxylic acid
		active ester (NHS)
		epoxy
		aldehyde
-SH	Cys	maleimide
		pyridyl disulfide
		vinyl sulfone
-COOH	Asp, Glu	amine
-OH	Ser, Thr	epoxy

Amine chemistry: lysine residues are the most commonly used anchor points for protein immobilisation, and they are typically on the exterior of the protein. However, the abundance of lysine residues can create multipoint attachment leading to heterogeneous immobilisation on the surface. N-Hydroxysuccinimide (NHS)-activated carboxylic acid is commonly utilized for coupling with amine groups, forming stable amide bonds (Patel et al 1997, Rao et al 1999). The immobilisation efficiency of NHS-esters depends on parameters such as pH, concentration, ionic strength and reaction time; the optimal parameters vary for different proteins.

Thiol chemistry: the unique thiol group in cysteine can create a disulphide bond (Jongsma & Litjens 2006). Oriented immobilisation is more likely to occur because of the small amount of cysteines in proteins comparing with lysines (< 1%). However, the low frequency of cysteines can necessitate their introduction to the surface of a target protein by protein engineering methods.

Carboxyl chemistry: mild coupling methods, such as carbodiimide activation (Fernandez-Lafuente et al 1993), can be used for covalent protein immobilisation via carboxylic groups through aspartic and glutamic acid, which are abundant on the surface of proteins.

Epoxy chemistry: epoxy chemistry shows stability at neutral pH values, in hydrated conditions, and is capable of forming strong bonds with minimal chemical modification of the protein. Though the covalent reactions between epoxy groups and proteins are known to be very slow, adsorbed proteins were shown to react at a high rate (Mateo et al 2002). Multifunctional groups with two moieties, one with groups for physical adsorption and the other with sufficient epoxy groups for covalent immobilisation, have been designed to improve the immobilization efficiency and protein stability (Grazú et al 2003, Wacker et al 2004).

Photoactive chemistry: photoactive chemistry requires heterobifunctional photo-linkers with one photo-reactive group and one chemical reactive group. Photoactive immobilisation starts from activation of photosensitive reagents by light of an appropriate wavelength, followed by chemical processes leading to the formation of covalent bonds between the photoactivated reagents and the biomolecules. The photoreaction is an efficient and fast reaction which can be performed at mild conditions, independent of pH and temperature. The commonly used photo-reagents, such as arylazides, diazirines, benzophenones, and nitrobenziles, are activated by light with $\lambda \geq 350$ nm, where most biomolecules are transparent. Photoactive chemistry also does not require functional groups from biomolecules, thus it shows a nice biological compatibility.

1.6 Techniques for fabricating patterns of proteins on surfaces

The increasing interest in the properties of microstructured or even nanostructured bio-materials forced improvements in fabrication techniques for immobilising biomolecules on surfaces with micrometre or nanometre scale precision. The fabrication process can be generally described as 'top-down' and 'bottom-up'. A 'top-down' process relies on lithographic techniques to pattern into a resistant medium on a surface. For example, the application of photolithography in the semiconductor industry which modifies a photoresist pattern with focused beams of light and develops it for the following cross-link. Similarly, electron-beam lithography also performs in a 'top-down' way but with higher resolution, for it uses the electron beam to expose the resist. The 'bottom-up' method, in contrast, relies on synthetic chemistry involving the breaking and reforming of covalent bonds to modify the functional groups on target molecules.

To fabricate biological material on surfaces with the size and shape in a controlled way, different external forces can be involved such as light, fields and gradients (Brusatori et al 2003, Caelen et al 2002, Ekblad et al 2009). The fabrication technique usually requires a direct deposition of target molecules or a surface modified by self-assembled monolayers (SAMs) of functional chemicals. The SAM chemicals generally have one head group with specific affinity for specific substrate (e.g. oxides, metals, metal-oxides, polymers, and semiconductors), an intermediate alkyl chain and a spacer, and a terminal functional group (e.g. acids, alcohols, amines, esters, fluorocarbons, nitriles) that can be stimulated by external force and be transformed for protein immobilisation.

In the following sections, the commonly used biomolecular fabrication techniques will be introduced including the original methods, the development of the processes, and some applications.

1.6.1 Soft lithography

Soft lithography is a non-photolithographic technique based on SAMs on surfaces and replicas from masters to create micro- or even nanofabrication (Xia & Whitesides 1998). Soft lithographic techniques are straightforward to apply, low in cost and effective in fabrication. Unlike photolithography which can be restricted by diffraction

limitation, soft lithography is capable of generating structures or patterns with feature sizes varying from 30 nm to 500 μm (Xia et al 1997, Zhao et al 1997). Moreover, soft lithography can generate structures in more than two dimensions with a wide variety of surface chemistries and materials. Soft lithography also shows disadvantages, such as inaccurate patterns generated by the stamp deformation, the defects in formed patterns caused by insufficient contact between the stamp and the substrate during printing, the difficulty of creating high-resolution structures because of the physical limitation of the stamps.

A large number of soft lithographic techniques have been established and they are all based on using an elastomeric stamp with relief structures to generate patterns. Several polymers can be used for stamp replication and the most widely used one is poly(dimethylsiloxane) (PDMS). PDMS has a good chemical stability and is unreactive towards most patterned molecules. PDMS is optically transparent to wavelengths down to 300 nm, so it allows the UV cross-linking to cure prepolymers even in mould form (Wilbur et al 1996). It is also stable to humidity and high temperature (up to 180 $^{\circ}\text{C}$), and it is durable so it can be used for over 50 times. The stamp is generally prepared by casting a liquid polymer precursor on a silanized master having relief structures on its surface, then it is cured and peeled off (Figure 1.19) (Zhao et al 1997). The master can be silanized by exposure to $\text{CF}_3(\text{CF}_2)_6(\text{CH}_2)_2\text{SiCl}_3$ vapour for ~ 30 min and the commonly used commercial PDMS elastomer kit is Sylgard[™] 184 obtained from DowCorning. The technical problems of PDMS stamps are from the collapse caused by gravity (when the height of the relief features $h \ll d$, the distance between them) or the deformation caused by the capillary force (when $h \gg d$) (Roca-Cusachs et al 2005, Sharp et al 2004). The proper ratio for a defect-free relief feature should be between 0.2 and 2 (Delamarche et al 1997). Other methods have been developed to overcome the deformation problem, such as backing the stamp with a rigid support, introducing a support for the noncontact regions, or using other stamp material like thermoplastics and fluorocarbon-modified siloxanes (Fichet et al 2002, Tsibouklis & Nevell 2003).

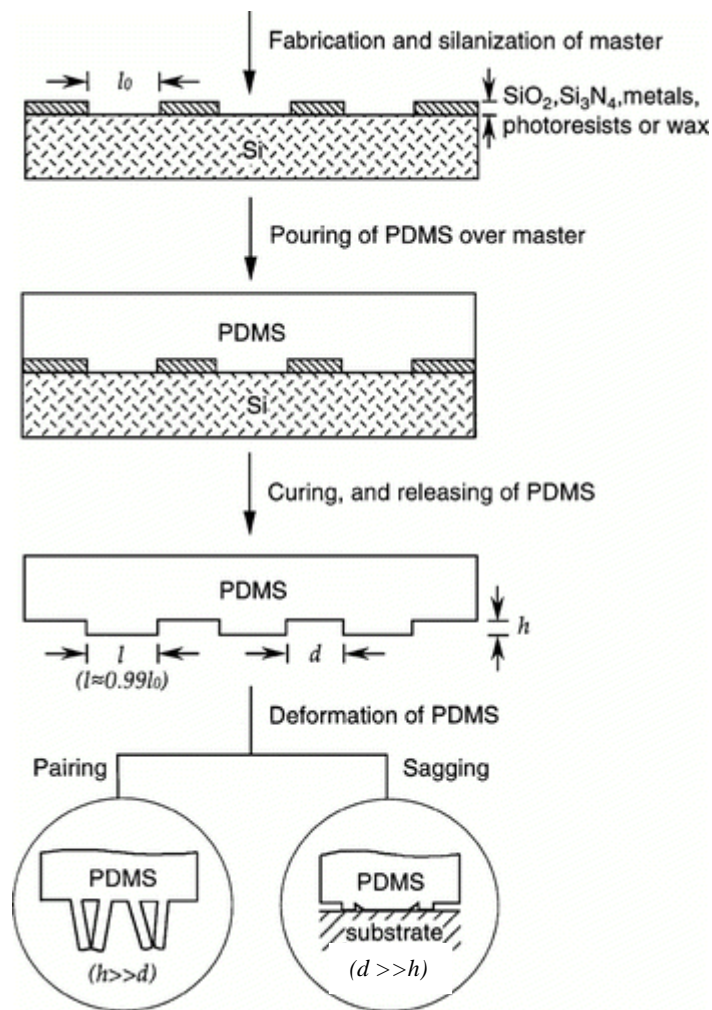


Figure 1.19. Schematic illustration of the procedure for casting PDMS replicas from a master having relief structures on its surface (Xia & Whitesides 1998).

Among all stamp based soft lithographic techniques, microcontact printing (μ CP) is the best known and most popular method (Kumar & Whitesides 1993). Other soft lithographic techniques include replica moulding (REM) (Lewis et al 2010, Xia et al 1996), microtransfer moulding (μ TM) (Lee et al 2005), micro-moulding in capillaries (MIMIC) (Lee et al 2008, Shim et al 2007), solvent-assisted micromoulding (SAMIM) (King et al 1997), and nanotransfer printing (Jeon et al 2004), etc.

When performing μ CP, the PDMS stamp is coated with ink (e.g. protein) and used to generate patterns on surfaces (Figure 1.20). This method can either generate SAMs as templates onto specific substrates, such as alkanethiols onto gold (Delamarche et al 1996), or it can directly print proteins onto target surfaces, such as chicken immunoglobulins (IgGs) onto glass and polystyrene surfaces (Bernard et al 1998). The

hydrophobic property of PDMS restricts its usage for water soluble inks, such as inorganic complexes or biomolecules (Gates et al 2005). However, this can be fixed by oxidising the PDMS surface using oxygen plasma or UV light, which then allows the printing of polar inks because of the formation of a thin silica-like surface layer during the oxidation (Ferguson et al 1993).

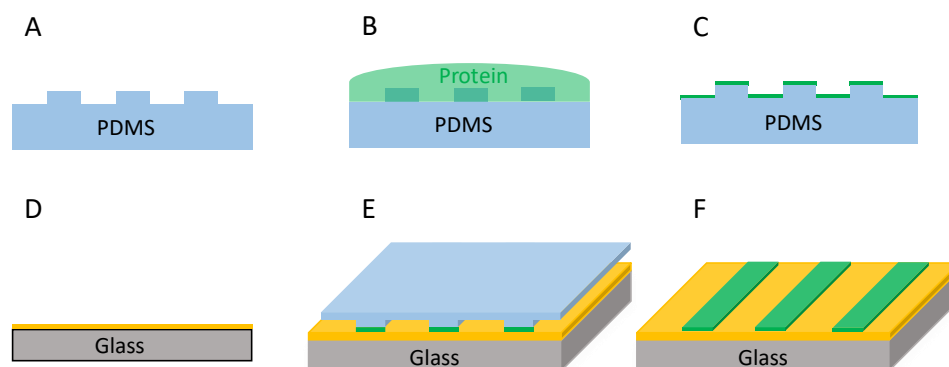


Figure 1.20. Schematic illustration of μ CP protein patterns using PDMS replicas.

The μ CP technique can be developed for multi-patterning to generate several different molecules on one surface. One way of doing this is performing the μ CP sequentially, e.g. sequential inking and printing. Stamps with different relief features can be printed many times onto the same surface, thus creating multiplexed patterns. One other way is parallel inking of a stamp followed by a single printing. This technique requires a flat stamp with no relief features so it is free from buckling or collapse problems (Perl et al 2009). The flat stamp is inked locally with different molecules in a patterned shape and it works as a molecule carrier, transferring the pre-patterned molecules to the target surfaces (Rozkiewicz et al 2007). Any patterning-by-adsorption method can be used for parallel μ CP. The resolution of parallel μ CP is limited by the inking system and microfluidic networks can offer physical limitation on exposed area during inking (Foley et al 2005, Juncker et al 2001).

μ CP has developed rapidly, based on the concept of transferring a molecule pattern to a surface by getting contact with the inked stamp. Various improvements to the process and the materials used overcame limitations of the original technique. Many molecules, polar or nonpolar, are currently compatible with the stamp and features below 100 nm can be reliably generated. The fabrication of multiple biomolecules

with high surface occupancy is still an open challenge, for both micro-scale and nano-scale patterns.

1.6.2 Nanoimprinting lithography

Nanoimprint lithography (NIL) is a parallel nanofabrication technique first introduced by Chou and co-workers in 1995 (Chou et al 1995, Chou et al 1996). It is a low-cost high-throughput method with a repeatable imprint process and durable imprint mould. The advantage of nanoimprint lithography is that it can easily pattern nanostructures at great precision on the nanometre scale over a large area. Unlike conventional photolithography, nanoimprint lithography does not rely on light beams, thus its resolution is not limited by diffraction limitation and its features are not affected by light scattering or interference. Chou first fabricated sub-25 nm patterns using nanoimprint lithography (Chou et al 1995), followed by the fabrication of sub-10 nm patterns (Guo 2007), and Austin even pushed the NIL feature resolution down to 5 nm (Austin et al 2004).

Nanoimprint lithography has two basic steps: imprint and pattern transfer (Figure 1.21). In the first imprint step, a mould with nanostructures on its surface is pressed into the resist coated substrate, followed by removal of the mould. This allows duplication of the features on the mould surface into the resist layer, creating a thickness contrast. The second step is pattern transfer where etching is used to remove the residual resist in the compressed area, thus transferring the thickness contrast pattern into the entire resist.

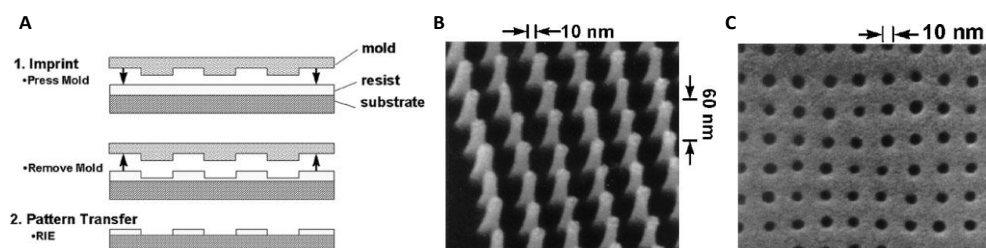


Figure 1.21. Schematic of the NIL process and SEM images of NIL fabrications

- A. Schematic of the originally proposed NIL process.
- B. Scanning electron microscopy (SEM) image of a fabricated mould with a 10 nm diameter.
- C. SEM image of hole arrays imprinted in poly(methyl methacrylate) by using such a mould.

(From Gao 2007)

The resist layer can either be a thermoplastic with a low glass transition temperature above which the resist becomes a viscous liquid (Chou et al 1995); or be a photopolymer that can be cured using UV exposure (Alkaisi & Mohamed 2010) (Figure 1.22). Unlike photopolymers, the thermoplastic resist has to be cooled down before the mould removal.

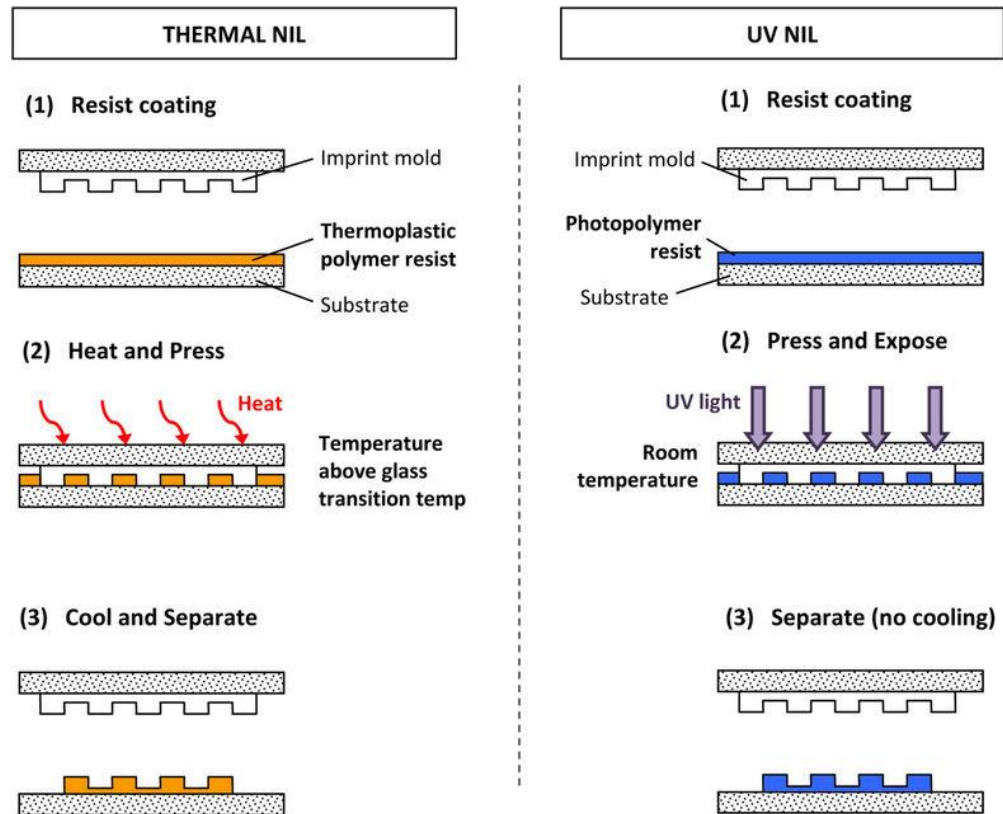


Figure 1.22. Schematic of thermal NIL and UV NIL processes (Kooy et al 2014)

The advantages of NIL have promoted this technology from laboratory to industry. NIL has been included in the International Technology Roadmap for Semiconductors as a candidate technology for 32- and 22-nm nodes. Moreover, NIL has been applied for fabrication of organic electronics (Cedeno et al 2002), organic lasers (Pisignano et al 2005), nanoscale control of polymer crystallization (Hu et al 2005), organic solar cells (Aryal et al 2008), and templates for tissue engineering (Truskett & Watts 2006).

Apart from those applications, NIL can create chemical patterns onto which proteins can self-assemble by biochemical interactions. NIL also allows the protein self-assembly process to be performed under liquid. These advantages help to protect the biomaterial from external pressure and maintain their structural integrity and

functionality. Hoff and co-workers extended the application for protein patterning and achieved a 75 nm pattern spatial dimension (Hoff et al 2004). Later, membrane protein complexes were self-assembled on chemically patterned glass using NIL (Escalante et al 2008b, Maury et al 2007). However, multi-biomolecule patterning using NIL remains a challenge and an alternative method combines NIL with other techniques such as micro- and nanomoulding in capillaries (Kumar et al 2009, Lee et al 2008, Shim et al 2007) (MIMIC), which has been used to inject different inks that bind specifically to the pre-patterned chemicals. Vasilev et al also fabricated a sub 100 nm LHCII/enhanced green fluorescent protein (EGFP) multi-pattern using a combination of NIL and replica transfer for self-assembly of functional groups (Vasilev et al 2014b) (Figure 1.23).

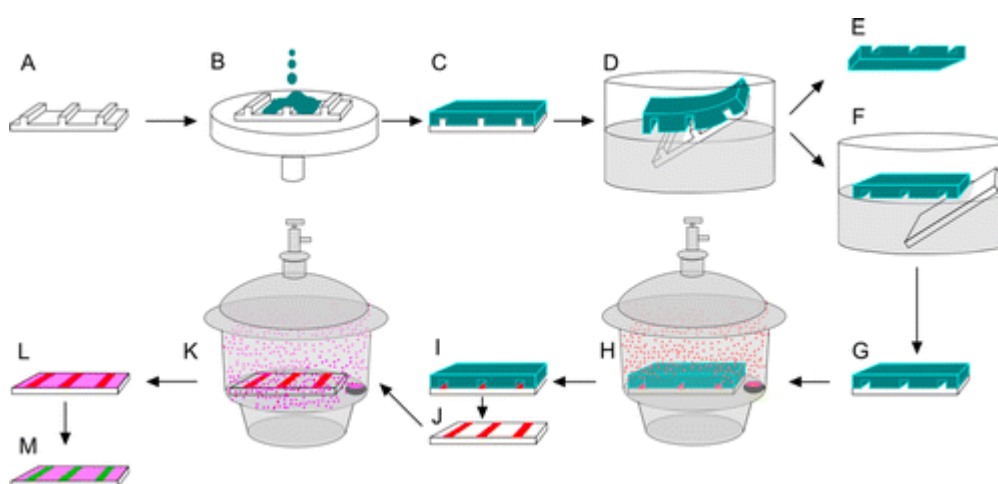


Figure 1.23. Schematic representation of the lithographic process.

The master template (A) is spin-coated (B) with a thin layer of polystyrene (PS), resulting in a sandwich structure where the PS layer replicates the topography of the master (C). The PS layer is then lifted from the master template in a water bath (D) and can be inverted for inspection (E). Then the PS film can be deposited on a clean flat substrate of glass or silicon (F, G), onto which an SAM of APTES is deposited in vapour phase (H). Subsequently, the masking PS layer is lifted off the substrate (I) and (J), followed by deposition of an SAM of MPTMS (K). The resulting chemically nanopatterned surface (L) is used for selective immobilization of LHCII and functionalized EGFP (M).

(From Vasilev, 2014)

1.6.3 Photolithography

Photolithography utilises light to introduce patterns into a light-reactive surface layer (del Campo et al 2005). This method has been used commercially to produce microelectronic devices with ~10 nm or sub-100 nm features, and to create features of functional chemical groups with micro- or nanometre dimensions, which is then used for fabrication of biological arrays (Chrisey et al 1996).

Photolithography is based on the interaction of light with a light-sensitive chemical resist (photoresist), often made using SAMs, because groups of individual molecules can be used to make layers thinner than 3 nm and smaller in area than 0.25 nm². Under irradiation in the UV range and in the presence of oxygen, the photoresist SAMs degrade and can be removed to form chemical patterns, such as for aryl- and alkylsilanes at 193 nm (Dulcey et al 1991). Similarly, patterns can be transferred to photosensitive and reactive SAMs which can be combined with many functional groups (Blawas & Reichert 1998). The procedure involves deposition of unprotected SAM groups and introducing photosensitive groups.

Patterns can be introduced onto surfaces by exposing the photosensitive SAMs to light in several ways, such as through a mask, using two interference light beams, or through a probe aperture on a scanning near-field optical microscope (SNOM). Whitesides and co-workers performed the first experiments using a mask to introduce micrometre patterns onto SAM-coated gold surfaces (Ryan et al 2004) (Figure 1.24). They deposited SAMs of polyfunctional alkanethiols on gold, presenting two photocleavable groups: the *o*-nitrobenzyl amine-protecting group and the thiolate bond (Au-S). The 365 nm light cleaves the amine-protecting group and the 220 nm light cleaves the entire SAM. The region exposed to 365 nm light can then cross-link to any group that contains a carboxylic acid, aldehyde, etc.; the region exposed to 220 nm light then allows a new SAM to form on it. Thus, a pattern of three SAMs having different properties can be produced on one gold substrate. Leggett and co-workers also reported using masks to fabricate micropatterns of different functional chemicals on either glass (Ahmad et al 2011, El Zubir et al 2017, Reynolds et al 2009, Xia et al 2016) or gold (Reynolds et al 2007) and micropatterns of polymer brushes on silicon surface (Johnson et al 2017). Those micropatterns can then be used for site specific protein immobilisation.

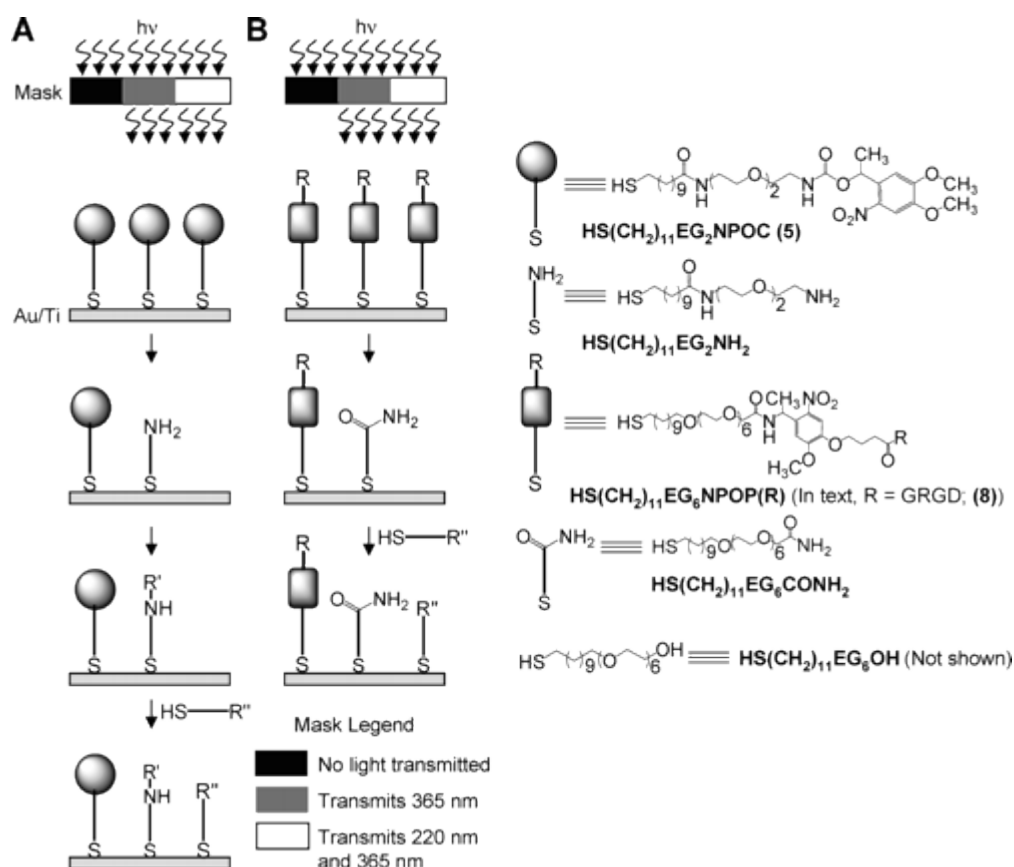


Figure 1.24. Patterning of a gold substrate with multiple, aligned SAMs using a photomask.

R represents any group that can be coupled to a carboxylic acid, e.g., amine, alcohol, etc.; R' represents any group that contains a carboxylic acid, aldehyde, etc. that can be coupled to an amine; R'' represents an arbitrary functionality that terminates with a thiol group.

A. A SAM terminates in amines after exposure to 365 nm light and 220 nm light.

B. A SAM terminates in primary amides after exposure to 365 nm light and 220 nm light.

(From Ryan et al 2004)

However, photolithography through masks lacks flexibility, in terms of changing the size and period of patterns. Interferometric lithography, in contrast, can fabricate patterns over very large areas (cm^2) (Adams et al 2010) (Figure 1.25). Interferometric lithography relies on the Fresnel mirror (Brueck 2005) to generate two interferometric beams. One beam projects directly onto the sample and the other beam is reflected by mirrors before reaching the sample, forming an optical path difference which leads to period variation in light intensity. When exposed to a specific wavelength, the photosensitive SAM forms sinusoidal patterns, with a period that depends on the wavelength of the laser beam used, the refractive index of the medium (the air), and the angle (θ) at which the two beam interfere (Brueck 2005)

(Figure 1.25). Interferometric patterned SAMs of different functional groups can then be used as templates to form patterns of biomolecules (Bird et al 2016, Moxey et al 2015, Patole et al 2015).

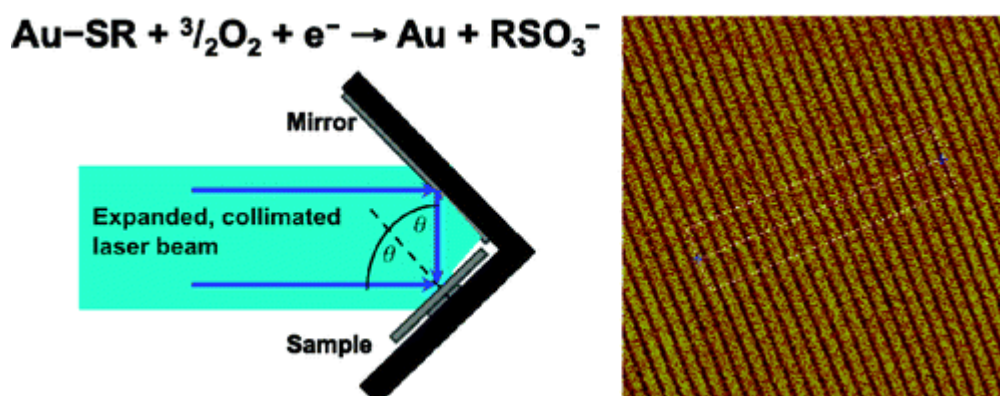


Figure 1.25. Interferometric lithography.

(Left) Schematic diagram of apparatus used in interferometric lithography and (right) the bovine serum albumin (BSA) pattern generated from interferometric exposures of OEG-terminated SAMs, followed by BSA incubation. (From Adams et al 2010)

One challenge of photolithography is the restriction on the spatial resolution of the fabricated pattern, which is determined by the diffraction limit; patterns with features below 200 nm are generally hard to achieve through photolithographic techniques. However, the invention of the SNOM overcomes this problem; scanning near-field photolithography (SNP) irradiates the surface by passing light through a narrow, sub-diffraction aperture at the tip of a probe (El Zubir et al 2017) (Figure 1.26). The spatial resolution achieved is determined by the size of the aperture rather than the wavelength of light, so SNP can fabricate 30 nm wide lines of octadecanethiol in a SAM of mercaptopropanoic acid (Sun & Leggett 2004). Moreover, lines of 9 nm in width has been fabricated into a SAM of mercaptoundecanoic acid on gold (Matthew Montague et al 2007). After patterning by SNP, the modified regions can be functionalised for site-specific protein attachment (Leggett 2012, Matthew Montague et al 2007, ul Haq et al 2010, Xia et al 2016). By applying SNP patterning steps sequentially, multiple proteins can be site-specifically immobilized at a single location (El Zubir et al 2017, Xia et al 2016).

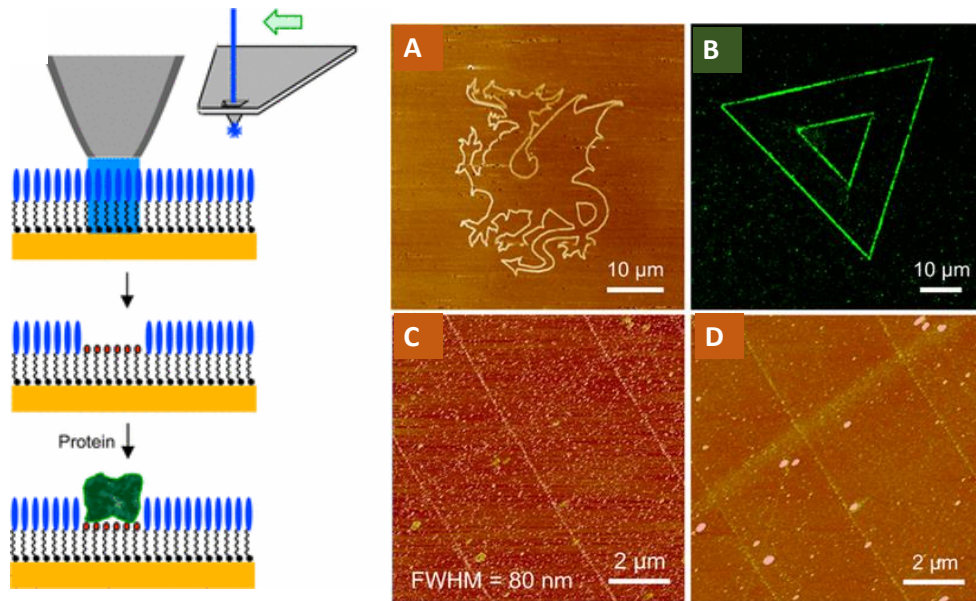


Figure 1.26. Scanning near-field photolithography

(Left) Schematic diagram of fabricating protein patterns by SNP. Near-field lithography with a fibre or cantilever probe leads to selective photoremoval of OEG-NPEOC protecting groups, exposing a protein-adhesive aminated surface onto which protein is adsorbed.

- A. Friction force microscopy image of a pattern fabricated by near-field exposure of an OEG-NPEOC-APTES film.
- B. Fluorescence microscopy image showing bright contrast from geometric shapes formed by near-field lithography followed by adsorption of FITC-labeled IgG.
- C. Tapping-mode phase image of YFP adsorbed to nanolines fabricated using an optical fibre probe in shear-force mode to modify OEG-NPEOC-APTES.
- D. Tapping mode height image of the lines shown in panel C.

(From El Zubir et al 2017)

1.6.4 AFM scanning probe lithography

A number of molecular patterning lithographic methods have been developed based on AFM scanning probe techniques. These lithographic methods either rely on physical processes to deposit or remove surface material; or rely on chemical reactions to modify surface molecules. AFM scanning probe lithography includes: dip-pen nanolithography, nanoshaving techniques, constructive nanolithography, and scanning near-field photolithography which can also be classified as photolithography (Figure 1.27) (Leggett 2012).

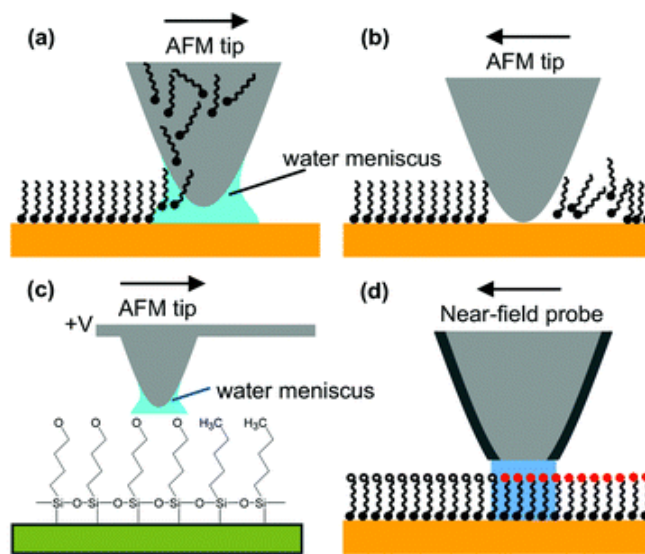


Figure 1.27. Schematic diagram of different AFM scanning probe lithography approaches.

Near-field lithography with a fibre or cantilever probe leads to selective photoremoval of OEG-NPEOC protecting groups, exposing a protein-adhesive aminated surface onto which protein is adsorbed.

- A. Dip-pen nanolithography.
- B. Nanoshaving.
- C. Constructive nanolithography.
- D. Scanning near-field photolithography.

(From Leggett 2012)

Dip-pen nanolithography, first reported by (Piner et al 1999), uses the AFM probe as a pen to directly write molecular solvent ink on surfaces (Demers et al 2002, Hong et al 1999, Hyun et al 2002, Ki-Bum Lee 2003, Lee et al 2002, Lee et al 2006a, Lee et al 2006b, Salaita et al 2006). The ink was initially a thiol but subsequently developed to include a number of biomolecules. Ink molecules are delivered from the AFM tip to

the surface via a meniscus between them. The size and shape of the nanofeatures can be controlled by adjusting the tip velocity for writing, the ambient humidity, surface chemistry and other parameters. Recently, Heath et al reported the fabrication of lipid lines with widths as low as 6 nm using dip-pen nanolithography (Heath et al 2014).

Nanoshaving techniques, in contrast, work by scanning an AFM tip across a sample surface, thus removing surface-bound molecules. The tip-scanned area is left blank for secondary chemical decoration (Amro et al 2000, Liu & Amro 2002, Wadu-Mesthrige et al 2001, Zhou et al 2003).

Both dip-pen nanolithography and nanoshaving are physical process, and neither of them performs surface chemical modification. Constructive nanolithography (also known as local-oxidation lithography), however, selectively modifies surface chemicals by applying a bias voltage between the AFM tip and the conductive substrate. Sagiv and co-workers first reported fabricating oxidation patterns on silane films (Maoz 2000a, Maoz 2000b), using constructive nanolithography. Subsequently, a number of specific bond-breaking operations have been reported using electron beams via constructive nanolithography. For example, selective reduction of the nitro group to amine on the nitrophenyl SAM (Golzhauer et al 2001); selective removal of the oligo(ethylene glycol) terminal group from the functionalised alkanethiols of a SAM for protein binding (Krakert et al 2010); selective oxidation of methyl-terminal groups on a hexadecyl SAM to carbonyl-containing groups, for cross-linking with protein via NHS-ester (Menglong Yang 2009); selective desorption of non-crosslinked material following by cross-linking with protein (Turchanin et al 2007).

As a direct-write, mask-less method, scanning probe lithography can bypass the diffraction limitation and fabricate patterns down to a few nanometres (Martínez et al 2007) (Figure 1.28). Such a small size just matches the size of most proteins and small biomolecules, which makes scanning probe lithography an attractive approach for nanoscale patterning of biomolecules.

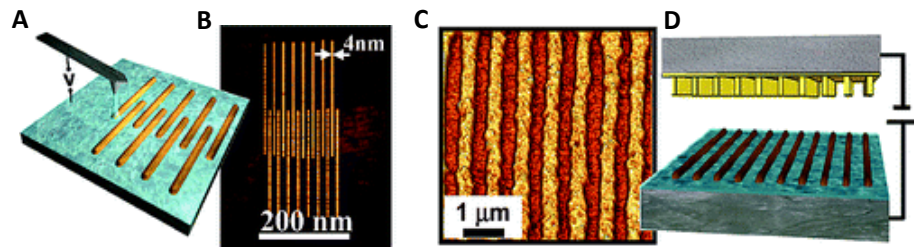


Figure 1.28. Schematics of constructive nanolithography and the generated patterns.

- A. Schematics of the constructive nanolithography by scanning probe AFM.
- B. AFM height image of a set of 16 interdigitated lines of 275 nm in length with a separation between nearest-neighbour lines of 10 nm.
- C. High resolution AFM image of the replica from the gold-coated DVD stamp with billions of reliefs. The replica shows a region of $20.8 \times 20.8 \mu\text{m}^2$ that contains 29 stripes with a periodicity of 740 nm.
- D. Schematics of the setup for performing the lithography in parallel using the gold-coated DVD stamp.

(From Martínez et al 2007)

1.6.5 Outlook for surface patterning of proteins

Native protein nanostructures such as complexes, supercomplexes, megacomplexes are important for both fundamental cellular studies and for novel protein-based biosensor design. Many patterning techniques have proved useful for the fabrication of functional protein assemblies on surfaces with controlled size and shape. However, such studies tend to focus on the methodology involved in surface chemistry and patterning a single type of usually a small, soluble protein, whilst patterning large membrane protein complexes, the retention of protein function, co-patterning different types of proteins, and protein-protein interactions are less explored following adsorption. The non-specific adsorption of proteins presents a major problem; protein consists of anionic, cationic, non-ionic, hydrophilic and hydrophobic structural units, and are strongly adhesive to most surfaces. Therefore, protein patterning techniques need to be improved to tackle the following challenges:

1. Non-specific and controlled attachment: protein deposition must be controlled in defined areas with nanometre precision.
2. Specific binding: proteins should be selectively introduced by specific interactions through different binding functional groups.

3. Retention of properties: proteins should remain functional after immobilisation.
4. Substrates: a variety of substrates must be explored, in order to study different properties and interactions of immobilised proteins. For example, transparent glass is ideal for studying optical properties of the protein but inappropriate for investigating its electrical properties; the opaque but conductive gold is just the opposite.
5. Multiple protein patterning: biochemical mechanisms rely upon protein-protein interactions; unless multiple protein types can be immobilised with controlled deposition, it will not be possible to make significant advances in nanobiotechnology, and in addressing biological problems.

The first two challenges listed above have been tackled through different methods, and the third challenge has received increasing attention, whilst the last two are still developing.

1.7 Förster resonance energy transfer

Förster resonance energy transfer (FRET) is an distance-dependent energy transfer mechanism first proposed by Thomas Förster in the 1940s (Förster 1946, Förster 1965). It describes the energy interaction between two light-sensitive molecules, known as a donor/acceptor pair. When FRET occurs, the excitation in the donor molecule is transferred to the adjacent acceptor molecule in a nonradiative manner. Thus, the excitation of the donor molecule results in the fluorescence emission of the acceptor molecule (Figure 1.29).

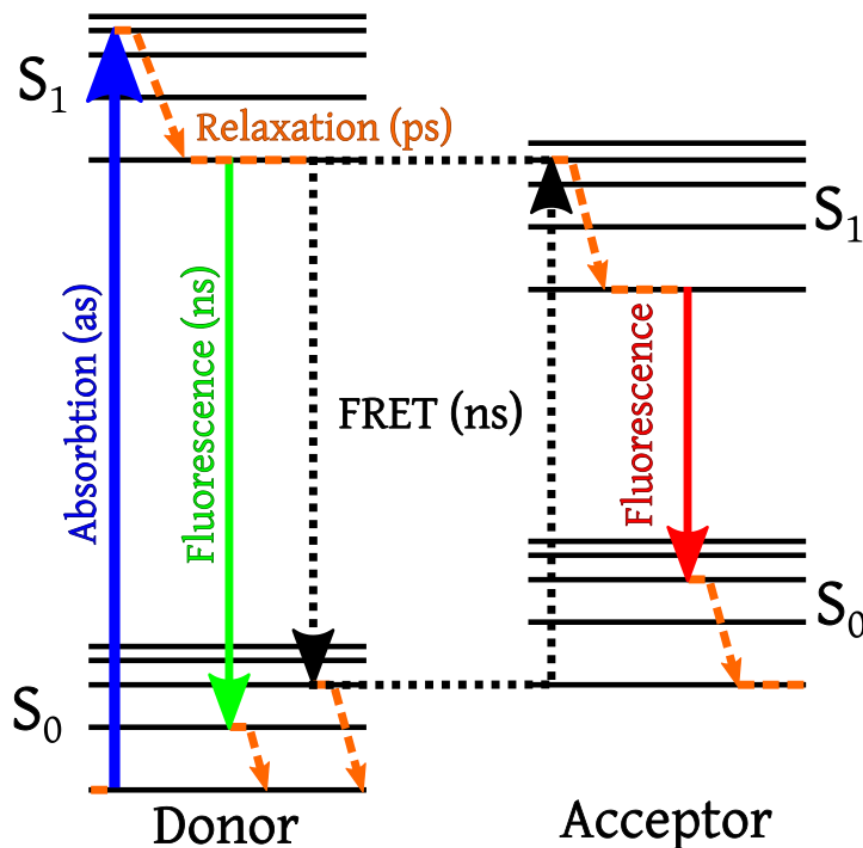


Figure 1.29. Jablonski diagram of FRET (Alex M Mooney - Own work, CC BY-SA 3.0, <https://commons.wikimedia.org/w/index.php?curid=23197114>)

In this diagram, electrons in the donor molecule absorb energy from excitation photons and transfer from the ground state (S_0) to the excited state (S_1) (blue arrow). Under typical fluorescence conditions, the excited electrons would release their energy by fluorescence emission and drop back to the ground state (green arrow). However, if a suitable acceptor molecule is close enough to the donor molecule (between 1 nm and 10 nm), the donor excitation energy can transfer directly to the

acceptor (blank arrows), and resulting in the nonradiative relaxation of the S_1 excited state to S_0 in the donor and the creation of an S_1 excited state in the acceptor. Thus, a decrease of donor fluorescence intensity can be observed accompanied by the increase of the acceptor fluorescence intensity (red arrow). The orange arrows represent vibrational relaxations.

Several primary conditions must be satisfied in order for resonance energy transfer to occur. First, the donor and the acceptor molecules must be within a certain distance (typically 1 nm to 10 nm); second, the absorption spectrum of the acceptor must overlap the fluorescence emission spectrum of the donor (Figure 1.30); third, the transition dipole orientation of the acceptor must be roughly parallel to that of the donor (Iqbal et al 2008, VanBeek et al 2007).

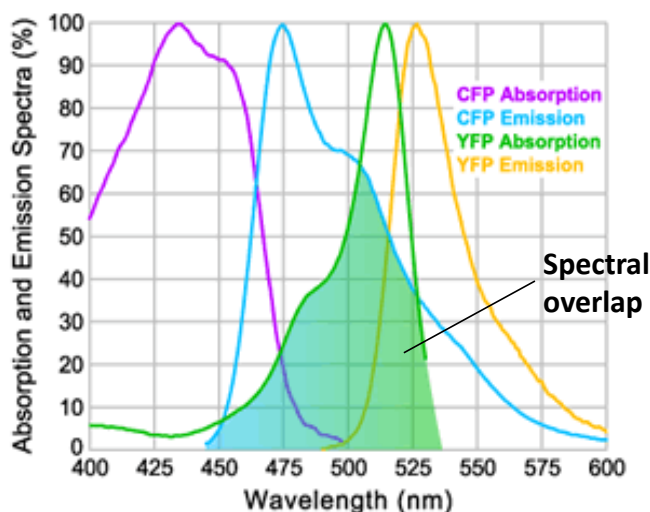


Figure 1.30. Spectral overlap of absorption and emission of CFP/YFP (taken from <https://www.semrock.com/fret.aspx>)

The FRET efficiency (E) refers to the quantum yield of the energy transfer and it is particularly sensitive to donor-acceptor distance (R) as represented by the equation:

$$E = \frac{1}{1 + (R/R_0)^6}$$

where R_0 is known as Förster radius and it stands for the critical distance at which energy transfer is 50% efficient. The value of R_0 depends on the spectral overlap of the donor and acceptor and the molecular orientation factor (K^2). The value of K^2 can range between 0 and 4. For a random orientation of the transition dipoles, the

average value of K^2 is 2/3. Table 1.2 listed typical values of R_0 between chlorophylls and bacteriochlorophylls (assuming $K^2=1$) (van Grondelle 1985).

Table 1.2. Förster radius (R_0) values for photosynthetic pigments (van Grondelle 1985).

Energy donor	Energy acceptor	R_0 (nm)
Chl <i>b</i>	Chl <i>a</i>	10
Chl <i>a</i>	Chl <i>a</i>	8-9
β -carotene	Chl <i>a</i>	~5
Bchl 875 in LH1	BChl 875 in LH1	9
BChl 800 in LH2	BChl 850 in LH2	6.6
BChl 800 in LH2	BChl 800 in LH2	10
Allophycocyanin	Chl <i>a</i>	7
Phycoerythrin	Phycocyanin	6

Due to the sensitivity to distance, FRET can be used in molecular biology to investigate protein-protein distance and interactions. In a FRET-pair protein system, the FRET mechanism results in changes in fluorescence emission intensity (an intensity drop from the donor and increase from the acceptor) and fluorescence lifetime (a shortened lifetime from the donor). The decrease in fluorescent lifetime from the donor, known as photobleaching, can be a convenient tool to measure the FRET efficiency. On the basis of the fluorescence lifetime, the FRET efficiency E is represented by the equation:

$$E = 1 - \frac{\tau_{DA}}{\tau_D}$$

where τ_{DA} and τ_D are the donor lifetime with and without the presence of the acceptor, respectively. The donor-acceptor distance, R , can be calculated by:

$$R = R_0 \left(\frac{1}{E} - 1 \right)^{\frac{1}{6}}$$

1.8 Sample imaging by atomic force microscopy

Conventional optical microscopy relies on illumination and lenses to obtain a magnified image of the sample. Due to the diffraction limit, the spatial resolution of optical microscopy is generally above 200 nm. In contrast, Atomic force microscopy (AFM) is based on an entirely different premise. AFM, as a scanning-probe microscopy method, is based on sensing the force between the AFM tip and the target sample to obtain the 3D topological images and the mechanical properties of the sample. Using a suitable tip, AFM can achieve a spatial resolution of a few nanometres, leading to the wide use of AFM in areas including material science, surface chemistry, molecular biology, cell biology and medicine.

1.81. Instrumentation

A scanning-probe AFM consists of a probe, a piezo scanner, laser feedback system (laser and detector), a controller and a computer (Figure 1.31). During AFM imaging, the sample is mounted onto the piezo scanner which moves the sample under the AFM probe on a scale from tens to hundreds of micrometres with a positional accuracy on the nanometre scale. The AFM probe consists of a flexible cantilever with a sharp probe at the end. The shape and spring constant of the cantilever and the tip radius of the probe are important factors for a high-resolution image. Generally, a sharp probe has a tip radius between 1 and 10 nm. During imaging, the probe is raster-scanned across the sample, tracing the sample surface. The uneven topology from the sample surface leads to deflection (bend) of the cantilever in varying different degrees and directions. A laser spot is directed onto the cantilever, and is reflected onto a position-sensitive photo-detector, thus monitoring cantilever deflection. The control system receives feedback from the detector and manipulates the piezoelectric scanner to adjust the sample position to maintain a constant interaction with the AFM probe and the sample. Based on the feedback required, the computer reconstructs a topography image of the sample surface from the line-by-line sample-probe interaction.

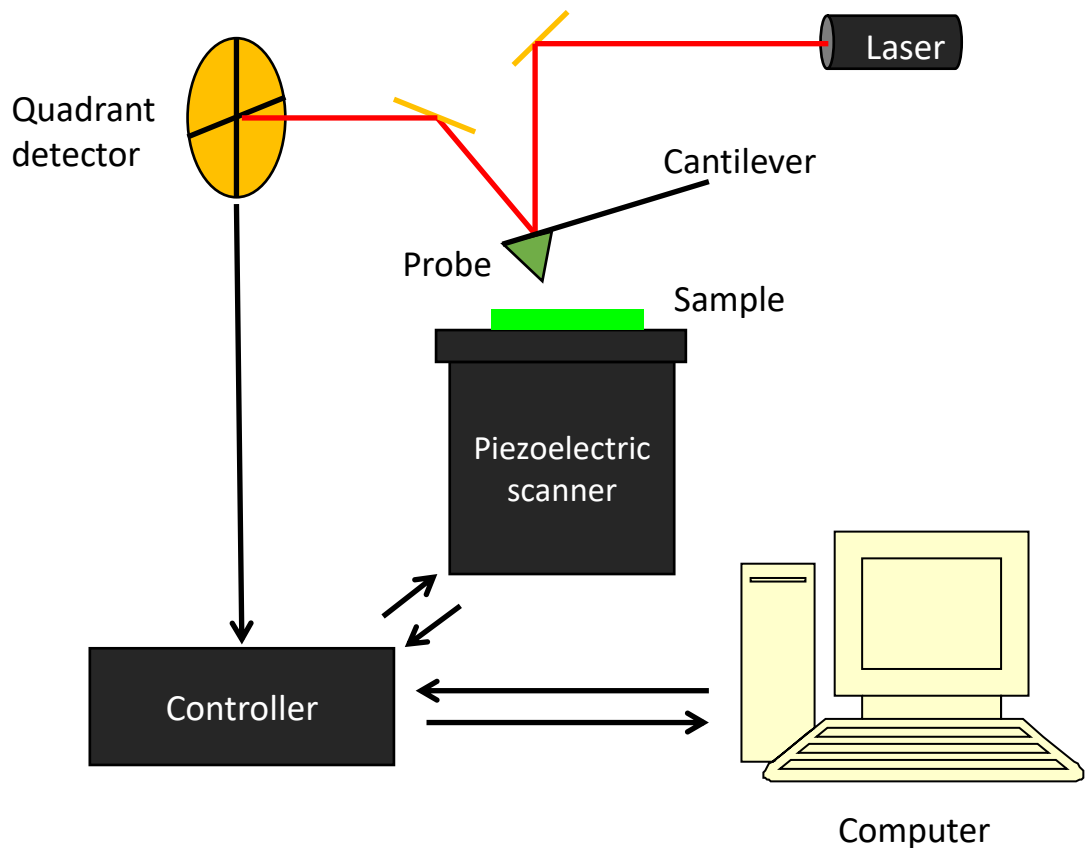


Figure 1.31. Schematic for AFM. (From MacGregor-Chatwin, 2014)

AFM samples are absorbed onto a flat substrate before imaging and freshly-cleaved mica is a good option because it is atomically flat and therefore shows no significant topography when imaged by AFM. Thus, all the topological features of biological material on mica arise from the sample. The sample-substrate is mounted on the piezo scanner which controls the precise movement of the sample in the x, y and z directions on the nanometre scale. The sample is scanned using the x and y piezo, and a computer-controlled feedback system adjusts the sample height via the z piezo, to maintain the close tracking of the probe.

Imaging can be performed either in air or in liquid. A 'fluid cell' is required when imaging in liquid, where the sample and probe are immersed in imaging buffer; this allows biological samples to be imaged under conditions similar to the native environment, and it also protects the sample from the capillary forces experienced during probe-sample interaction in air.

1.8.2 Imaging modes

The AFM can be run in two modes: contact mode and tapping mode. In contact mode, the probe is in constant contact with the sample during scanning and the cantilever deflection is measured. When the probe scans over a highly protruding structure, the cantilever deflection increases; the feedback system then adjusts the height of the sample and restores the cantilever deflection to its original position. From the height adjustment, the software can build a protrusion profile for each scan-line over the sample. During scanning, the force between tip and sample is kept constant. Abrasive forces can cause damage to the protruding structures or remove some weakly immobilised sample piece from the mica surface (Zhong et al 1993).

Alternatively, in tapping mode the probe is not in constant contact with the sample but it oscillates vertically over the sample during the scan, interacting transiently with the sample. This minimises the forces applied to the sample, which is important when imaging biological samples (e.g. cells membranes) (Möller et al 1999). Cantilevers with different resonant frequencies can be chosen and the AFM can be tuned to oscillate the cantilever at the appropriate frequency.

In tapping mode, the system monitors the amplitude of the tip resonance, which is lowered when the tip comes in contact with the sample. The AFM feedback system then lowers the sample position to restore the amplitude. The software then reconstructs a height profile of the sample surface according to the sample position adjustment.

Not long ago, a new tapping mode called “Peak Force Tapping” (PFT) (trademark, Bruker Nano Surfaces Business) was invented. In PFT mode, multiple force curves are generated at every pixel where the probe approaches towards and moves away from the sample. The force varies during the whole process due to the change of distance between the tip and the sample surface. In order to measure the force curve, the probe is oscillated at a fixed frequency, typically at 2 kHz. By analysing the force curve, extra properties of the sample can be measured, such as sample adhesion and deformation. Therefore, PFT offers more information about the sample compared to standard tapping mode.

Although tapping mode AFM protects the sample from damage by the scan force, it generally shows lower lateral resolution than contact mode AFM. However, some high-resolution tapping mode AFM has also performed on biological membranes and individual protein complexes, and even subunits, can be distinguished in the membrane (Adams & Hunter 2012, Bahatyrova et al 2004a, Olsen et al 2014, Olsen et al 2008). PFT also enables control over the scan force with high precision, thus PTF mode is also a preferred technique when imaging biological samples.

1.8.3 Advantages and limitations

AFM has several advantages in imaging, compared to conventional optical microscopy and transmission electron microscopy. First, AFM has achieved a very high resolution of 0.01 nm vertically and 0.1 nm laterally, enabling visualisation of protein subunits. Second, AFM has a high signal-to-noise ratio, allowing direct imaging of single molecules, with no averaging as required by X-ray crystallography or cryo-electron microscopy; thus native membrane proteins can be visualised without any computational processing. Third, AFM can image samples at atmospheric pressure and under liquid in near-native buffer condition, thus minimising the effect on the sample.

However, AFM also shows a few disadvantages. The image quality is highly dependent on variable factors: sample adsorption on the substrate, tip sharpness, vibrational interference and electrical interference. The tip manufacturing does not routinely produce perfect tip and some tips can be blunt or have defects such as a second apex (known as 'double-tip'). Thus, the image can look blurred or show a 'double image'. These drawbacks can be improved by choosing tip carefully, electrical and physical isolating the microscope, and choosing the appropriate buffers.

1.9 Aims of this work

The 3D structures of bacterial and plant photosystem complexes reveal the internal arrangements of cofactors that enable efficient solar energy harvesting and charge separation in photosynthesis (Ferreira et al 2004, Jones et al 2002, Jordan et al 2001, McDermott et al 1995, Roszak et al 2003). Atomic force microscopy (AFM) allows us to obtain the structural information for the membrane surface, showing the 2D organisation of these complexes (Sturgis et al 2009). However, the energy transfer and trapping behaviour of the natural photosynthetic membranes is still not fully explained. It is now feasible to use nanotechnology approaches to construct artificial photosynthetic systems that can simplify native arrangements and allow the study of photosystem architecture in a less complex way.

The distance scales for native energy transfer and trapping networks such as the chromatophore vesicles of purple bacteria, chlorosomes, or the thylakoids of cyanobacteria, algae and plants, are in nm scale, from 50 nm to 500 nm. Thus, nanotechnology can fabricate dots and lines on such scales (Escalante et al 2008a, Escalante et al 2008b, Reynolds et al 2007) and can address important issues regarding LH antenna: RC trap ratios, and their collective properties, organisation and distribution. Proteo-liposome reconstitution can assemble LH antenna and RC complexes into a lipid bilayer, tens to hundreds of nanometers in scale. The reconstitution system can mimic the natural surroundings of the proteins and can control the types of proteins studied, and their ratios (Sumino et al 2011a, Sumino et al 2011b). Also, it is possible to study mixtures of complexes, such as hybrid bacterial/plant photosystems, or de novo designed maquettes and natural complexes, that would be impossible to assemble in a living organism through genetic means.

Although nanopatterning technology and proteo-liposome reconstitution techniques allow light harvesting complexes to be assembled on surfaces or in a lipid system, challenges still remain: assembly of arrays of light-harvesting complexes, sufficiently closely packed for long-range energy migration; assembly of multiple types of protein complexes on the same surface to form an artificial light-harvesting and energy transfer system; retained functionality of the light harvesting complexes within the assembled artificial system. Could such assemblies harvest light and perform energy

migration, and eventually a charge separation, as in the natural photosynthetic membrane?

The work in this thesis explored a variety of techniques to tackle the challenges mentioned above. These include the following approaches.

1. The use of soft lithography to fabricate micrometre patterns of both LH2 and RCLH1 complexes, with intersecting regions on glass surfaces. Protein arrangements were studied by AFM and energy migration in the patterned system was verified using a combination of fluorescence lifetime and spectral imaging microscopy.

2. The development of conductive nanolithography, and its use to pattern LH2, RCLH1 and LHCII complexes on semiconductive silicon substrates, including co-patterning multiple complexes on one surface at the same location. The achievement of a high density of protein packing in the nanopatterns and observation of energy transfer from LH2 to RCLH1.

3. Reconstitution of LH2 and RCLH1 complexes in a mixed liposome system, with a series of LH2: RCLH1 ratios. Protein arrangements were investigated by AFM, and light harvesting and energy migration were studied under different conditions using fluorescence lifetime imaging microscopy.

4. The use of soft lithography to fabricate micrometre patterns of both LHCII and RCLH1 complexes, with intersecting regions on glass surfaces. Energy migration in the patterned system was verified using a combination of fluorescence lifetime and spectral imaging microscopy.

Materials and Methods

2.1 Standard buffers, reagents and media

All buffers and culture media were prepared as described, unless otherwise stated (Maniatis et al 1982). All media and solutions were prepared using distilled water purified using the Milli-Q system (Millipore). Growth media were made following the manufacturer's instructions, using distilled water and sterilised by autoclaving for at least 20 minutes at 15 psi above atmospheric pressure. All other solutions were sterilised by filtration through 0.45 µM filters before using. Heat labile solutions, such as vitamins and antibiotics, were added to culture medium only when they had cooled to below 45 °C.

2.2 *Rhodobacter sphaeroides* strains and growth

2.2.1 *Rhodobacter sphaeroides* strains

All *Rhodobacter sphaeroides* (*Rba. sphaeroides*) strains used for this work are listed in Table 2.1. *Rhodobacter sphaeroides* or *Rba. sphaeroides* refers to the wild type (WT) *Rba. sphaeroides* strain 2.4.1, unless otherwise stated. Strains were grown in M22+ medium (See Appendix: Growth medium for *Rhodobacter sphaeroides*) (Hunter & Turner 1988) and supplemented with 10,000 X vitamins (0.08 M nicotinic acid, 0.01 M thiamine, 7.3 mM 4-aminobenzoic acid, 0.4 mM d-biotin), to a final concentration of 1 X, at 34°C.

2.2.2 Growth on agar plates

Cells were streaked out from glycerol stocks onto plates of M22+ agar (see Appendix: Growth medium for *Rhodobacter sphaeroides*). Plates were incubated at 34 °C for approximately three days until single colony could be observed.

Table 2.1 *Rhodobacter sphaeroides* strains

Strain	Properties	Source/reference
2.4.1	Wild type	S. Kaplan, University of Texas
$\Delta pufBALMX$	In frame genomic deletion of <i>pufBALMX</i> .	E. Martin, University of Sheffield
$\Delta puc1BA \Delta puc2BA$	In-frame genomic deletion of <i>puc1BA</i> and <i>puc2BA</i> .	E. Martin, University of Sheffield
RCH-His	Genomic modification to give a C-terminally tagged reaction centre-H subunit	(Vasilev et al 2014a)
$\Delta crtB$	In frame genomic deletion of <i>crtB</i> .	(Grayson et al 2017)

2.2.3 Semi-aerobic growth

Rba. sphaeroides cultures were routinely grown semi-aerobically in the dark at 34 °C in an orbital shaker set at 160 rpm. These conditions induced the maximal biosynthesis of pigments (Niederman et al 1976). Single colonies were inoculated into 10 ml of M22+ medium and grown at 34 °C with 160 rpm shaking for 48 hours. Subsequently, the 10 ml culture was added to a 125 ml conical flask containing 80 ml of M22+ medium and grown under the same conditions overnight. These cultures were then grown further by transfer to a 2 L conical flask containing 1.5 L of M22+ medium or transfer to an appropriate vessel for photosynthetic growth (Section 2.2.4).

2.2.4 Photosynthetic growth

For growth under photosynthetic conditions, anaerobic cultures were exposed to either 20 W MEGAMAN® CFL bulbs, or 116 W Osram Halogen Eco Pro bulbs to achieve the desired light intensity. Light intensity was measured in $\mu\text{mol photons s}^{-1} \text{m}^{-2}$ using a LI-250A Light Meter equipped with a LI-190 Quantum Sensor (LI-COR

Biosciences). 1 ml semi-aerobic culture was added into a 30 ml universal tube, then filled with M22+ medium and incubated in the light for 48 hours with a magnetic stir bar for gentle agitation. This culture was used to inoculate a 500ml medical flat bottle filled to the top with M22+ medium, grown with a magnetic stir bar for gentle agitation, to the desired cell density.

2. 3 Purification of protein complexes from *Rba. sphaeroides*

2.3.1 Cell harvesting and breakage

Cells were pelleted at 4,000 x *g* for 30 minutes at 4 °C, then resuspended in standard 'Membrane Buffer' (20 mM HEPES, 5 mM EDTA, pH 7.5) at approximately 5 g of cells per 10 ml buffer. A small spatula of lysozyme and deoxyribonuclease I from bovine pancreas (Sigma) were added to the cells, then incubated at 25 °C for 30 min in the dark. The cells were disrupted twice in a French pressure cell at 18,000 psi. Unbroken cells were removed by centrifugation at 33, 000 x *g* at 4 °C for 20 minutes. The supernatant was transferred to a clean tube ready for loading onto a sucrose gradient.

2.3.2 Preparation of intracytoplasmic membranes (ICM)

High concentrations of intracytoplasmic membranes (ICM) were prepared using a 15/40 % (w/w) discontinuous sucrose gradient. 5 ml of broken cells (Section 2.3.1) were layered onto the 15 % sucrose band and centrifuged at 27, 000 rpm (65,000 x *g*) in a Beckman Type 45 Ti rotor at 4 °C for 8-12 hours. A pigmented band of ICM formed at the 15/40 % interface, which was collected. The ICM sample was diluted three-fold in working buffer (20 mM HEPES, pH 7.5) and spun at 40,000 rpm (125,171 x *g*) in a Beckman Type 45 Ti rotor for 2 hours at 4 °C to pellet the membrane. The pellets were homogenised in approximately 3 ml of the working buffer.

2.3.3 Solubilisation of ICM by detergent

Membranes harvested from discontinuous sucrose gradients (Section 2.3.2) were solubilised in 3 % (v/v) β -DDM by stirring in the dark at 4 °C for 45 min. The solubilized membrane solution was diluted at least three-fold in working buffer and centrifuged for 1 hour in a Beckman Ti 70.1 rotor at 48,000 rpm (160,000 x *g*) at 4 °C to remove insolubilized material. The supernatant was collected.

2.3.4 Purification of His-tagged proteins

His-tagged RCLH1 (His₁₂-RCLH1) complexes were purified on a 5 ml Chelating Sepharose fast-flow Ni-NTA column (GE Healthcare). The column was first washed with 20 ml QH₂O to wash away the ethanol used for storing the column. Solubilised membranes (Section 2.3.3) were applied to the column, equilibrated with 10 mM HEPES pH 7.4, 500 mM NaCl, 10 mM imidazole, 0.03% w/v β -DDM buffer. A gradient of 10 mM to 400 mM imidazole was applied and the His₁₂-RCLH1 eluted at an imidazole concentration of \sim 300 mM. Eluted protein was then applied to a DEAE-Sepharose column equilibrated with 10 mM HEPES pH 7.4, 50 mM NaCl, 0.03% w/v β -DDM buffer. A gradient of 50 mM to 300 mM NaCl was applied with the main peak of pure protein eluting at a NaCl concentration of \sim 280 mM. Fractions with an A880:A280 absorbance ratio greater than 1.9 were pooled and applied to a HPLC column (Phenomenex BioSep) eluting at a flow rate of 0.3 ml min⁻¹. The second elution peak (corresponding to the monomeric fraction of RC-His₁₂-LH1-PufX) was collected and concentrated using Amicon 100,000 MWCO spin filters (Millipore) in 10 mM HEPES pH 7.4, 50 mM NaCl, 0.03% w/v β -DDM buffer.

2.3.5 Purification of proteins using ion-exchange chromatography

Proteins lacking a His-tag, for instance WT-LH2, WT-RCLH1, Δ *crtB* RCLH1, were purified on a 5 ml DEAE-Sepharose (Sigma) ion-exchange column. The column was first washed with 20 ml QH₂O in order to remove the ethanol used for storing the column. Solubilized membranes (Section 2.3.3) were applied to the column, which was equilibrated with 100 ml of buffer A (20 mM HEPES, 0.03 % β -DDM, pH 7.8). A gradient with an increasing NaCl concentration at 1 mM ml⁻¹min⁻¹ was applied to the column using high salt buffer B (20 mM HEPES, 0.03 % w/v β -DDM, pH 7.8, 1 M NaCl). The bound LH2 and RCLH1 eluted at a NaCl concentrations of \sim 150 mM and \sim 280 mM, respectively. After the first DEAE-Sepharose column, fractions with an absorbance ratio greater than level 1 (Table 2.2) were collected, diluted twice in Buffer A and applied again to a DEAE-Sepharose column. The same washing and elution protocol was applied. After elution, fractions having a ratio greater than level 2 (Table 2.2) were pooled and concentrated using Amicon 100,000 MWCO spin filters (Millipore) in 10 mM HEPES pH 7.8, 50 mM NaCl, 0.03% w/v β -DDM buffer.

Table 2.2 Absorbance ratios for collection of purified complexes

Protein	Reference absorbance bands	Ratio level 1	Ratio level 2
WT-LH2	A850:A280	2.2	3.3
WT- RCLH1	A870:A280	1.7	1.9
<i>ΔcrtB</i> RCLH1	A870:A280	1.7	2.0

2.4 Purification of LHCII from spinach

2.4.1 Spinach sources

Briefly, mature spinach leaves were purchased from a local supermarket.

2.4.2 Thylakoid preparation

Spinach leaves were placed in a pre-cooled kitchen blender. Ice-cold buffer (50 mM Na₃PO₄, pH 7.4, 5 mM MgCl₂, 300 mM sucrose) was added to leaf material at a ratio of 1:1 (v/w). The material was homogenised for approximately 30 seconds and filtered twice: firstly, through two layers of muslin cloth and, secondly, through a layer of cotton wool sandwiched between two sheets of muslin cloth. The filtered material was centrifuged at 3, 000 x *g* for 15 min at 4°C. The pellet was resuspended in 50 ml osmotic break buffer (10 mM Tricine, pH 7.4, 5 mM MgCl₂) before mixing with 50 ml of osmotic halting buffer (10 mM Tricine, pH 7.4, 5 mM MgCl₂, 400 mM sucrose) and centrifuged again at 3, 000 x *g* for 10 min. The resulting pellet yielded thylakoids.

2.4.3 Thylakoid digestion

Thylakoids extracted from spinach leaves (see above) were digested using n-Dodecyl α -maltoside (α -DDM). Unbroken thylakoids were removed by centrifugation at 1, 000 x *g* for 5 min.

2.4.4 Purification of LHCII trimers

Trimeric LHCII from spinach was prepared following well-established protocols as previously described by (Ruban et al 1994), with some modifications to give a high level of purity. Briefly, LHCII trimers were isolated from digested thylakoids by

sucrose gradient sedimentation (8-14% sucrose, centrifugation at 100,000 x *g* for 36 hours at 4 °C) and the trimeric form was purified by subsequent high-resolution size-exclusion FPLC (AKTA).

2. 5 Room temperature absorption spectra

Room-temperature absorbance spectra were recorded on a Cary 60 UV-Vis spectrophotometer (Agilent) at wavelengths 950 nm - 260 nm in an ultra violet (UV) cuvette with a 1 cm path length. Baselines were corrected in the same range. Dilutions were made using the appropriate buffer or growth medium.

2. 6 Room temperature fluorescence emission spectra in solution

All emission and excitation fluorescence spectra were recorded in either buffer A (20 mM HEPES, 20mM NaCl, 0.03% w/v β -DDM) or buffer B (20 mM HEPES, 20mM NaCl). Measurements were recorded at room temperature in a 1 cm path-length quartz cuvette on a HORIBA FluoroLog spectrofluorometer (HORIBA Inc.). Excitation was provided from a tungsten light source in the visible-IR region of the spectrum. Fluorescence emission spectra were recorded using an excitation wavelength of 470 nm with 14 nm excitation slit widths and scanning emission from 500 nm - 950 nm, with 4 nm emission slit widths. All fluorescence spectra were acquired as averages of 10 scans.

2.7 Fluorescence life-time imaging microscopy (FLIM)

2.7.1 Home-built fluorescence microscope

The fluorescence emission properties of samples were measured on a home-built time-resolved fluorescence microscope. The microscope is equipped with 2 sets of light sources: a 420 nm LED (Thorlabs, M420L2) and a 470 nm LED (Thorlabs, M470L2) for wide field fluorescence images; and a 420/485 nm picosecond diode laser (PicoQuant, PDL 828) for spectral and lifetime measurements. The excitation light is focused by a 100 \times objective (PlaneFluorite, NA = 1.4, oil immersion, Olympus) and the fluorescence emission is collected from the same focal spot on the sample. The collected light is then filtered by dichroic beam-splitters to remove the background excitation light using the 458 nm dichroic beam-splitter (Semrock) when exciting with

the 420 nm LED or the 425 nm laser, or using the 495 nm dichroic beam-splitter (Semrock) when exciting with the 470 nm LED or the 485 nm laser. A filter wheel was equipped with 6 filters to allow filter selection as each measurement requires. A spectrometer (Acton SP2558, Princeton Instruments) was used for measurements requiring wavelength selection, an electron-multiplying charge-coupled device (EMCCD) detector (ProEM 512, Princeton Instruments) was used for photon collecting and a hybrid detector (HPM-100-50, Becker & Hickl) was used for photon counting. The modulation of the laser was synchronized with a time correlated single-photon counting (TCSPC) module (SPC-150, Becker & Hickl) for lifetime decay measurements. The objective is equipped with a piezo scanner (nPoint) to allow laser scanning of the sample for acquiring fluorescence spectral images and fluorescence lifetime images.

2.7.2 Fluorescence images

Samples were excited by the 420 nm LED or the 470 nm LED light source and fluorescence emission was filtered by individual bandpass (BP) filters: a 900/32 nm BP for RCLH1 complexes, an 857/30 nm BP for LH2, and a 679/41 nm BP for LHCII complexes. The entrance slit of the spectrometer was fully opened to collect all emission from the objective field. Fluorescence images were recorded by the EMCCD camera.

2.7.3 Measurement of fluorescence emission spectra

Samples were excited by the 420/485 nm laser and the fluorescence emission selected by long-pass filters before being diffracted by the spectrometer and recorded by the EMCCD. To work in a confocal mode, the entrance slit of the spectrometer was closed to 100 μm and only 15 pixel arrays of the EMCCD were involved in spectral recording. A grating with 150 lines/mm (150T) was used to select the wavelength for spectrum recording. Fluorescence spectral images were recorded by scanning the excitation laser on the sample using the piezo scanner (nPoint).

2.7.4 Measurement of fluorescence lifetimes

Samples were excited by the 420/485 nm pulsed laser at 1 MHz. Time-Correlated Single-Photon Counting (TCPSC) was applied for triggering the laser and counting the photon arrival time. TCPSC is a well-established and a common technique for fluorescence lifetime measurements. It detects single photons and measures their

arrival times in respect to the light source. For the measurements in this work, the entrance slit of the spectrometer was closed to 100 μm . A grating with 150 lines/mm was used to select the wavelength. A specific bandpass filter (Section 2.7.2) and a secondary exit slit on the spectrometer were used to narrow the recording wavelength range to 3 nm. Fluorescence lifetime images were recorded by scanning the excitation laser over the sample using the piezo scanner (nPoint).

2.7.5 Analysis of fluorescence data

Wide field fluorescence images were analysed by Image J, Spectral data were analysed by OriginPro, and the fluorescence decay curves were analysed by OriginPro and TRI2 (open source), with fitting using the multi-exponential decay function:

$$I(t) = A_1 \exp\left(\frac{-t}{\tau_1}\right) + A_2 \exp\left(\frac{-t}{\tau_2}\right) + B$$

Where τ is the fluorescence lifetime, A is the fractional amplitude contribution of the decay component, and B is the background. The quality of the fit was judged on the basis of the reduced χ^2 statistic:

$$\chi^2_{\text{red}} = \frac{\sum_{k=1}^n \frac{[I(t_k) - I_c(t_k)]^2}{I(t_k)}}{n - p} = \frac{\chi^2}{n - p}$$

where t_k is the time point k , $I(t_k)$ is the data at the time point k , $I_c(t_k)$ is the fit at the time point k , n is the number of the data points and p is the number of the variable fit parameters ($n - p = \text{degrees of freedom}$).

Using a mirror to replace the sample, the time delay of the laser from the pulse starting point to the instrument responding point was measured. Such time delay was defined as the instrument response (IRF), which was approximately 130 ps on the home-built fluorescence microscope. The IRF was taken into account when the fitting was performed for the decay curves.

2. 8 Atomic force microscope (AFM) imaging

2.8.1 Instrumentation

All images were acquired on the Multimode VIII instrument controlled by the NanoScope 5.0 controller (Bruker Nano Surfaces Business) and NanoScope software

(Bruker, v8.15). Data analysis and image processing was done by NanoScope Analysis 1.5, Gwyddion (open source), OriginPro 2015 and ImageJ (open source).

2.8.2 Buffer and sample adsorption

Buffer conditions varied depending on the nature of the sample. For liposome-protein samples, the adsorption buffer contained 20 mM MOPS (pH 7.8), 20 mM NaCl and 5 mM MgCl₂, and the imaging buffer contained 20 mM MOPS (pH 7.8) and 20 mM NaCl. The liposome-protein samples were pipetted onto freshly cleaved mica discs (9 mm mica discs, from Agar Scientific) and incubated for 1 hour at 4°C in the adsorption buffer. Prior to imaging, the adsorption buffer was removed by pipetting and the mica was washed three times by imaging buffer.

For the rest of the samples (protein patterns on silicon surfaces), AFM images were recorded either in air or in imaging buffer containing 20 mM HEPES (pH 7.8) and 20 mM NaCl. The samples were imaged on their silicon substrate rather than on mica.

2.8.3 Imaging patterned samples created by PDMS soft-patterning lithography

Topography details were recorded by the AFM for protein patterns created by PDMS soft-patterning lithography (Section 2.9). AFM images were recorded by tapping mode in air using silicon probes with an aluminium reflective coating (OTESPA-R3, Bruker, nominal spring constant $\sim 26\text{N/m}$, nominal resonance frequency $\sim 300\text{ kHz}$). Images were taken with 512 x 512-pixel arrays.

2.8.4 Imaging nanopatterned samples created by local oxidation lithography

Topography and friction images of the oxidised molecules from the local oxidation nanopatterning (Section 2.10) were recorded immediately following local oxidation lithography. AFM imaging was performed in contact mode in air by a conductive AFM probe (Bruker, CONTV-PT) coated by a Pt-Ir layer. When protein immobilisation was complete, protein patterns were imaged in peak-force tapping mode in imaging buffer (Section 2.8.2) using 'SNL-10' probes (56 kHz, $k\sim 0.24\text{Nm}^{-1}$) (Bruker Nano). The peak-force amplitude was 10 nm and images were taken using 256 x 256 or 512 x 512-pixel arrays. The peak-force set point varied between 50-1000 pN and the scan rate was between 0.5-1.0 Hz.

2.8.5 Imaging liposome-protein samples

Liposome-protein samples (Section 2.11) were diluted to a usable concentration in adsorption buffer (Section 2.8.2) and incubated on mica for imaging. AFM images were recorded in peak-force tapping mode in imaging buffer (Section 2.8.2) at a peak-force frequency of 2 kHz unless otherwise stated. SNL-10 probes (56 kHz, $k \sim 0.24 \text{ Nm}^{-1}$) (Bruker Nano) were used for peak-force tapping. When imaging under liquid the standard fluid cell was used to house the AFM probe and to control it. Once the probe had been inserted into the fluid cell, the reservoirs were filled with imaging buffer (Section 2.8.2) and mounted on top of the sample where the laser was aligned with the probe. The peak-force amplitude was 10 nm and images were taken using either 256 x 256 or 512 x 512 pixel arrays. The peak-force set point varied between 50-1000 pN and the scan rate was between 0.5-1.0 Hz.

2. 9 PDMS soft-patterning

2.9.1 Stamp preparation

The Si master template (Mikromasch, TGZ11), with rectangular arrays of 5 μm width, 10 μm pitch and 1.35 μm step height, was used as master to replicate a polydimethylsiloxane (PDMS) stamp (Zhao et al 1997). Prior to casting of the PDMS mixture, the Si master template was treated in trichlorosilane (Sigma-Aldrich) vapour under vacuum (20 mbar) for 16 hours. The PDMS mixture was prepared by mixing a Sylgard184 silicon elastomer base (Dow Corning) and a Sylgard184 silicon elastomer curing agent (Dow Corning) at a ratio of 10:1. The PDMS mixture was stirred for five minutes to reach uniformity and centrifuged at 3,000 x g for 15 min to remove air bubbles. Then the PDMS mixture was cast onto the Si master and cured at 74°C for 8 hr, before being carefully detached as a PDMS replica stamp.

2.9.2 Active cross-linking of substrates

The PDMS soft-patterning was performed on a poly-L-lysine coated substrate, either a glass coverslip (Fisher scientific, Corning BioCoat, REF 354085) or silicon. The substrate was treated with 20 mM dimethyl suberimidate.2HCl (DMS) (Thermo Fisher Scientific, Prod #20700) for 40 min at pH 8.5 to activate lysine as the cross-linker for amine attachment.

2.9.3 Immobilising light-harvesting complexes by soft-patterning

The PDMS stamp was immersed into a solution of LH2 complexes (15 μ M protein in buffer consisting of 20 mM HEPES, 0.03 % β -DDM, pH 7.8) for 5 min, then blown dry with Argon to form a surface layer of LH2. The LH2 inked stamp was gently placed onto the substrate to print LH2 arrays and left for 5 minutes before being gently lifted away. Samples with cross-patterned LH2 and RCLH1 arrays were made using the same printing steps performed for the RCLH1 complexes (either $\Delta crtB$ RCLH1 or WT RCLH1) with the second printing orientation at roughly 90 degrees to the previous LH2 arrays. AFM was used to image samples prepared on silicon substrates in air. Samples prepared on glass coverslips were sealed either in a dry N₂ atmosphere or in a 20mM HEPES buffer, pH 7.8 with protocatechuate-dioxygenase (50 nM)/ 3,4-Dihydroxybenzoic acid (2.5 mM) enzymatic oxygen scavenging system (Swoboda et al 2012) before being imaged by fluorescence life-time microscopy for energy transfer studies.

2.10 Local oxidation nanopatterning

2.10.1 Preparation of mPEO-terminated silane monolayers on silicon substrate

Uncoated, p-type (Boron) doped silicon (1 0 0) wafers (Sievert wafer) with a thickness of 0.5 mm were used as the substrate. Silicon substrates and glass vials were cleaned by immersion for 40 min in a piranha solution consisting of 30% hydrogen peroxide (Fisher Scientific) and 95% sulphuric acid (Fisher Scientific) at a ratio of 3:7. The cleaned silicon substrates were immersed in a solution of 15 mM 2-[methoxy (polyethyleneoxy) 6-9propyl] trichlorosilane (mPEO chlorosilane) (Gelest) in 99.8% anhydrous toluene (Sigma-Aldrich) for 2 hours to form a self-assembled monolayer of mPEO-terminated silane (mPEO-SAM). After the SAM formation, the substrates were rinsed thoroughly with toluene and acetone and dried under a stream of argon.

2.10.2 Creation of nanopatterns on mPEO-SAM silicon by local oxidation

lithography

The mPEO-SAM coated silicon substrates then went through the local oxidation process to create protein attachable regions on the protein resistant mPEO surface. The oxidation process was performed by the AFM (Multimode 8, Bruker) in contact mode in air at a relative humidity of approximately 40%. Silicon substrates were stuck

onto SPM specimen discs (Agar Scientific) by silver conductive adhesive (RS Components) and solidly mounted on the AFM sample holder. A conductive AFM probe (Bruker, CONTV-PT), coated by a Pt-Ir layer, scanned the silicon surface with a voltage bias, locally oxidising the $-\text{CH}_3$ groups on the mPEO to $-\text{COOH}$ groups (Choi et al 2006, Maoz 2000a, Maoz 2000b). 10 μm lines of $-\text{COOH}$ groups were made by scanning the AFM tip at a pixel resolution of 25.6 pixels/ μm ; 5x5 μm squares of $-\text{COOH}$ groups were made by scanning the AFM tip at a pixel resolution of 51.2 pixels/ μm . The oxidation was performed with varying bias values (V) and bias durations (ms/pixel) (Avouris et al 1997, Fontaine et al 1998).

2.10.3 Activation of the $-\text{COOH}$ group to an NHS ester

Silicon substrates with $-\text{COOH}$ patterns were rinsed 3 times using ultrapure water and immersed for 1 hour in a solution consisting of 20 mM HEPES (Sigma-Aldrich), 20 mM 1-ethyl-3-[3-dimethylaminopropyl]carbodiimide hydrochloride (EDC) (Thermo Scientific) and 20 mM N-hydroxysuccinimide (NHS) (Thermo Scientific). The incubation was at room temperature at pH 5.8, which allowed the reaction between the $-\text{COOH}$ and the NHS to form an NHS ester for protein immobilisation.

2.10.4 Protein immobilisation

Following the formation of the amine-reactive NHS ester, the substrate was immersed in a solution of 2 μM photosynthetic complexes, 20 mM HEPES and 0.03% w/v β -DDM at pH 7.4. The incubation time varied from 40 min to 20 hours. Then, the sample was rinsed 3 times by detergent buffer (20 mM HEPES, 0.03% w/v β -DDM) to remove weakly binding complexes. Samples were imaged by the AFM in buffer (20 mM HEPES, 20 mM NaCl, 5 mM MgCl_2) for the topography and by FLIM in buffer (20 mM HEPES, 0.03% w/v β -DDM) for optical properties and for energy transfer studies.

2. 11 Proteoliposome reconstitution

2.11.1 Liposome preparation

Liposomes, also known as lipid vesicles, was prepared by the extrusion technique using a 0.2 μm pore filter. Working buffer consisted of 20 mM MOPS (pH 7.8) and 20 mM NaCl, and liposome preparation used the lipid 1,2-dioleoyl-*sn*-glycero-3-phosphocholine (DOPC) (Avanti Polar Lipids, Inc.). 20 mg/ml DOPC in chloroform was

evaporated in a dry argon stream and formed a lipid cake which then was mixed with 1 ml of working buffer for adequate agitation by vortex to form large multi-lamellar vesicles (LMV). The LMV suspension was downsized by extruding 40 times through a 0.2 μm pore polycarbonate membrane (Whatman Nucleopore) to form small uni-lamellar vesicles. Thus, liposomes were prepared with an average diameter of ~ 260 nm. All processes were performed at room temperature.

2.11.2 Reconstitution of light-harvesting complexes into the liposome

Following the formation of liposomes, β -DDM was added to the liposome solution at a final concentration of 0.03% w/v and the mixture was incubated for 30 min. Then, light-harvesting complexes purified from *Rba. sphaeroides* (Section 2.3) were incubated in liposome solution for 1 hour in the dark at 4°C to form a proteoliposome solution. The lipid/protein ratio for incubation was fixed at 500:1 (mol/mol).

2.11.3 Purification of proteoliposome suspensions

Redundant β -DDM in the proteoliposome solution was gradually removed by adding nonpolar polystyrene biobeads (BIO-RAD, Bio-Beads SM-2 Adsorbents) into the solution and rolling on a roller mixer (Stuart, SRT6) overnight at 4°C in the dark. Aggregated complexes were removed by sucrose density gradient centrifugation. Sucrose solutions were prepared in buffer (20 mM MOPS, 20 mM NaCl, pH 7.8) and the gradient formed with steps at 10%, 20%, 30%, 40% and 50% (w/w). Proteoliposomes were loaded onto the 10% sucrose layer and the gradients were centrifuged at 154,000 $\times g$ for 15 hours at 4°C in the SW41Ti rotor (Beckman). Pigmented bands were carefully collected from the 25%-30% interface using a peristaltic pump. Absorbance spectra of the proteoliposome samples were recorded to identify the protein components and the ratios between them. Topographic images were recorded for using AFM. Fluorescence measurements were performed for the optical properties and energy transfer studies.

2. 12 Calculation of protein concentration in proteoliposomes

Room-temperature absorbance spectra of proteoliposome samples were recorded on a Cary 60 UV-Vis spectrophotometer (Agilent) at wavelengths between 1000 nm - 450 nm in an ultra violet (UV) cuvette with a 1 cm path length. Baseline were corrected in

the same range. Dilutions were made using the appropriate buffer or growth medium.

Spectra were processed by scatter correcting and deconvoluting the contributions of RC-LH1-PufX and LH2 using a modified version of an Excel spreadsheet by Prof O'Haver available at <https://terpconnect.umd.edu/~toh/spectrum/CurveFittingB.html>. The spreadsheet adds spectra of the two complexes and a scatter curve to achieve a best fit to the data and returns spectra for the three components according to their fitted contributions (Swainsbury et al 2018). The scatter curve used was calculated using $\lambda^{-2.6}$, and the RC-LH1-PufX and LH2 reference spectra were produced from proteins purified as described in Section 2.3. Concentrations of RC-LH1-PufX and LH2 were determined from their calculated components using extinction coefficients of 4410000 M/cm⁻¹ and 3745500 M/cm⁻¹ at 875 nm and 850 nm, respectively (Dr Pu Qian's personal communication).

Excitation energy transfer and trapping in fabricated microarrays constructed from photosynthetic antenna and reaction centre complexes

3.1 Summary

LH2 and RCLH1 complexes were purified from *Rba. sphaeroides* and cross-patterned on glass surfaces, then sealed under physiological conditions for energy transfer studies. FLIM results show that both complexes retained their light-harvesting and energy transfer function. When the complex pattern was excited with 470 nm or 485 nm light, fluorescence emission intensity and fluorescence lifetime decay from the LH2 complexes show evidence of energy transfer to RCLH1 complexes.

Since absorption of carotenoids around 485 nm complicates the assignment of energy transfer, carotenoid-less RCLH1 complexes were purified from the $\Delta crtB$ RCLH1 strain. $\Delta crtB$ RCLH1 and LH2 complexes were cross-patterned on a glass surface and sealed under physiological conditions. Energy transfer from LH2 to $\Delta crtB$ RCLH1 was observed, shown by the lifetime of fluorescence emission from LH2 complexes, which was shortened from 653 ps to 395 ps.

To explore the possibility of the artificial light-harvesting system working when not under liquid, $\Delta crtB$ RCLH1 and LH2 were cross-patterned on glass surface and sealed under a protective Argon atmosphere. Results show that both complexes retained their functions and are capable of energy transfer. Repeated FLIM measurements conducted over an extended time period show that the LH2/ $\Delta crtB$ RCLH1 patterns can last for 60 days with their fluorescence properties and with energy transfer capability retained.

AFM imaging of the $\Delta crtB$ RCLH1 and LH2 patterns on silicon show that both complexes retained their structure after being printed on silicon surface. In the intersecting regions, where energy transfer were observed, the AFM results show a mixed arrangement of $\Delta crtB$ RCLH1 sitting either beside LH2 or on top of LH2 complexes.

3.2 Introduction

The first stages of photosynthesis involve harvesting solar energy by light-harvesting (LH) antenna complexes, then transfer to a specialized, membrane-bound complex called the reaction centre (RC) where this energy is trapped as a charge separation. The LH function can be performed either by large pigment-protein complexes such as chlorosomes or phycobilisomes that sit on the membrane and deliver harvested energy to an underlying RC, or by a series of repeating LH units that sit alongside the RC in the membrane (Saer & Blankenship 2017). This latter case includes the photosynthetic apparatus of plants and, at a simpler level, the photosynthetic membranes found in purple phototrophic bacteria. The level of structural and functional characterisation for the phototrophic bacterium *Rhodobacter (Rba.) sphaeroides* has reached a level where all of the steps of photosynthesis, from absorption of solar energy, through to trapping at the RC, generation of a protonmotive force and the production of ATP, have been combined into an in silico model of the photosynthetic membrane (Cartron et al 2014, Sener et al 2016, Şener et al 2010). The power of this membrane model is such that it can account for the doubling time of the bacterium (Hitchcock et al 2017), and it also encourages the design and 'bottom up' fabrication of biohybrid energy trapping systems that capture, convert and store solar energy.

New biohybrid energy transfer and trapping assemblies take many forms, and range from incorporating new chromophores into native (Dutta et al 2014a, Dutta et al 2014b, Gundlach et al 2009, Harris et al 2014a, Harris et al 2013, Harris et al 2014b, Meadows et al 1995, Springer et al 2012, Yoneda et al 2015) and de novo designed (Kodali et al 2017, Mancini et al 2017, Meadows et al 1995) proteins, to using a variety of lithographic patterning methods to precisely position a single type of photosynthetic complex (Escalante et al 2010, Escalante et al 2008a, Escalante et al 2008b, Patole et al 2015, Reynolds et al 2007, Vasilev et al 2014b). In this case, the assembly of extensive 2-dimensional architectures for energy harvesting, transfer and trapping requires the ability to direct the relative positions of two or more types of photosynthetic complex on the same surface. The two complexes chosen for this two-protein patterning work are the LH2 antenna of *Rba. sphaeroides*, and its native energy acceptor, the RCLH1 complex (Cartron et al 2014, Qian et al 2013). Both are

membrane-intrinsic, multi-subunit proteins in which transmembrane polypeptides bind light-absorbing bacteriochlorophyll and carotenoid pigments (Freer et al 1996). The short distances between pigments ensure the rapid delocalization of excited states and their transfer within and between complexes in the native membrane (Freer et al 1996, Noy et al 2006, Şener et al 2009). Here we use a simple, robust lithographic procedure to construct intersecting lines of LH antenna and RC complexes, effectively creating a new micron-scale 'photosynthetic unit'. A two-stage micro-contact printing method was used to fabricate a 2-D grid of cross-patterned LH2 and RCLH1 proteins, which was interrogated by fluorescence microscopy. Spectral and lifetime imaging shows that light absorbed by the LH2 antenna is transferred to RCLH1 complexes; thus, these arrays contain functionally coupled components for absorbing and transferring excitation energy, thereby performing the first two steps of photosynthesis.

3.3 Results

3.3.1 Directed formation of crossed-patterned LH2 and RCLH1 complexes on glass and silicon

We created artificial light-harvesting networks using a very simple and low cost soft-lithographic technique, based on the micro-contact printing approach (Alom Ruiz & Chen 2007, Bernard et al 2000, Xia & Whitesides 1998), schematically represented in Figure 3.1. Optically transparent glass functionalized with poly-L-lysine (PLL) was chosen as a substrate, to facilitate characterisation of immobilized protein complexes by fluorescence microscopy. As a first step, the LH2 complexes (in green, Figure 3.1G and H) were printed onto the substrate using a soft PDMS stamp (Figure 3.1B and C) then inked with the protein solution (Figure 3.1D), followed by the printing of *ΔcrtB* RCLH1 complexes (in red, Figure 3.1I), performed in a similar way but at a 90° angle to the LH2 lines.

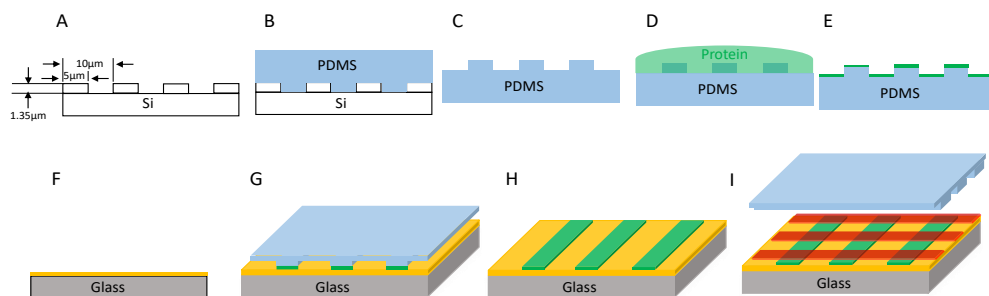


Figure 3.1. Schematic diagram of the micro-contact printing method used to fabricate the cross-patterned LH2 and RCLH1 protein arrays.

- A. Si master with rectangular arrays of 5 μm width, 10 μm pitch and 1.35 μm step height.
- B. Casting a PDMS replica of the master.
- C. PDMS replica.
- D. Inking the stamp with LH2 (green).
- E. PDMS stamped covered with LH2 ink.
- F. PLL coated glass activated by DMS (yellow).
- G. Printing LH2 on glass.
- H. LH2 arrays on glass.
- I. Printing RCLH1 complexes (red) on glass orthogonally to LH2 arrays.

3.3.2 Excitation energy transfer between LH2 and RCLH1 under physiological conditions

In bacterial photosynthetic systems the LH2 antenna complexes harvest light energy and transfer it to the RCLH1 core complex, where the excitation energy is stabilized as a photo-chemical charge separation. Native biological light-harvesting networks are stabilized in membrane bilayers and operate under tightly controlled physiological conditions, so the cross-printed energy transfer assemblies were sealed in imaging buffer (20 mM HEPES, pH 7.8) to promote retention of their optical and structural properties. The artificial microarrays of cross-printed LH2 and RCLH1 complexes were characterized by fluorescence lifetime and spectral imaging in a home-built FLIM set-up. This microscope is equipped with 485 nm pulsed laser and 470 nm LED excitation light sources; an EMCCD camera is coupled to a monochromator for wide-field and spectral imaging, and a single photon detector for time-correlated single photon counting (TCSPC) is used to acquire lifetime decay images. The samples were excited either at 485 nm or at 470 nm in the absorption band of the carotenoids present in both the LH2 and RCLH1 complexes (Figure 3.2). The excitation energy is absorbed by carotenoids and transferred to B800 and B850 bacteriochlorophylls (BChls) within the LH2 complexes, where energy is partly emitted as fluorescence and partly transferred to the B875 pigments in the RCLH1 complexes. In turn, LH1 B875 BChls can either emit some of the excitation energy as fluorescence, or transfer it to the RC, where it is trapped as a charge separation.

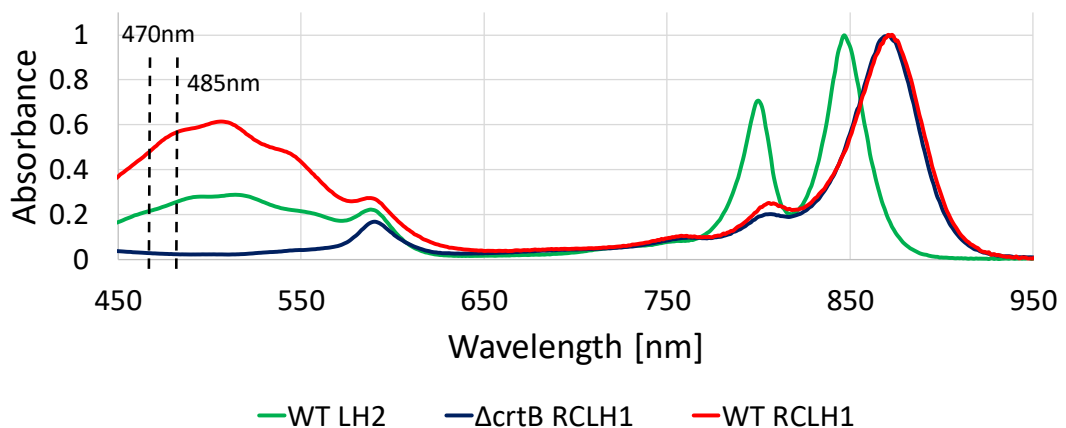


Figure 3.2. Absorption spectra of purified complexes.

LH complexes were excited either at 470 nm or 485 nm for fluorescence emission. At 485 nm, the absorbances of RCLH1, LH2 and Δ crtB RCLH1 are 0.57, 0.26 and 0.02, respectively. At 470nm, the absorption of RCLH1, LH2 and Δ crtB RCLH1 are 0.50, 0.22 and 0.02 OD units, respectively.

Figure 3.3 shows fluorescence data acquired from a sample cross-printed with LH2 and RCLH1 complexes on glass, and sealed in imaging buffer (20 mM HEPES). The false-color fluorescence image (Figure 3.3A) of the sample, acquired in epifluorescence mode illuminated by the 470 nm LED source, shows the surface distribution of the LH complexes; the green regions correspond to LH2 complexes (857/30 nm bandpass filter), and those in red are from RCLH1 complexes (900/32 nm bandpass filter). When switching to scanning confocal mode, and using 485 nm pulsed laser excitation, we were able to record the spectral map of fluorescence emission of the sample. The photon fluence of about 2.0×10^{14} photons pulse⁻¹ cm⁻² was sufficiently low to minimise excitonic annihilation in the LH complexes. The fluorescence intensity maps acquired at 860 nm and 890 nm (Figure 3.3 B and C, respectively), confirm the immobilisation of the LH2 complexes along the near-horizontal lines and immobilisation of the RCLH1 complexes along the near-vertical lines. A striking observation in the cross-over area (marked with number 2 in Figure 3.3 B and C), where LH2 and RCLH1 complexes are in close proximity, is the decrease in the LH2 emission intensity, accompanied by a comparable increase in RCLH1 emission. This observation is confirmed by the deconvolution of the spectra extracted from the pixel marked with the number 2 (cross-over area), orange curve in Figure 3.3D, and its comparison with the individual spectra, green and red in Figure 3.3D, extracted from the pixels marked with the numbers 1 and 3 in panel B (LH2-only and RCLH1-only areas, respectively). We interpret these changes in the emission intensities as an indication for excitation energy transfer (EET) between the LH2 and RCLH1 complexes. In order to study the EET in more detail we recorded a fluorescence lifetime map of the immobilised LH2 complexes. An amplitude-averaged lifetime image of the cross-patterned sample, recorded at 860 nm (the LH2 peak emission wavelength), is shown in Figure 3.3E with two individual fluorescence decay curves shown in Figure 3.3F. From Figure 3.3E, the LH2 only areas (green) generally show longer lifetime of about between 750~900 ps, comparing with the LH2- RCLH1 cross-over area (pink) of about between 400~550 ps. In Figure 3.3F, the green decay curve was extracted from the pixel marked 5 (Figure 3.3E) corresponding to the LH2-only area, and the bi-exponential decay function fitting result shows an amplitude-averaged lifetime $\tau_{av} = 904$ ps, with components $A_1 = 0.39$, $\tau_1 = 1119$ ps and $A_2 = 0.61$, $\tau_2 = 678$ ps; the orange curve represents the fluorescence decay in the cross-over

area (marked 4, Figure 3.3E), and the bi-exponential decay function fitting result shows an amplitude-averaged lifetime $\tau_{av} = 541$ ps, with components $A_1 = 0.09$, $\tau_1 = 1138$ ps and $A_2 = 0.91$, $\tau_2 = 348$ ps. This reduction of the LH2 fluorescence lifetime indicates EET from the LH2 complex to RCLH1 complex in the cross-over areas where the two protein molecules are in very close proximity.

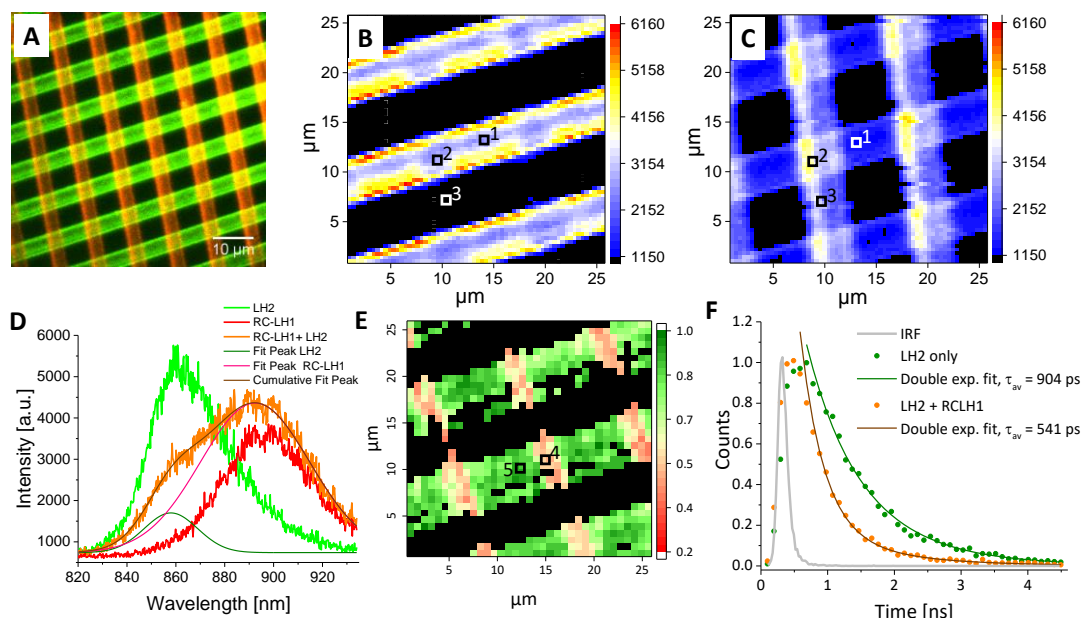


Figure 3.3. Fluorescence spectrum and lifetime data from a cross-patterned WT LH2 and RCLH1 complexes under physiological conditions (in imaging buffer) on a functionalised glass substrate.

- False colour fluorescence image (wide field excitation at 470 nm), showing the LH2 (green) and RCLH1 (red) lines in a grid-like pattern with a period of 10 μm and line width of 5 μm .
- Spectral map excited by laser, showing the emission intensity at 860 nm (LH2 emission peak), the excitation is by 485 nm laser pulsed (1 MHz repetition rate, 2×10^{14} photons pulse $^{-1}$ cm $^{-2}$), scan size 26 μm .
- Simultaneously acquired spectral map showing the emission intensity at 890 nm (RCLH1 emission peak), scan size 26 μm .
- Individual emission spectra recorded in the pixels of the images in panels B and C marked with 1 (LH2 only), 2 and 3 (RCLH1 only), respectively. The spectral deconvolution in D shows a clear drop in the LH2 emission (olive peak fit) compared to the LH2 emission outside the cross-over area, accompanied with a corresponding increase in the (pink peak fit), again, compared to the RCLH1 emission outside the cross-over area.
- Amplitude weighted average lifetime image obtained at 485 nm excitation (1 MHz repetition rate, 2×10^{14} photons pulse $^{-1}$ cm $^{-2}$), and 860 nm emission (LH2 complex emission peak), clearly showing a decrease in the lifetime in the cross-over areas, where the two complexes are in close proximity, scan size 26 μm .
- Individual decay curves recorded in the pixels of the lifetime image in panel E marked with 4 (orange, average lifetime of 541 ps) and 5 (green, average lifetime of 904 ps), respectively.

(Data obtained by Dr Cvetelin Vasilev.)

3.3.3 Energy transfer from LH2 to $\Delta crtB$ RCLH1 under physiological conditions

RCLH1 contains carotenoid pigments, therefore the LH2 and RCLH1 complexes studied in Figure 3.3 were both excited by the 485 nm light source, which complicates the assignment of energy transfer between them. In order to overcome this problem, we purified $\Delta crtB$ RCLH1 complexes from the $\Delta crtB$ RCLH1 strain, which has no carotenoids and therefore has negligible absorption at the excitation wavelength of 485 nm (Figure 3.2). Accordingly, when LH2 and $\Delta crtB$ RCLH1 are immobilised on a glass surface, only LH2 complexes are efficient at capturing 485 nm light. Using the same printing process and the same fluorescence measurement setting as for Figure 3.3, LH2 and $\Delta crtB$ RCLH1 were cross-patterned on glass and sealed in 20 mM HEPES buffer for fluorescence measurements.

As expected, cross-patterned LH2 and $\Delta crtB$ RCLH1 retain their optical properties and energy transfer capability (Figure 3.4). Figure 3.4A is the merged wide field false colour fluorescence image of complexes illuminated by 470 nm LED and recorded by EMCCD. The green lines are fluorescence filtered by the 857/30 nm bandpass filter, which indicates the distribution of LH2 complexes. The red squares are fluorescence filtered by 900/32 nm bandpass filter, which shows the location of fluorescent $\Delta crtB$ RCLH1 complexes. Clearly, there are some fluorescent $\Delta crtB$ RCLH1 complexes in the cross-over area, because nearby LH2 complexes are acting as an antenna and delivering excitation energy, $\Delta crtB$ RCLH1 complexes without connected LH2 complexes cannot harvest energy, stay unexcited and give the black gaps in the fluorescent image. Same results are observed in fluorescence spectral intensity images when the sample is excited with the 485 nm laser. The fluorescence intensity images at 857 nm and 890 nm are shown in Figure 3.4B and 3.4C separately. Typical emission spectra from marked pixels are plotted in Figure 3.4D.

FLIM provided further evidence for energy transfer between LH2 and $\Delta crtB$ RCLH1. An amplitude-averaged lifetime image of the cross-patterned sample, recorded at 857 nm (LH2 peak emission wavelength) is shown in Figure 3.4E with two individual fluorescence decay curves shown in Figure 3.4F. From Figure 3.4E, the LH2 only areas (green) generally show a longer lifetime of about between 550~700 ps, compared with the LH2- $\Delta crtB$ RCLH1 cross-over area (pink) of about between 350~500 ps. In Figure 3.3F, the green decay curve was extracted from the pixel marked 5 (Figure 3.4E)

corresponding to the LH2-only area, and the bi-exponential decay function fitting result shows an amplitude-averaged lifetime $\tau_{av} = 653$ ps, with components $A_1 = 0.64$, $\tau_1 = 711$ ps and $A_2 = 0.36$, $\tau_2 = 146$ ps; the orange curve represents the fluorescence decay in the cross-over area (marked 4, Figure 3.4E), and the bi-exponential decay function fitting result shows an amplitude-averaged lifetime $\tau_{av} = 395$ ps, with components $A_1 = 0.32$, $\tau_1 = 529$ ps and $A_2 = 0.68$, $\tau_2 = 275$ ps. Again, the reduction of the LH2 fluorescence lifetime confirms the EET from the LH2 complex to $\Delta crtB$ RCLH1 complex in the cross-over areas where the two protein molecules are in close proximity.

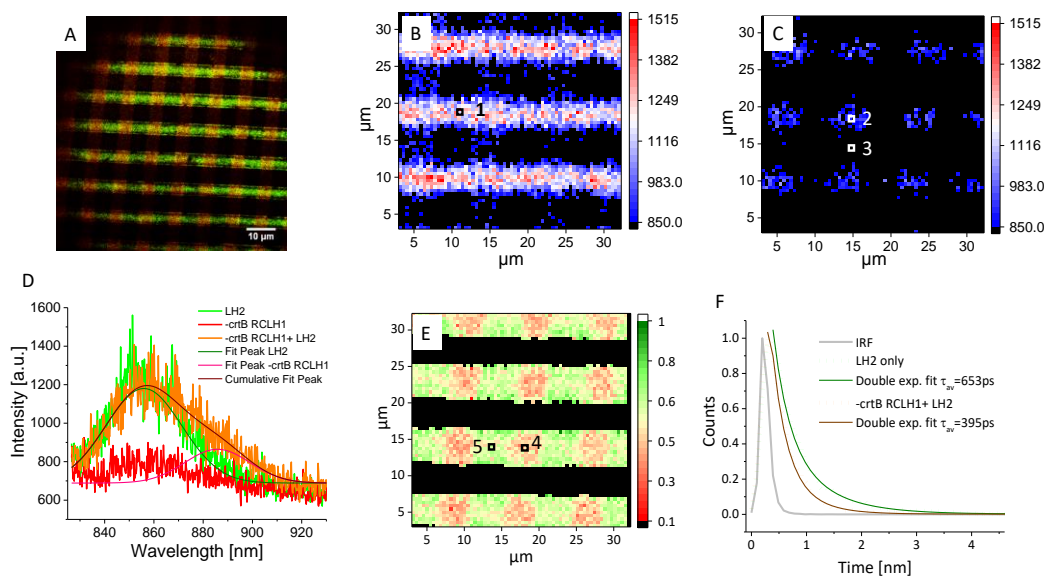


Figure 3.4. Fluorescence spectrum and lifetime from cross-patterned LH2 and $\Delta crtB$ RCLH1 complexes imaged under physiological conditions

- False colour fluorescence image (470 nm wide field excitation), showing the LH2 (green) and $\Delta crtB$ RCLH1 (red) lines, filtered by 857/30 nm and 900/32 nm bandpass filters, respectively.
- Spectral map showing the emission intensity at 860 nm (LH2 emission), excitation source is 485 nm laser pulsed (1 MHz repetition rate, 2×10^{14} photons pulse⁻¹ cm⁻²), scan size 32 μ m;
- Simultaneously recorded spectral map showing the emission intensity at 890 nm ($\Delta crtB$ RCLH1 emission), scan size 32 μ m;
- Individual emission spectra recorded in the pixels of the images in panels B and C marked with 1 (LH2 only, green line), 2 (cross-over area, orange line) and 3 ($\Delta crtB$ RCLH1 only, red line), respectively.
- Intensity-averaged lifetime image obtained with 485 nm excitation and 857 nm emission (LH2 emission), clearly showing a decrease in the lifetime in the cross-over areas, where the two complexes are in close proximity, scan size 32 μ m.
- Individual decay curves recorded in the pixels of the lifetime image in panel E marked with 4 (orange, average lifetime of 395 ps) and 5 (green, average lifetime of 653 ps), respectively.

3.3.4 Energy transfer from LH2 to $\Delta crtB$ RCLH1 in an argon protective environment

Due to the lack of carotenoids $\Delta crtB$ RCLH1 is expected to be less photo stable compared to WT RCLH1, so a protective Ar atmosphere was used to minimise photo-oxidative damage to this complex. For this work $\Delta crtB$ RCLH1 and LH2 complexes were patterned on a glass substrate, but not kept under liquid; instead they were partially dried in a partially dehydrated manner and then sealed under a protective Argon (Ar) atmosphere.

Figure 3.5A shows a false colour epifluorescence image of cross-patterned LH2 (green) and $\Delta crtB$ RCLH1 (red) complexes, with wide field excitation at 470 nm and the emission signals filtered by 857/30 nm and 900/32nm bandpass filters, respectively. Figure 3.5A shows the precision of patterning of the two types of complex, delineating their positions, and the differing emission bands provide evidence that the immobilised complexes have retained their properties and structural integrity under the protective conditions of our experiment. Spectral imaging of the co-patterned complexes (Figure 3.5B) shows lines arising from LH2 emission at 860 nm. Orthogonal $\Delta crtB$ RCLH1 lines are absent because absorption of the 485 nm excitation light is very weak, so fluorescence emission was barely detectable over the background in the areas where the $\Delta crtB$ RCLH1 complexes were immobilised on their own. As expected, the spectral intensity map shows that the lines of LH2 emission were not uniform; individual emission spectra, corresponding to the pixels in Figure 3.5B,C and marked with the numbers 1(LH2-only area, green), 2 (LH2/ $\Delta crtB$ RCLH1 cross-over area, orange), and 3 ($\Delta crtB$ RCLH1-only area, red), are shown in Figure 3.5D. Spectral deconvolution shows a clear drop in the LH2 emission (olive peak fit) at the LH2/ $\Delta crtB$ RCLH1 intersection and an increase in the $\Delta crtB$ RCLH1 emission (pink peak fit), compared to the $\Delta crtB$ RCLH1 emission outside the cross-over area (pixel 3, red). A simultaneously acquired spectral map of emission intensity at 890 nm from $\Delta crtB$ RCLH1 complexes (Figure 3.5C) shows major signals at the LH2/ $\Delta crtB$ RCLH1 intersections; given that excitation is specific for LH2, this $\Delta crtB$ RCLH1 emission must have arisen from excitation energy transfer from neighbouring LH2 complexes. Closer inspection of Figure 3.5C shows that a low level of fluorescence emission in the $\Delta crtB$ RCLH1 channel is found in the vertical lines outside the LH2/RCLH1 intersections, a

possible indication of migration of EET to neighbouring $\Delta crtB$ RCLH1 complexes arrayed in the vertical lines.

Figure 3.5E shows an amplitude-weighted fluorescence lifetime map of surface-attached LH2 and $\Delta crtB$ RCLH1 complexes, with excitation at 485 nm and emission monitored at 857 nm, the peak emission wavelength of LH2. Individual decay curves corresponding to pixels 4 and 5 of the lifetime image are shown in Figure 3.5F. From Figure 3.5E, the LH2 only areas (green) generally show longer lifetime of about between 700~900 ps, comparing with the LH2- $\Delta crtB$ RCLH1 cross-over area (pink) of about between 400~500 ps. In Figure 3.5F, the green decay curve was extracted from the pixel marked 5 (Figure 3.5E) corresponding to the LH2-only area, and the bi-exponential decay function fitting result shows an amplitude-averaged lifetime $\tau_{av} = 794$ ps, with components $A_1 = 0.45$, $\tau_1 = 974$ ps and $A_2 = 0.55$, $\tau_2 = 512$ ps; the orange curve represents the fluorescence decay in the cross-over area (marked 4, Figure 3.5E), and the bi-exponential decay function fitting result shows an amplitude-averaged lifetime $\tau_{av} = 438$ ps, with components $A_1 = 0.25$, $\tau_1 = 645$ ps and $A_2 = 0.75$, $\tau_2 = 284$ ps. Again, the reduction of the LH2 fluorescence lifetime confirms the EET from the LH2 complex to $\Delta crtB$ RCLH1 complex in the cross-over areas where the two protein molecules are in close proximity.

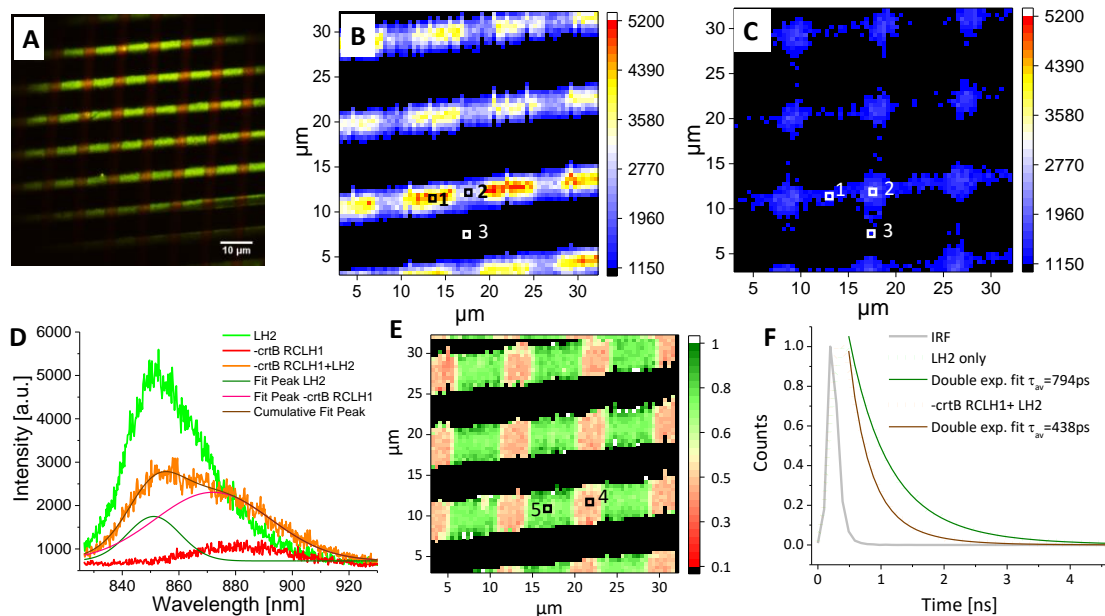


Figure 3.5. Fluorescence spectrum and lifetime from cross-patterned LH2 and $\Delta crtB$ RCLH1 complexes on a functionalised glass substrate imaged in a protective atmosphere of argon

- A. False colour fluorescence image (wide field excitation at 470 nm), showing the LH2 (green) and $\Delta crtB$ RCLH1 (red) lines, filtered by 857/30nm and 900/32nm bandpass filters, respectively.
- B. Spectral map showing the emission intensity at 860 nm (LH2 emission), excitation is by a 485nm pulsed laser (1 MHz repetition rate, 2×10^{14} photons pulse⁻¹ cm⁻²), scan size 32 μ m.
- C. Simultaneously acquired spectral map showing the emission intensity at 890 nm ($\Delta crtB$ RCLH1 emission), scan size 32 μ m.
- D. Individual emission spectra recorded in the pixels of the images in panels B and C marked with 1 (LH2 only, green line), 2 (cross-over area, orange line) and 3 ($\Delta crtB$ RCLH1 only, red line), respectively. The spectral deconvolution shows a clear drop in the LH2 emission (olive peak fit) and an increase in the $\Delta crtB$ RCLH1 emission (pink peak fit), compared to the LH2 emission and the $\Delta crtB$ RCLH1 emission outside the cross-over area.
- E. Amplitude weighted average lifetime image obtained at 485nm excitation (1 MHz repetition rate, 2×10^{14} photons pulse⁻¹ cm⁻²) and 857nm emission (LH2 emission), clearly showing a decrease in the lifetime in the cross-over areas, where the two complexes are in close proximity, scan size 32 μ m.
- F. Individual decay curves recorded in the pixels of the lifetime image in panel E marked with 4 (orange, average lifetime of 438 ps) and 5 (green, average lifetime of 794 ps), respectively.

3.3.5 Long-term stability of cross-patterned LH2 and $\Delta crtB$ RCLH1 complexes on glass surfaces

In order to test the stability and “shelf life” of these artificial light-harvesting systems, the cross-patterned complexes samples were sealed in Argon atmosphere and stored at 4°C in the dark. Regular FLIM measurements, taken over approximately two months, showed that both LH2 and $\Delta crtB$ RCLH1 are quite stable under these

conditions. From days 1 to 60, there is a small variation in the fluorescence lifetime of LH2 complex in both LH2 only area (typical amplitude-averaged lifetime of 740 ± 90 ps) and LH2+ $\Delta crtB$ RCLH1 cross-over area (typical amplitude-averaged lifetime of 400 ± 50 ps) (Table 3.1). Lifetime data were fitted by a bi-exponential decay function. Parameter τ_1 refers to the longer lifetime component, τ_2 refers to the shorter lifetime one and τ_{av} refers to amplitude-weighted average lifetimes. ‘LH2’ refers to areas covered only by LH2; ‘LH2+ $\Delta crtB$ RCLH1’ refers to cross-over areas covered by both LH2 and $\Delta crtB$ RCLH1.

Table 3.1. Fluorescence lifetimes of LH2 at 860 nm.

	τ_1 [ps] LH2+ $\Delta crtB$ RCLH1	τ_1 [ps] LH2	τ_2 [ps] LH2+ $\Delta crtB$ RCLH1	τ_2 [ps] LH2	τ_{av} [ps] LH2+ $\Delta crtB$ RCLH1	τ_{av} [ps] LH2
Day 1	640	1040	280	520	430	770
Day 5	480	1040	290	500	380	740
Day 10	510	950	280	430	380	680
Day 15	600	1100	360	600	450	840
Day 20	490	1010	280	500	370	770
Day 30	450	950	290	470	350	710
Day 60	540	840	320	430	410	650

Furthermore, the fluorescence lifetime images clearly show excitation energy transfer between LH2 and $\Delta crtB$ RCLH1 60 days after sample preparation (Figure 3.6), on the basis of quenching of the LH2 fluorescence observed in the intensity and lifetime channels (Figure 3.6B and E). Individual decay curves corresponding to pixels 4 and 5 of the lifetime image are shown in Figure 3.6F. From Figure 3.6E, the LH2 only areas (green) generally show longer lifetime of about between 0.6~0.75 ns, comparing with the LH2- $\Delta crtB$ RCLH1 cross-over area (pink) of about between 0.35~0.5 ns. In Figure 3.6F, the green decay curve was extracted from the pixel marked 5 (Figure 3.6E) corresponding to the LH2-only area, and the bi-exponential decay function fitting result shows an amplitude-averaged lifetime $\tau_{av} = 683$ ps, with components $A_1 = 0.26$, $\tau_1 = 964$ ps and $A_2 = 0.74$, $\tau_2 = 488$ ps; the orange curve represents the fluorescence decay in the cross-over area (marked 4, Figure 3.6E), and the bi-exponential decay function fitting result shows an amplitude-averaged lifetime $\tau_{av} = 382$ ps, with components $A_1 = 0.30$, $\tau_1 = 507$ ps and $A_2 = 0.70$, $\tau_2 = 285$ ps. The fluorescence intensity images at 857 nm (Figure 3.6B) and 890 nm (Figure 3.6C), respectively, show

that the pattern is well preserved on the functionalised glass substrate with no diffusion of protein complexes, while the emission spectra (Figure 3.6D) indicate that both LH2 and $\Delta crtB$ RCLH1 complexes remain undamaged.

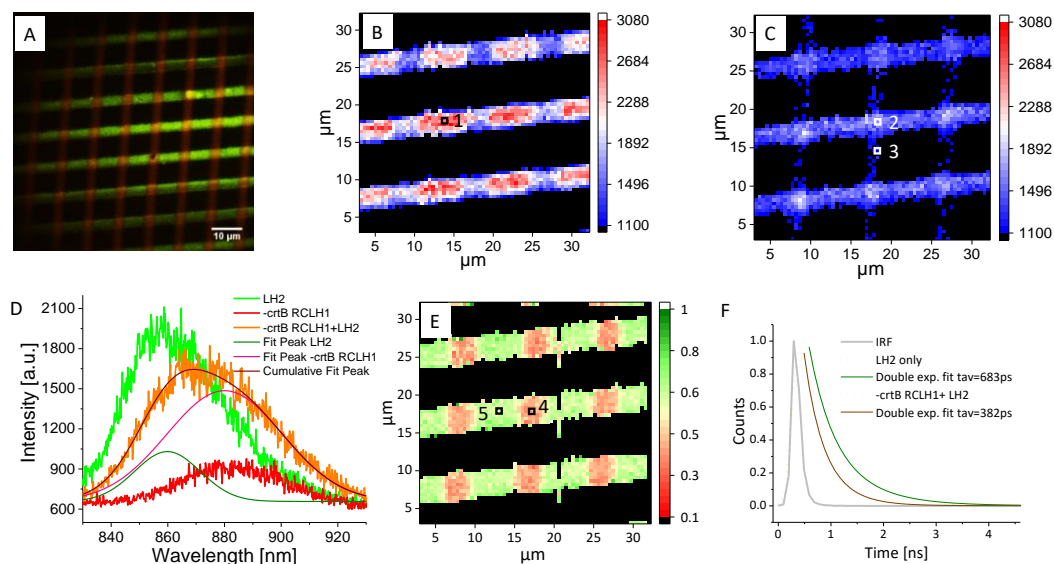


Figure 3.6. Fluorescence spectrum and life-time data obtained 60 days after the sample preparation showing long-term stability of the cross-patterned LH2 and $\Delta crtB$ RCLH1 complexes.

- A. False colour fluorescence image (470 nm wide field excitation) showing the LH2 (green) and $\Delta crtB$ RCLH1 (red) lines, filtered by 857/30 nm and 900/32 nm bandpass filters, respectively.
- B. Spectral map showing the emission intensity at 857 nm (LH2 emission); the excitation source is a 485nm pulsed laser (1 MHz repetition rate, 2×10^{14} photons pulse⁻¹ cm⁻²), scan size 32 μ m.
- C. Simultaneously acquired spectral map showing the emission intensity at 890 nm ($\Delta crtB$ RCLH1 emission), scan size 32 μ m.
- D. Individual emission spectra recorded in the pixels of the images in panels A and B marked with 1 (LH2 only, green line), 2 (cross-over area, orange line) and 3 ($\Delta crtB$ RCLH1 only, red line), respectively. The spectral deconvolution shows a clear drop in the LH2 emission (olive peak fit) and an increase in the $\Delta crtB$ RCLH1 emission (pink peak fit), compared to the LH2 emission and the $\Delta crtB$ RCLH1 emission outside the cross-over area.
- E. Intensity-averaged lifetime image obtained at 485 nm excitation and 857 nm emission (LH2 emission), clearly showing a decrease in the lifetime in the cross-over areas, where the two complexes are in close proximity, scan size 32 μ m.
- F. Individual decay curves recorded in the pixels of the lifetime image in panel E marked with 4 (orange, average lifetime of 382 ps) and 5 (green, average lifetime of 683 ps), respectively.

3.3.6 Visualising the arrangement of patterned protein complexes on a glass substrate

Initial characterisation had investigated the surface density, orientation and surface coverage of the immobilized protein complexes on the substrate. Atomic force microscopy (AFM) of micropatterns showed that the surface roughness of the PLL-functionalized glass substrates was too high for accurate measurement of the height of the protein complexes (data not shown). Substrates such as silicon wafers, on the other hand, are opaque but are much better substrates for AFM measurement of the micropatterned LH complexes. Consequently, artificial LH networks were fabricated on two different types of substrates – micropatterned LH complexes on functionalized glass for fluorescence lifetime imaging microscopy (FLIM), and on silicon for examining the topography of immobilized complexes by AFM.

Figure 3.7 shows AFM topographs of LH2 and $\Delta crtB$ RCLH1 complexes cross-printed on a Si wafer in air. The LH2 complexes were printed in the horizontal direction and, subsequently, the $\Delta crtB$ RCLH1 complexes were printed in the vertical direction, forming a zone of intersection shown in Figure 3.7A. The cross-section across the LH2 line (green line, Figure 3.7A) reveals heights in the range 5 ~ 6 nm (Figure 3.7B), while the cross-section across the $\Delta crtB$ RCLH1 line (red line, Figure 3.7A) reveals heights around 9 nm (Figure 3.7C). Both values conform with the known sizes of the two complexes and with a previous AFM measurements (Bahatyrova et al 2004a). Interestingly, three distinct height values are found for the topographic cross-section of the intersecting area: 5 ~ 6 nm (as found for the LH2 only area), around 9 nm (as for the $\Delta crtB$ RCLH1 only area), and heights of around 14 nm. The results indicate that, during the second printing step, $\Delta crtB$ RCLH1 complexes in the cross-over area can be immobilised not only next to the existing LH2 molecules on the substrate (similar to their relative disposition in the majority of the biological LH networks), but also on top of them, thus forming a vertical stacks of LH complexes (an arrangement which does not exist in the nature for that particular pair of LH complexes).

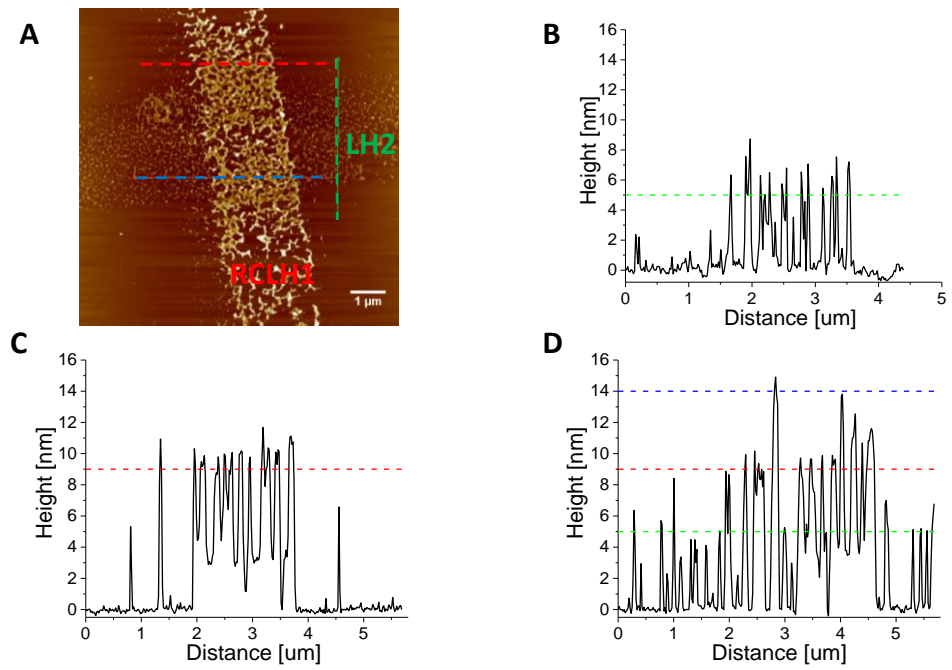


Figure 3.7. Topography of the cross-patterned LH2 / $\Delta crtB$ RCLH1 complexes on a Si substrate.

- A. AFM topography image acquired under ambient conditions (air), with three sections indicated: green – LH2; Red – $\Delta crtB$ RCLH1; blue intersection.
- B. Cross-section across the LH2 lines (green line), with a typical height around 5 nm.
- C. Cross-section across the $\Delta crtB$ RCLH1 lines (red line), with a typical height around 9 nm.
- D. Cross-section across the LH2+ $\Delta crtB$ RCLH1 intersecting area (blue cursor), with typical heights of 5 nm, 9 nm and 14 nm.

3.4 Discussion

Previous work using reconstituted membranes has shown that energy transfer can be observed in mixed assemblies of LH2 and RCLH1 complexes (Hunter et al 1979, Sumino et al 2011a, Uragami et al 2015), but controlling the nanoscale location, relative stoichiometries and 2-D organization of a series of photosynthetic complexes presents new challenges. For some time it has been possible to construct nanoarrays of single types of photosynthetic complex, starting with the light-harvesting LH2 complex of *Rba. sphaeroides* (Escalante et al 2008a, Escalante et al 2008b, Reynolds et al 2007), and later the RCLH1 complex (Patole et al 2015) and the LHCII complex of plants (Vasilev et al 2014b). In each case the function of the complex, in terms of fluorescence emission, was retained; for LHCII it was possible to directly image the ability of immobilised molecules of LHCII to switch between fluorescent and quenched states. For LH2, there were indications of long-range excitation energy transfer; 80 nm-wide nanolines of LH2 complexes exhibit energy propagation on micron length scales, which greatly exceed the natural energy propagation lengths found in native photosynthetic membranes (Escalante et al 2010). Excitation energy is generally trapped before it migrates for more than 50-100 nm within natural energy transfer and trapping networks such as the chromatophore vesicles of purple bacteria, or the thylakoids of cyanobacteria, algae and plants.

Nanoarrays of two or more types of photosynthetic complex would be valuable tools to investigate LH antenna networks, in terms of RC trap ratios, and exploring length scales and geometries of energy migration and trapping that lie beyond those found in biology. However, progress with these aims relies on the ability to co-pattern two or more types of complex on the same surface and on the application of spectral and time-resolved microscopies to assess the functional state of immobilised assemblies. Recent developments in surface chemistries do allow multiprotein patterning (El Zubir et al 2017), and an alternating linear LHCII/EGFP pattern has been reported (Vasilev et al 2014b). Here, we have used a simple lithographic method to cross-print LH and energy trapping complexes, and at the points of intersection we demonstrate collection of light by one complex, LH2, and its subsequent transfer to the RCLH1 complex. Thus, this assembly can be regarded as a new type of 'photosynthetic unit', where the complexes adopt a predetermined, geometric configuration.

Although the stability of surface-immobilised proteins is a potential problem, many studies have shown that photosystem complexes are stable on a variety of substrates. Purified bacterial RCs, stabilised using peptide surfactants, retain their function when deposited on indium-tin oxide (ITO)-coated glass (Das et al 2004) or gold electrodes (Ham et al 2010, Trammell et al 2007, Zhao et al 2002) or Gallium Arsenide (Frolov et al 2008). Stable coatings of RCLH1, Photosystem II (Badura et al 2006, Terasaki et al 2008) and Photosystem I complexes on electrodes have been reported (Faulkner et al 2008, Krassen et al 2009, Yehezkeli et al 2010). To our knowledge, there has been no systematic study of the long-term stability of surface-attached complexes on a functionalised glass substrate, so we undertook a 60-day test with the cross-patterned arrays of photosynthetic complexes sealed in argon and stored at 4°C in the dark. These artificial light-harvesting systems proved to be extremely stable under these conditions, and further work will examine the stability of other natural and de novo designed maquette complexes.

The means to control the relative positions of two or more types of molecule on the same surface allows construction of 'mix and match' combinations of molecules that could not be created through genetic means, such as arrays comprising mixed bacterial/plant, or plant/artificial maquette complexes. Further functional tests will include measuring the nanoelectrical properties of RC traps within native, biohybrid and bioinspired photosynthetic arrays, deposited on conducting substrates. This development would add a third function of charge separation to the absorption and transfer of energy demonstrated in the present work.

Nanoscale patterning of photosynthetic complexes on silicon by local oxidation lithography

4.1 Summary

Patterns of photosynthetic complexes were created on mPEO-SAM coated silicon surfaces by local oxidation lithography. Scanning an AFM tip with a voltage bias over an mPEO-SAM coated silicon surface locally oxidised the $-CH_3$ groups to $-COOH$, preparing the surface for protein immobilisation. Following a systematic survey of experimental conditions, a bias potential of 12 V and a dwell time of 100 ms/pixel were chosen for the local oxidation, and 4 hours was found to be optimal for protein incubation, with regard to the fluorescence emission intensity from the immobilised proteins. Three photosynthetic complexes, bacterial RCLH1 and LH2, and the plant LHCII complex, were immobilised on oxidised mPEO-SAM coated silicon surfaces. AFM images and fluorescence emission spectra show that these complexes had retained their native functional and therefore structural properties.

In order to create an artificial photosynthetic system for light harvesting and energy transfer, dual intersecting patterns of LH2 and RCLH1 complexes were formed on a silicon surface using local oxidation lithography. The RCLH1 nanolines were created by the first local oxidation, followed by orthogonal LH2 nanolines created by a second local oxidation. AFM topographies of the intersecting regions show that the RCLH1 complexes were removed by the second local oxidation and replaced by the LH2 complexes. However, there was no evidence for LH2→RCLH1 excitation energy transfer, presumably due to the limited contact area between two complexes.

A $5 \times 5 \mu\text{m}$ square area of LH2 complexes was fabricated with four intersecting RCLH1 nanolines, in order to increase the contact area for energy transfer. The fluorescence lifetime of the LH2 complexes decreased from 900-1300 ps in the LH2-only regions to 300-500 ps at the intersection points, indicating that, following light harvesting by LH2 complexes, excitation energy is being delivered to the RCLH1 acceptor complexes.

4.2 Introduction

Light is harvested by light-harvesting antenna pigments within (bacterio) chlorophyll-protein complexes and solar energy is transformed to excitation energy, which migrates among other light-harvesting complexes, until it arrives at the specialised complexes, reaction centres, where charge separation takes place and the excitation energy is converted into biochemical energy. In photosynthetic bacteria light harvesting and energy transfer occur in a system of intracytoplasmic membranes. In the case of *Rba. sphaeroides* these membranes take the form of vesicles, which are generally 50-60 nm in diameter (Tucker et al 2010). The processes of energy transfer and trapping take approximately 65 ps, and the quantum efficiency is approximately 95% (Şener et al 2009, Şener et al 2007a, Şener & Schulten 2009). Exploiting this characteristic of light-harvesting and reaction centre complexes, in terms of the very high energy transfer and charge separation efficiency, is a major goal in producing bio-inspired solar cells. Developing procedures for controlling the nanoscale distribution of light-harvesting antennas and reaction centres that remain functionally active on conductive substrates is an important step towards this goal.

Substrates such as gold and glass are widely used for the immobilisation of proteins. The surface properties of these substrates are generally modified by physical or chemical means to control the attachment of the target molecule. Self-assembled monolayers (SAMs), as the most extensively studied method, are generally used in modifying gold, silicon and glass substrates (Delamarche et al 1996, Nuzzo & Allara 1983, Ulman 1996, Wen et al 2008). These SAMs have been applied to study the attachment of a variety of biological materials. Photosynthetic complexes have previously been attached onto insulating substrates such as glass (Escalante et al 2008a, Escalante et al 2008b, Vasilev et al 2014b), and conductive substrate such as gold (Kondo et al 2007, Patole et al 2015, Reynolds et al 2007) and ITO (Suemori et al 2006). These studies reported that immobilised photosynthetic complexes retained their functional properties. Other studies, of immobilised charge separating reaction centres on conductive surfaces, measured a photocurrent in (Kamran et al 2014, Kamran et al 2015, Kondo et al 2007, Tan et al 2012). However, such studies generally do not control the distribution of the reaction centres on conductive surfaces, either laterally or in terms of the numbers of layers deposited. Developments in fabrication

techniques make it possible to create nanometre scale molecular assemblies and direct the distribution of monolayers of protein complexes (Leggett 2012). These techniques include photolithography (Nicholas P. Reynolds et al 2009, Patole et al 2015, Reynolds et al 2007, Sorribas et al 2002, Xia et al 2016), dip-pen nanolithography (DPN) (Ki-Bum Lee 2003, Lee et al 2002, Lee et al 2006a, Lee et al 2006b), nanoimprint lithography (NIL) (Escalante et al 2010, Escalante et al 2008a, Escalante et al 2008b), scanning near-field photolithography (SNP) (Ehtsham UI-Haq 2013, Sun & Leggett 2004, Sun et al 2006) and local oxidation lithography (Choi et al 2006, Choi et al 2008, Maoz 2000a, Maoz 2000b). However, most of the efforts in nanopatterning of photosynthetic complexes have focused on attaching a single type of complex such as LH2, RCLH1 or LHCII to a surface, and no comparative study has been reported on attachment of two types of photosynthetic complex on one conductive surface with their relative distributions controlled on the nanometre scale.

In this work, we created nanometre scale of photosynthetic complexes patterns such as LHCII, LH2 and RCLH1 on mPEO-SAM modified silicon surfaces by local oxidation lithography. This approach provides greater flexibility in designing protein nanoarrays with specific geometries and composition compared to other recently developed nanopatterning methods. Experimental conditions have been varied, in order to find the most efficient protocol for surface molecule oxidation and protein immobilisation. AFM images and fluorescence emission results showed that photosynthetic complexes retained their structural and optical properties after being immobilised on silicon surfaces. Performing two successive local oxidations creates dual patterns of complexes of LH2 and RCLH1 on the silicon substrate. Energy transfer from the LH2 to the RCLH1 complexes is observed by monitoring fluorescence lifetimes. This work establishes a method for patterning multiple types of complexes on a conductive surface with their distribution controlled on a nanometre scale. This approach paves the way to fabricate conductive bio-chips for light harvesting and charge separation purposes, and it represents a useful step forward for producing bio-inspired nanoscale architectures for biosensors and for solar cells.

4.3 Results

4.3.1 Nanopatterning photosynthetic complexes on silicon using local oxidation lithography

Nanopatterns of photosynthetic complexes were created by local oxidation lithography on mPEO-SAM coated silicon surfaces. The processes of surface molecule oxidation and spatially controlled protein attachment are schematically represented in Figure 4.1. Specifically, an mPEO monolayer was first self-assembled onto a piranha cleaned silicon surface (panel A). Then, the self-assembled monolayer was locally oxidised by the current from a scanning conductive AFM probe with an applied bias between 6 V to 12 V (panel B). Such a bias contributes to the formation of water meniscus between the tip and the silicon surface, which induces a current sufficient to cause the oxidation of terminal $-CH_3$ groups on the mPEO-SAM to $-COOH$ groups (Daan Wouters et al 2005, Hoepfner 2002, Krakert et al 2010, Maoz 2000b, Menglong Yang 2009); the silicon surface is oxidised to silicon oxide (Avouris et al 1997, Fontaine et al 1998). Following the local oxidation reaction, a mixed NHS and EDC solution was applied to transform $-COOH$ groups into NHS ester groups, which are active in amine crosslinking and capable of attachment to photosynthetic complexes (panel C). Since the rest of the mPEO-SAM remained protein resistant, photosynthetic complexes were specifically immobilised on the silicon surfaces (panel D). The distribution and occupancy of the protein patterns were then imaged by AFM, following the method in Section 2.8. The home-built FLIM system was used to check for the retained function and the potential for light harvesting and energy transfer, following the method in Section 2.7.

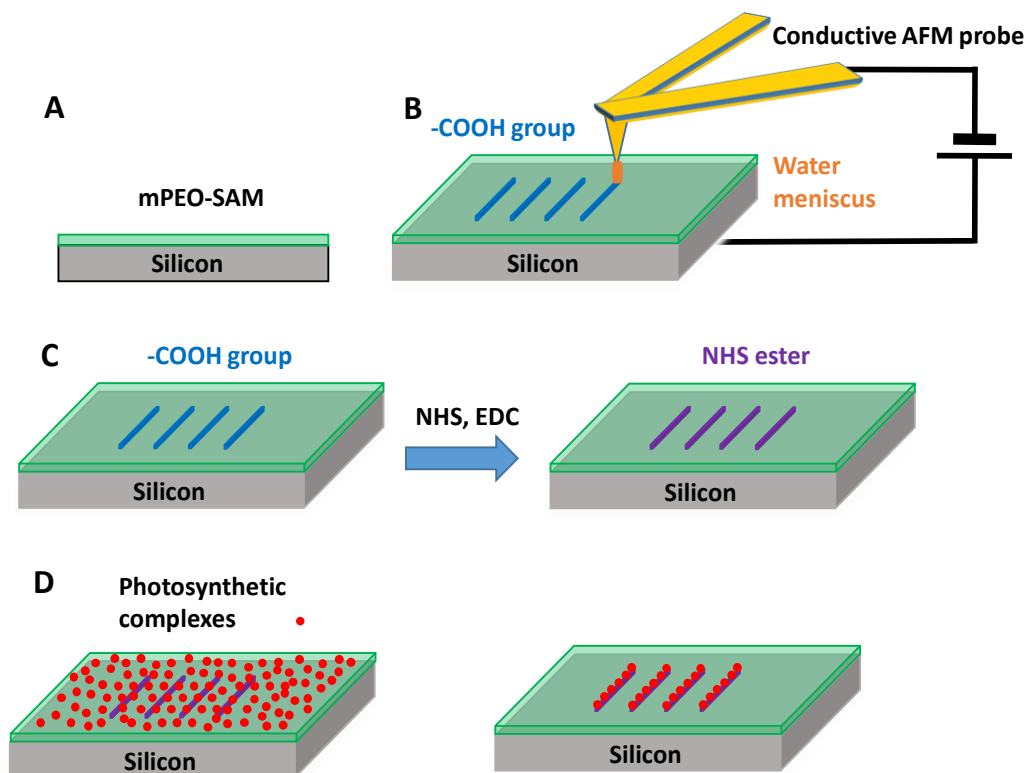


Figure 4.1. Schematic for protein immobilisation by local oxidation lithography.

- mPEO-SAM coated silicon.
- Locally oxidise mPEO to yield -COOH by applying bias between the substrate and the AFM tip in contact mode.
- Activation reaction between NHS and -COOH groups at pH 5.8 to form NHS ester groups.
- Immobilise photosynthetic complexes by cross-linking amine to NHS ester at pH 7.4.

4.3.2 AFM imaging of surface oxidation and protein immobilisation

Following the oxidation reaction and protein immobilisation, AFM images were recorded to check the formation of -COOH groups (Figure 4.2) and the distribution of immobilised photosynthetic complexes (Figure 4.3). During the local oxidation process, the AFM tip scanned at a fixed rate holding the bias duration at 100 ms/pixel, whilst the bias applied between the silicon surface and the AFM tip varied from 6 V to 12V to find out how bias would affect the oxidation. Figure 4.2A shows the height details of oxidised mPEO/COOH and silicon oxide nanolines on mPEO-SAM coated silicon. The four nanolines from left to right were created by bias from 6 V to 12V as marked underneath each line, with their average height plotted in Figure 4.2B. The increasing heights of the nanolines mainly arise from the oxidation of silicon substrate to silicon oxide, whilst the oxidised mPEO molecules make a very limited contribution.

As can be seen in Figure 4.2B, the nanoline created by the 6 V bias is 0.37 nm in height; with the bias increased to 8 V, 10 V and 12 V, the nanolines grew to 0.43 nm, 0.65 nm and 0.76 nm, respectively. Therefore, higher bias value results in more silicon oxidation, forming a thicker layer of silicon oxide. Multiple passes of the conductive AFM probe were required to efficiently oxidise the mPEO, resulting in broadening of the lines created; the full width half maximum (FWHM) of each oxidised nanoline varied between 339 nm and 414 nm and generally showed an increasing trend according to the rising bias. Figure 4.2C is the friction image of the mPEO/COOH pattern; Molecules terminated with a -COOH group show brighter contrast than -CH₃ terminated mPEO. The average friction of each nanoline is plotted in Figure 4.2D. -COOH group terminated nanolines generally show an increasing trend in terms of friction amplitude and FWHM. Specifically, the nanoline oxidised at 12 V of bias shows the brightest relative friction contrast value of 1.1 V and the largest FWHM of 258 nm, whilst the other three nanolines show a relative friction contrast from 0.8 V to 0.9 V and FWHM values from 185 nm to 221 nm.

Following local oxidation and friction image scanning, the oxidised mPEO sample went through the RCLH1 incubation process, as described in Section 2.10. AFM height images were recorded to check the RCLH1 distribution (Figure 4.3). Figure 4.3A shows the topology of the RCLH1 nanolines. The average height of each RCLH1 nanoline is plotted in Figure 4.3B, which takes into account the height of immobilised complexes and any vacant positions. As a result, low occupancies yield a lower average height, as seen in Figure 4.3B. Nanolines created at higher bias result in more efficient oxidation and better RCLH1 attachment and therefore a larger average height; RCLH1 nanolines made by biases at 6 V, 8 V, 10 V and 12 V show average heights of 5.5 nm, 7.2 nm, 8.7 nm and 11.5 nm respectively; and average FWHM of 221 nm, 256 nm, 320 nm and 348 nm respectively.

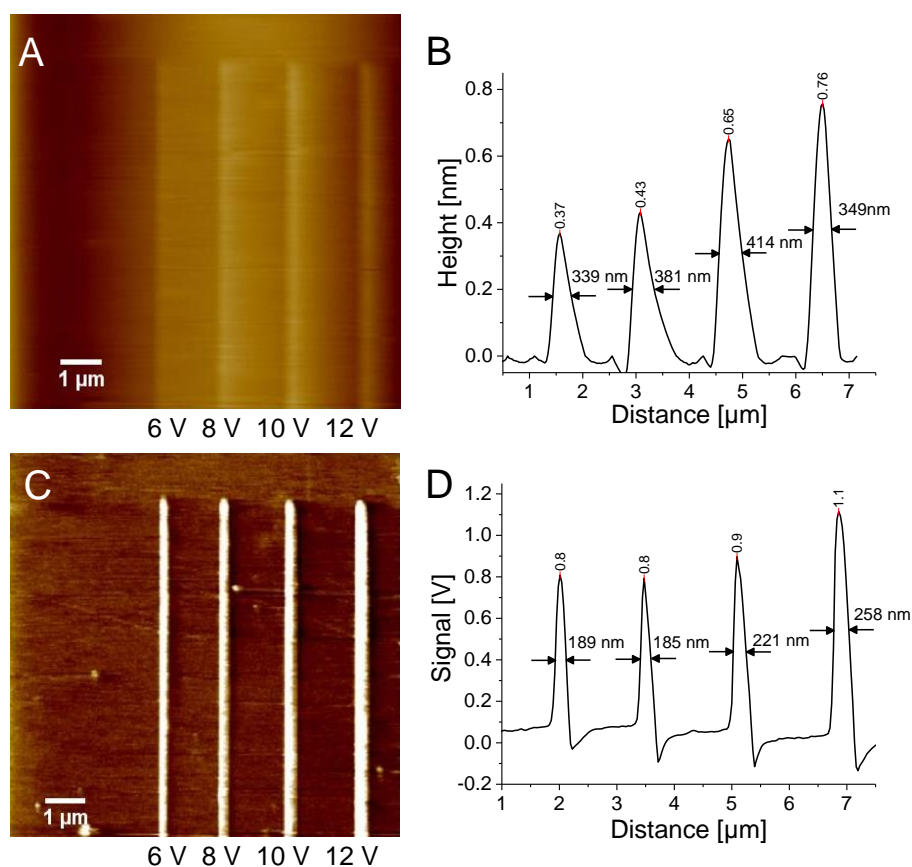


Figure 4.2. AFM images of the mPEO/COOH lines formed by local probe oxidation on a silicon surface

Local oxidation was performed at a bias from 6 V to 12 V and a bias duration of 100 ms/pixel. Height and friction image of the mPEO/COOH pattern were recorded in contact mode in air using the same tip for the local oxidation.

- Height image of the mPEO/COOH pattern on the silicon surface.
- Average height of each mPEO/COOH line and their FWHM according to topography.
- Friction image of the mPEO/COOH pattern on the silicon surface.
- Average relative friction of each mPEO/COOH line and their FWHM according to relative friction.

To study RCLH1 attachment at a specific location on a given nanoline, sections were plotted across the four lines in Figure 4.3A (white dashed line), and the profiles are displayed in Figure 4.3C. Again, nanolines oxidised at higher bias show better RCLH1 attachment, which does affect the average height but to a lesser degree than in Figure 4.3B. RCLH1 nanolines made by biases above 8 V are approximately 9.8nm in height, whilst the line oxidised at 6 V of bias is only 6.3 nm.

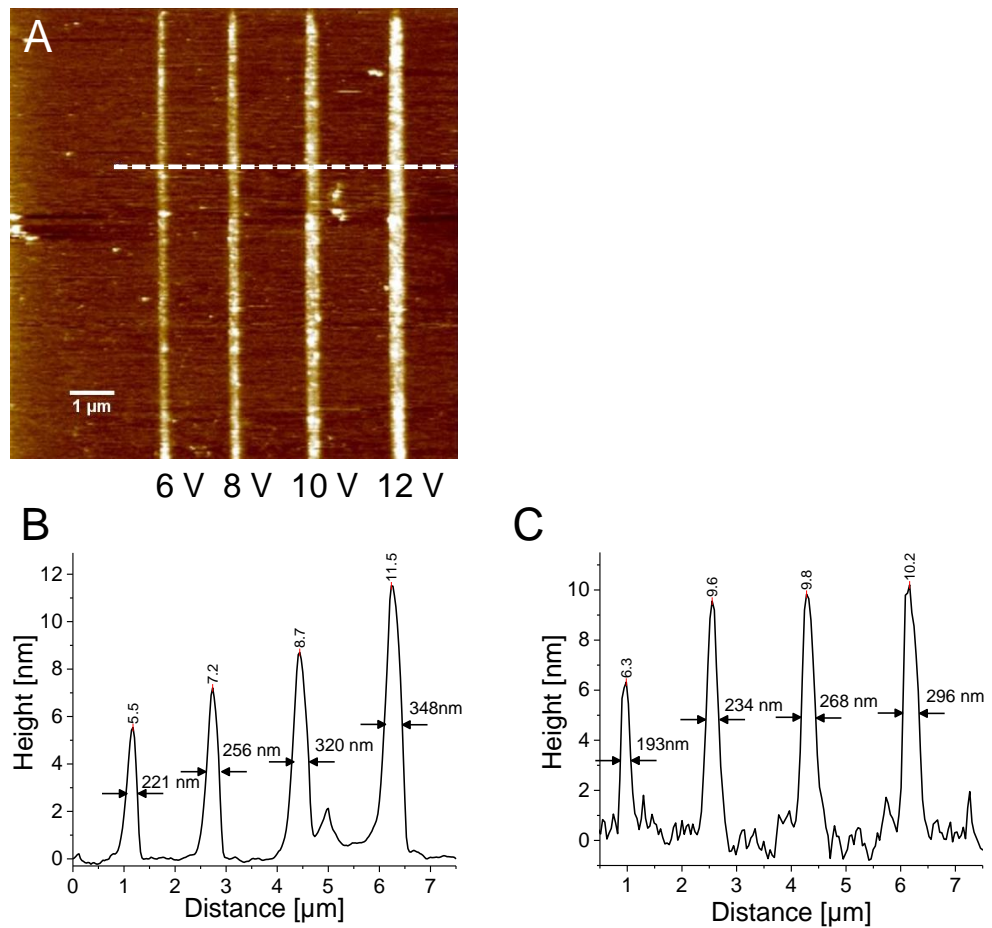


Figure 4.3. AFM images of RCLH1 complexes immobilised on NHS ester activated COOH patterns.

The incubation time for RCLH1 complexes was 6 hours. Height images of the immobilised RCLH1 complexes on the oxidised pattern were obtained in peak-force tapping mode in liquid using an SNL probe, cantilever C.

- A. Height image of RCLH1 complexes immobilised on an NHS ester activated -COOH pattern.
- B. Average height and average FWHM recorded along each RCLH1 nanoline.
- C. Height details for the line section marked in panel A by the white dashed line.

4.3.3 Improvements in local oxidation scanning for high quality protein nanolines

To obtain high quality nanopatterns of photosynthetic complexes, effective experimental conditions are required to efficiently oxidise exposed $-CH_3$ groups to $-COOH$. By varying AFM scanning bias and bias duration, a series of patterns of immobilised RCLH1 nanolines was created on mPEO-SAM coated silicon surfaces and their fluorescence emission properties were recorded (Figure 4.4). Figure 4.4A shows false colour fluorescence images of RCLH1 nanolines created by different scanning settings. Each group of nanolines shown in each image was created at the same bias duration, with bias voltages between 6 V and 12 V, as marked on the images. The total fluorescence intensity from each RCLH1 nanoline was quantified by ImageJ and plotted in Figure 4.4B. As can be seen, for a fixed bias duration, the fluorescence intensity of RCLH1 nanolines rises when scanning bias increases. Similarly, at a fixed scanning bias, the fluorescence intensity rises when the bias duration is prolonged.

The highest fluorescence intensity is observed from the RCLH1 nanoline created at a bias of 12 V and a bias duration of 100 ms/pixel, as marked by a white rectangle in Figure 4.4A. The fluorescence emission spectrum from this RCLH1 nanoline (Figure 4.4C) shows that the immobilised RCLH1 complexes were still functional. The 890 nm emission maximum from immobilised RCLH1, and the shape of the spectrum, largely match the fluorescence emission spectrum from RCLH1 complexes in solution (20 mM HEPES, pH 7.8, 0.03% β -DDM), indicating that the complexes retained their structural and optical property after immobilisation on the silicon surface.

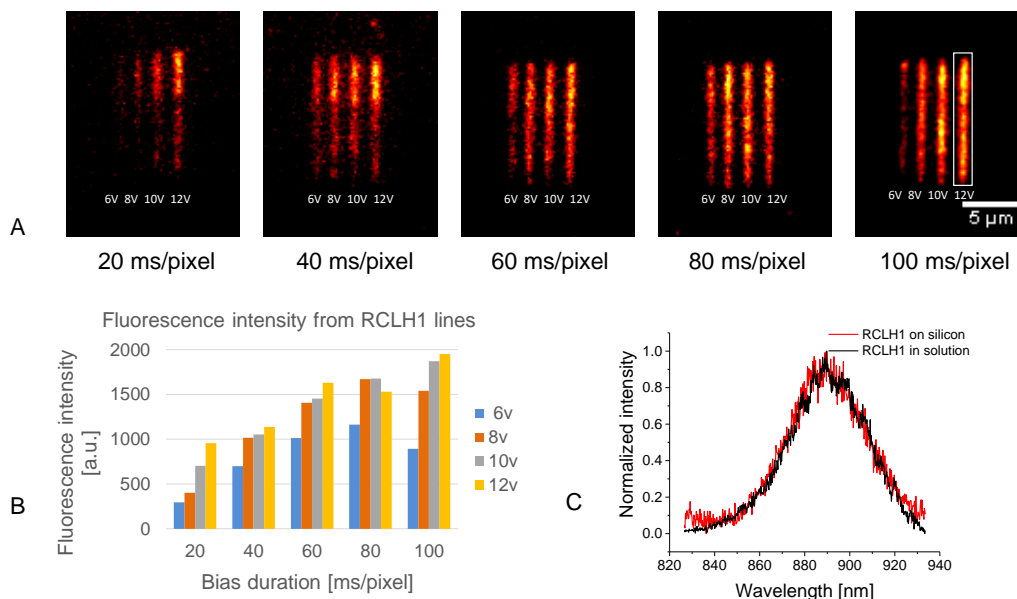


Figure 4.4. Fluorescence emission from the immobilised RCLH1 complexes on local probe oxidised nanolines.

During the oxidation process, the relative ambient humidity was around 40%. Whenever necessary the AFM tip was replaced before it lost sharpness and the writing pixel resolution was at 256 pixels over 10 μm length (25.6 pixel/μm). For protein immobilisation, RCLH1 solution was at a concentration of 2 μM and the incubation time was 6 hours.

- False colour fluorescence image of RCLH1 nanolines. Samples were excited at 470 nm by an LED light and fluorescence emission was recorded through a 900/32 nm bandpass filter. The four lines from left to right in each image were produced at biases from 6 V to 12 V, as marked under each line. The five images from left to right were produced at bias durations between 20 ms/pixel and 100 ms/pixel, as marked.
- Quantified fluorescence intensity of each RCLH1 nanoline in panel **A**; each line was cropped in ImageJ and its intensity counted.
- Normalised emission spectra of RCLH1 complexes immobilised on silicon and in solution, both excited by a 470 nm LED.

4.3.4 Bias duration over 100 ms/pixel shows no further improvement on the local oxidation

The results from Section 4.3.2 and 4.3.3 show that a higher bias value and a longer bias duration contribute to a more efficient mPEO oxidation and improved immobilisation of complexes. Since 12 V is the maximum bias output from the AFM, the bias duration was deliberately prolonged from 80 ms/pixel to 240 ms/pixel to find out if values over 100 ms/pixel would contribute to further oxidation of mPEO molecules. Nanolines of RCLH1 complexes were created and their fluorescence emission intensity was quantified by ImageJ. The normalised fluorescence intensity is plotted in Figure 4.5. The results show that for values of bias duration over 80 ms/pixel there is no consistent improvement in fluorescence intensity. For subsequent experiments bias of 12 V and duration of 100 ms/ pixel was chosen as the standard experimental condition.

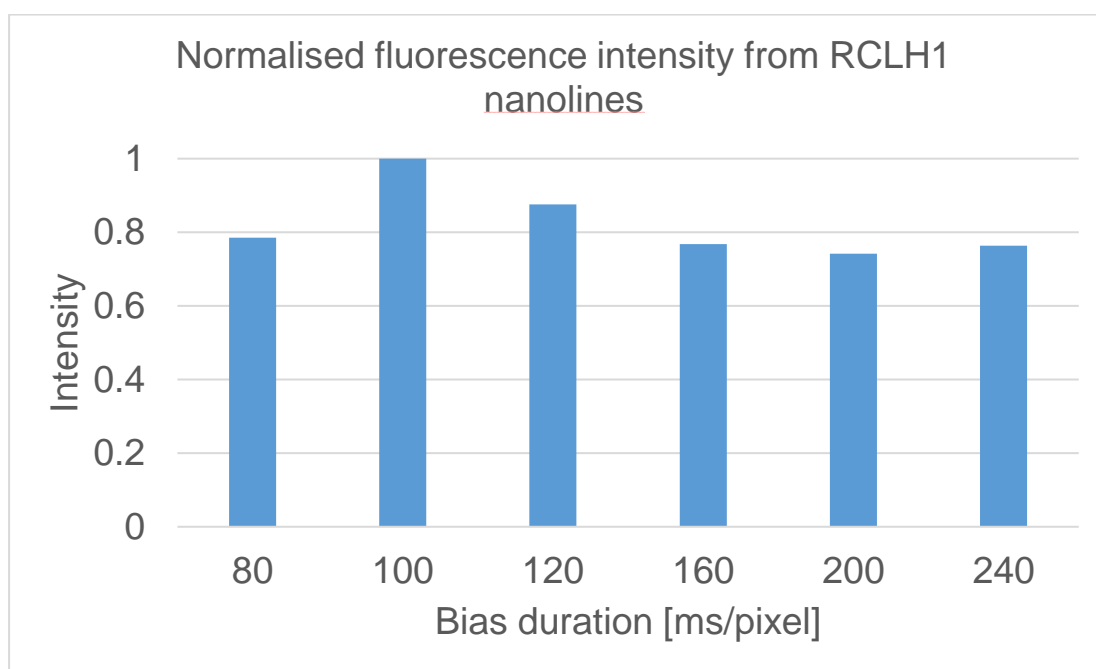


Figure 4.5. Normalised fluorescence intensity from RCLH1 nanolines created by local oxidation for bias duration from 80 ms/pixel to 240 ms/pixel.

Local oxidation was performed at a bias of 12 V. The incubation time for RCLH1 complexes was 6 hours.

4.3.5 Determination of the most efficient incubation time for photosynthetic complexes on oxidised mPEO

Following efficient mPEO oxidation, the protein incubation condition became another factor that affects the immobilisation of photosynthetic complexes. To find out the best incubation time, the RCLH1 photosynthetic complex was incubated at 4 °C from 40 min to 20 hours on the mPEO/COOH patterns oxidised optimally as in Section 4.3.4. For each incubation time, the fluorescence intensity from the RCLH1 nanoline was quantified by ImageJ (Figure 4.6). As seen, the emission intensity increased slightly when the incubation time was prolonged from 40 min to 2 hours; followed by a sharp rise for the incubation of 4 hours and a drop when the incubation was prolonged to 20 hours. Therefore, 4 hours of incubation, yielding the maximum RCLH1 fluorescence intensity, was chosen as the most efficient time.

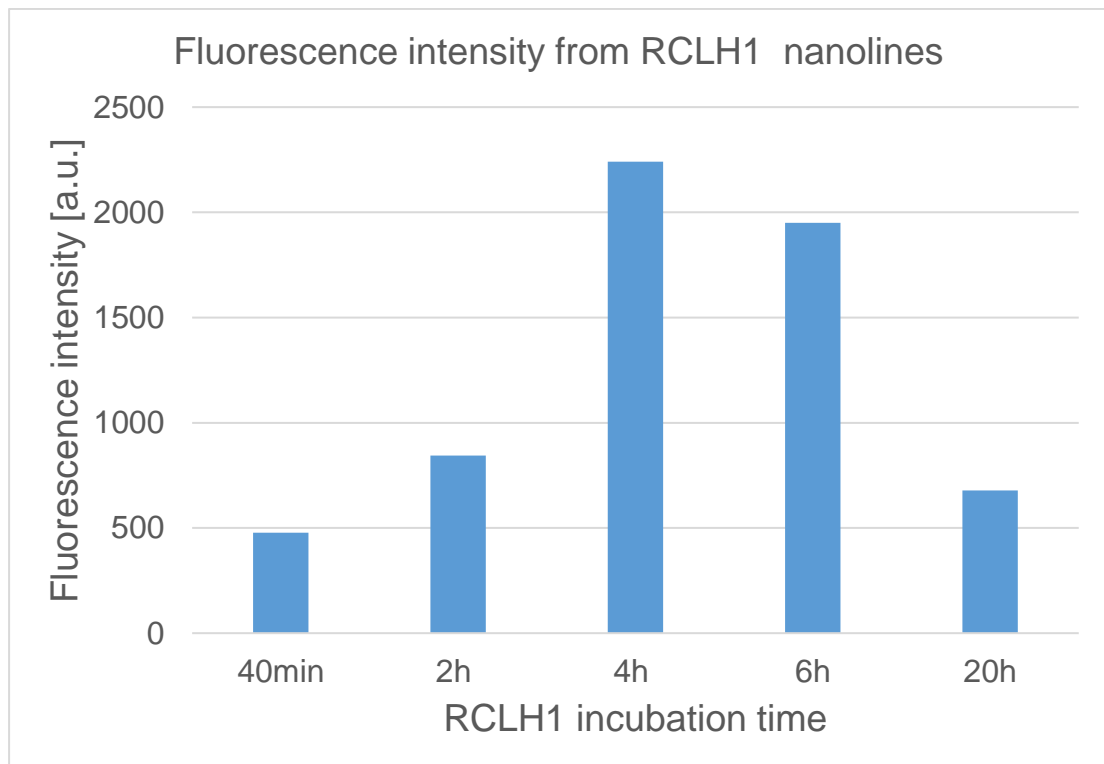


Figure 4.6. Fluorescence intensity from RCLH1 nanolines created by cross-linking incubation time from 40 minutes to 20 hours.

4.3.6 Immobilisation of LH2 complexes on mPEO-SAM coated silicon surface by local oxidation

Previous experiments, from Section 4.3.2 to Section 4.3.5, show that the most efficient mPEO oxidation occurs at 12 V of bias and 100 ms/pixel of bias duration; and the most efficient protein attachment requires 4 hours of incubation. With such experimental conditions, RCLH1 complexes have been efficiently attached on silicon surface to form nanoscale patterns, while retaining their structural properties and optical functions. Using the same experimental conditions, nanolines of LH2 complexes were created on the mPEO-SAM coated silicon surfaces.

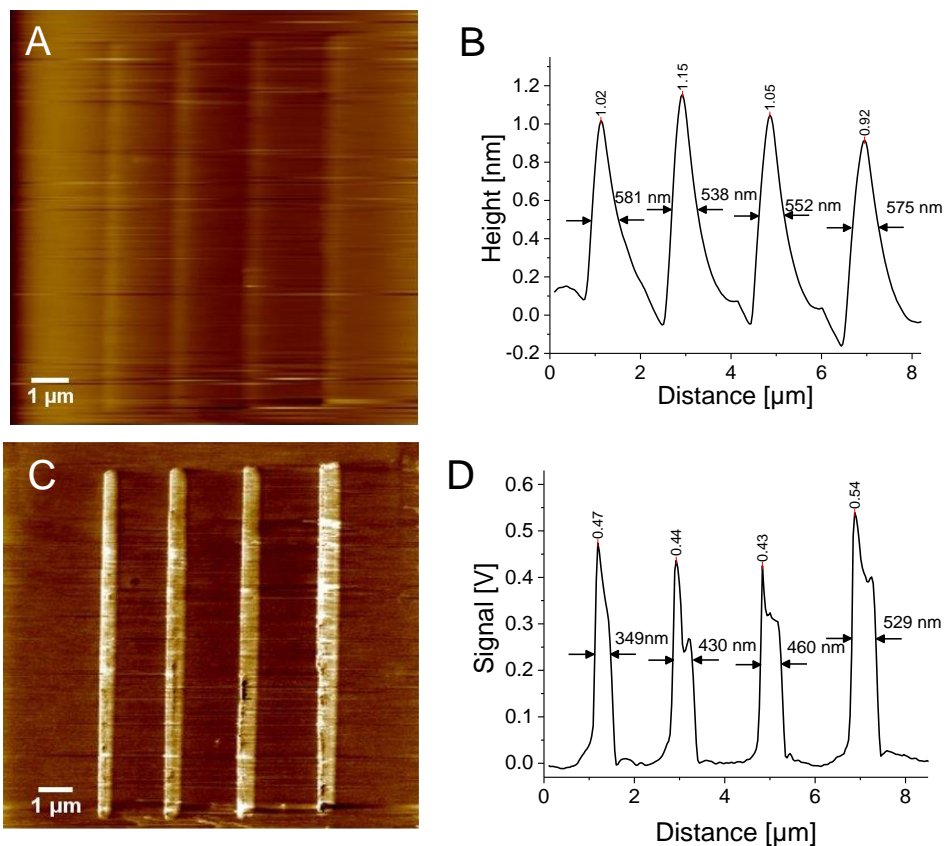


Figure 4.7. AFM images of mPEO/COOH lines formed by local probe oxidation on a silicon surface

Local oxidation was performed at a bias of 12 V and a bias duration of 100 ms/pixel at relative ambient humidity around 40%. Images were recorded in contact mode in air with the same tip used for the local oxidation.

- Height image of the mPEO/COOH pattern on the silicon surface.
- Average height of each mPEO/COOH line and the corresponding FWHM.
- Friction image of the mPEO/COOH pattern on the silicon surface.
- Average relative friction of each mPEO/COOH line and the corresponding FWHM.

Figure 4.7 shows the AFM images of locally oxidised mPEO/COOH nanolines on an mPEO-SAM coated silicon surface. The lines are about 1 nm above the silicon surface with approximate FWHMs around 560 nm (Figure 4.7A and 4.7B). The relative friction contrasts of each line, shown in panel C and D, are around 4.7 V in amplitude and 440 nm in FWHM. The height (Figure 4.7B) and friction amplitude (Figure 4D) were obtained by averaging all signals along each line.

The oxidised mPEO-SAM coated silicon then went through the incubation process for LH2 immobilisation as described in Section 2.10. AFM topography was recorded to check the LH2 occupancy of the oxidised mPEO/COOH lines (Figure 4.8). Figure 4.8A shows the topology of the LH2 nanolines with a zoomed-in image of a segment from a specific line (marked by a red rectangle). Considering the unexpectedly high topology of some lines, possibly arising from some protein aggregates, the aggregate-free regions were chosen for plotting the average height along each line (Figure 4.8B), as marked by the green dashed rectangle in Figure 4.8A. Taking into account the height of the immobilised LH2 and any vacant positions, the lines show an average height of around 6 nm and the average FWHM from 436 nm to 523 nm. The LH2 attachment at a specific location on a given nanoline was studied by plotted the average height for sections across the four lines in Figure 4.8A (white dashed line). The profiles displayed in Figure 4.3C show the LH2 nanolines are around 7.0 nm in height, with the FWHM varying from 304 nm to 546 nm.

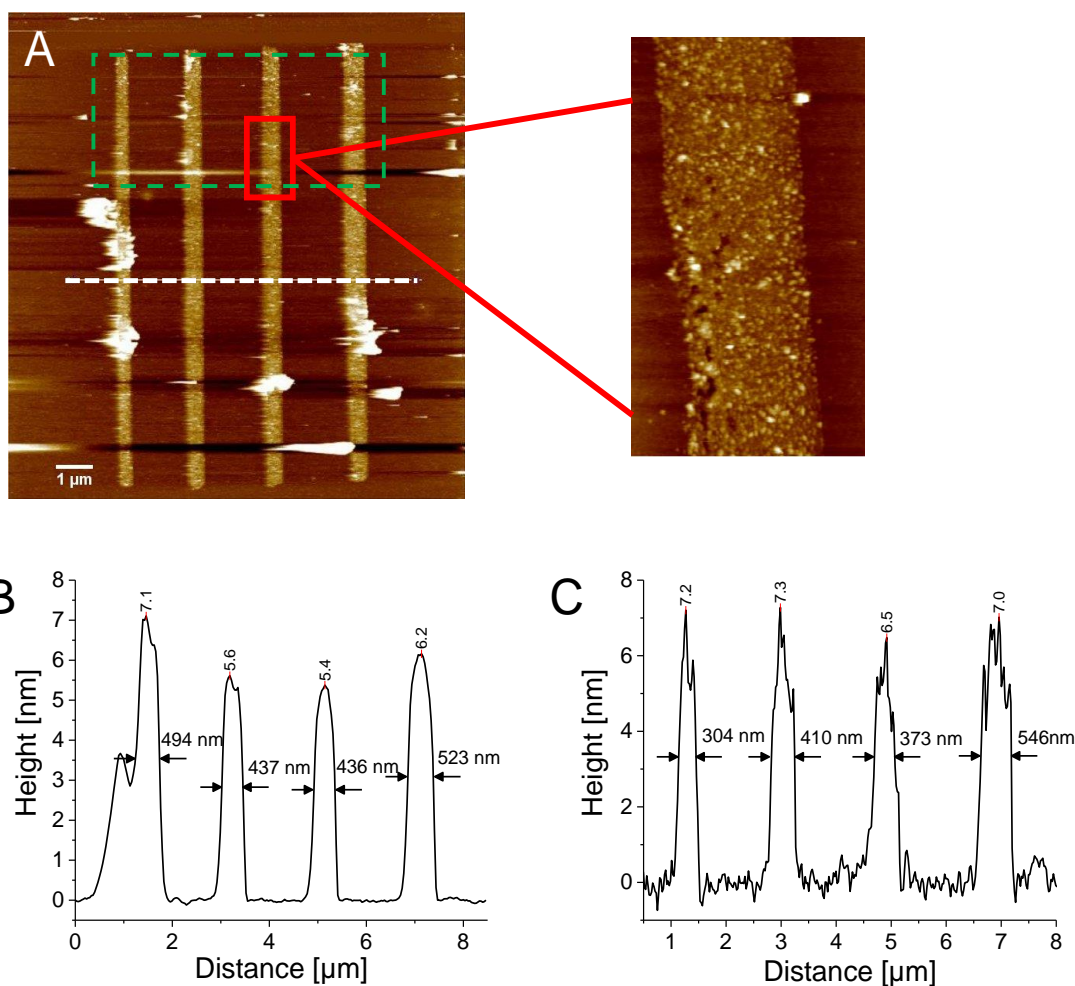


Figure 4.8. AFM images of LH2 complexes immobilised on an NHS ester activated COOH pattern.

The incubation time for LH2 complexes was 4 hours. Height images of the immobilised LH2 complexes on the oxidised pattern were obtained in peak-force tapping mode in liquid using an SNL probe, cantilever C.

- Height image of LH2 complexes immobilised on the NHS ester activated -COOH pattern. Zoomed-in details of LH2 occupancy are shown in the red rectangle.
- Average height and average FWHM recorded along each LH2 nanoline in the green dashed rectangle marked in panel A.
- Height details for the line section marked in panel A by the white dashed line.

Fluorescence images of the lines were recorded to check the functionality of LH2 complexes after immobilisation on the silicon surface. Figure 4.9A shows false colour fluorescence images of the LH2 nanolines and Figure 4.9B shows the fluorescence emission spectrum from the LH2 lines in the area marked by the white box. The 854 nm emission maximum from immobilised LH2, and the shape of the spectrum, match the fluorescence emission spectrum from LH2 complexes in solution (20 mM HEPES,

pH 7.8, 0.03% β -DDM), indicating the complexes retained their structural and optical property after immobilisation on the silicon surface.

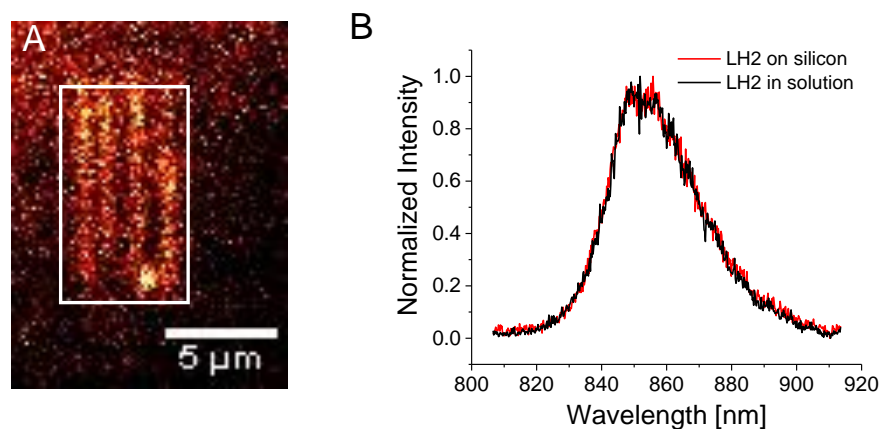


Figure 4.9. Fluorescence emission from nanolines of LH2 complexes

Local oxidation was performed at a bias of 12 V and a bias duration of 100 ms/pixel at relative ambient humidity around 40%. Whenever necessary the AFM tip was replaced before it lost sharpness and the writing pixel resolution was at 256 pixels over 10 μm length (25.6 pixel/μm). For protein immobilisation, LH2 solution was at a concentration of 2 μM and the incubation time was 4 hours.

- A. False colour fluorescence image of LH2 nanolines. The sample was excited at 470 nm by an LED light and the fluorescence emission was recorded through an 857/30 nm bandpass filter.
- B. Normalised emission spectra of LH2 complexes immobilised on silicon and in solution, excited at 470 nm by an LED.

4.3.7 Immobilisation of LHCII complexes on mPEO-SAM coated silicon surface by local oxidation

Following the nanopatterning of photosynthetic complexes from *Rba. sphaeroides*, LHCII complexes from spinach were also attached onto silicon surfaces with controlled distribution.

Figure 4.10 shows the AFM results of locally oxidised mPEO/COOH patterns on the mPEO-SAM coated silicon surface. Using the local oxidation method described in Section 2.10, two nanolines of -COOH groups were created at 12 V of bias and 100 ms/pixel of bias duration. The topographs in panels A and B show that both nanolines are about 0.4 nm in height and 400 nm in FWHM. For both nanolines, the relative friction images in panel C and D shows that their relative friction contrasts are around 0.4 V in terms of amplitude and 254 nm in terms of FWHM. The height (Figure 4.10B)

and friction amplitude (Figure 4.10D) were obtained by averaging all signals along each line.

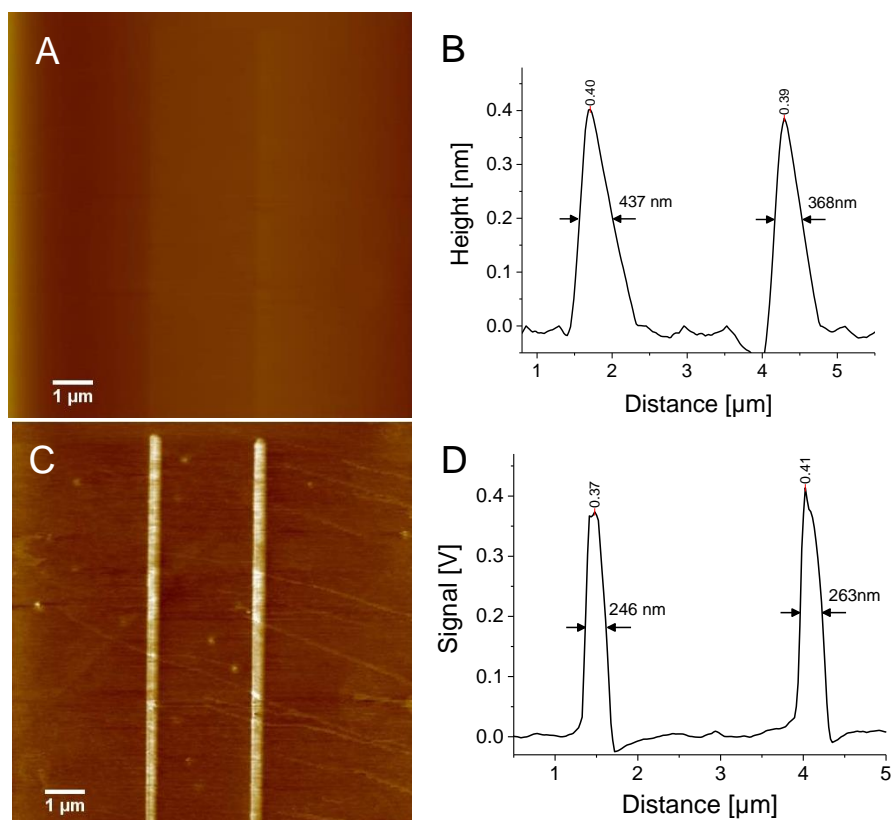


Figure 4.10. AFM images of mPEO/COOH lines formed by local probe oxidation on a silicon surface

Local oxidation was performed at a bias of 12 V and a bias duration of 100 ms/pixel. Height image and friction images of the mPEO/COOH pattern were recorded in contact mode in air with the same tip used for local oxidation.

- A. Height image of the mPEO/COOH pattern on the silicon surface.
- B. Average height of each mPEO/COOH line and their FWHM.
- C. Friction image of the mPEO/COOH pattern on the silicon surface.
- D. Average relative friction of each mPEO/COOH line and their FWHM.

Following surface oxidation, the substrate was incubated with LHCII complexes, using conditions described in Section 2.10. AFM images were recorded to study the topology of immobilised LHCII on the oxidised silicon surface, and therefore the quality of packing (Figure 4.11). Figure 4.11A shows the topology image of the LHCII nanolines and the zoomed-in image showing the LHCII occupancy is outlined by the red rectangle. The zoomed-in image shows that the LHCII nanoline varies in height, which possibly is caused by the LHCII stacking to form layers of 2-3 complexes during immobilisation. The average heights along the LHCII nanolines are 7.6 nm and 5.3 nm

and their FWHMs are 196 nm and 186 nm, as plotted in Figure 4.11B. Three cross-sections were chosen from both lines to check the LHCII stacking (Figure 4.11C); the blue dashed line show heights of 6.3 nm, indicating single layers of LHCII complexes, whereas the section marked in red shows a maximum height of 16.1 nm, indicating a possibility of a triple layer of complexes; the section marked by the green dashed line shows heights of 13.2 nm and 20.8 nm, indicating a possibility of 2-4 layers of stacked LHCII complexes.

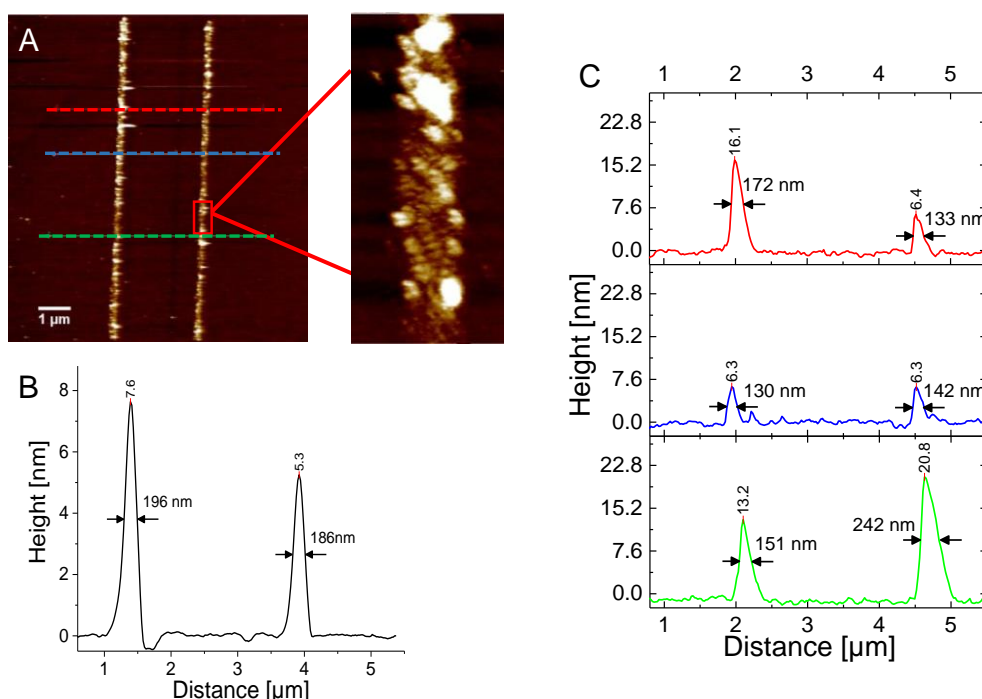


Figure 4.11. AFM images of the LHCII complex immobilisation on the NHS ester activated COOH pattern.

The incubation time for LHCII complexes was 4 hours. Height images of the immobilised LHCII complexes on the oxidised pattern were obtained in peak-force tapping mode in liquid with SNL probe, cantilever C.

- A. Height image of LHCII complexes immobilised on the NHS ester activated -COOH pattern. Zoomed-in details of LHCII occupancy are shown in the red rectangle.
- B. Average height and average FWHM recorded along each LHCII nanoline.
- C. Height details of line sections marked in panel A by green, red and blue dashed lines.

Fluorescence emission of immobilised LHCII complexes was recorded to check the retention of their optical properties. Figure 4.12A is the false colour fluorescence image of the LHCII nanolines recorded through a 679/41 nm bandpass filter. Figure 4.12B shows the fluorescence emission spectrum from the LHCII nanoline marked in

the white box in figure 4.12A. The 680 nm maximum emission and the shape of the spectrum matches the fluorescence emission in solution (20mM HEPES, pH 7.8, 0.03% β -DDM). Therefore, the LHCII complexes are still optically functional after immobilisation on the silicon surface.

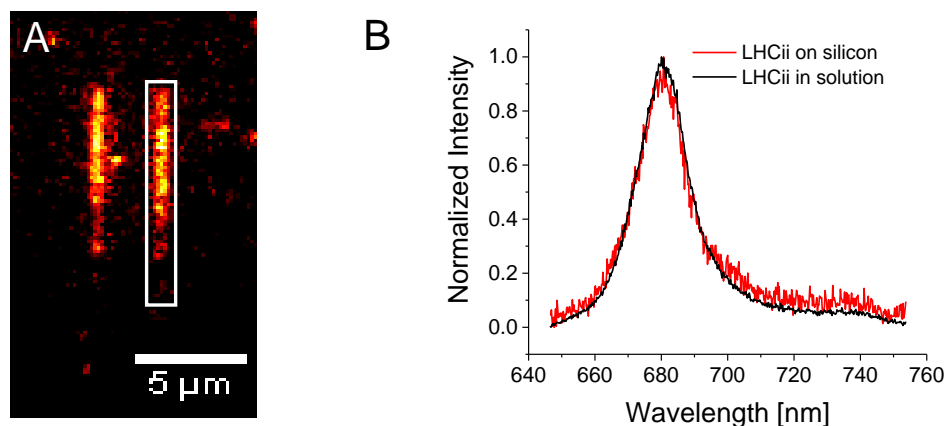


Figure 4.12. Fluorescence emission from nanolines of LHCII complexes.

During local oxidation process, the AFM tip was replaced before it lost sharpness and the writing pixel resolution was at 256 pixels over a 10 μm length (25.6 pixel/μm). For the protein immobilisation, LHCII solution was at a concentration of 2 μM and the incubation time was 4 hours.

- A. False colour fluorescence image of LHCII nanolines. The sample was excited at 470 nm by an LED light and fluorescence emission was recorded through a 679/41 nm bandpass filter.
- B. Normalised the fluorescence emission of LHCII complexes immobilised on silicon and in solution, excited at 470 nm by an LED light source.

4.3.8 Co-patterning two types of photosynthetic complex on mPEO-SAM coated silicon surface by local oxidation

In photosynthetic cells of *Rba.sphaeroides* energy trapping starts with absorption of light by LH2 complexes, followed by energy transfer via LH1 complexes to the reaction centre where excitation energy is trapped and transformed into chemical energy. To mimic this process on a silicon surface, two photosynthetic complexes must be patterned on one silicon surface so that their distributions intersect. Based on the immobilisation of single types of complex, i.e. RCLH1, LH2 and LHCII complexes, (see Sections from 4.3.2 to 4.3.7), successive local oxidation reactions and protein incubations were performed to pattern both RCLH1 complexes and LH2 complexes on the same silicon surface (Figure 4.13). Specifically, RCLH1 complexes were

immobilised on the four -COOH nanolines oxidised by the first AFM scanning; the second AFM scanning was performed locally but at 90 ° to the RCLH1 lines, creating three -COOH lines for the attachment of LH2 complexes. Wild-type complexes, with normal carotenoid content, were used for this work.

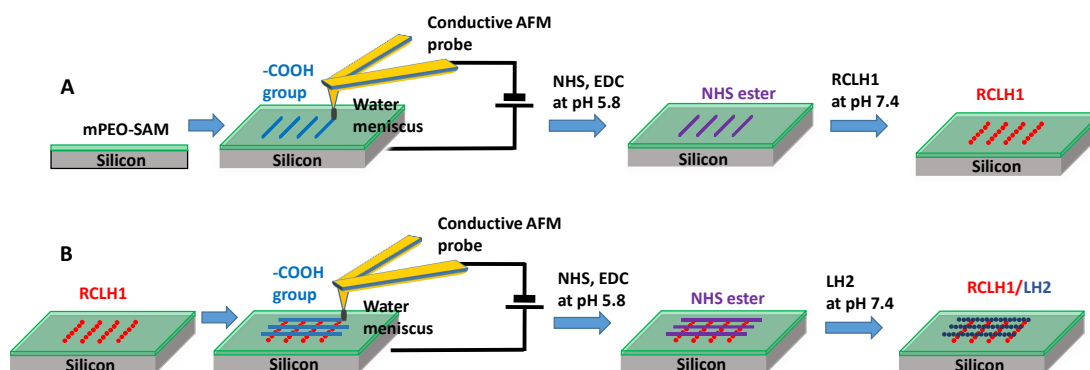


Figure 4.13. Schematic for multiple protein immobilisation by local oxidation lithography.

- A. First local oxidation of four lines for RCLH1 immobilisation.
- B. Second local oxidation of three lines for LH2 immobilisation. Local oxidation was performed at the same location orthogonal to the RCLH1 lines.

Figure 4.14 shows the AFM images of mPEO/COOH patterns from the first local oxidation. Panel A and B show that the average heights along the oxidised nanolines (mPEO/COOH and Si/SiO₂) vary from 1.0 nm to 1.5 nm and the relative average FWHM are between 471 nm and 687 nm. Panel C and D show that the average friction contrast values along the mPEO/COOH nanolines are uniformly around 0.23 V in relative friction value and with FWHM of 500 nm.

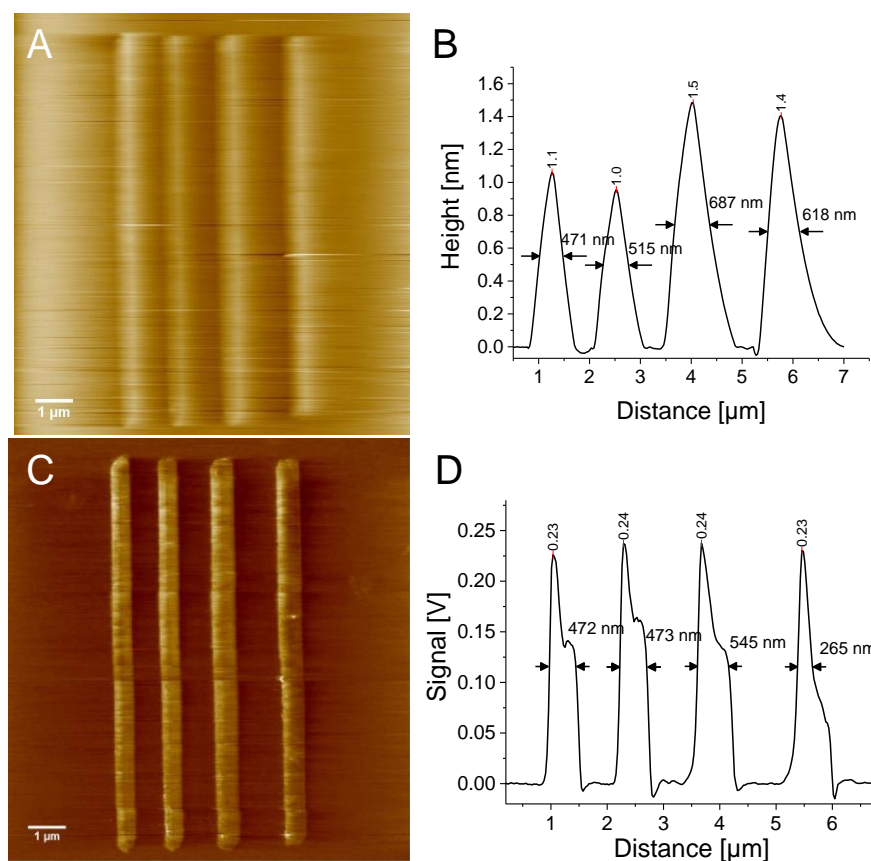


Figure 4.14. AFM images of mPEO/COOH lines made by the first local oxidation on a silicon surface

Local oxidation was performed at a bias of 12 V and a bias duration of 100 ms/pixel at relative ambient humidity around 40%. AFM images were recorded in contact mode in air using the same tip for the local oxidation.

- C. Height image of the mPEO/COOH pattern on the silicon surface.
- D. Average height of each mPEO/COOH line and their FWHM.
- E. Friction image of the mPEO/COOH pattern on the silicon surface.
- F. Average relative friction of each mPEO/COOH line and their FWHM.

Figure 4.15 shows the AFM results of the RCLH1 complexes immobilised on the nanolines from the first local oxidation. Figure 4.15A is the topology of the RCLH1 nanolines with a zoomed-in detail showing the protein occupancy. The average heights of each RCLH1 nanoline in Figure 4.15B show the RCLH1 nanolines are around 9 nm in height and 350 nm in FWHM. To study the RCLH1 occupancy at a specific location on a given nanoline, sections were plotted across the four lines in Figure 4.15A (white dashed line), and the profiles are displayed in Figure 4.15C. Results show that the RCLH1 nanolines are around 10.5 nm in height and 353 nm in FWHM.

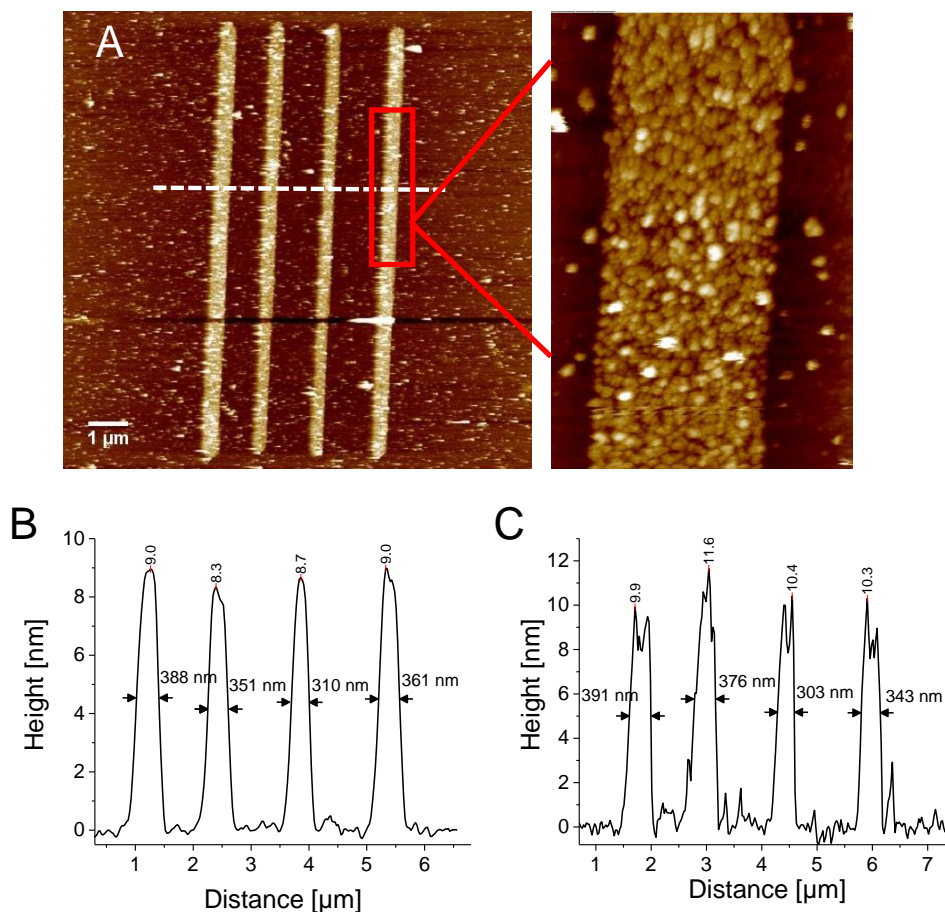


Figure 4.15. AFM images of RCLH1 complexes immobilised on an NHS ester activated COOH pattern following the first local oxidation.

The incubation time for RCLH1 complexes was 4 hours. Height images of the immobilised RCLH1 complexes on the oxidised pattern were obtained in peak-force tapping mode in liquid using an SNL probe, cantilever C.

- A. Height image of the RCLH1 complexes immobilised on the NHS ester activated -COOH pattern. Zoomed-in details on RCLH1 occupancy are shown in the red rectangle.
- B. Average height and average FWHM recorded along each RCLH1 nanoline.
- C. Height details for the line section marked in panel A by the white dashed line.

Figure 4.16 shows the AFM images from the second local oxidation performed at 90° to the RCLH1 nanolines. The images were recorded in contact mode in air with the same conductive AFM tip used in the second local oxidation process. The height measurements in panel A and B show that RCLH1 patterns are about 5 nm and the oxidised mPEO/COOH (Si/SiO₂) lines are about 1 nm. The drop in the height of RCLH1 is possibly caused by the high scanning speed of 1.5 Hz, the low scanning resolution of 128x 128 pixel and the high contact pressure setting for the AFM imaging. Panels C

and D show that RCLH1 patterns are roughly ten times larger in friction contrast than the mPEO/COOH patterns.

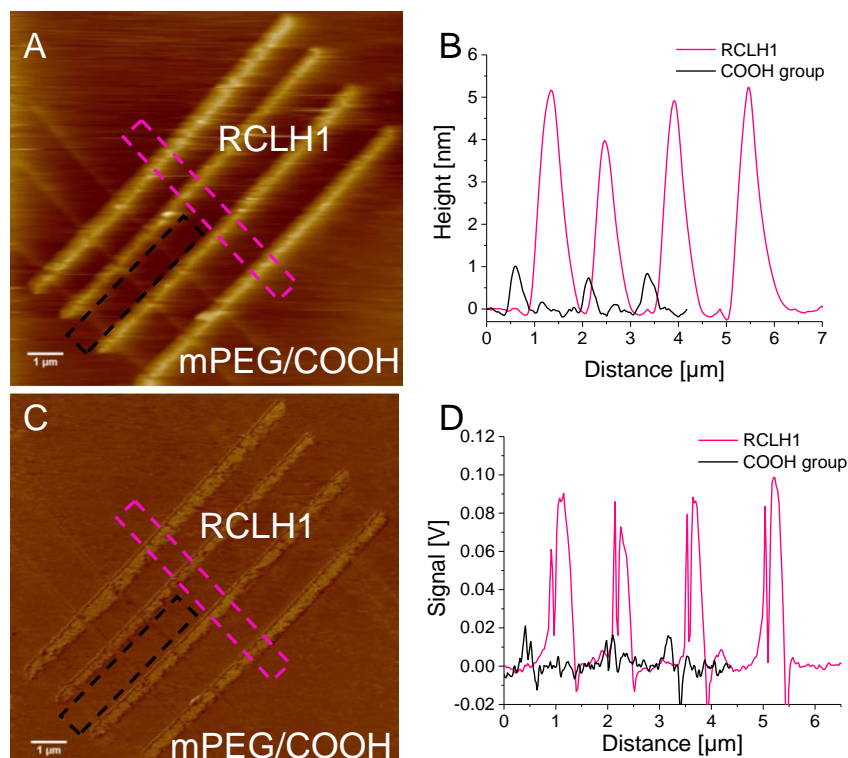


Figure 4.16. AFM images of the RCLH1 pattern from the first local oxidation and the mPEO/COOH pattern from the second local oxidation.

The second local oxidation was performed at a bias of 12 V and a bias duration of 100 ms/pixel in a perpendicular direction to the RCLH1 lines. Images were recorded in contact mode in air using the same tip as for the second local oxidation.

- Height image of the RCLH1 pattern and the mPEO/COOH pattern.
- Average height of each RCLH1 line marked in the pink rectangle and that of each mPEO/COOH line marked in the black rectangle in panel A.
- Friction image of the RCLH1 pattern and the mPEO/COOH pattern.
- Average relative friction of each RCLH1 lines marked in pink rectangle and that of each mPEO/COOH line marked in black rectangle in panel C.

Figure 4.17 shows the AFM images of the RCLH1 complexes and the LH2 complexes immobilised on a silicon surface. Both RCLH1 and LH2 nanolines are 10 μm in length and the overview of protein distribution is shown in Figure 4.17A. The zoomed-in image marked with the red rectangle reveals the detailed topology of the crossover region (Figure 4.17B). As can be seen, the RCLH1 lines are interrupted where the LH2 lines intersect, indicating that the original RCLH1 complexes were replaced by the LH2 complexes in the second stage of protein deposition. Topologies of lines at specific locations, marked with the white dashed line in Figure 4.17B, are plotted in Figure

4.17C. The RCLH1 lines are about 10 nm in height and the LH2 lines are about 7 nm in height. To study the protein occupancy, average heights in randomly chosen regions along each LH2 (marked by the green dashed rectangle) and RCLH1 (marked by the pink dashed rectangle) nanoline were plotted in Figure 4.17D and 4.16E, respectively. The average heights along the three LH2 nanolines are around 4.5 nm and those along the four RCLH1 lines are about 10 nm. The FWHM of the LH2 and RCLH1 lines are approximately 170 nm and 320 nm respectively. Therefore, the first local oxidation seems more efficient than the second one with a higher protein occupancy and a larger FWHM on each line.

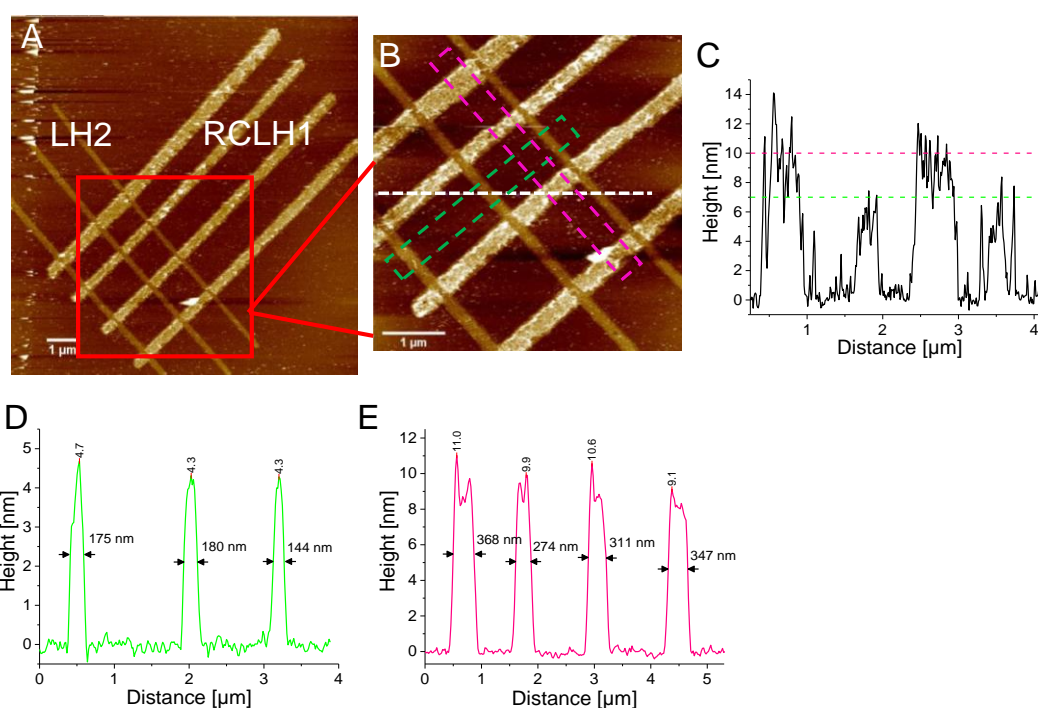


Figure 4.17. AFM images of the intersecting RCLH1 and LH2 nanolines created by successive local oxidations on a silicon surface.

The incubation time for the photosynthetic complexes was 4 hours. Height images of the immobilised LH2/RCLH1 complexes on the oxidised pattern were obtained in peak-force tapping mode in liquid using an SNL probe, cantilever C.

- Height image of the LH2/RCLH1 complexes immobilised on the NHS ester activated -COOH pattern.
- Zoomed-in details of the LH2/RCLH1 lines corresponding to the red rectangle in panel A.
- Height profile for the line section marked in panel B by the white dashed line.
- Average height and average FWHM details recorded along each LH2 line marked in green rectangle in panel B.
- Average height and average FWHM details recorded along each RCLH1 line marked in pink rectangle in panel B.

4.3.9 Energy transfer between LH2 and RCLH1 complexes immobilised on a silicon surface

Nanolines of LH2 and RCLH1 created in Section 4.3.8 failed to show evidence of energy transfer due to the limited contact area at the intersections. Therefore, a larger area of LH2 in the form of a 5x5 μm square, with four intersecting RCLH1 nanolines, was fabricated in order to increase the contact area for this energy transfer study. A 5 μm square of mPEO/COOH was created followed by incubation with LH2 complexes. Then, four 10 μm long mPEO/COOH nanolines were oxidised across the LH2 square (Figure 4.18C), followed by the incubation with RCLH1 complexes. Local oxidation was performed at 12 V of bias and 4 ms/pixel of bias duration for the 5 μm square (51.2 pixels/ μm for scanning); and 12 V and 100 ms/pixel for the 10 μm long lines (25.6 pixels/ μm for scanning). Referring to the roughly 400 nm FWHM of nanolines oxidised by previous line scanning (Section 4.3.2 to 4.3.8), the mPEO/COOH lines swell during the serial oxidation to form the square pattern, the effect is to oxidise mEPO molecules several times over, roughly an extra 10 times. Moreover, the pixel density on the square is twice of that on the line; thus, the 4 ms/pixel bias duration for formation of the square is equivalent to 80 ms/pixel when performing line oxidation.

Figure 4.18 shows the AFM images of the two local oxidations. The LH2 complexes were immobilised following the first oxidation, but before the second oxidation. Panel A is the friction image of the square created by the first local oxidation. Then the sample was incubated with the LH2 complexes followed by the second local oxidation creating four mPEO/COOH nanolines. Panel C and E show the friction and topology images of the LH2 square and the COOH lines. The relative friction value and heights of the line sections are plotted in Panel B, D and E corresponding to the dashed lines in Panel A, C and E respectively. The height of LH2 square in panel F is about 1.3 nm. Such a drop is possibly caused by the high scanning speed of 1.5 Hz, the low scanning resolution of 128x 128 pixel and the high contact pressure setting for the AFM imaging.

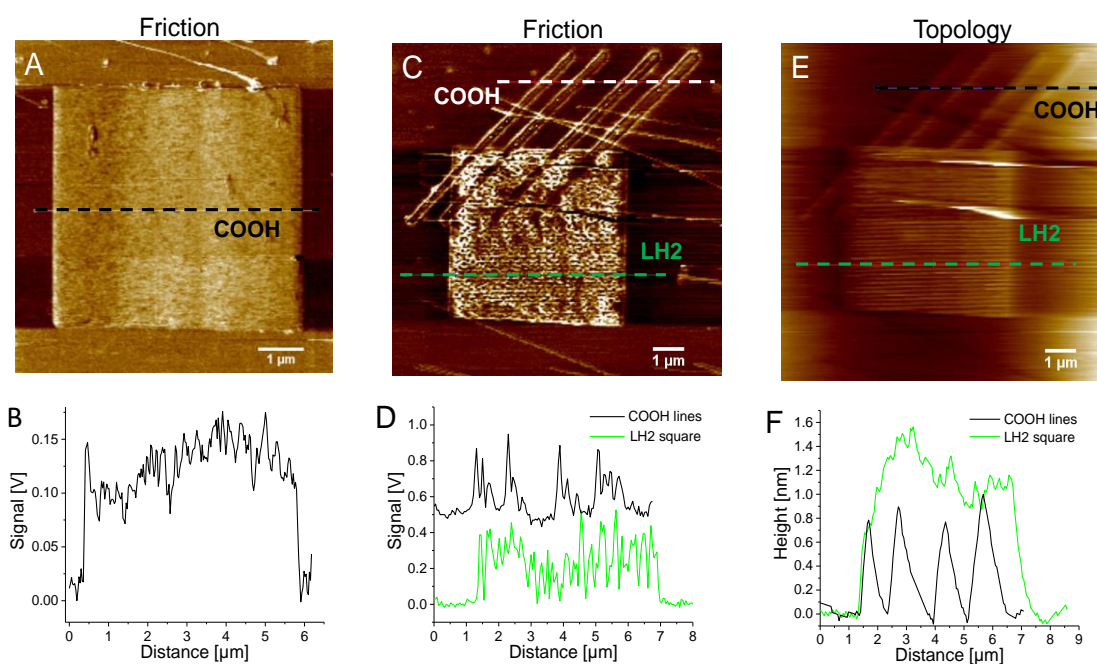


Figure 4.18. AFM images of two local oxidations.

The incubation time for LH2 complexes was 4 hours. The LH2 complexes were immobilised following the first oxidation, and then was the second oxidation. The RCLH1 complexes were not immobilised yet.

All the images were recorded in contact mode in air by the same conductive AFM tip used in the local oxidation.

- Friction image of the mPEO/COOH pattern square from the first local oxidation.
- Relative friction value of the line section marked by the black dashed line in panel A.
- Friction image of the immobilised LH2 square and the four mPEO/COOH lines from the second local oxidation.
- Relative friction values of the line sections marked by the white and green dashed lines in panel C.
- Topology of the immobilised LH2 square and the four mPEO/COOH lines from the second local oxidation.
- Heights of the line sections marked by the black and green dashed lines in panel E.

Following the second local oxidation, the sample was incubated with the RCLH1 complexes for 4 hours. The surface distribution of the immobilised LH2 and RCLH1 complexes is shown in Figure 4.19A, whilst panel B shows the height profile of the line section marked by the black dashed line in panel A. As seen in Panel B, the RCLH1 lines are about 8 nm in height and the LH2 square are about 6 nm in height, marked by the pink and green dashed line respectively. Referring to the topology in Figure 4.18E, after the immobilisation of the RCLH1, some unexpectedly high topologies were noticed in Panel A (pink ovals), possibly arising from the aggregates of the RCLH1 complexes. Heights of the RCLH1 aggregates are shown in panel C and D

corresponding to the line sections marked in blue and red dashed lines in panel A, respectively. As can be seen, those aggregates are between 30 nm and 80 nm in height.

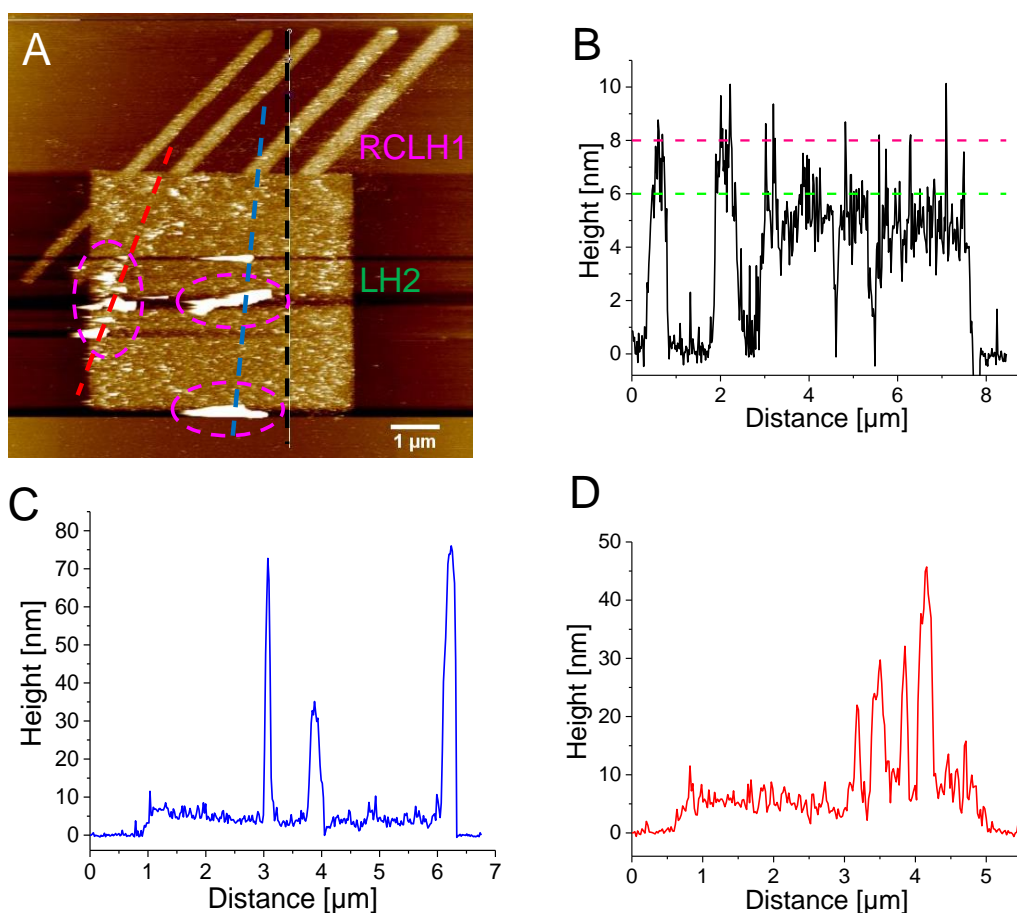


Figure 4.19. AFM images of co-patterned LH2 square and RCLH1 lines.

- A. Peak-force tapping AFM image recorded in liquid with SNL probe (cantilever C). Topology of the immobilised LH2 square and the four RCLH1 lines.
- B. Heights of the line section marked by the black dashed line in panel A.
- C. Heights of the line section marked by the blue dashed line in panel A.
- D. Heights of the line section marked by the red dashed line in panel A.

Zoomed-in AFM images were recorded to see the details of occupancy of complexes on the co-pattern (Figure 4.20). Each image is a zoom from the region marked by the red dashed square in the previous image, corresponding in order from A to E. As seen in panel E, the complexes are about 10 nm to 20 nm in diameter, and they are fully packed on the silicon surface.

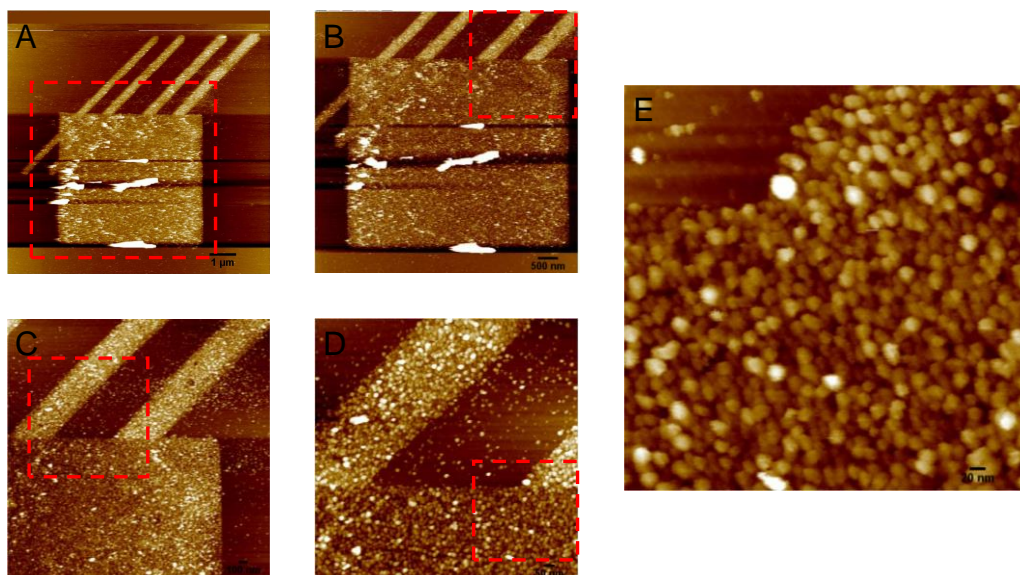


Figure 4.20. Zoomed-in AFM images of co-patterned LH2 square and RCLH1 lines.

- A. Whole topology view of the co-patterned LH2 square and the RCLH1 lines.
- B. Zoomed-in image of the red dashed square marked in panel A.
- C. Zoomed-in image of the red dashed square marked in panel B.
- D. Zoomed-in image of the red dashed square marked in panel C.
- E. Zoomed-in image of the red dashed square marked in panel D.

Fluorescence emission from the co-patterned LH2 and RCLH1 complexes was recorded to check if the immobilised complexes retained function and to see if any energy transfer occurred from LH2 to RCLH1 complexes (Figure 4.21). Figure 4.21A and B shows the fluorescence wide-field images excited by the 470 nm LED; the fluorescence emission was recorded either through an 857/30 nm bandpass filter for the LH2 distribution or a 900/32 nm bandpass filter for the RCLH1 distribution. Despite the apparent selectivity of the 857/30 nm bandpass filter, which should favour LH2 complexes, the 30 nm bandwidth does allow some signal from RCLH1 complexes to reach the detector. The same applies to the 900/32 nm bandpass filter for the LH2 complexes.

Figure 4.21 D is the fluorescence lifetime image from the co-patterned complexes. The complexes were excited at 485 nm by a pulse laser and fluorescence emission photons were collected at $857 \text{ nm} \pm 3 \text{ nm}$ to study the lifetime of the LH2 complexes. In the fluorescence lifetime image, fluorescence from RCLH1 complexes is unlikely to reach the detector because of the 3 nm bandwidth narrowed by the grating and the slit in front of the detector. Thus, the fluorescence lifetime image represents a 'pure' LH2 signal. As seen, regions marked in the green dashed ovals are where the four

RCLH1 nanolines exist, whereas the red ovals delineate three areas where large numbers of aggregated RCLH1 complexes lie on the LH2 surface. These aggregates are clearly seen in topographic profiles in Figure 4.21C; they are also seen in the wide-field fluorescence image in Figure 4.21A and B. The lifetimes of LH2 in the regions with RCLH1 aggregates (red dashed ovals) are between 300 and 600 ps (Figure 4.21D), likely because the overlying RCLH1 complexes act as acceptors for energy absorbed by LH2. In the regions where the LH2 square intersects with the RCLH1 lines (green dashed ovals), the LH2 lifetimes are shortened from ~ 900 - 1300 ps to ~ 300 - 500 ps, indicating the likelihood of energy transfer between the two types of complexes.

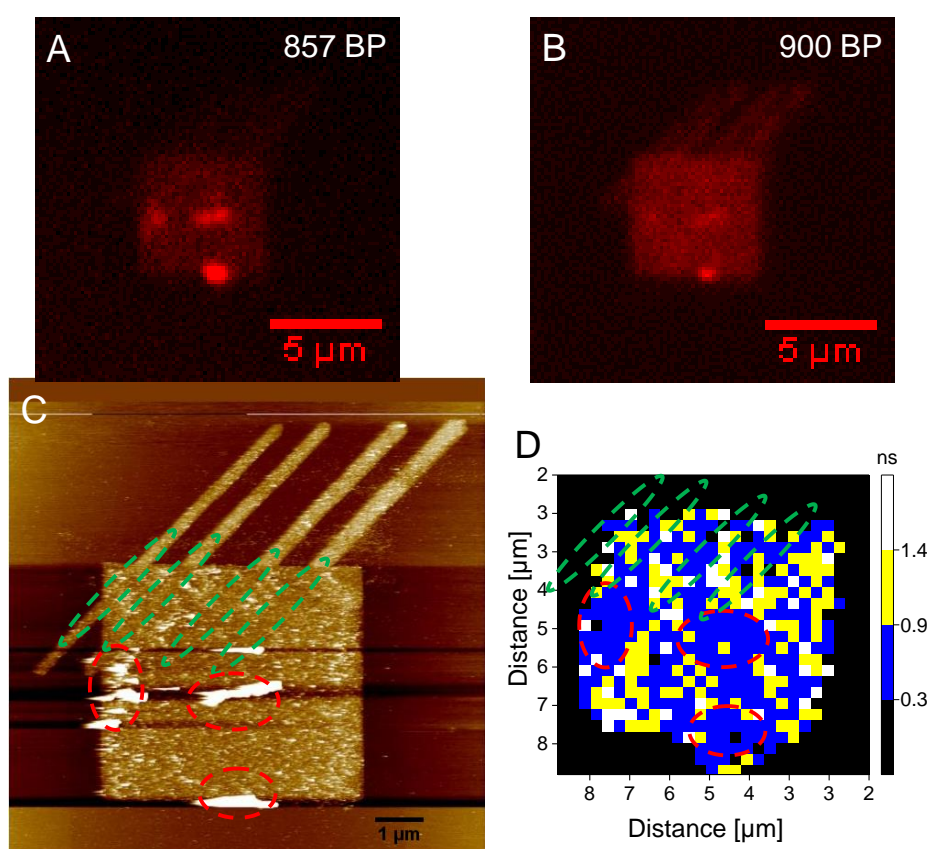


Figure 4.21. Fluorescence images of co-patterned LH2 square and RCLH1 lines.

The 470 nm LED was used for recording the wide-field fluorescence images in panel A and B. Fluorescence lifetime imaging in panel D used the 485 nm pulsed laser.

- A. Wide-field fluorescence image recorded through 857/30 nm bandpass filter.
- B. Wide-field fluorescence image recorded through 900/32 nm bandpass filter.
- C. Topology of the immobilised LH2 square, the four RCLH1 lines and the RCLH1 aggregates.
- D. Fluorescence lifetime image recorded at 857 ± 3 nm by scanning the 485 nm laser over the sample.

4.4 Discussion

Exploiting the characteristic high energy transfer and charge separation efficiency of photosynthetic complexes is an important step in producing bio-inspired solar cells. Research on surface immobilisation and patterning has been performed mostly on a single type of photosynthetic complex such as LH2, RCLH1 or LHCII on non-conductive surfaces like glass (Escalante et al 2008a, Escalante et al 2008b, Vasilev et al 2014b), or conductive surfaces such as gold or ITO (Kondo et al 2007, Patole et al 2015, Reynolds et al 2007, Suemori et al 2006). Although energy transfer in nature always involves more than one complex, no comparable study has been reported on attaching dual photosynthetic complexes on one conductive surface with their distribution controlled on the nanometre scale.

In this work, patterns of photosynthetic complexes, such as LHCII, LH2 and RCLH1, have been created on semi-conductive silicon surfaces on a nanometer scale. The most efficient experimental conditions have been found for mPEO molecule oxidation and protein immobilisation. Two types of complexes have been immobilised on one silicon surface with controlled placement and retained functional properties. The complexes studied in the present work are still capable of light harvesting and energy transfer, and so constitute an artificial light-harvesting system.

4.4.1 Over long bias duration will not contribute to further oxidation of mPEO molecules on the silicon surface

Experimental conditions such as tip bias voltage and bias duration were studied for the most efficient mPEO oxidation. Results show that larger bias value and longer bias duration generally contribute to more efficient mPEO oxidation (Figure 4.4) (Menglong Yang 2009). However, this does not mean that unreasonably increasing the tip bias and prolonging the bias duration will result in the optimal mPEO oxidation. Results from Section 4.3.4 show that at 12 V of bias, a bias duration over 100 ms/pixel (at 25.6 pixel/ μm of scanning resolution) barely contribute to further oxidation of the mPEO; accordingly, no increase in fluorescence intensity was observed for subsequently immobilised RCLH1 complexes (Figure 4.5). At this point, it is possible that no further oxidation of mPEO is possible, considering the very high protein occupancy on the oxidised patterns; another factor could be the oxidation of the underlying silicon on the substrate surface, producing a swollen layer of non-

conductive SiO₂, which reduces the electric field strength as the oxide thickness increases (Avouris et al 1997). At 12 V of bias voltage and 100 ms/pixel of bias duration, the oxide thickness was around 1 nm, so taking into consideration the original 2.5 nm SiO₂ coating, the total thickness of the SiO₂ was about 3.5 nm. Previous research reported the thickness of SiO₂ generally reaches less than 5 nm, whilst in some extreme condition there is swelling to 8 nm (Fang 2004, Fontaine et al 1998, Yang et al 2005, Yang et al 2006). Therefore, the experimental conditions for mEPO oxidation in this work were set as 12 V of bias voltage and 100 ms/pixel of bias duration (at 25.6 pixel/ μ m of scanning resolution).

4.4.2 Photosynthetic complexes retained their structural and fluorescence properties after immobilisation on the silicon surface

The AFM line sections show that the heights of immobilised RCLH1 complexes are about 10.5 nm above the silicon surface (Figure 4.15C) and the LH2 complexes are about 7 nm (Figure 4.8C). Considering the underlying swollen SiO₂ of approximately 1 nm in height (Figure 4.7B and 4.13 B), the net heights for the immobilised RCLH1 and LH2 are about 9.5 nm and 6 nm respectively. Both values conform with the known sizes of the two complexes from previous AFM measurements (Bahatyrova et al 2004a). Likewise, those locations where the upper surface of the LHCII complexes is approximately 6.3 nm above the silicon surface (Figure 4.11C) indicates deposition of a single layer of LHCII. The swollen SiO₂ in this experiment was slightly low, at 0.4 nm in height (Figure 4.10B), thus the net height of the immobilised LH2 is about 5.9 nm, which is in good agreement with the 6 nm height of the LHCII trimers (Liu et al 2004, Standfuss et al 2005). The varying heights of the LHCII lines (Figure 4.11C), show that in places 2-4 layers of stacked LHCII complexes were formed during immobilisation (Johnson 2016, Wood et al 2018).

The fluorescence emission spectra of all the three immobilised complexes showed a consistent spectral shapes and emission maxima, comparable with fluorescence spectra of purified complexes solubilised in detergent (Figure 4.4C, 4.9B and 4.12B).

4.4.3 Fluorescence quenching caused by the silicon substrate

Patterning photosynthetic complexes on cheap, plentiful conductive surfaces can be a useful and scalable way to couple light-harvesting and energy transfer to charge

separation in the RC and produce a photocurrent. Photosynthetic complexes have been immobilised on conductive surfaces such as gold and ITO (Kondo et al 2007, Patole et al 2015, Reynolds et al 2007, Suemori et al 2006). Those substrates are either too expensive to be scalable or the surface is too rough for the AFM. Silicon is a cheap, pure and stable material, it is abundant in the Earth's crust and is widely used in modern technology. Thus silicon was chosen for the nanopatterning of the complexes using local oxidation lithography. However, despite the advantages of silicon, the fluorescence of immobilised complexes, particularly LH2, was unexpectedly quenched to a high degree. Similarly, LH2 fluorescence has been reported to be quenched when this complex is immobilized on a gold surface. Escalante et al reported a drop in emission intensity when LH2 complexes were adsorbed on a gold surface compared with glass (Escalante Marun 2009). Magis et al reported the fluorescence emission of isolated LH2 adsorbed on gold decreased within seconds to zero (Magis et al 2010). Fluorescence quenching of the LHCII complexes was also observed when they were attached to semiconductor quantum dots (QDs) (Werwie et al 2018).

4.4.4 Energy transfer between immobilised LH2 and RCLH1 on the silicon surface

This chapter reports the first immobilisation of photosynthetic complexes, and also transfer of excitation energy between complexes. By performing two successive local oxidations, lines of LH2 and RCLH1 have been patterned on a single silicon surface (Section 4.3.8). AFM images show that this procedure preserved the structure of both complexes, although at the crossover area the RCLH1 complexes created by the first local oxidation were removed during the second local oxidation and replaced by the second complex (Figure 4.17). Due to the limited contact area at the intersections, the crossed nanolines failed to show evidence of energy transfer between two types of complexes. An attempt was made to increase the intersection area by patterning a 5x5 μm square of LH2 with four intersecting RCLH1 nanolines; a drop in the LH2 fluorescence lifetime was observed at the projected locations of the RCLH1 lines (Section 4.3.9). Figure 4.21 C and D show that the fluorescence lifetime of LH2 was shortened from $\sim 900\text{-}1300$ ps (Chen et al 2005, Pflock et al 2011b, Sumino et al 2013) to 300-500 ps at some points within the intersecting regions, indicating that some harvested excitation energy has been delivered from the LH2 to the RCLH1. The AFM

images show that intersections between the RCLH1 lines and the LH2 square (Figure 4.19A) are not as obvious as those for the LH2 lines and RCLH1 lines (Figure 4.17B), possibly because relatively few RCLH1 complexes had replaced the initially patterned LH2 complexes following the second oxidation. This would account for the limited evidence for energy transfer from LH2 to RCLH1.

4.4.5 Additional work

This work demonstrates that photosynthetic complexes can be patterned on semi-conductive silicon surface on the nanometre scale with high protein occupancy. Due to the high refractive index of the silicon substrate (likely 3-fold higher than for glass), a high proportion of the emitted light from the protein complexes lies within the evanescent field and is refracted into the substrate, so less emission is available for detection. A possible solution could be performing the patterning on the conductive but transparent ITO surface, which would make the fluorescence study much easier.

In this work, we deliberately chose the silicon over the widely used glass because of its semi-conductivity. Such conductivity allowed the exploration of conductive patterning and could also enable the use of the Peak-force TUNA AFM to study photocurrent from the RC. With both LH2 and RCLH1 cross-patterned on one conductive surface, one can specifically excite the LH2 complexes, monitor energy transfer by fluorescence emission and then observe localised generation of a photocurrent by RC. The use of a carotenoid-less RCLH1 acceptor complex might help to provide clearer evidence for excitation energy transfer.

4.4.6 Conclusion

Efficient experimental conditions have been found for fabricating nanopatterns of photosynthetic complexes, such as LHCII, LH2 and RCLH1, on semi-conductive silicon surfaces. These complexes retained their capacity for light harvesting and energy transfer, and so constitute an artificial light-harvesting system. This approach opens up new possibilities for the creation of artificial photosynthetic systems on conductive surfaces.

Energy transfer in reconstituted LH2/ $\Delta crtB$ RCLH1 proteoliposomes

5.1 Summary

LH2 and $\Delta crtB$ RCLH1 complexes were purified from *Rba. sphaeroides* and reconstituted with lipids to form artificial proteoliposomes for energy transfer studies. Five different LH2/ $\Delta crtB$ RCLH1 ratios were used for the reconstitution process; sucrose density gradient centrifugation was used to purify the proteoliposomes, which migrated to the 20%-30% sucrose gradient interface. Dynamic Light Scattering was employed to measure the average size of the proteoliposomes, which was 197 nm before the sucrose gradient and 262 nm after.

The absorption spectrum of each proteoliposome sample was fitted using the component spectra for the LH2 and $\Delta crtB$ RCLH1 complexes. Based on the fitting result, the LH2/ $\Delta crtB$ RCLH1 ratio of each proteoliposome sample was calculated, which roughly matched the ratios used for protein incubation during the proteoliposome reconstitution. AFM topographs were recorded to investigate the distribution and clustering of both complexes in the proteoliposome membranes.

Fluorescence emission spectra demonstrated excitation energy transfer from LH2 to the $\Delta crtB$ RCLH1 complexes in the proteoliposomes, which was abolished when the proteoliposomes were solubilised by 2% β -DDM. The spectra shifted more toward the $\Delta crtB$ RCLH1 emission with decreasing LH2/ $\Delta crtB$ RCLH1 ratios. Inter-complex energy transfer was further verified by measuring the fluorescence lifetime decay of the LH2 complexes. The lifetime of the LH2 donor in the proteoliposome is much shorter than when the proteoliposome is solubilised, when it is uncoupled from the $\Delta crtB$ RCLH1 energy transfer acceptor.

Sodium ascorbate and Coenzyme Q₀ were applied to mimic the active RC condition in the proteoliposomes, but no obvious change were observed in the fluorescence emission spectra nor for the fluorescence lifetime decay for both LH2 and LH1 complexes.

5.2 Introduction

Photosynthesis is a process by which phototrophic organisms capture solar energy and convert it into the energy source for most living organisms on Earth. The primary photosynthetic process is initiated when sunlight is absorbed by light-harvesting (LH) complexes and excitation energy migrates towards the reaction centre (RC) where charge separation occurs (Figure 5.1). In photosynthetic purple bacteria, energy transfer and trapping take place in intracytoplasmic membranes. The antenna complexes involved are the peripheral light-harvesting 2 (LH2) complexes and the core light-harvesting 1 (LH1) complexes (Blankenship 2013).

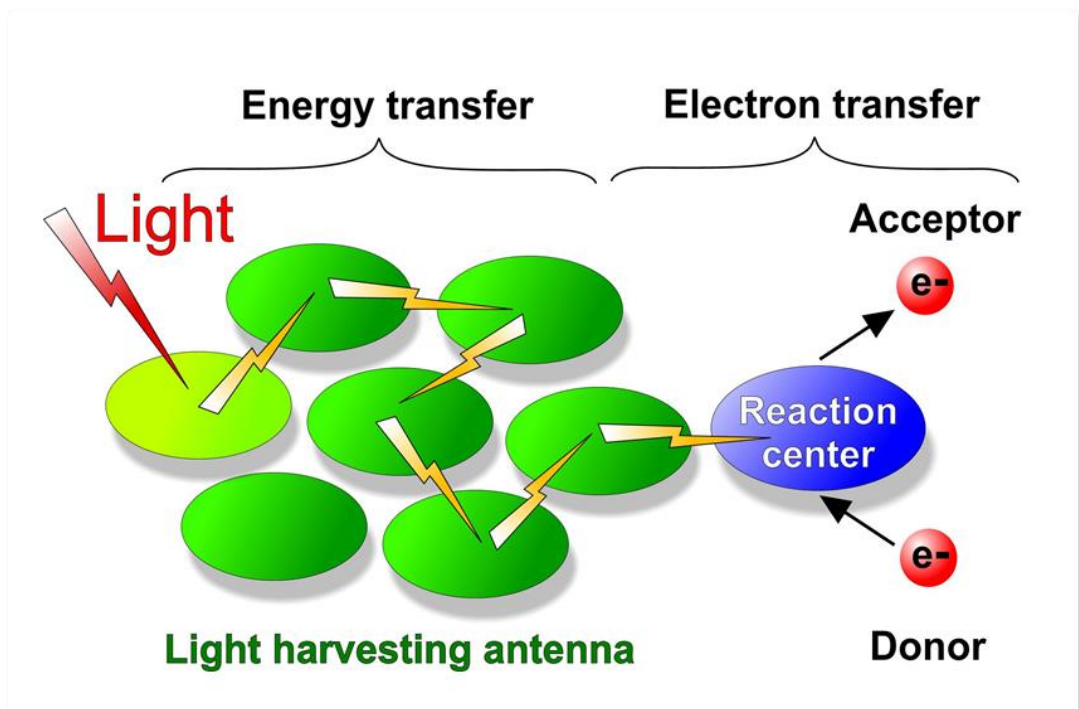


Figure 5.1 Model of an antenna-energy trapping system

3D structures of light-harvesting (LH) and reaction centre (RC) complexes (Ferreira et al 2004, Jones et al 2002, Jordan et al 2001, McDermott et al 1995) have been studied at resolutions down to 1.9 Å, which revealed the internal arrangements of chlorophyll-protein complexes that foster efficient solar energy harvesting and charge separation. However, detailed structural information of individual light-harvesting complexes has to be augmented by knowledge of arrangements of light-harvesting complexes in the membrane. Atomic force microscopy (AFM) allows us to observe the supramolecular organization of individual complexes when forming a

'photosynthetic unit' in the membrane, such as high resolution AFM images of native *Rba. sphaeroides* membranes (Bahatyrova et al 2004a, Kumar et al 2016, Sturgis et al 2009) and membranes from mutant strains (Adams et al 2011, Ng et al 2011, Olsen et al 2014, Olsen et al 2008). Still, there is an unsolved question of how supramolecular organization affects the primary photosynthetic processes of light harvesting and energy transfer. Addressing this question would aid understanding of the basic mechanisms of energy trapping and provide molecular-level strategies for the construction of artificial photosynthetic systems.

Atomic structures of complexes have been docked into AFM membrane maps to construct models of whole membrane assemblies (Şener et al 2010, Şener et al 2007b) that predict energy transfer and trapping behaviour and identify desirable design motifs for artificial photosynthetic systems (Cartron et al 2014, Sener et al 2016). One approach to construct such artificial systems is to reconstitute light-harvesting complexes into a lipid bilayer supported on a solid substrate (Sackmann 1996, Tanaka & Sackmann 2005). Sumino and co-workers reconstituted LH2 and LH1-RC into phospholipid (DOPC, DOPG and asolectin) bilayers and observed enhanced energy transfer from LH2 to LH1-RC in the artificially reconstituted system compared to that in a homogeneous micellar solution (Sumino et al 2011b). Other studies also showed that when LH2 complexes (from *Rhodospseudomonas acidophila*) and LH1-RC complexes (from *Blastochloris viridis*) were combined into a lipid bilayer system, the ratio of LH2 to LH1-RC complexes affects their local organisation (Uragami et al 2015). Moreover, another study found that *Rba. sphaeroides*, grown under different light levels, produced different ratios of LH2 to LH1-RC in the photosynthetic membrane, which influences the efficiency of light harvesting and the rates of energy migration toward the RC traps (Timpmann et al 2014).

In wild type *Rba. sphaeroides*, light harvesting generally starts from the BChls in the LH2 antenna complexes followed by excitation energy transfer via the LH1 antenna complexes to the RC. The energy migration route is: B800 (LH2) → B850 (LH2) → B875 (LH1) → RC (Dahlberg et al 2017). The carotenoid works mainly as an excitation energy quencher to protect the photosynthetic organism from photo-oxidative damage (Guiraud & Foote 1976). However, carotenoids can also act as an accessory antenna pigment to assist light harvesting and pass the excitation energy to the BChl

such as B800, B850 and B875. Thus the energy transfer route can be: carotenoid → B800 (LH2) → B850 (LH2) → B875 (LH1) → RC; or carotenoid → B875 (LH1) → RC.

To specifically excite the LH2 and monitor energy transfer from LH2 to the RCLH1, a carotenoidless *ΔcrtB* RCLH1 mutant was created and a 485 nm pulsed laser, targeted at carotenoids within the LH2 energy transfer donor, was used as light source. The carotenoid-containing LH2 and *ΔcrtB* RCLH1 complexes were reconstituted at five different LH2/ *ΔcrtB* RCLH1 ratios into proteoliposomes. Photosynthetic complexes were clearly observed in AFM topographs of the reconstituted proteoliposome membrane. Fluorescence emission spectra and fluorescence lifetime decay show that energy transfer efficiency could reach 73% in the proteoliposomes and LH2/ *ΔcrtB* RCLH1 ratios higher than 1 would not yield further improvements to inter-complex energy transfer.

5.3 Results

5.3.1 Reconstitution of LH2 and $\Delta crtB$ RCLH1 complexes into liposomes

LH2 and $\Delta crtB$ RCLH1 were purified from *Rba. sphaeroides* and were reconstituted in different ratios with lipids to form artificial proteoliposome systems for light harvesting and energy transfer. Liposomes were made by an extrusion method using DOPC lipid, by following the 'Liposome Preparation Protocol' described on the Avanti website (<https://avantilipids.com/tech-support/liposome-preparation/>). Specifically, DOPC in chloroform was dried to form DOPC lipid films, which were hydrated in buffer (20 mM MOPS, 20 mM NaCl, pH 7.8) and agitated by vortex to produce a suspension of large, multilamellar vesicles (LMV). Each lipid bilayer in the LMV is separated by a water layer. The stable and hydrated LMVs were then downsized by an extrusion process, where they were forced through a polycarbonate filter. The polycarbonate filter used in this chapter has a defined pore size of 200 nm, which yields liposomes with mean diameters of approximately 200 nm. Photosynthetic membrane proteins were then reconstituted into liposomes following the process shown in Figure 5.2. The liposomes were incubated with 0.03% w/v β -DDM for 30 min, then with photosynthetic membrane protein complexes at a fixed lipid / protein ratio of 500: 1 (mol/mol) for 1 hour. Each sample was left with Biobeads for 3 hours to remove the β -DDM and to form proteoliposomes. Five different proteoliposome samples were prepared using different LH2: $\Delta crtB$ RCLH1 ratios (Table 5.1):

#1 LH2-only

#2 $\Delta crtB$ RCLH1-only

#3 2LH2:1 $\Delta crtB$ RCLH1

#4 1LH2:1 $\Delta crtB$ RCLH1

#5 1LH2:2 $\Delta crtB$ RCLH1

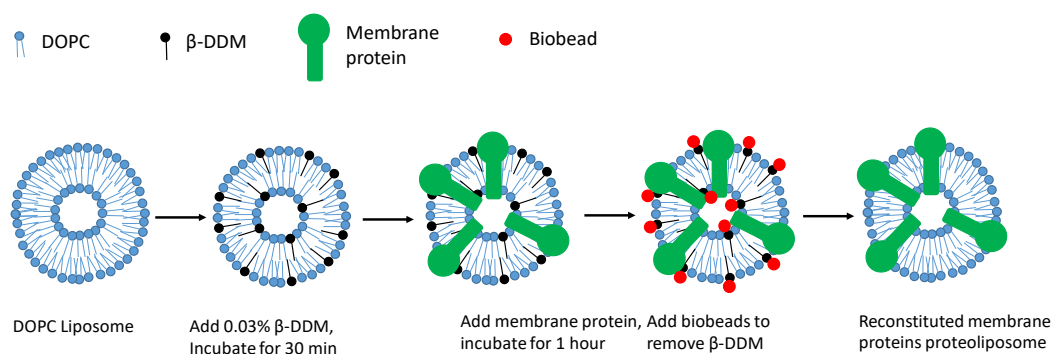


Figure 5.2. Schematic diagram of reconstituting membrane proteins into proteoliposomes

Table 5.1. Ratios (mol/mol) between lipid and protein complexes for proteoliposome reconstitutions

Sample	DOPC	LH2	$\Delta crtB$ RCLH1	LH2 / $\Delta crtB$ RCLH1 ratio
#1	1500	3	0	LH2 only
#2	1500	0	3	$\Delta crtB$ RCLH1 only
#3	1500	2	1	2 : 1
#4	1500	1.5	1.5	1 : 1
#5	1500	1	2	1 : 2

5.3.2 Sucrose gradient fractionation of reconstituted LH2/ $\Delta crtB$ RCLH1 proteoliposomes

Following the reconstitution process, the five proteoliposome samples were fractionated on discontinuous sucrose density gradients as described in Section 2.11.3. Purified liposomes containing pigment-proteins migrated to the 20% - 30% sucrose interface (Figure 5.3). Pigmented bands were harvested and the sucrose concentrations were measured for each sample band as listed in Table 5.2.

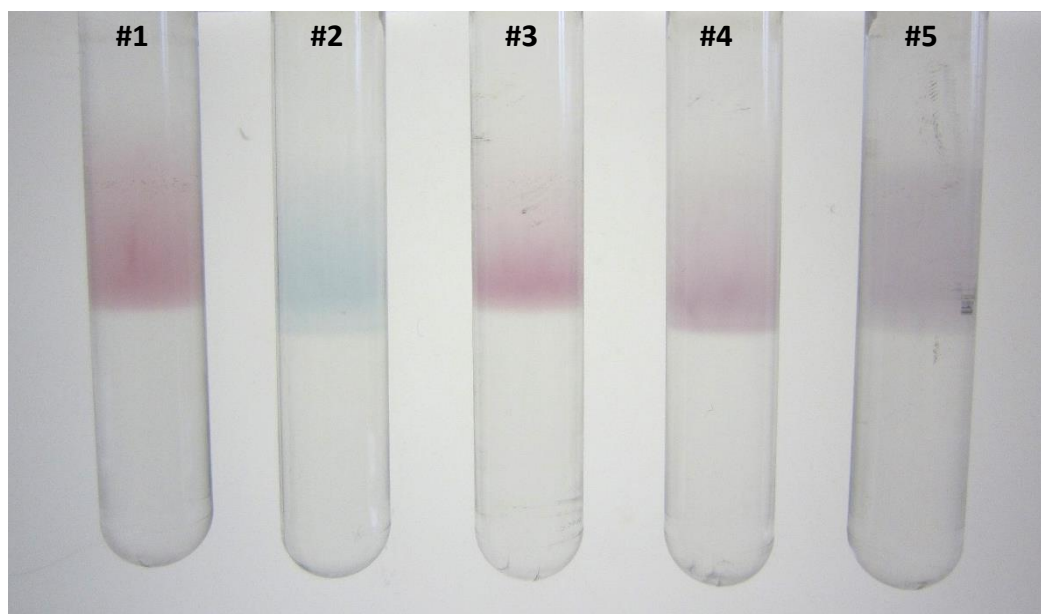


Figure 5.3. Sucrose gradient fractionation of LH2/ Δ crtB RCLH1 proteoliposomes

300 μ l of each sample was loaded on discontinuous sucrose gradients consisting of steps of 10%, 20%, 30%, 40 % and 50 % (w/w) sucrose in 20 mM HEPES, 20 mM NaCl, pH 7.8. The sucrose gradients centrifuged at 154,000 x g for 15 hours at 4 °C.

Table 5.2. Sucrose concentrations of purified LH2/ Δ crtB RCLH1 proteoliposomes samples

Sucrose concentration	#1	#2	#3	#4	#5
	25 %	28 %	27 %	27 %	27 %

5.3.3 Size of the reconstituted proteoliposomes

The sizes of the reconstituted proteoliposomes were monitored by Dynamic Light Scattering (DSL). Two DSL measurements were taken for sample #1, one for just after the reconstitution before the sucrose gradient and one for after the sucrose gradient. The size distribution curves from the two measurements are shown in Figure 5.4. Only one peak is seen for both distribution curves, which means the LH2 proteoliposomes were relatively uniform in size as a monodisperse sample both before and after the sucrose gradient.

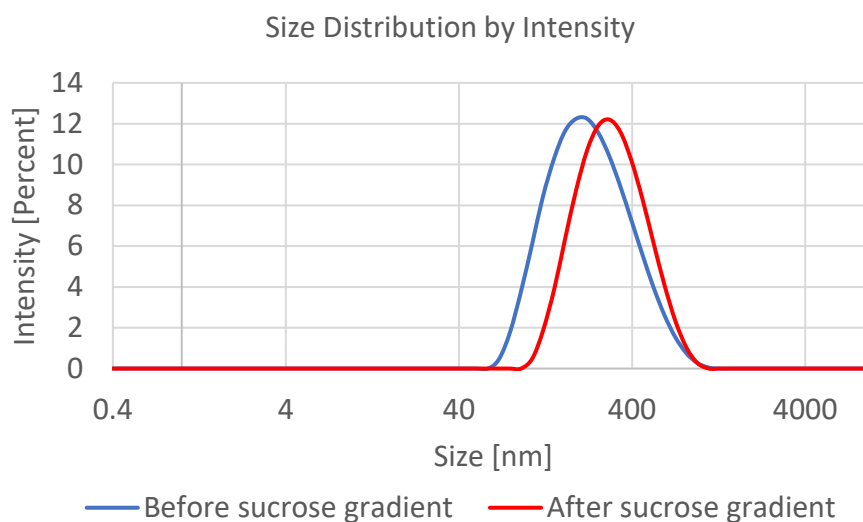


Figure 5.4. Size distribution of LH2 proteoliposomes (sample #1)

The blue curve shows the size distribution of LH2 proteoliposomes just following the reconstitution and before the sucrose gradient; the red curve shows the size distribution of LH2 proteoliposomes after the sucrose gradient.

Statistics of size distribution curves are listed in Table 5.3. The peak position corresponds to the size at the strongest scattering intensity; the average size stands for the intensity-based overall average size; the polydispersity index (PDI) indicates the width of the overall distribution; a monodisperse sample would have a low PDI would be a good way to describe, and a PDI greater than 0.7 indicates that the sample has a broad size distribution. The strongest scattering was from proteoliposomes with diameters of 257 nm and 328 nm before and after sucrose gradient separation, respectively. The average sizes of the proteoliposomes are 197 nm and 262 nm, close to the extrusion filter pore size of 200 nm. For both measurements, the PDI values are reasonably low, just below 0.2.

Table 5.3. Size distribution of LH2 proteoliposomes (sample #1)

Sucrose gradient	Peak size (nm)	Average size (nm)	PDI
Before	257	197	0.199
After	328	262	0.199

5.3.4 Absorption spectra of LH2/ $\Delta crtB$ RCLH1 proteoliposomes

In *Rba. sphaeroides* the pigments involved in light harvesting are bacteriochlorophylls (BChls) and carotenoids. Carotenoid exist in both WT-LH2 and WT-RCLH1 complexes, and absorb light in visible range between 450 nm and 600 nm. The LH2 complex has two absorption maxima at 800 nm and 850 nm in the near-infra-red range, arising from BChls known as B800 and B850 (Cogdell 1985); and the LH1 complex has a single BChl absorbance band at 875 nm, arising from BChls known as B875. These absorption wavelengths, allow analyses of levels of relevant protein complexes in the proteoliposome preparations.

Figure 5.5 shows the normalised absorption spectra of the membranes from semi-aerobically grown *Rba. sphaeroides*, the purified LH2 and the $\Delta crtB$ RCLH1 complexes from *Rba. sphaeroides*, and the five LH2/ $\Delta crtB$ RCLH1 reconstituted proteoliposome samples. The absorption spectra from the purified LH2 and $\Delta crtB$ RCLH1 complexes act as a reference for the *Rba. sphaeroides* membrane, where the LH2: RCLH1 ratio is about 2.13 : 1, and for the reconstituted liposomes. Sample #1, LH2-only proteoliposomes (blue) and #2, $\Delta crtB$ RCLH1-only proteoliposomes (magenta), have the same absorption spectra as the purified LH2 (blank) and the purified $\Delta crtB$ RCLH1 (grey) samples respectively, indicating the retention of protein absorption following reconstitution. When both LH2 and $\Delta crtB$ RCLH1 complexes are reconstituted, sample #3 proteoliposomes with 2LH2/1 $\Delta crtB$ RCLH1 (olive) shows similar absorption to the native membrane (purple) in the infrared range, and they share a similar ratio of LH2 to RCLH1 at around 2:1. As the ratio of LH2 to $\Delta crtB$ RCLH1 decreased in the proteoliposome preparations, in sample #4 with 1LH2/1 $\Delta crtB$ RCLH1 (red) and #5 1LH1/2 $\Delta crtB$ RCLH1 (violet) there is a relative intensity decrease at both 800 nm and 850 nm accompanied by an intensity increase at 875 nm.

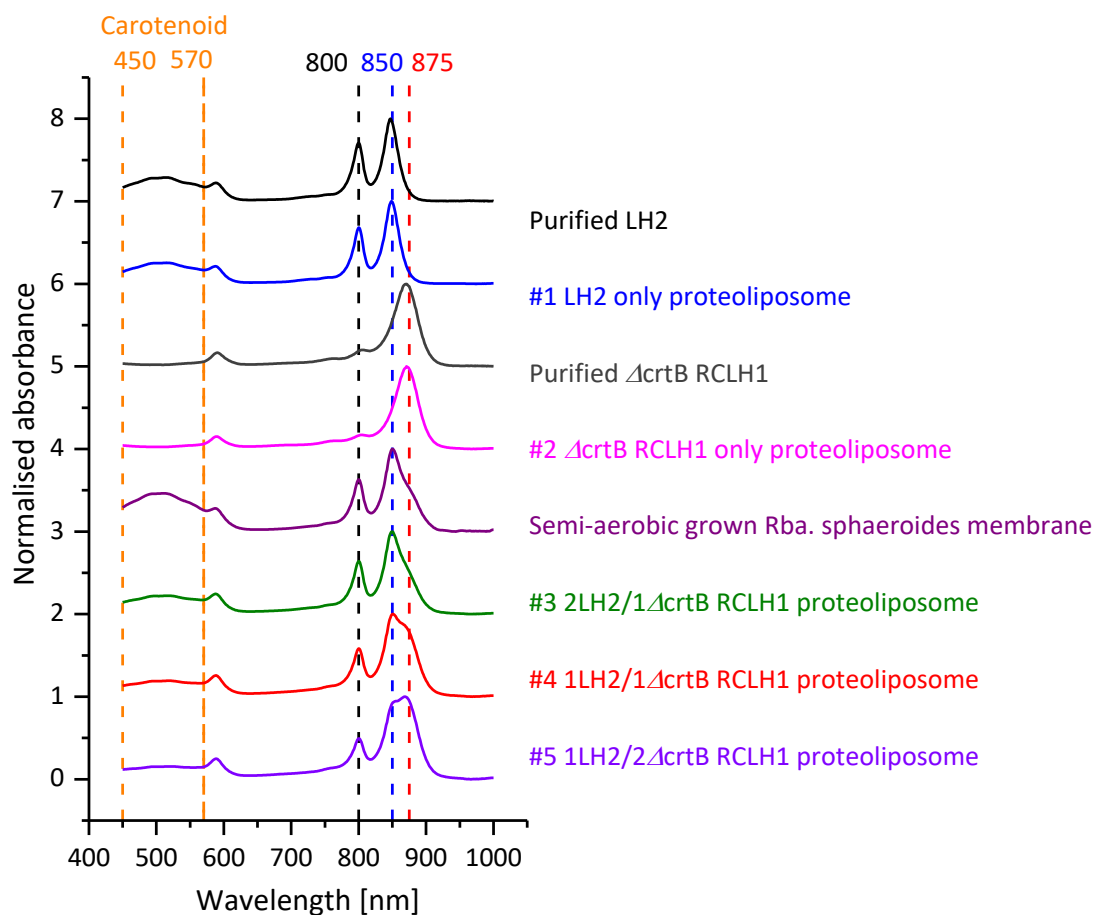


Figure 5.5. Normalised absorption spectra from native *Rba. sphaeroides* membranes, purified LH2 and $\Delta crtB$ RCLH1 complexes, and the five LH2/ $\Delta crtB$ RCLH1 reconstituted proteoliposome samples.

Spectra fitting was performed using purified LH2 and $\Delta crtB$ RCLH1 spectra as standard absorption curves, and the protein ratios in the proteoliposome samples were calculated from the absorption spectra fitting results (Table 5.4) using the method described in Section 2.12. Clearly, the calculated protein ratios from the fitting match very well with the actual protein ratios used during the protein incubation, which means both LH2 and $\Delta crtB$ RCLH1 have been efficiently reconstituted into proteoliposomes.

Table 5.4. LH2 / $\Delta crtB$ RCLH1 ratios in reconstituted proteoliposomes calculated from absorption spectrum fitting results, and compared with protein ratios used during incubation (Table 5.1)

Sample	LH2 / $\Delta crtB$ RCLH1 ratio	
	Spectrum fitting result	Protein ratio used during incubation
#1	LH2 only	LH2 only
#2	$\Delta crtB$ RCLH1 only	$\Delta crtB$ RCLH1 only
#3	1.92 : 1	2 : 1
#4	0.90 : 1	1 : 1
#5	1 : 2.06	1 : 2

According to the absorption spectra in Figure 5.5, LH2 can be excited either through the carotenoid pigments between 450 nm and 600 nm, or through BChls at 800 nm or 850 nm. Although the main absorption band of the RCLH1 complex is at 875 nm, some light can also be absorbed at 800 nm and 850 nm. Therefore, excitation at 800 nm and/or 850 nm is not a clean way to excite only the LH2 and monitor energy transfer to RCLH1. The carotenoidless version of RCLH1 (Section 2.2.1) (Grayson et al 2017) provides unambiguous excitation of the LH2 donor complex.

Figure 5.6 shows absorption spectra from the purified LH2 complexes and the purified $\Delta crtB$ RCLH1 complexes, normalised at the near-IR maxima. As can be seen, the $\Delta crtB$ RCLH1 barely shows any absorbance in the carotenoid absorption range (450 nm- 580 nm), and its absorption at 485 nm is only 8% of that of LH2. Therefore, when the LH2/ $\Delta crtB$ RCLH1 proteoliposomes are excited by 485 nm light, hardly any $\Delta crtB$ RCLH1 complexes are excited compared with LH2. Thus, energy transfer from the LH2 to the $\Delta crtB$ RCLH1 in the proteoliposomes can be studied, because the energy transfer would follow the route: carotenoid \rightarrow B800 (LH2) \rightarrow B850 (LH2) \rightarrow B875 (LH1) \rightarrow RC.

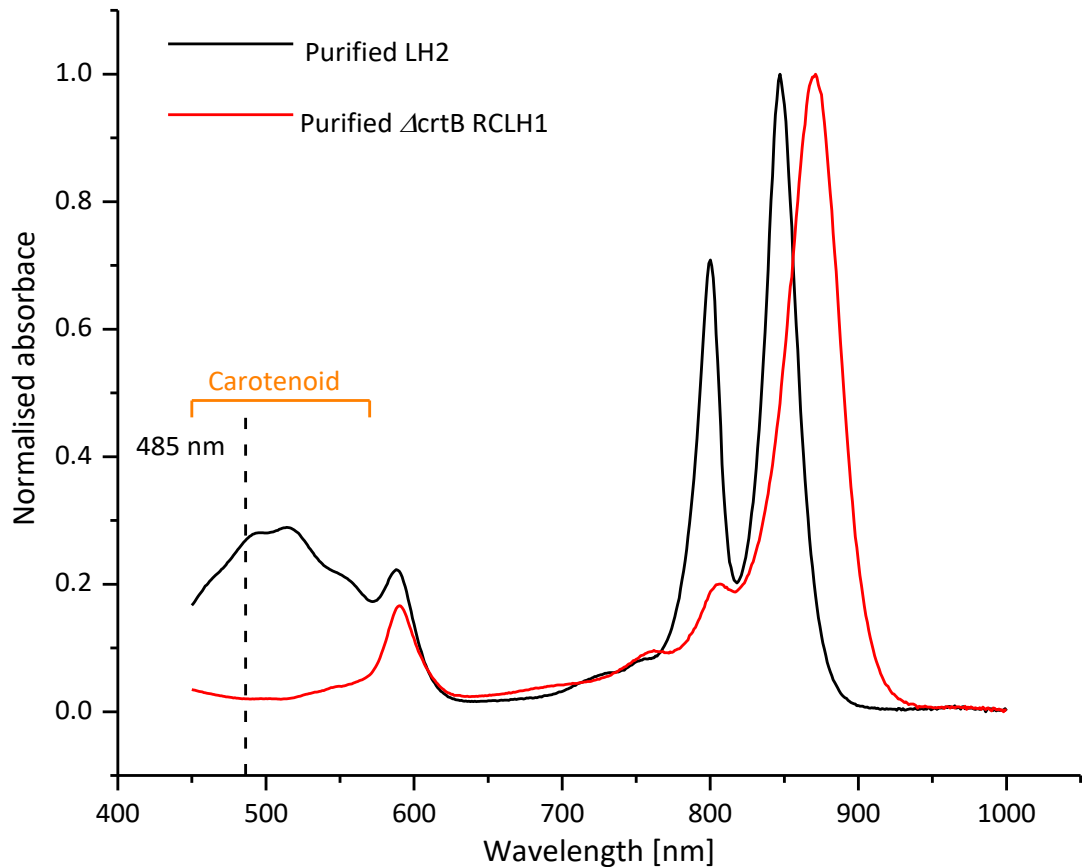


Figure 5.6. Normalised absorption spectra showing the absorption intensity of the carotenoid at 485 nm.

Absorption intensities at 485 nm are 0.27 for the purified LH2 complex and 0.021 for the $\Delta crtB$ RCLH1 complex.

5.3.4 AFM observation of the assembled LH2/ $\Delta crtB$ RCLH1 in the proteoliposomes

AFM was applied to visualise the arrangement of individual complexes within the proteoliposomes, which were adsorbed onto a mica substrate.

Figure 5.7A shows an AFM topograph of sample #1, the LH2 only proteoliposomes, which distinguishes three height levels: the mica (dark), the DOPC bilayer (brown) and the clusters of LH2 complexes (bright). Figure 5.7B shows the height profile along the red dashed line in Figure 5.7A, where the DOPC bilayer is about 4 nm in height and the LH2 complexes are about 6.5 nm in height.

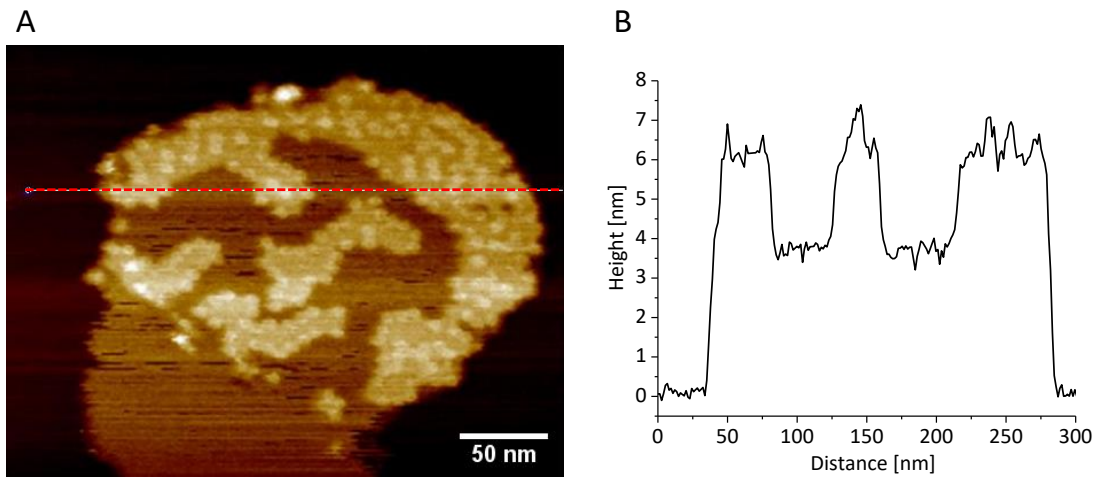


Figure 5.7. AFM image of sample #1 LH2 only proteoliposome and the height profile.

Figure 5.8A shows the AFM image taken at a higher magnification and it shows a cluster of LH2 in the DOPC bilayer with two height levels of LH2 apparent, as found in native membranes (Olsen et al 2008) and possibly including an ‘up-down’ orientation, as found in two-dimensional crystals (Bahatyrova et al 2004b). The ring diameters of the LH2 complexes are about 6-7 nm. Figure 5.8B shows the AFM image of an unbroken proteoliposome vesicle, where arrays of LH2 complexes can be spotted on the vesicle in a rectangular pattern, as seen for 2D crystals of LH2 (Bahatyrova et al 2004b).

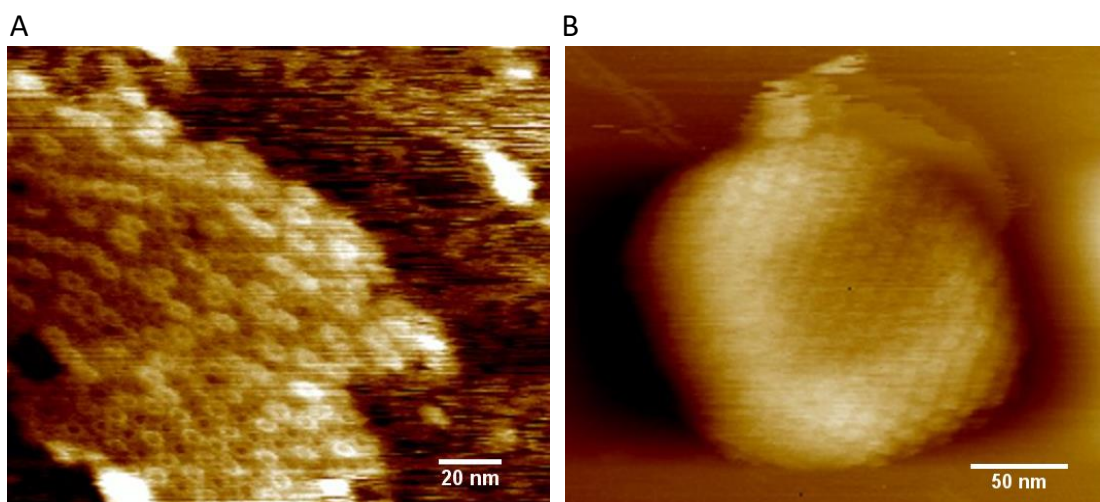


Figure 5.8. AFM image of sample #1 LH2 only proteoliposome.

Figure 5.9 shows the AFM image of sample #2 $\Delta crtB$ RCLH1 only proteoliposomes and the height profile along the red dashed line. The lipid bilayer is almost fully packed with $\Delta crtB$ RCLH1 and the height of RCLH1 complexes is around 9-11 nm.

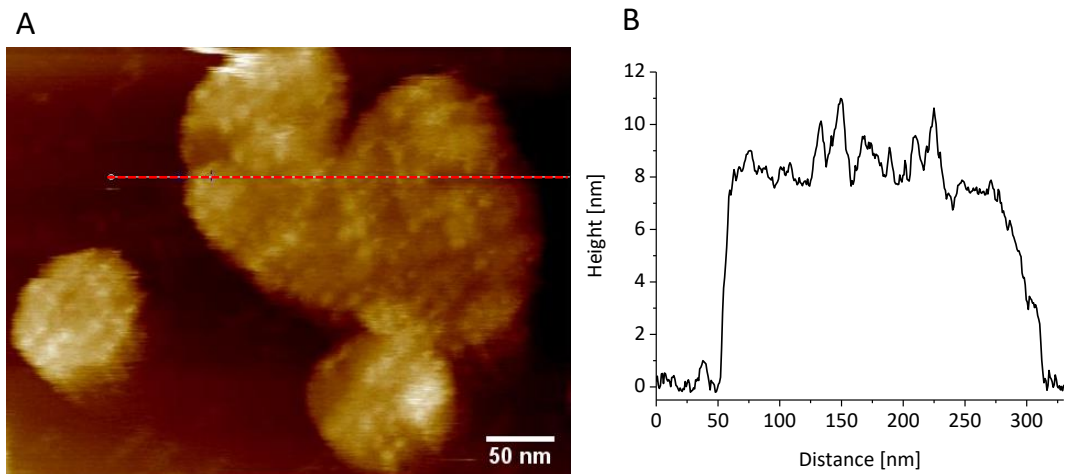


Figure 5.9. AFM image of sample #2 $\Delta crtB$ RCLH1 only proteoliposome and the height profile.

Figure 5.10 shows the AFM image of sample #3 2LH2/1 $\Delta crtB$ RCLH1 proteoliposomes. The LH2 complexes are indicated by green arrows and the $\Delta crtB$ RCLH1 complexes are indicated by red arrows.

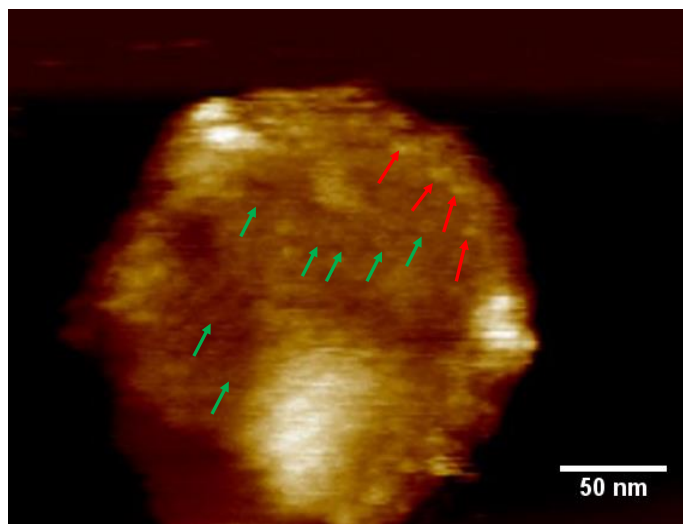


Figure 5.10. AFM image of sample #3 2LH2/1 $\Delta crtB$ RCLH1 proteoliposome.

Figure 5.11 shows AFM images of sample #4 1LH2/1 $\Delta crtB$ RCLH1 proteoliposomes. The boxed region in the left image is shown at higher resolution in the right image. The LH2 complexes are indicated by green arrows and the $\Delta crtB$ RCLH1 complexes are indicated by red arrows. The diameter of LH2 rings is about 8 nm and the diameter of RCLH1 rings is about 12 nm.

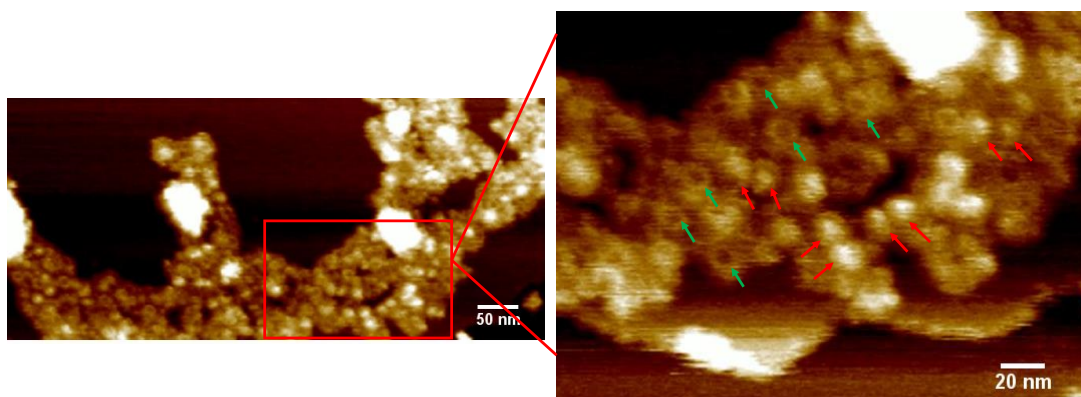


Figure 5.11. AFM image of sample #4 1LH2/1 $\Delta crtB$ RCLH1 proteoliposome.

Figure 5.12 shows AFM images of sample #5 1LH2/2 $\Delta crtB$ RCLH1 proteoliposomes. The LH2 complexes are indicated by green arrows and the $\Delta crtB$ RCLH1 complexes are indicated by red arrows.

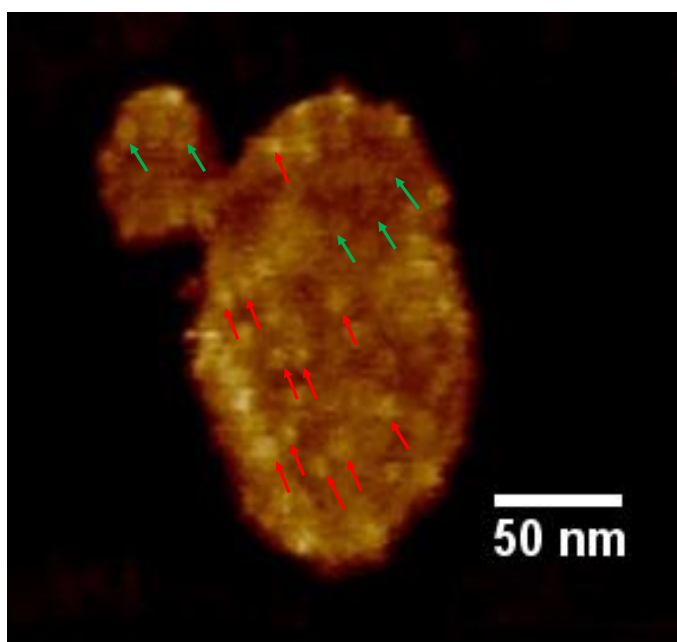


Figure 5.12. AFM image of sample #5 1LH2/2 $\Delta crtB$ RCLH1 proteoliposomes.

5.3.5 Fluorescence emission spectra of the LH2/ $\Delta crtB$ RCLH1 proteoliposomes

LH2 complexes within the LH2/ $\Delta crtB$ RCLH1 proteoliposome samples were specifically excited by a 485 nm pulsed laser. Fluorescence emission spectra were recorded to study transfer of excitation energy, with separately recorded spectra of purified LH2 and $\Delta crtB$ RCLH1 complexes in detergent protected buffer (20 mM HEPES, pH 7.4, 0.03% β -DDM) used as controls. Figure 5.13A shows the spectra of purified LH2 (blank) and $\Delta crtB$ RCLH1 (grey) complexes, together with those of sample #1 LH2 only proteoliposome (blue) and #2 $\Delta crtB$ RCLH1 only proteoliposome (magenta). Clearly, sample #1 and the purified LH2 complex show a same spectral shape, indicating the LH2 complexes have retained their absorption properties following the proteoliposome reconstitution. Sample #2 and the purified $\Delta crtB$ RCLH1 complexes barely show any LH1 emission at ~ 883 nm because genetic removal of carotenoids has eliminated their ability to absorb light at 485 nm.

Fluorescence emission spectra of all five reconstituted proteoliposome samples are shown in Figure 5.13B. In general, compared with LH2-minus sample #2 (magenta), samples #3 (olive), #4 (red) and #5 (violet) show fluorescence emission from both LH2 (around 854 nm) and $\Delta crtB$ RCLH1 (around 883 nm), indicating that the $\Delta crtB$ RCLH1 complexes in these three samples have obtained excitation energy from LH2. Apparently, efficient energy transfer requires a reasonable ratio between the LH2 and the $\Delta crtB$ RCLH1 complexes. Although the rising proportion of $\Delta crtB$ RCLH1 and the dropping proportion of LH2 from sample #3 to #5 (Table 5.1) lead to an increasingly obvious red shift of the fluorescence emission maximum, it does not indicate that sample #5 has the highest energy transfer efficiency. Instead, fluorescence lifetime decays of LH2 complexes were recorded in order to study the energy transfer efficiency (Section 5.3.6).

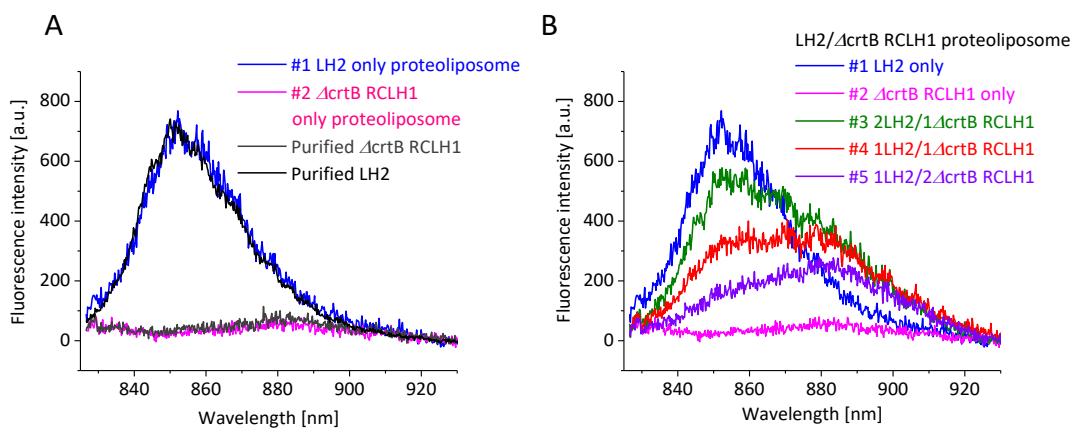


Figure 5.13. Fluorescence emission spectra of purified protein complexes and the five LH2/ $\Delta crtB$ RCLH1 proteoliposome samples.

Each spectrum is an average of five measurements.

- A. Fluorescence emission spectra of samples #1 and #2 compared with spectra of purified LH2 and $\Delta crtB$ RCLH1 complexes in detergent (0.03% β -DDM) buffer;
- B. Fluorescence emission spectra of sample #1 to #5.

To provide more evidence of $\Delta crtB$ RCLH1 complexes as recipients of excitation energy from LH2, each proteoliposome sample was incubated with 2% of β -DDM in the ice for 1 hour. At such a high concentration the β -DDM solubilises the proteoliposomes, resulting in separation of the closely packed LH2 and $\Delta crtB$ RCLH1 into individual complexes. Figure 5.14 shows the fluorescence emission spectra of the solubilised proteoliposome samples, with 485 nm excitation. For samples #1, #3, #4 and #5, only emission from the LH2 (peaking around 852 nm) was observed and the $\Delta crtB$ RCLH1 emission decreased sharply. Comparing with the LH2 emission (peaking around 854 nm) from proteoliposomes, the LH2 in solubilised solution shows a 2 nm blue shift on the spectral wavelength. Similarly, a blue shift in absorption from 850 nm to 848 nm was observed for proteoliposome and detergent solubilised LH2 complexes, respectively (Pflock et al 2008). The falling intensity from the related fluorescence emission reflects the decreasing proportion of LH2 complexes (Table 5.1). Specifically, sample #1 (blue) with 100% of protein as LH2 shows the highest fluorescence emission intensity, followed sample #3 (olive) with 67% protein as LH2, sample #4 (red) with 50% and sample #5 (violet) with 33%. Sample #2 (magenta) with 100% of $\Delta crtB$ RCLH1 still shows almost no emission when the proteoliposome is solubilised.

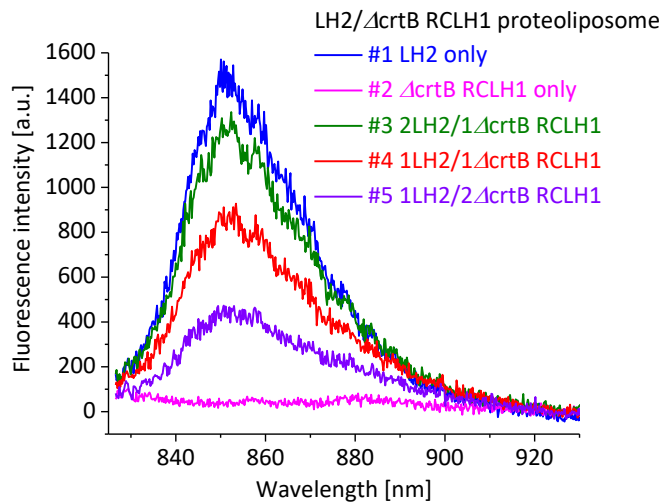


Figure 5.14. Fluorescence emission spectra of the five LH2/ $\Delta crtB$ RCLH1 proteoliposome samples, following addition of 2% β -DDM.

Each spectrum is an average of five measurements.

Figure 5.15 shows fluorescence emission spectra before (red spectra) and after (black) β -DDM addition to the proteoliposomes; the data analysis takes into account dilution by the β -DDM. The blue fitting curves peaking around 854 nm represent the LH2 emission; the magenta curves peaking around 883 nm represent the $\Delta crtB$ RCLH1 emission; the green curves are the cumulative fit results.

Figure 5.15A shows the fluorescence emission intensity of the LH2-only sample #1. Addition of β -DDM nearly doubles the amplitude of LH2 emission, showing the quenching effects of creating closely packed LH2 arrays, as shown by the AFM topography in Fig. 5.7. Therefore, even without RCLH1 traps, the LH2 complexes can still behave like an antenna system, harvesting light and transferring energy within its own network.

Figure 5.15B shows that the $\Delta crtB$ RCLH1 complexes barely emit any fluorescence either in proteoliposomes or in 2% β -DDM solution, due to their inability to absorb 485 nm wavelength excitation (Figure 5.6).

Figure 5.15C shows the fluorescence emission of sample #3, with a 2:1 LH2: $\Delta crtB$ RCLH1 ratio. When both complexes are packed in proteoliposomes (red), the fitting result shows an emission intensity of 254 a.u. from the LH2 (blue) and 428 a.u. from

the $\Delta crtB$ RCLH1 (pink). Solubilisation of the proteoliposomes and separation of the LH2 and $\Delta crtB$ RCLH1 complexes disrupts energy transfer so, with the same amount of LH2, the fluorescence emission intensity at 854 nm rises to 1300 a.u. (blank) whilst the relative emission from the $\Delta crtB$ RCLH1 at 880-890 nm decreases.

Similar fluorescence emission characteristics were seen for samples #4 (Figure 5.15D) and #5 (Figure 5.15E). In the case of sample #4, spectral fitting yields emission amplitudes from LH2 and $\Delta crtB$ RCLH1 of 114 a.u. (blue) and 348 a.u. (pink) respectively; when the proteoliposome is solubilised, the LH2 emission rises to 890 a.u. (blank). Similarly, for sample #5, the fitted amplitudes for emission from LH2 and $\Delta crtB$ RCLH1 were 105 a.u. (blue) and 235 a.u. (pink) respectively; when the proteoliposome is solubilised, the LH2 emission rises to 450 a.u. (blank). For both samples, fluorescence emission from $\Delta crtB$ RCLH1 complexes decreases when the proteoliposomes were solubilised.

5.3.6 Fluorescence lifetime decay of LH2 complexes in proteoliposomes

Apart from sample #2, which has no LH2, the fluorescence lifetimes of LH2 complexes were recorded at 857 ± 3 nm to study the efficiency of energy transfer in the reconstituted proteoliposomes. Figure 5.16 shows the fluorescence lifetimes of the LH2 complexes from samples #1, #3, #4 and #5. The red squares are the lifetimes of LH2 in the proteoliposome, and the black dots are the LH2 lifetime when the proteoliposomes are solubilised by 2% β -DDM. The specific values are listed in Table 5.2. When the complexes are in proteoliposomes, sample #1 containing LH2 as the only complex shows the longest lifetime of 0.725 ns. When $\Delta crtB$ RCLH1 complexes are present, the LH2 lifetime is shortened. In sample #3, where 2/3 of complexes are LH2, the fluorescence lifetime is 0.428 ns; the lifetime drops further to 0.355 ns for sample #4, which has an equal proportion of LH2 and $\Delta crtB$ RCLH1 complexes; sample #5, with 1/3 of complexes as LH2 and 2/3 as $\Delta crtB$ RCLH1, shows an LH2 lifetime of 0.368 ns which is slightly longer than that of sample #4. However, when the proteoliposomes were solubilised, the LH2 lifetimes of all samples rise to approximately 1.3 ns, indicating that solubilisation disrupts energy transfer networks and stops the transfer of excitation energy from the LH2 antenna to $\Delta crtB$ RCLH1 complexes.

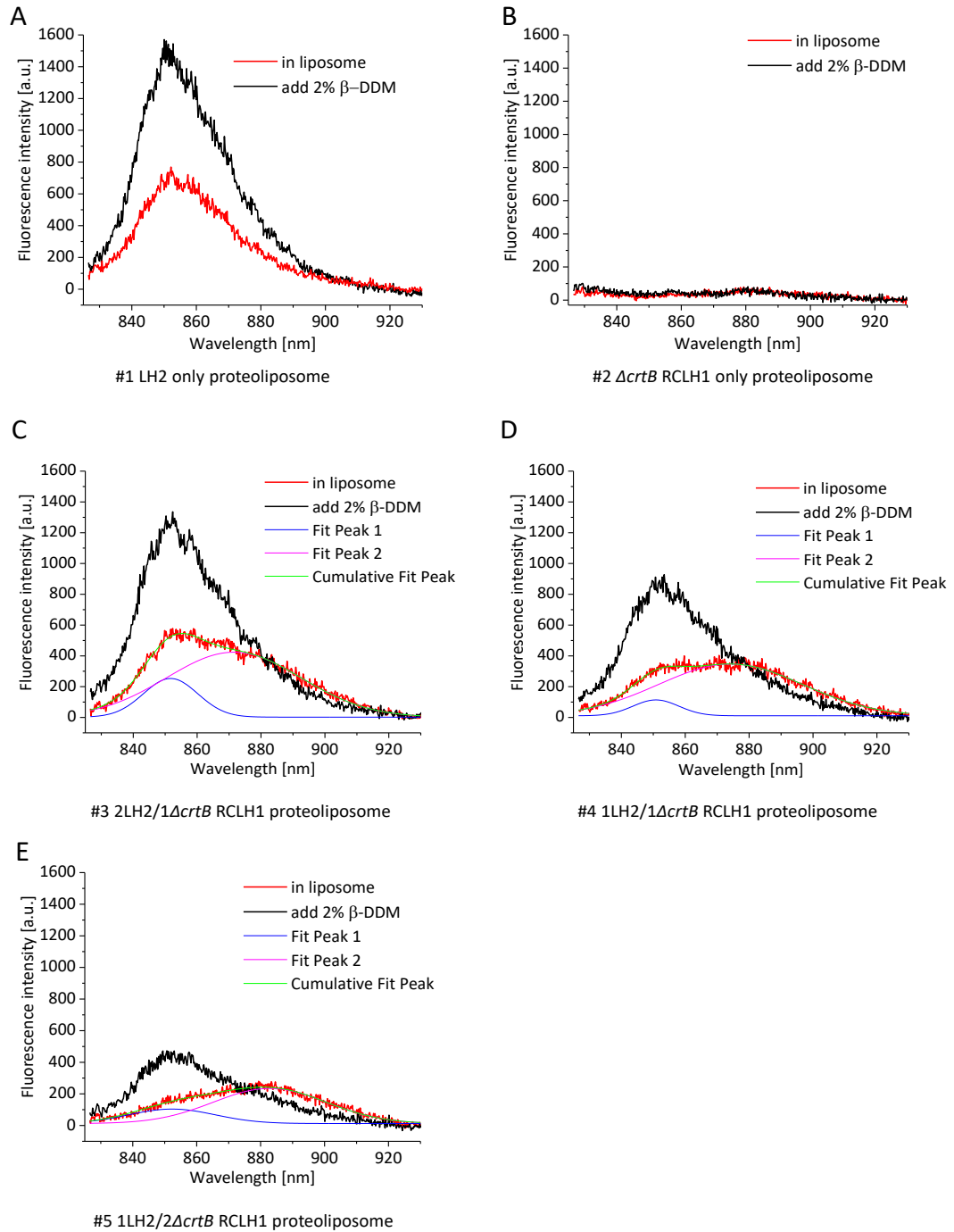


Figure 5.15. Fluorescence emission spectra from each LH2/ $\Delta crtB$ RCLH1 proteoliposome sample before and after solubilisation by 2% β -DDM

Referring to the LH2 lifetime, energy transfer efficiency from the LH2 to the LH2 or the LH1 can be calculated by equation:

$$E = 1 - \frac{\tau_{DA}}{\tau_D}$$

where τ_{DA} and τ_D are the donor lifetime with and without the presence of the acceptor, respectively. In reconstituted proteoliposomes, excited LH2 complexes act as energy donors, delivering excitation energy to acceptors such as the nearby LH2 or $\Delta crtB$ RCLH1 complexes. As listed in Table 5.5, sample #1 shows the lowest energy transfer efficiency of 44%, followed by sample #3 of 67% and sample #5 of 72%. Sample #4 shows the highest energy transfer efficiency of 73%. This indicates that energy transfer from LH2 to LH1 is more efficient than among LH2 (sample #3 compared with #1); and a reasonably high proportion of LH1 improves the overall energy transfer efficiency (sample #4 compared with #3), whilst over which no further improvement would be expected (sample #4 compared with #5).

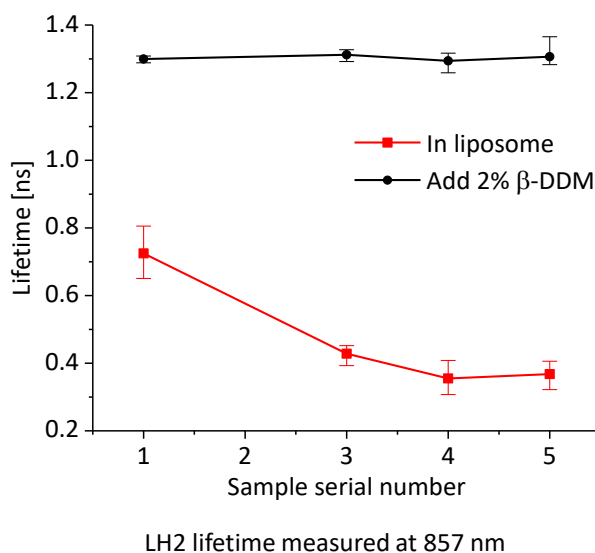


Figure 5.16 Fluorescence lifetimes of LH2 in proteoliposomes compared with the LH2 lifetime when the proteoliposomes are solubilised by 2% of β -DDM.

Each lifetime result is the average of more than 5 measurements and the error bar shows the maximum/ minimum deviation in each measurement data group.

Table 5.5. LH2 lifetime measured at 857 nm when proteins are in proteoliposomes and when the proteoliposomes are solubilised by 2% β -DDM.

857nm	#1	#2	#3	#4	#5
Proteins in the proteoliposome	0.725	n/a	0.428	0.355	0.368
Proteoliposome solubilised	1.300	n/a	1.312	1.294	1.306
Energy transfer efficiency	44%	n/a	67%	73%	72%

Representative LH2 lifetime decay curves in proteoliposomes (dots) and their fitting results (dashed lines) are shown in Figure 5.17. For the case of proteoliposomes solubilised by 2% β -DDM, the LH2 decay for sample #1 (ddm_#1) was chosen as the representative decay curve for the other solubilised proteoliposome samples. The grey solid line is the Instrument Response Function (IRF).

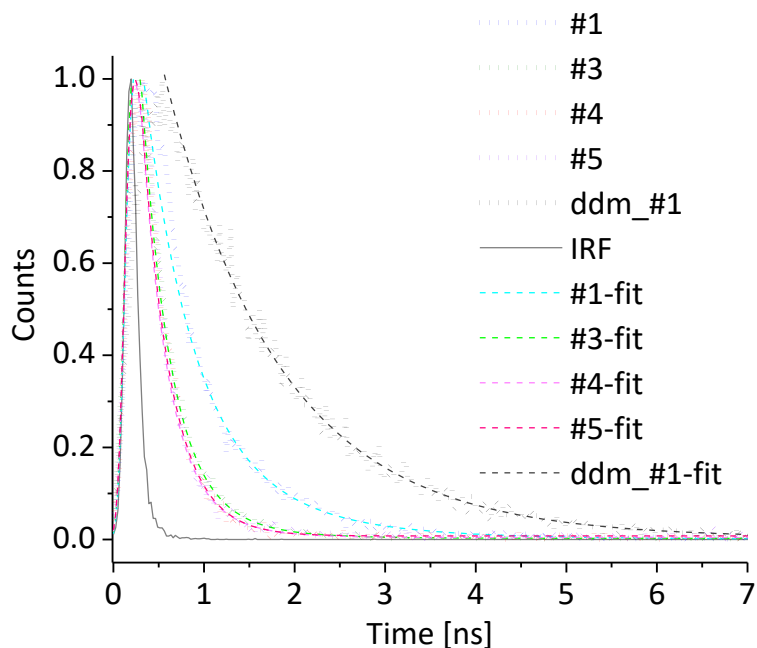


Figure 5.17. Fluorescence lifetime decay curves of the LH2 complexes

Each lifetime decay curve is a randomly chosen individual decay curve from a measurement data group.

In an attempt to maintain RCs in an open state ascorbate/ Q_0 (250 μ M sodium ascorbate, 1 mM Coenzyme Q_0) was added to proteoliposomes. However, this treatment had no effects on the amplitude or lifetime of LH2 fluorescence. Timpmann et al (Timpmann et al 2014) showed that open RC traps shorten the overall fluorescence lifetime in membranes from high- and low-light grown cells of *R. sphaeroides*, from approximately 200 ps (closed) to 70 ps (open RCs). The values of \sim 350 ps for LH2 lifetimes indicate that the decay kinetics were measured on LH2/RCLH1 proteoliposomes with RCs in the closed state. In the FLIM experimental setup used in this chapter, the 130 ps instrument response function would not allow measurement of the 70 ps lifetimes typical of membranes with open RCs.

5.4 Discussion

In wild type *Rba. sphaeroides*, light harvesting energy transfer and trapping require two types of membrane protein complexes, LH2 and RCLH1, the proportions of which vary according to the incident light levels (Adams & Hunter 2012, Cartron et al 2014, Timpmann et al 2014). One-way to simplify functional analyses for light harvesting and energy transfer, and to examine non-physiological LH2:LH1 ratios and photosystem dimensions of microns rather than nanometers, is to reconstitute membrane protein complexes into liposomes, which is the approach taken in this chapter.

A fixed ratio of *Rhodopseudomonas palustris* LH2 and RCLH1 complexes was reconstituted into phospholipids and evidence for excitation energy transfer from LH2 to RCLH1 was obtained by exciting the LH2 using 800 nm light and recording fluorescence emission spectra (Sumino et al 2011b). No time-resolved experiments were performed and there were no estimates of energy transfer efficiency between the two complexes. Sumino (Sumino et al 2013) subsequently performed several LH2-only reconstitutions and studied energy transfer efficiency between LH2 complexes using time-resolved spectroscopy. Finally, three LH2:RCLH1 ratios were reconstituted into liposomes, using LH2 from *Rhodopseudomonas acidophila* and RCLH1 from *Blastochloris viridis* (Uragami et al 2015). Excitation energy transfer was observed, on the basis of fluorescence emission spectroscopy.

In this chapter, several LH2:RCLH1 reconstitution ratios were examined, using a homologous LH2/RCLH1 system based on *Rba. sphaeroides*, in which the genetically engineered loss of carotenoids from RCLH1 complexes established the selectivity of excitation of LH2. Also, fluorescence emission and lifetime microscopy were used to establish the efficiency of excitation energy transfer.

5.4.1 LH2 and $\Delta crtB$ RCLH1 complexes have been reconstituted into proteoliposomes at the expected ratio with their functional properties retained

Proteoliposomes of ~200 nm diameter were formed by extrusion method. Absorption spectra showed that photosynthetic complexes had been successfully reconstituted into the proteoliposomes, and the calculated ratios match the ratio of protein complexes used during reconstitutions.

AFM images of the proteoliposomes show that clusters of LH2 have formed, as well as protein-free (empty) regions (Figure 5.7) (Pflock et al 2011a). Similarly, clusters of protein complexes are observed for the $\Delta crtB$ RCLH1 proteoliposome sample (Figure 5.9). For proteoliposome samples with both LH2 and $\Delta crtB$ RCLH1, AFM images show evidence of both complexes in the proteoliposome (Figures 5.10, 5.11 and 5.12), with evidence for some segregation into LH2-only and RCLH1-only zones, as well as some intermixing. Segregation is a likely consequence of shape and curvature mismatches between the two types of complex, as shown in Monte Carlo simulations of LH2/RCLH1 interactions (Frese et al 2008).

5.4.2 LH2 and $\Delta crtB$ RCLH1 complexes retain their light-harvesting and energy transfer properties when reconstituted in proteoliposomes

The fluorescence emission spectra of LH2 and the $\Delta crtB$ RCLH1 complexes reconstituted separately into proteoliposomes show consistent spectral shapes, comparable with fluorescence spectra of purified complexes solubilised in detergent (Figure 5.13A), indicating retention of function following reconstitution. Comparing with purified LH2 complexes in detergent, a 2nm red shift of the emission maxima was observed when LH2 complexes were reconstituted in proteoliposomes (Pflock et al 2008). Mixed LH2/RCLH1 proteoliposomes create the conditions for excitation energy transfer, which can be clearly assigned because of the selective excitation of carotenoid-containing LH2 complexes by the 485 nm light source used. Solubilisation of the samples by 2% β -DDM reversed the reconstitution process, and provided a useful negative control.

Pflock (Pflock et al 2008) measured the fluorescence decay kinetics of detergent-solubilized LH2 complexes from *R. sphaeroides*; the monoexponential fluorescence lifetime of 0.93 ns can be compared with the value of 1.3 ns in this chapter (Table 5.5). These authors reconstituted *R. sphaeroides* LH2 complexes into lipid vesicles, and observed bi-exponential fluorescence decay curves with time constants of $\tau_1 = 600$ -720 ps and $\tau_2 = 70$ ps, depending on the lipid:protein ratio. The authors concluded that the $\tau_2 = 70$ ps decay component arises from clustering of the LH2 complexes following reconstitution, which promotes efficient energy transfer between complexes and increases the chances of annihilation of excited states. The work

reported in this chapter on LH2 in proteoliposomes shows a monoexponential fluorescence decay of 725 ps.

5.4.3 Decreasing LH2/ $\Delta crtB$ RCLH1 ratios progressively increase energy transfer efficiency in the reconstituted proteoliposomes

LH2 lifetimes for proteoliposome samples #1 (LH2-only), #3, #4 and #5 were 0.73 ns, 0.43 ns, 0.36 ns and 0.37 ns respectively. Calculations in Table 5.5 show that LH2/ $\Delta crtB$ RCLH1 ratios of 2:1, 1:1 and 1:2 produce energy transfer efficiencies of 67%, 73% and 72% respectively, so for these reconstitution experiments at least a 1:1 molar ratio of LH2 and LH1 complexes is optimal. The AFM topography of sample #4 (Fig. 5.11) shows multiple contacts between intermixed LH2 and RCLH1 complexes, consistent with an efficiently reconstituted photosystem, so LH2 energy donors are likely to sit adjacent to $\Delta crtB$ RCLH1 acceptors. When higher levels of LH2 are present, as in the 2:1 LH2:RCLH1 ratio of sample #3, AFM shows evidence for more extensive LH2-only domains that might increase the chances of excitation annihilation, as proposed by Pflock (Pflock et al 2008). When the LH2/ $\Delta crtB$ RCLH1 ratio is lowered 1:2, there is no increase in energy transfer efficiency; with abundant $\Delta crtB$ RCLH1 complexes around as energy acceptors at a 1:1 ratio, all available LH2 donors are apparently already connected for energy transfer so increasing the proportion of RCLH1 acceptors produces no benefits.

Recently, two-dimensional electronic spectroscopy was used to follow all energy transfer processes in living cells of *R. sphaeroides*, including the wild-type, LH2-only and LH1-only strains (Dahlberg et al 2017). The fluorescence lifetime for LH2-only membranes was found to be 250–300 ps, a smaller value than found for LH2-only proteoliposomes. For the WT, which in this case had a ratio of approximately 1.8 LH2:LH1, 83% of excitations were trapped by the RCs present. In these whole cell samples, the RCs were maintained in an open (reduced) state, available for efficient energy trapping. Timpmann (Timpmann et al 2014) examined a range of *R. sphaeroides* membranes, including LH2-only, RCLH1-only and native membranes with contrasting LH2:RCLH1 ratios. Fluorescence lifetimes varied from ~490 ps for LH2-only membranes, to ~250 ps for wild-type LH2/RCLH1 membranes. The overall lifetime increased as the proportion of LH2 increased, consistent with the data on proteoliposome samples #3 (2LH2:1RCLH1) and #4 (1LH2:1RCLH1). Timpmann et al

did not examine LH2 lifetimes specifically: some of their lifetime experiments used 800 nm excitation and fluorescence was integrated between 820 and 940 nm, which therefore merges LH2 and LH1 signals. In other experiments, 590 nm excitation was used, which was absorbed by both LH2 and LH1 complexes. In the present work, the use of carotenoid-containing LH2 and carotenoid-less RCLH1 allowed the 485 nm excitation to selectively excite only the LH2 complexes.

5.4.5 Conclusion

This work demonstrates that photosynthetic complexes LH2 and $\Delta crtB$ RCLH1 can be reconstituted into proteoliposomes and that they perform light harvesting and energy transfer functions. The energy transfer efficiency between LH2 and $\Delta crtB$ RCLH1 is related to the ratio between the two types of complexes in the proteoliposomes. This approach opens up new possibilities for the creation of mix-and-match photosynthetic systems, for instance studying the possibility of energy transfer between photosynthetic complexes from different types of photosynthetic organisms, or between natural and artificial maquette proteins.

Excitation energy transfer from LHCII to RCLH1 in fabricated microarrays of bacterial/plant photosynthetic complexes

6.1 Summary

LHCII complexes purified from spinach and $\Delta crtB$ RCLH1 purified from *Rba. sphaeroides* were cross-patterned on glass surfaces, to form a hybrid plant/bacterial photosynthetic system. Fluorescence spectral and lifetime measurements show that both complexes retained their optical properties following immobilisation. In cross-patterned areas, where LHCII and $\Delta crtB$ RCLH1 are in very close proximity, a decrease in the LHCII fluorescence emission intensity is observed, accompanied by a lowered LHCII fluorescence lifetime to 0.7-1.0 ns, relative to 1.4-1.9 ns in LHCII-only areas. These measurements indicate a coupling of LHCII energy transfer donors to $\Delta crtB$ RCLH1 acceptors, and formation of a biohybrid photosynthetic unit.

6.2 Introduction

Photosynthesis in living organisms starts when solar energy is absorbed by light-harvesting (LH) pigment-protein complexes, such as the LH2 in the phototrophic bacterium *Rhodobacter (Rba.) sphaeroides*, or the light-harvesting complex II (LHCII) in plants. These LH complexes are the major membrane proteins in their respective organisms, and form extensive networks that capture light energy and transfer it to the reaction center complexes (RC), such as the RC in the phototrophic bacterium *Rhodobacter (Rba.) sphaeroides*, and the photosystem I (PSI) and photosystem II (PSII) complexes in plants (Blankenship 2013, Johnson 2016, Saer & Blankenship 2017). In the RC, this energy is trapped as a charge separation (Bixon et al 1991, Dekker & Van Grondelle 2000). There are many examples of immobilisation of RCs on various materials, examining their ability to generate electric current in response to light (Das et al 2004, den Hollander et al 2011, Friebe et al 2016, Frolov et al 2005, Gerster et al 2012, Kamran et al 2015, Liu et al 2018, Tan et al 2012). There are also examples of

immobilization of LH complexes on different surfaces, where they retain their functional properties (Lauterbach et al 2010, Liu et al 2008, Nagata et al 2012).

The development of lithographic techniques, such as nanoimprinting (Escalante et al 2008a, Escalante et al 2008b) and light-based photolithography (Reynolds et al 2007) have allowed patterning of a single type of photosynthetic complex of either LH or RC on surfaces, while controlling their distribution and organisation, which creates the possibility of studying their light-harvesting and energy transfer properties. However, the assembly of extensive two-dimensional architectures that not only harvest energy but also transfer it to a RC trap requires the ability to direct the relative positions of two or more types of photosynthetic complex on the same surface. Vasilev et al (Vasilev et al 2014b) reported nanopatterning of 'two-colour' arrays of photosynthetic complexes (LHCII) and YFP proteins, but there was no evidence of energy transfer between the YFP and the LHCII components. Chapter 3 in this thesis discussed methods to co-pattern two photosynthetic complexes, the LH2 antenna of *Rhodobacter sphaeroides*, and its native energy acceptor, the RCLH1 complex (Cartron et al 2014, Qian et al 2013) on the same surface and observed energy transfer between these complexes. The short distances between the two types of complexes ensure the rapid delocalization of excited states and their transfer within and between complexes, as also found in the native membrane (Freer et al 1996, Noy et al 2006, Şener et al 2009). This inspires the fabrication of patterns of 'mix and match' combinations of molecules on the same surface that could not be created through genetic means, such as arrays comprising mixed bacterial/plant, or plant/artificial maquette complexes.

Here, a simple, robust lithographic procedure is used to construct intersecting lines of the LHCII antenna from plants and bacterial RCLH1 complexes, effectively creating a new micron-scale 'photosynthetic unit'. A two-stage micro-contact printing method was used to fabricate a 2-D grid of cross-patterned LHCII and $\Delta crtB$ RCLH1 proteins, which was interrogated by fluorescence microscopy. The presence of carotenoids in donor LHCII, but not in the acceptor $\Delta crtB$ RCLH1 complexes, ensured the directionality of energy migration. Spectral and lifetime imaging were used to show transfer of light energy absorbed by the LHCII antenna to $\Delta crtB$ RCLH1 complexes; thus, these arrays contain functionally coupled components for absorbing and

transferring excitation energy, thereby performing the first two steps of photosynthesis.

6.3 Results

6.3.1 Directed formation of crossed-patterned LHCII and $\Delta crtB$ RCLH1 complexes on glass

Based on the same micro-contact printing approach described in Section 3.3.1 (Alom Ruiz & Chen 2007, Bernard et al 2000, Xia & Whitesides 1998), artificial light-harvesting networks of crossed-patterned LHCII and $\Delta crtB$ RCLH1 complexes were created on a glass surface functionalized with poly-L-lysine (Figure 6.1). The optically transparent glass facilitates characterisation of immobilized protein complexes by fluorescence microscopy. As a first step, the LHCII complexes (in green, Figure 6.1G and H) were printed onto the substrate using a soft PDMS stamp (Figure 6.1B and C) inked with the protein solution (Figure 6.1D), followed by the printing of $\Delta crtB$ RCLH1 complexes (in red, Figure 6.1I), performed in a similar way but at a 90° angle to the LHCII lines. Sample was sealed in an argon protective atmosphere to minimise photo-oxidative damage to the $\Delta crtB$ RCLH1 complex.

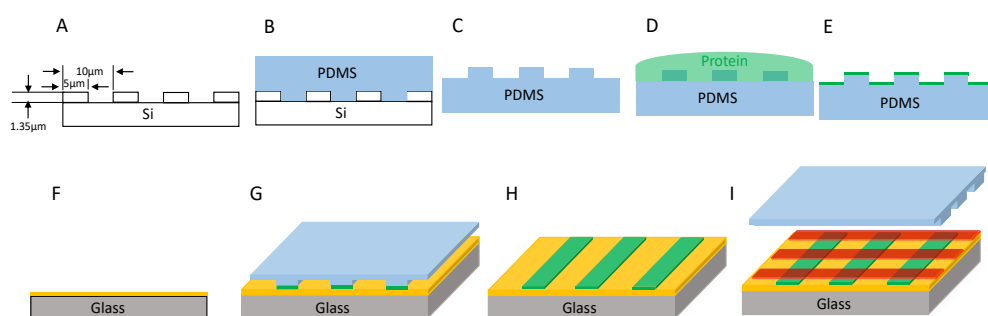


Figure 6.1. Schematic diagram of the micro-contact printing method used to fabricate cross-patterned LHCII and $\Delta crtB$ RCLH1 protein arrays.

- A. Si master with rectangular arrays of 5 μm width, 10 μm pitch and 1.35 μm step height.
- B. Casting a PDMS replica of the master.
- C. PDMS replica.
- D. Inking the stamp with LHCII (green).
- E. PDMS stamped covered with LHCII ink.
- F. PLL coated glass activated by DMS (yellow).
- G. Printing LHCII on glass.
- H. LHCII arrays on glass.
- I. Printing $\Delta crtB$ RCLH1 complexes (red) on glass orthogonally to LHCII arrays.

6.3.2 Absorption spectra of purified LH2CII and $\Delta crtB$ RCLH1 complexes in detergent

The absorption and fluorescence emission spectra of LHCII complexes, and the absorption spectrum of the $\Delta crtB$ RCLH1 complexes, are shown in Figure 6.2. The LHCII contains carotenoid whilst the $\Delta crtB$ RCLH1 does not, therefore the absorption of LHCII in the 450 - 570 nm carotenoid region is much greater than for $\Delta crtB$ RCLH1; the absorbance values of LHCII and $\Delta crtB$ RCLH1 are 1.12 and 0.02, respectively at 485 nm, and at 470 nm these values are 1.37 and 0.02, respectively. The LHCII fluorescence emission spectrum (green; excitation at 485 nm) and the $\Delta crtB$ RCLH1 absorption spectrum (red) overlap between 650 – 750 nm, which presents the possibility of transfer of excitation energy from LHCII to the $\Delta crtB$ RCLH1 by the Förster resonance transfer mechanism, as long as the two types of complex are within a 10 nm distance. Accordingly, we can monitor the energy transfer between the LHCII and the $\Delta crtB$ RCLH1 complexes in the crossed-patterned fabrication by exciting the fabricated pattern at either 470 nm or 485 nm and recording emission from RCLH1 complexes at 890 nm.

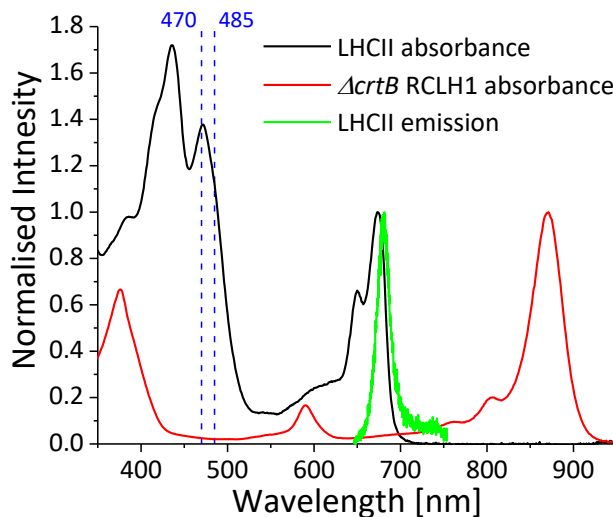


Figure 6.2. Spectra of purified LHCII and $\Delta crtB$ RCLH1 complexes.

The 470 nm and 485 nm dashed lines show the normalised protein absorbance at the 470 nm and 485 nm excitation wavelength.

6.3.3 LH complexes retain their optical properties following immobilisation on glass

In bacterial photosynthetic systems the LH2 antenna complexes harvest light energy and transfer it to the RCLH1 core complex, where the excitation energy is stabilized as

a photo-chemical charge separation. In this work, the plant photosynthetic complex LHCII was used to replace the LH2 bacterial complex, and to test if the mix-match artificial system can fulfill the tasks of light harvesting and energy transfer. For such processes to happen, it is important to ensure that the protein complexes retain their optical properties following their immobilization on the substrate. Thus, the artificial microarrays of cross-printed LHCII and $\Delta crtB$ RCLH1 complexes were characterized by fluorescence lifetime and spectral imaging in a home-built FLIM set-up. Figure 6.3A shows the false colour wide-field fluorescence emission image of the artificial microarrays, acquired in epi-fluorescence mode and illuminated by a 470 nm LED source. Emission from the green horizontal arrays was recorded through a 679/41 nm bandpass filter, and corresponds to LHCII fluorescence; emission from the red vertical arrays was recorded through a 900/32 nm bandpass filter, and corresponds to RCLH1 emission. Clearly, the LHCII can efficiently absorb 470 nm light and shows a bright fluorescence emission whilst the $\Delta crtB$ RCLH1 is barely visible. The lowered fluorescence amplitude of LHCII at the intersections with the RCLH1 lines, suggests some quenching of LHCII emission by RCLH1.

The fluorescence emission spectrum of the LHCII from the crossed-patterns was recorded, which is similar in shape and maximum to the spectrum of purified LHCII complexes in detergent solution (Figure 6.3B). Due to the poor absorption at 485 nm, the fluorescence emission from the $\Delta crtB$ RCLH1 is very weak and noisy, but still shows a similar trend when comparing with the spectrum of purified RCLH1 (containing carotenoids) complexes in detergent solution (Figure 6.3C).

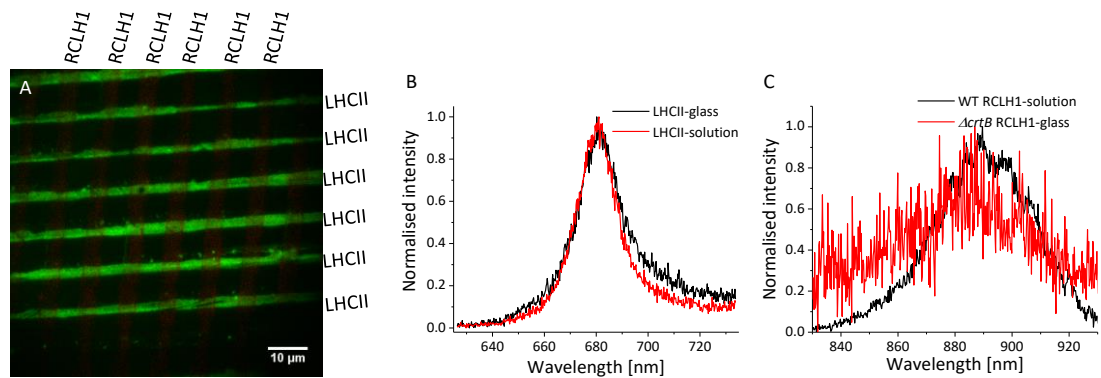


Figure 6.3. False colour fluorescence image of crossed-patterns of LHCII and $\Delta crtB$ RCLH1, and fluorescence emission spectra of LHCII and $\Delta crtB$ RCLH1 complexes

- False colour fluorescence image (wide field excitation at 470 nm), showing the LHCII (green) and $\Delta crtB$ RCLH1 (red) lines in a grid-like pattern with a period of 10 μm and line width of 5 μm ;
- Fluorescence emission spectra from LHCII patterned on glass and purified LHCII in detergent buffer, excited by a 485 nm laser.
- Fluorescence emission spectra from the $\Delta crtB$ RCLH1 patterned on glass and the purified RCLH1 (contains carotenoids) in detergent buffer, excited by a 485 nm laser.

6.3.4 Energy transfer from LHCII to $\Delta crtB$ RCLH1 in a biohybrid plant/bacterial artificial photosystem

Figure 6.4 shows fluorescence data acquired from the cross-printed LHCII and $\Delta crtB$ RCLH1 complexes on glass; the sample was sealed in an argon protective atmosphere to minimise photo-oxidative damage to the $\Delta crtB$ RCLH1 complex. Under scanning confocal mode, and using 485 nm pulsed laser excitation, we were able to record the pixel-by-pixel spectral intensity map of fluorescence emission of the sample. The fluorescence intensity maps acquired at 680 nm and at 890 nm (Figure 6.4 A and B, respectively), confirm the immobilisation of the LHCII complexes along the near-horizontal lines and immobilisation of the $\Delta crtB$ RCLH1 complexes along the near-vertical lines. A striking observation in the cross-over area (marked with number 2 in Figure 6.4 A), where LHCII and $\Delta crtB$ RCLH1 complexes are in very close proximity, is the $\sim 40\%$ decrease in the LHCII emission intensity, compared with the LHCII only area (marked with number 1 in Figure 6.4 A). Correspondingly, $\Delta crtB$ RCLH1 complexes in the cross-over area (marked with number 3 in Figure 6.4 B) show a slightly increase in the fluorescence emission (peaking around 884 nm), comparing with the $\Delta crtB$ RCLH1 only area (marked with number 4 in Figure 6.4 B). These changes in the fluorescence

emission intensity indicates excitation energy transfer (EET) from the LHCII to the $\Delta crtB$ RCLH1 in the cross-over area.

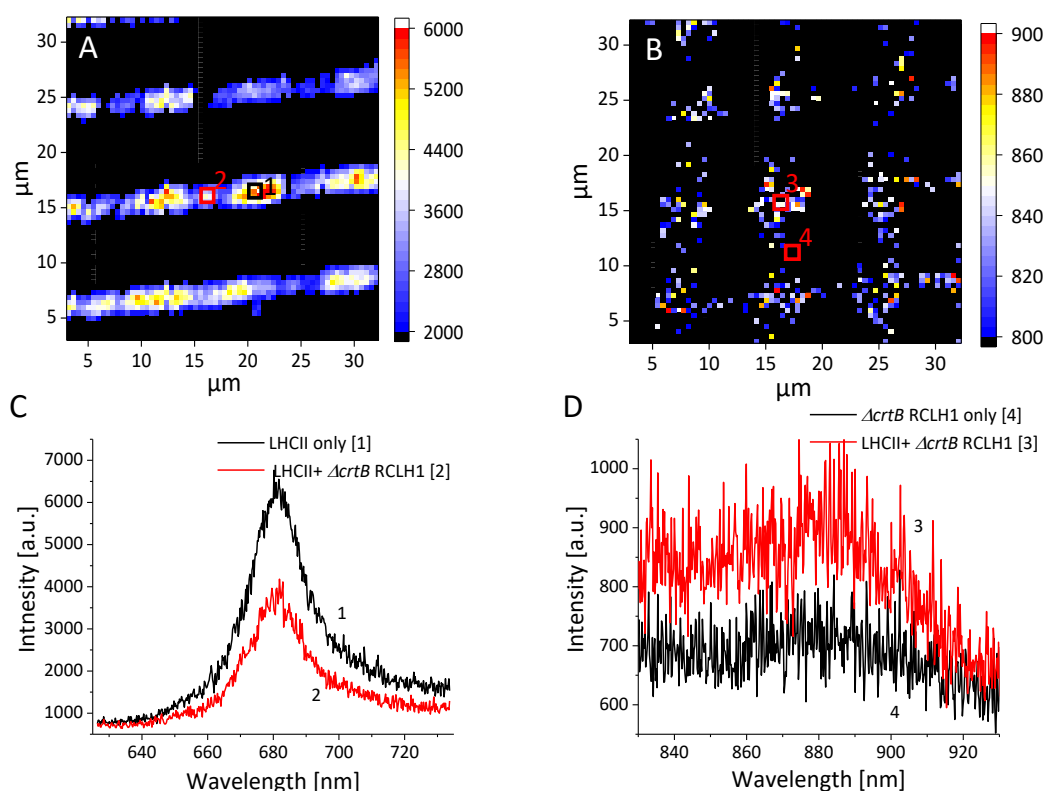


Figure 6.4. Fluorescence intensity images and fluorescence spectra from cross-patterned LHCII and $\Delta crtB$ RCLH1 complexes on a functionalised glass substrate.

- Spectral intensity map showing the emission intensity at 680 nm (LHCII emission). The excitation is by a 485 nm pulsed laser (1 MHz repetition rate, 2×10^{14} photons pulse⁻¹ cm⁻²), scan size 26 μ m.
- Spectral intensity map showing the emission intensity at 890 nm ($\Delta crtB$ RCLH1 emission), with excitation as in A.
- Individual emission spectra recorded in the pixels of the images in panels A marked with 1 (LHCII only) and 2 ($\Delta crtB$ RCLH1 + LHCII crossed-over), respectively.
- Individual emission spectra recorded in the pixels of the images in panels B marked with 3 ($\Delta crtB$ RCLH1 + LHCII crossed-over) and 4 ($\Delta crtB$ RCLH1 only), respectively.

In order to study the EET in more detail, we recorded a fluorescence lifetime map of the LHCII complexes from the cross-patterned fabrication, under scanning confocal mode, and using 485 nm pulsed laser excitation. Lifetime decay data from each scanning pixel was fitted by bi-exponential decay function (Section 2.7.5). The amplitude-averaged lifetime image of the cross-patterned sample, recorded at 680 nm (LHCII peak emission wavelength), is shown in Figure 6.5A with two individual fluorescence decay curves shown in Figure 6.5B. From Figure 6.5A, the LHCII-only

areas (orange) generally have a longer lifetime of between 1.4-1.9 ns, when comparing with the LHCII- $\Delta crtB$ RCLH1 cross-over area (blue) of between 0.7-1.0 ns. In Figure 6.5B, the green decay curve was extracted from the pixel marked 1 (Figure 6.5A) corresponding to the LHCII-only area, and the bi-exponential decay function fitting result shows an amplitude-averaged lifetime $\tau_{av} = 1.53$ ns, with components $A_1 = 0.18$, $\tau_1 = 2.51$ ns and $A_2 = 0.82$, $\tau_2 = 0.55$ ns; the red curve represents the fluorescence decay in the cross-over area (marked 2, Figure 6.5A) and the bi-exponential decay function fitting result shows an amplitude-averaged lifetime $\tau_{av} = 0.77$ ns, with components $A_1 = 0.06$, $\tau_1 = 1.9$ ns and $A_2 = 0.94$, $\tau_2 = 0.41$ ns. This reduction of the LHCII fluorescence lifetime indicates EET from the LHCII complex to $\Delta crtB$ RCLH1 complex in the cross-over areas where the two types of protein complex must be in very close proximity.

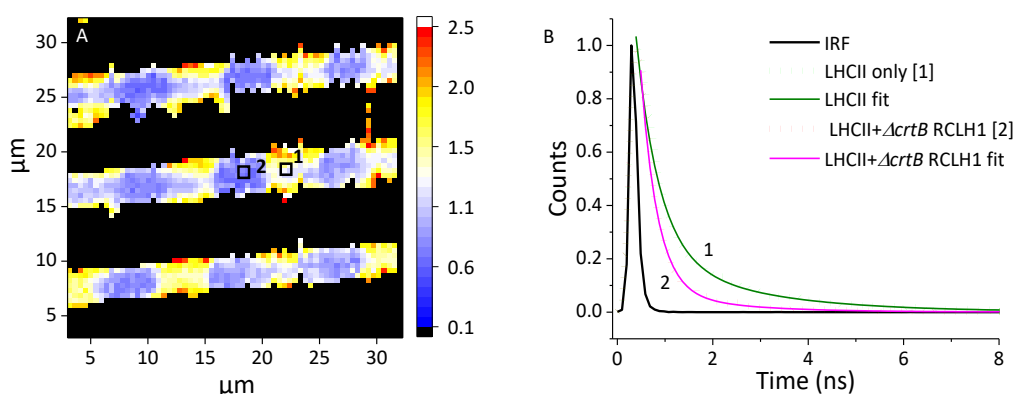


Figure 6.5. Fluorescence lifetime data from cross-patterned LHCII and $\Delta crtB$ RCLH1 complexes on a functionalised glass substrate.

- A. Amplitude weighted average lifetime image obtained at 485 nm excitation (1 MHz repetition rate, 2×10^{14} photons pulse⁻¹ cm⁻²), and 680 nm emission (LHCII complex emission peak), clearly showing a decrease in the lifetime in the cross-over areas, where the two complexes are in close proximity, scan size 26 μm ;
- B. Individual decay curves recorded in the pixels of the lifetime image in panel A marked with 1 (green, LHCII only) and 2 (red, LHCII+ $\Delta crtB$ RCLH1 crossed-over), respectively.

6.4 Discussion

Previous work has shown energy transfer in mixed assemblies of LH2 and RCLH1 complexes (Hunter et al 1979, Sumino et al 2011a, Uragami et al 2015), but there was no control over the 2-D arrangement location of the photosynthetic complexes. Various lithography techniques can overcome the challenges of constructing nanoarrays of single types of photosynthetic complex, starting with the light-harvesting LH2 complex of *Rba. sphaeroides* (Escalante et al 2008a, Escalante et al 2008b, Reynolds et al 2007), and later the RCLH1 complex (Patole et al 2015) and the LHCII complex of plants (Vasilev et al 2014b). In each case, those immobilised complexes retained their structural and optical functions. Specifically, the immobilised LHCII retained the capability to switch between fluorescent and quenched states (Vasilev et al 2014b); long-range energy transfer was observed in the 80 nm-wide nanolines of LH2 complexes (Escalante et al 2010), the micron length scale of which greatly exceeds its natural energy propagation length of 50-100 nm.

To explore the geometries of energy transfer and trapping, it would be meaningful to pattern two or more types of photosynthetic complex on the same surface, with one type of antenna and the other type of trap in very close proximity. However, there are no published successes in co-patterning two or more types of photosynthetic complex on the same surface for spectral and time-resolved microscopies to assess the functional state of immobilised assemblies. Recent developments in surface chemistries do allow multiprotein patterning (El Zubir et al 2017), and an alternating linear LHCII/EGFP pattern has been reported (Vasilev et al 2014b). Here, we have used a soft lithographic method to cross-print LHCII and $\Delta crtB$ RCLH1. Energy transfer was observed between the LHCII and the $\Delta crtB$ RCLH1 complexes in the cross-patterned areas, by monitoring the fluorescence emission intensity from the LHCII and the $\Delta crtB$ RCLH1 along with the fluorescence lifetime decrease from the energy donor LHCII complexes. This is the first time that plant antenna complexes have been functionally coupled with bacterial RC complexes, a combination that would not be possible to achieve through genetic means in a bacterial or plant host. This assembly can be regarded as a new type of biohybrid 'photosynthetic unit', where the complexes adopt a predetermined, geometric configuration and perform basic energy transfer functions. The mixed bacterial/plant arrays from natural organisms have

showed their energy transfer capability as a working system, and future work can be extended to create mix-and-match combinations such as construction of plant/artificial maquette complex arrays. Further explorations can also include patterning mix-and-match complexes on conductive surfaces to test the electrical properties of RC traps in the biohybrid and bioinspired photosynthetic arrays. This would help us to measure charge separation and energy trapping in the assembled artificial system demonstrated in the present work.

7.1 Concluding remarks

In this research diverse fabrication techniques were used to direct the assembly of purified photosynthetic complexes from *Rhodobacter sphaeroides* and spinach on different surfaces. Artificial light-harvesting systems were created by fabricating multiple types of photosynthetic complexes on micro- and nanometre scales, and energy transfer behaviours were explored. Another artificial light-harvesting system used for energy transfer study was the proteoliposome reconstituted using photosynthetic complexes from *Rhodobacter sphaeroides*. AFM imaging in combination with FLIM imaging were applied to characterize the photosynthetic complexes localizations and energy transfer in these artificial systems.

Chapter 3 details a pilot study to explore the light harvesting and energy transfer in a surface-assembled artificial light-harvesting system. LH2 and RCLH1 complexes purified from *Rhodobacter sphaeroides* were cross-printed on a PLL coated glass surface to form micron-scale 'photosynthetic units'. The carotenoid-less RCLH1 complexes were used to ensure the directionality of energy migration, and we demonstrated light collection by one complex, LH2, and its subsequent transfer to the RCLH1 complex. A 60-day test of the 'photosynthetic units' sealed in argon and stored at 4°C in the dark showed that, the artificial 'photosynthetic units' are extremely stable. To my knowledge, this is the first time that a systematic study has been done on the long-term stability of immobilised photosynthetic complexes.

As photosynthetic membrane vesicles in *Rhodobacter sphaeroides* are of 50-100 nm in diameters, it would be desirable to bring the micrometre 'photosynthetic units' down to a nanometre scale, in order to mimic nature more accurately. The photolithography method reported by Xia *et al* (2016) and the nanolithography method reported by Vasilev *et al* (2014b) show approaches to create nano-scale arrays of photosynthetic complexes patterns on glass surfaces. Furthermore, to test the nanoelectrical properties of RC traps, photosynthetic need to be deposited on conducting substrates, as reported by Kamran *et al* (2015) and Tan *et al* (2012). These ideas lead to the study in chapter 4.

In chapter 4 shows how photosynthetic complexes can be patterned on semiconductive silicon surface using a local oxidation nanolithography. Multiple types of complexes were patterned on the nanometre scale with high protein occupancy. Fluorescence emission spectra and AFM images proved these complexes retained their structural and fluorescence properties on silicon. However, as reported by Escalante *et al* (2009) and Magis *et al* (2010), the fluorescence emission intensity dropped dramatically when LH2 complexes were adsorbed on a gold surface compared with glass. The same drop was observed for both LH2 and RCLH1 when immobilised on silicon, which hindered us from acquiring strong evidence for excitation energy transfer between the two complexes. Furthermore, the low conductivity of the silicon substrate apparently led to failure to obtain photocurrent from the immobilised RCs. Nevertheless, this study opens up the possibilities of patterning artificial light-harvesting systems on conductive surfaces and using Peak-force TINA AFM to explore the locally light induced photocurrent from the RC. Future work can focus on patterning artificial light-harvesting complexes on a transparent and conductive ITO substrate, which hopefully will allow the fluorescence emission and the photocurrent acquisition.

In chapter 5, LH2 and $\Delta crtB$ RCLH1 purified from *Rhodobacter sphaeroides* were reconstituted into proteoliposomes at five different LH2/ $\Delta crtB$ RCLH1 ratios. The use of carotenoid-containing LH2 and carotenoid-less RCLH allowed the selective excitation of LH2 at 485 nm and unequivocal observation of energy transfer from LH2 to $\Delta crtB$ RCLH1. Fluorescence emission spectra and fluorescence lifetime decay show that energy transfer efficiency between LH2 and $\Delta crtB$ RCLH1 is related to the ratio between the two types of complexes in the proteoliposomes, and the highest energy transfer efficiency of 73% happens at the LH2/ $\Delta crtB$ RCLH1 ratio of 1:1. This approach shows the possibility of creating 'mix and match' photosynthetic systems for studying energy transfer between non-native photosynthetic complex pairs.

Chapter 3 discussed methods to co-pattern the LH2 and its native energy acceptor, the RCLH1 complex, on the same surface and observed energy transfer between these complexes. This inspires the study in chapter 6, where 'mix and match' combinations of bacterial/plant complexes were fabricated on glass surface which cannot be created through genetic means. The fluorescence spectra and fluorescence

lifetime show energy transfer between LHCII and RCLH1. This is the first time that plant antenna LHCII complexes have been functionally coupled with bacterial RC complexes, in terms of light-harvesting and energy transfer. Future work can explore the combination of natural antenna complexes with artificial RC maquettes patterned either on glass surfaces for energy transfer study or on conductive surfaces for testing the electrical properties of the RC maquettes in the biohybrid photosynthetic arrays.

Appendix: Growth medium for *Rhodobacter sphaeroides* M22+ medium (10× stock)

The following were weighed and mixed in 2 L deionised water: 122.4 g KH_2PO_4 , 120.0 g K_2HPO_4 , 100.0 g sodium lactate, 20.0 g $(\text{NH}_4)_2\text{SO}_4$, 20.0 g NaCl, 173.7 g sodium succinate, 10.8 g sodium glutamate, 1.6 g aspartic acid. 800 ml Solution C was added and the solution was made up to 4 L with water, pH adjusted to 6.8, then autoclaved.

Solution C

The following were weighed and dissolved in 2 L water: 40.0 g nitrilotriacetic acid, 96.0 g MgCl_2 , 13.4 g CaCl_2 , 500 mg EDTA, 1.0 g ZnCl_2 , 1.0 g FeCl_2 , 360 mg MnCl_2 , 37 mg ammonium molybdate, 31 mg CuCl_2 , 50 mg $\text{Co}(\text{NO}_3)_2$, 23 mg orthoboric acid. The solution was made up to 4L and stored in 800 ml aliquots at $-20\text{ }^\circ\text{C}$ until required.

Vitamins (10000× stock)

The following were weighed and mixed into 100 ml water: 1.0 g nicotinic acid, 0.5 g thiamine, 100 mg *p*-aminobenzoic acid, 10 mg *d*-biotin. The solution was filter sterilised and stored at $4\text{ }^\circ\text{C}$.

M22+ liquid media

400 ml M22+ 10 × stock and 80 ml 5% (w/v) casamino acids were mixed and made up to 4 L with water. The medium was transferred to the required growth vessels, sealed with a lid or bung, then autoclaved. Immediately prior to usage, an appropriate volume of vitamins was added (to 1× concentration), and antibiotics if required.

M22+ agar

100 ml M22+ 10 × stock was made up to 1 L. To 100 ml aliquots, 1.6 g bacto-agar was added and then the solution was autoclaved. When required, aliquots were heated in a microwave to dissolve the agar and left to cool at $\sim 50\text{ }^\circ\text{C}$ in a water bath. An appropriate volume of vitamins was added (to 1× concentration), and antibiotics if required. The molten agar was poured into plastic petri dishes and left to set and dry.

References

- Aagaard J, Sistrom W. 1972. Control of synthesis of reaction center bacteriochlorophyll in photosynthetic bacteria. *Photochemistry and Photobiology* 15: 209-25
- Adams J, Tizazu G, Janusz S, Brueck S, Lopez G, Leggett G. 2010. Large-area nanopatterning of self-assembled monolayers of alkanethiolates by interferometric lithography. *Langmuir* 26: 13600-06
- Adams PG, Hunter CN. 2012. Adaptation of intracytoplasmic membranes to altered light intensity in *Rhodobacter sphaeroides*. *Biochimica et Biophysica Acta (BBA)-Bioenergetics* 1817: 1616-27
- Adams PG, Mothersole DJ, Ng IW, Olsen JD, Hunter CN. 2011. Monomeric RC-LH1 core complexes retard LH2 assembly and intracytoplasmic membrane formation in PufX-minus mutants of *Rhodobacter sphaeroides*. *Biochimica et Biophysica Acta (BBA)-Bioenergetics* 1807: 1044-55
- Ahmad SA, Wong LS, ul-Haq E, Hobbs JK, Leggett GJ, Micklefield J. 2011. Protein micro- and nanopatterning using aminosilanes with protein-resistant photolabile protecting groups. *J Am Chem Soc* 133: 2749-59
- Alkaisi MM, Mohamed K. 2010. Three-dimensional patterning using ultraviolet nanoimprint lithography In *Lithography*, ed. M Wang: InTech
- Alom Ruiz S, Chen CS. 2007. Microcontact printing: A tool to pattern. *Soft Matter* 3: 168-77
- Amro NA, Xu S, Liu G-Y. 2000. Patterning surfaces using tip-directed displacement and self-assembly. *Langmuir* 16: 3006-09
- Amunts A, Drory O, Nelson N. 2007. The structure of a plant photosystem I supercomplex at 3.4 Å resolution. *Nature* 447: 58
- Anderson SL, McIntosh L. 1991. Light-activated heterotrophic growth of the cyanobacterium *Synechocystis* sp. strain PCC 6803: a blue-light-requiring process. *Journal of Bacteriology* 173: 2761-67
- Andersson B, Anderson JM. 1980. Lateral heterogeneity in the distribution of chlorophyll-protein complexes of the thylakoid membranes of spinach chloroplasts. *Biochimica et Biophysica Acta (BBA)-Bioenergetics* 593: 427-40
- Aryal M, Buyukserin F, Mielczarek K, Zhao X-M, Gao J, et al. 2008. Imprinted large-scale high density polymer nanopillars for organic solar cells. *Journal of Vacuum Science & Technology B: Microelectronics and Nanometer Structures Processing, Measurement, and Phenomena* 26: 2562-66
- Austin JR, Staehelin LA. 2011. Three-dimensional architecture of grana and stroma thylakoids of higher plants as determined by electron tomography. *Plant Physiology* 155: 1601-11

- Austin MD, Ge H, Wu W, Li M, Yu Z, et al. 2004. Fabrication of 5 nm linewidth and 14 nm pitch features by nanoimprint lithography. *Applied Physics Letters* 84: 5299-301
- Avouris P, Hertel T, Martel R. 1997. Atomic force microscope tip-induced local oxidation of silicon: kinetics, mechanism, and nanofabrication. *Applied Physics Letters* 71: 285-87
- Badura A, Esper B, Ataka K, Grunwald C, Wöll C, et al. 2006. Light-Driven Water Splitting for (Bio-) Hydrogen Production: Photosystem 2 as the Central Part of a Bioelectrochemical Device. *Photochemistry and Photobiology* 82: 1385-90
- Bahatyrova S, Frese RN, Siebert CA, Olsen JD, van der Werf KO, et al. 2004a. The native architecture of a photosynthetic membrane. *Nature* 430: 1058-62
- Bahatyrova S, Frese RN, van der Werf KO, Otto C, Hunter CN, Olsen JD. 2004b. Flexibility and size heterogeneity of the LH1 light harvesting complex revealed by atomic force microscopy Functional significance for bacterial photosynthesis. *Journal of Biological Chemistry* 279: 21327-33
- Beekman LM, van Mourik F, Jones MR, Visser HM, Hunter CN, van Grondelle R. 1994. Trapping kinetics in mutants of the photosynthetic purple bacterium *Rhodobacter sphaeroides*: influence of the charge separation rate and consequences for the rate-limiting step in the light-harvesting process. *Biochemistry* 33: 3143-47
- Ben-Shem A, Frolow F, Nelson N. 2003. Crystal structure of plant photosystem I. *Nature* 426: 630
- Bernard A, Delamarche E, Schmid H, Michel B, Bosshard HR, Biebuyck H. 1998. Printing patterns of proteins. *Langmuir* 14: 2225-29
- Bernard A, Renault JP, Michel B, Bosshard HR, Delamarche E. 2000. Microcontact Printing of Proteins. *Advanced Materials* 12: 1067-70
- Bird S, El-Zubir O, Rawlings A, Leggett G, Staniland S. 2016. A novel design strategy for nanoparticles on nanopatterns: interferometric lithographic patterning of Mms6 biotemplated magnetic nanoparticles. *Journal of Materials Chemistry C* 4: 3948-55
- Bixon M, Jortner J, Michel-Beyerle M. 1991. On the mechanism of the primary charge separation in bacterial photosynthesis. *Biochimica et Biophysica Acta (BBA)-Bioenergetics* 1056: 301-15
- Blankenship RE. 2013. *Molecular mechanisms of photosynthesis*. John Wiley & Sons.
- Blankenship RE, Olson JM, Miller M. 1995. Antenna complexes from green photosynthetic bacteria In *Anoxygenic Photosynthetic Bacteria*, pp. 399-435: Springer
- Blawas A, Reichert W. 1998. Protein patterning. *Biomaterials* 19: 595-609
- Bradforth SE, Jimenez R, van Mourik F, van Grondelle R, Fleming GR. 1995. Excitation transfer in the core light-harvesting complex (LH-1) of *Rhodobacter sphaeroides*: an

- ultrafast fluorescence depolarization and annihilation study. *Journal of Physical Chemistry* 99: 16179-91
- Brueck S. 2005. Optical and interferometric lithography-Nanotechnology enablers. *Proceedings of the IEEE* 93: 1704-21
- Brune DC. 1995. Sulfur compounds as photosynthetic electron donors In *Anoxygenic Photosynthetic Bacteria*, ed. R.E. Blankenship, M. T. Madigan, CE Bauer, pp. 847-70: Kluwer
- Brunisholz RA, Zuber H. 1992. Structure, function and organization of antenna polypeptides and antenna complexes from the three families of Rhodospirillaneae. *Journal of Photochemistry and Photobiology B: Biology* 15: 113-40
- Brusatori MA, Tie Y, Van Tassel PR. 2003. Protein adsorption kinetics under an applied electric field: An optical waveguide lightmode spectroscopy study. *Langmuir* 19: 5089-97
- Bryant DA, Costas AMG, Maresca JA, Chew AGM, Klatt CG, et al. 2007. Candidatus *Chloracidobacterium thermophilum*: an aerobic phototrophic acidobacterium. *Science* 317: 523-26
- Caelen I, Gao H, Sigrist H. 2002. Protein density gradients on surfaces. *Langmuir* 18: 2463-67
- Cartron ML, Olsen JD, Sener M, Jackson PJ, Brindley AA, et al. 2014. Integration of energy and electron transfer processes in the photosynthetic membrane of *Rhodobacter sphaeroides*. *Biochimica et Biophysica Acta (BBA)-Bioenergetics* 1837: 1769-80
- Cedeno CC, Seekamp J, Kam A, Hoffmann T, Zankovych S, et al. 2002. Nanoimprint lithography for organic electronics. *Microelectronic Engineering* 61: 25-31
- Chen X-H, Zhang L, Weng Y-X, Du L-C, Ye M-P, et al. 2005. Protein structural deformation induced lifetime shortening of photosynthetic bacteria light-harvesting complex LH2 excited state. *Biophysical Journal* 88: 4262-73
- Choi I, Kang SK, Lee J, Kim Y, Yi J. 2006. In situ observation of biomolecules patterned on a PEG-modified Si surface by scanning probe lithography. *Biomaterials* 27: 4655-60
- Choi I, Kang SK, Lee J, Kim Y, Yi J. 2008. Fabrication of island-type microelectrode via AFM lithography for a highly sensitive Pt-ion detection system. *Sensors and Actuators B: Chemical* 129: 734-40
- Chou SY, Krauss PR, Renstrom PJ. 1995. Imprint of sub-25 nm vias and trenches in polymers. *Applied Physics Letters* 67: 3114-16
- Chou SY, Krauss PR, Renstrom PJ. 1996. Nanoimprint lithography. *Journal of Vacuum Science & Technology B: Microelectronics and Nanometer Structures Processing, Measurement, and Phenomena* 14: 4129-33

- Chrisey LA, O'Ferrall CE, Spargo BJ, Dulcey CS, Calvert JM. 1996. Fabrication of patterned DNA surfaces. *Nucleic Acids Research* 24: 3040-47
- Clayton RK, Haselkorn R. 1972. Protein components of bacterial photosynthetic membranes. *Journal of Molecular Biology* 68: 97-105
- Cogdell RJ. 1985. Carotenoids in photosynthesis. *Pure and Applied Chemistry* 57: 723-28
- Cogdell RJ, Howard TD, Bittl R, Schlodder E, Geisenheimer I, Lubitz W. 2000. How carotenoids protect bacterial photosynthesis. *Philosophical Transactions of the Royal Society B: Biological Sciences* 355: 1345-49
- Cooper DE, Rands MB, Woo C-P. 1975. Sulfide reduction in fellmongery effluent by red sulfur bacteria. *Journal (Water Pollution Control Federation)*: 2088-100
- Crouch LI, Jones MR. 2012. Cross-species investigation of the functions of the *Rhodobacter* PufX polypeptide and the composition of the RC-LH1 core complex. *Biochimica et Biophysica Acta (BBA)-Bioenergetics* 1817: 336-52
- Daan Wouters, Ron Willems, Stephanie Hoepfener, Cees F. J. Flipse, Schubert US. 2005. Oxidation Conditions for Octadecyl Trichlorosilane Monolayers on Silicon: A Detailed Atomic Force Microscopy Study of the Effects of Pulse Height and Duration on the Oxidation of the Monolayer and the Underlying Si Substrate. *Adv. Funct. Mater.* 15: 938-44
- Dahlberg PD, Ting P-C, Massey SC, Allodi MA, Martin EC, et al. 2017. Mapping the ultrafast flow of harvested solar energy in living photosynthetic cells. *Nature Communications* 8: 988
- Das R, Kiley PJ, Segal M, Norville J, Yu AA, et al. 2004. Integration of photosynthetic protein molecular complexes in solid-state electronic devices. *Nano Letters* 4: 1079-83
- Dekker JP, Van Grondelle R. 2000. Primary charge separation in photosystem II. *Photosynthesis Research* 63: 195-208
- del Campo A, Boos D, Spiess HW, Jonas U. 2005. Surface Modification with Orthogonal Photosensitive Silanes for Sequential Chemical Lithography and Site-Selective Particle Deposition. *Angewandte Chemie International Edition* 44: 4707-12
- Delamarche E, Michel B, Biebuyck HA, Gerber C. 1996. Golden interfaces: The Surface of Self-Assembled Monolayers. *Advanced Materials* 8: 719-29
- Delamarche E, Schmid H, Michel B, Biebuyck H. 1997. Stability of molded polydimethylsiloxane microstructures. *Advanced Materials* 9: 741-46
- Demers L, Ginger D, Park S-J, Li Z, Chung S-W, Mirkin C. 2002. Direct patterning of modified oligonucleotides on metals and insulators by dip-pen nanolithography. *Science* 296: 1836-38

den Hollander M-J, Magis JG, Fuchsenberger P, Aartsma TJ, Jones MR, Frese RN. 2011. Enhanced photocurrent generation by photosynthetic bacterial reaction centers through molecular relays, light-harvesting complexes, and direct protein–gold interactions. *Langmuir* 27: 10282-94

Dulcey CS, Georger JH, Krauthamer V, Stenger DA, Fare TL, Calvert JM. 1991. Deep UV photochemistry of chemisorbed monolayers: patterned coplanar molecular assemblies. *Science* 252: 551-54

Dutta PK, Levenberg S, Loskutov A, Jun D, Saer R, et al. 2014a. A DNA-directed light-harvesting/reaction center system. *Journal of the American Chemical Society* 136: 16618-25

Dutta PK, Lin S, Loskutov A, Levenberg S, Jun D, et al. 2014b. Reengineering the optical absorption cross-section of photosynthetic reaction centers. *Journal of the American Chemical Society* 136: 4599-604

Ehtsham Ul-Haq, ‡ Samson Patole,‡,§ Mark Moxey,‡ Esther Amstad, Cvetelin Vasilev,§ C. Neil Hunter,§ Graham J. Leggett,‡,* Nicholas D. Spencer, and Nicholas H. Williams‡. 2013. Photocatalytic Nanolithography of Self-Assembled Monolayers and Proteins. *American Chemical Society* 7: 7610–18

Ekblad T, Andersson O, Tai F-I, Ederth T, Liedberg B. 2009. Lateral control of protein adsorption on charged polymer gradients. *Langmuir* 25: 3755-62

El Zubir O, Xia S, Ducker RE, Wang L, Mullin N, et al. 2017. From Monochrome to Technicolor: Simple Generic Approaches to Multicomponent Protein Nanopatterning using Siloxanes with Photoremovable Protein-Resistant Protecting Groups. *Langmuir* 33: 8829-37

Escalante M, Lenferink A, Zhao Y, Tas N, Huskens J, et al. 2010. Long-range energy propagation in nanometer arrays of light harvesting antenna complexes. *Nano Letters* 10: 1450-57

Escalante M, Maury P, Bruinink CM, van der Werf K, Olsen JD, et al. 2008a. Directed assembly of functional light harvesting antenna complexes onto chemically patterned surfaces. *Nanotechnology* 19: 025101-06

Escalante M, Zhao Y, Ludden MJ, Vermeij R, Olsen JD, et al. 2008b. Nanometer arrays of functional light harvesting antenna complexes by nanoimprint lithography and host– guest interactions. *Journal of the American Chemical Society* 130: 8892-93

Escalante Marun M. 2009. Nanofabrication of bioinspired architectures with light harvesting proteins. *Phd Thesis, University of Twente*

Fang T-H. 2004. Mechanisms of nanooxidation of Si(100) from atomic force microscopy. *Microelectronics Journal* 35: 701-07

Faulkner CJ, Lees S, Ciesielski PN, Cliffel DE, Jennings GK. 2008. Rapid assembly of photosystem I monolayers on gold electrodes. *Langmuir* 24: 8409-12

- Feher G. 1971. Some chemical and physical properties of a bacterial reaction center particle and its primary photochemical reactants. *Photochemistry and Photobiology* 14: 373-87
- Ferguson GS, Chaudhury MK, Biebuyck HA, Whitesides GM. 1993. Monolayers on disordered substrates: self-assembly of alkyltrichlorosilanes on surface-modified polyethylene and poly (dimethylsiloxane). *Macromolecules* 26: 5870-75
- Fernandez-Lafuente R, Rosell C, Rodríguez V, Santana C, Soler G, et al. 1993. Preparation of activated supports containing low pK amino groups. A new tool for protein immobilization via the carboxyl coupling method. *Enzyme and Microbial Technology* 15: 546-50
- Ferreira KN, Iverson TM, Maghlaoui K, Barber J, Iwata S. 2004. Architecture of the Photosynthetic Oxygen-Evolving Center. *Science* 303: 1831-38
- Fichet G, Stutzmann N, Muir BV, Huck W. 2002. Microembossing of elastomeric triblock copolymers. *Advanced Materials* 14: 47-51
- Foley J, Schmid H, Stutz R, Delamarche E. 2005. Microcontact printing of proteins inside microstructures. *Langmuir* 21: 11296-303
- Fontaine PA, Dubois E, Stiévenard D. 1998. Characterization of scanning tunneling microscopy and atomic force microscopy-based techniques for nanolithography on hydrogen-passivated silicon. *Journal of Applied Physics* 84: 1776-81
- Förster T. 1946. Energy transport and fluorescence. *Naturwissenschaften* 6: 166-75
- Förster T. 1965. *Delocalized excitation and excitation transfer*. Florida State University.
- Francia F, Wang J, Venturoli G, Melandri BA, Barz WP, Oesterhelt D. 1999. The Reaction Center– LH1 Antenna Complex of *Rhodobacter sphaeroides* Contains One PufX Molecule Which Is Involved in Dimerization of This Complex. *Biochemistry* 38: 6834-45
- Freer A, Prince S, Sauer K, Papiz M, Lawless AH, et al. 1996. Pigment–pigment interactions and energy transfer in the antenna complex of the photosynthetic bacterium *Rhodospseudomonas acidophila*. *Structure* 4: 449-62
- Frese RN, Pàmies JC, Olsen JD, Bahatyrova S, van der Weij-de CD, et al. 2008. Protein shape and crowding drive domain formation and curvature in biological membranes. *Biophysical Journal* 94: 640-47
- Frese RN, Siebert CA, Niederman RA, Hunter CN, Otto C, van Grondelle R. 2004. The long-range organization of a native photosynthetic membrane. *Proceedings of the National Academy of Sciences USA* 101: 17994-99
- Friebe VM, Delgado JD, Swainsbury DJ, Gruber JM, Chanaewa A, et al. 2016. Plasmon-Enhanced Photocurrent of Photosynthetic Pigment Proteins on Nanoporous Silver. *Advanced Functional Materials* 26: 285-92

- Frolov L, Rosenwaks Y, Carmeli C, Carmeli I. 2005. Fabrication of a photoelectronic device by direct chemical binding of the photosynthetic reaction center protein to metal surfaces. *Advanced Materials* 17: 2434-37
- Frolov L, Rosenwaks Y, Richter S, Carmeli C, Carmeli I. 2008. Photoelectric junctions between GaAs and photosynthetic reaction center protein. *Journal of Physical Chemistry C* 112: 13426-30
- Gates BD, Xu Q, Stewart M, Ryan D, Willson CG, Whitesides GM. 2005. New approaches to nanofabrication: molding, printing, and other techniques. *Chemical Reviews* 105: 1171-96
- Gerster D, Reichert J, Bi H, Barth JV, Kaniber SM, et al. 2012. Photocurrent of a single photosynthetic protein. *Nature Nanotechnology* 7: 673
- Golzhauser A, Eck W, Geyer W, Stadler V, Weimann T, et al. 2001. Chemical nanolithography with electron beams. *Advanced Materials* 13: 806-06
- Grayson KJ, Faries KM, Huang X, Qian P, Dilbeck P, et al. 2017. Augmenting light coverage for photosynthesis through YFP-enhanced charge separation at the *Rhodobacter sphaeroides* reaction centre. *Nature Communications* 8: 13972
- Grazú V, Abian O, Mateo C, Batista-Viera F, Fernández-Lafuente R, Guisán JM. 2003. Novel bifunctional epoxy/thiol-reactive support to immobilize thiol containing proteins by the epoxy chemistry. *Biomacromolecules* 4: 1495-501
- Grigorieva G, Shestakov S. 1982. Transformation in the cyanobacterium *Synechocystis* sp. 6803. *FEMS Microbiology Letters* 13: 367-70
- Guiraud HJ, Foote CS. 1976. Chemistry of superoxide ion. III. Quenching of singlet oxygen. *Journal of the American Chemical Society* 98: 1984-86
- Gundlach K, Werwie M, Wiegand S, Paulsen H. 2009. Filling the “green gap” of the major light-harvesting chlorophyll *a/b* complex by covalent attachment of Rhodamine Red. *Biochimica et Biophysica Acta (BBA)-Bioenergetics* 1787: 1499-504
- Guo LJ. 2007. Nanoimprint lithography: methods and material requirements. *Advanced Materials* 19: 495-513
- Ham M-H, Choi JH, Boghossian AA, Jeng ES, Graff RA, et al. 2010. Photoelectrochemical complexes for solar energy conversion that chemically and autonomously regenerate. *Nature Chemistry* 2: 929-36
- Harris JM. 2013. *Poly (ethylene glycol) chemistry: biotechnical and biomedical applications*. Springer Science & Business Media.
- Harris MA, Jiang J, Niedzwiedzki DM, Jiao J, Taniguchi M, et al. 2014a. Versatile design of biohybrid light-harvesting architectures to tune location, density, and spectral coverage of attached synthetic chromophores for enhanced energy capture. *Photosynthesis Research* 121: 35-48

- Harris MA, Parkes-Loach PS, Springer JW, Jiang J, Martin EC, et al. 2013. Integration of multiple chromophores with native photosynthetic antennas to enhance solar energy capture and delivery. *Chemical Science* 4: 3924-33
- Harris MA, Sahin T, Jiang J, Vairaprakash P, Parkes-Loach PS, et al. 2014b. Enhanced Light-Harvesting Capacity by Micellar Assembly of Free Accessory Chromophores and LH1-like Antennas. *Photochemistry and Photobiology* 90: 1264-76
- Heath GR, Roth J, Connell SD, Evans SD. 2014. Diffusion in low-dimensional lipid membranes. *Nano Letters* 14: 5984-88
- Hess S, Akesson E, Cogdell R, Pullerits T, Sundström V. 1995a. Energy transfer in spectrally inhomogeneous light-harvesting pigment-protein complexes of purple bacteria. *Biophysical Journal* 69: 2211-25
- Hess S, Chachisvilis M, Timpmann K, Jones M, Fowler G, et al. 1995b. Temporally and spectrally resolved subpicosecond energy transfer within the peripheral antenna complex (LH2) and from LH2 to the core antenna complex in photosynthetic purple bacteria. *Proceedings of the National Academy of Sciences USA* 92: 12333-37
- Hitchcock A, Hunter CN, Sener M. 2017. Determination of Cell Doubling Times from the Return-on-Investment Time of Photosynthetic Vesicles Based on Atomic Detail Structural Models. *Journal of Physical Chemistry B* 121: 3787-97
- Hoeppener SM, R.; Cohen, S. R.; Chi, L. F.; Fuchs, H.; Sagiv, J. Adv. Mater. 2002. Metal Nanoparticles, Nanowires, and Contact Electrodes Self-Assembled on Patterned Monolayer TemplatesOA Bottom-Up Chemical Approach. *Adv. Mater.* 14: 1036-41
- Hoff JD, Cheng L-J, Meyhöfer E, Guo LJ, Hunt AJ. 2004. Nanoscale protein patterning by imprint lithography. *Nano Letters* 4: 853-57
- Hong S, Zhu J, Mirkin CA. 1999. Multiple ink nanolithography: toward a multiple-pen nano-plotter. *Science* 286: 523-25
- Hsin J, Gumbart J, Trabuco LG, Villa E, Qian P, et al. 2009. Protein-induced membrane curvature investigated through molecular dynamics flexible fitting. *Biophysical Journal* 97: 321-29
- Hu Z, Baralia G, Bayot V, Gohy J-F, Jonas AM. 2005. Nanoscale control of polymer crystallization by nanoimprint lithography. *Nano Letters* 5: 1738-43
- Hunter CN, Turner G. 1988. Transfer of Genes Coding for Apoproteins of Reaction Centre and Light-harvesting LH1 Complexes to *Rhodobacter sphaeroides*. *Microbiology* 134: 1471-80
- Hunter CN, Van Grondelle R, Holmes NG, Jones OT. 1979. The reconstitution of energy transfer in membranes from a bacteriochlorophyll-less mutant of *Rhodospseudomonas sphaeroides* by addition of light-harvesting and reaction centre pigment-protein complexes. *Biochimica et Biophysica Acta (BBA)-Bioenergetics* 548: 458-70

- Hyun J, Ahn SJ, Lee WK, Chilkoti A, Zauscher S. 2002. Molecular recognition-mediated fabrication of protein nanostructures by dip-pen lithography. *Nano Letters* 2: 1203-07
- Imhoff JF. 1995. Taxonomy and physiology of phototrophic purple bacteria and green sulfur bacteria In *Anoxygenic Photosynthetic Bacteria*, ed. R.E. Blankenship, M. T. Madigan, CE Bauer, pp. 1-15: Kluwer
- Iqbal A, Arslan S, Okumus B, Wilson TJ, Giraud G, et al. 2008. Orientation dependence in fluorescent energy transfer between Cy3 and Cy5 terminally attached to double-stranded nucleic acids. *Proceedings of the National Academy of Sciences USA* 105: 11176-81
- Jeon S, Menard E, Park JU, Maria J, Meitl M, et al. 2004. Three-Dimensional Nanofabrication with Rubber Stamps and Conformable Photomasks. *Advanced Materials* 16: 1369-73
- Jimenez R, Dikshit SN, Bradforth SE, Fleming GR. 1996. Electronic excitation transfer in the LH2 complex of *Rhodobacter sphaeroides*. *Journal of Physical Chemistry* 100: 6825-34
- Johnson A, Madsen J, Chapman P, Alswieleh A, Al-Jaf O, et al. 2017. Micrometre and nanometre scale patterning of binary polymer brushes, supported lipid bilayers and proteins. *Chemical Science* 8: 4517-26
- Johnson MP. 2016. Photosynthesis. *Essays In Biochemistry* 60: 255-73
- Johnson MP, Vasilev C, Olsen JD, Hunter CN. 2014. Nanodomains of cytochrome *b₆f* and photosystem II complexes in spinach grana thylakoid membranes. *The Plant Cell* 26: 3051-61
- Jones MR, Fyfe PK, Roszak AW, Isaacs NW, Cogdell RJ. 2002. Protein- lipid interactions in the purple bacterial reaction centre. *Biochimica et Biophysica Acta - Biomembranes* 1565: 206-14
- Jongsma MA, Litjens RH. 2006. Self-assembling protein arrays on DNA chips by auto-labeling fusion proteins with a single DNA address. *Proteomics* 6: 2650-55
- Joo T, Jia Y, Yu J-Y, Jonas DM, Fleming GR. 1996. Dynamics in isolated bacterial light harvesting antenna (LH2) of *Rhodobacter sphaeroides* at room temperature. *Journal of Physical Chemistry* 100: 2399-409
- Jordan P, Fromme P, Witt H, Klukas O, Saenger W, Krauss N. 2001. Three- dimensional structure of cyanobacterial photosystem I at 2.5 angstrom resolution. *Nature* 411: 909-17
- Juncker D, Schmid H, Bernard A, Caelen I, Michel B, et al. 2001. Soft and rigid two-level microfluidic networks for patterning surfaces. *Journal of Micromechanics and Microengineering* 11: 532

- Kamran M, Delgado JD, Friebe V, Aartsma TJ, Frese RN. 2014. Photosynthetic protein complexes as bio-photovoltaic building blocks retaining a high internal quantum efficiency. *Biomacromolecules* 15: 2833-38
- Kamran M, Friebe VM, Delgado JD, Aartsma TJ, Frese RN, Jones MR. 2015. Demonstration of asymmetric electron conduction in pseudosymmetrical photosynthetic reaction centre proteins in an electrical circuit. *Nat Commun* 6: 6530
- Kaneko T, Tabata S. 1997. Complete genome structure of the unicellular cyanobacterium *Synechocystis* sp. PCC6803. *Plant and Cell Physiology* 38: 1171-76
- Ki-Bum Lee J-HL, and Chad A. Mirkin*. 2003. Protein Nanostructures Formed via Direct-Write Dip-Pen Nanolithography. *Journal of the American Chemical Society* 125: 5588-89
- King E, Xia Y, Zhao XM, Whitesides GM. 1997. Solvent-assisted microcontact molding: A convenient method for fabricating three-dimensional structures on surfaces of polymers. *Advanced Materials* 9: 651-54
- Ko K-S, Jaipuri FA, Pohl NL. 2005. Fluorous-based carbohydrate microarrays. *Journal of the American Chemical Society* 127: 13162-63
- Kodali G, Mancini JA, Solomon LA, Episova TV, Roach N, et al. 2017. Design and engineering of water-soluble light-harvesting protein maquettes. *Chemical Science* 8: 316-24
- Koepke J, Hu X, Muenke C, Schulten K, Michel H. 1996. The crystal structure of the light-harvesting complex II (B800–850) from *Rhodospirillum rubrum*. *Structure* 4: 581-97
- Kondo M, Nakamura Y, Fujii K, Nagata M, Suemori Y, et al. 2007. Self-assembled monolayer of light-harvesting core complexes from photosynthetic bacteria on a gold electrode modified with alkanethiols. *Biomacromolecules* 8: 2457-63
- Kooy N, Mohamed K, Pin LT, Guan OS. 2014. A review of roll-to-roll nanoimprint lithography. *Nanoscale Research Letters* 9: 320
- Krakert S, Ballav N, Zharnikov M, Terfort A. 2010. Adjustment of the bioresistivity by electron irradiation: self-assembled monolayers of oligo(ethyleneglycol)-terminated alkanethiols with embedded cleavable group. *Phys Chem Chem Phys* 12: 507-15
- Krassen H, Schwarze A, Friedrich Br, Ataka K, Lenz O, Heberle J. 2009. Photosynthetic hydrogen production by a hybrid complex of photosystem I and [NiFe]-hydrogenase. *ACS Nano* 3: 4055-61
- Kumar A, Whitesides GM. 1993. Features of gold having micrometer to centimeter dimensions can be formed through a combination of stamping with an elastomeric stamp and an alkanethiol “ink” followed by chemical etching. *Applied Physics Letters* 63: 2002-04

- Kumar G, Tang HX, Schroers J. 2009. Nanomoulding with amorphous metals. *Nature* 457: 868
- Kumar S, Cartron MIL, Mullin N, Qian P, Leggett GJ, et al. 2016. Direct imaging of protein organization in an intact bacterial organelle using high-resolution atomic force microscopy. *ACS Nano* 11: 126-33
- Lauterbach R, Liu J, Knoll W, Paulsen H. 2010. Energy Transfer between surface-immobilized light-harvesting chlorophyll *a/b* complex (LHCII) studied by surface plasmon field-enhanced fluorescence spectroscopy (SPFS). *Langmuir* 26: 17315-21
- Lee J-H, Kim H-E, Im JH, Bae YM, Choi JS, et al. 2008. Preparation of orthogonally functionalized surface using micromolding in capillaries technique for the control of cellular adhesion. *Colloids and Surfaces B: Biointerfaces* 64: 126-34
- Lee JH, Kim CH, Ho KM, Constant K. 2005. Two-Polymer Microtransfer Molding for Highly Layered Microstructures. *Advanced Materials* 17: 2481-85
- Lee KB, Park SJ, Mirkin CA, Smith JC, Mrksich M. 2002. Protein nanoarrays generated by dip-pen nanolithography. *Science* 295: 1702-5
- Lee M, Kang DK, Yang HK, Park KH, Choe SY, et al. 2006a. Protein nanoarray on Prolinker surface constructed by atomic force microscopy dip-pen nanolithography for analysis of protein interaction. *Proteomics* 6: 1094-103
- Lee SW, Oh BK, Sanedrin RG, Salaita K, Fujigaya T, Mirkin CA. 2006b. Biologically Active Protein Nanoarrays Generated Using Parallel Dip-Pen Nanolithography. *Advanced Materials* 18: 1133-36
- Leggett GJ. 2012. Light-directed nanosynthesis: near-field optical approaches to integration of the top-down and bottom-up fabrication paradigms. *Nanoscale* 4: 1840-55
- Lewis CL, Choi C-H, Lin Y, Lee C-S, Yi H. 2010. Fabrication of uniform DNA-conjugated hydrogel microparticles via replica molding for facile nucleic acid hybridization assays. *Analytical Chemistry* 82: 5851-58
- Liu G-Y, Amro NA. 2002. Positioning protein molecules on surfaces: A nanoengineering approach to supramolecular chemistry. *Proceedings of the National Academy of Sciences USA* 99: 5165-70
- Liu J, Friebe VM, Swainsbury DJ, Crouch LI, Szabo DA, et al. 2018. Engineered photoproteins that give rise to photosynthetically-incompetent bacteria are effective as photovoltaic materials for biohybrid photoelectrochemical cells. *Faraday Discussions* 207: 307-27
- Liu J, Lauterbach R, Paulsen H, Knoll W. 2008. Immobilization of light-harvesting chlorophyll *a/b* complex (LHCIIb) studied by surface plasmon field-enhanced fluorescence spectroscopy. *Langmuir* 24: 9661-67

- Liu Z, Yan H, Wang K, Kuang T, Zhang J, et al. 2004. Crystal structure of spinach major light-harvesting complex at 2.72 Å resolution. *Nature* 428: 287
- Lopez GP, Albers MW, Schreiber SL, Carroll R, Peralta E, Whitesides GM. 1993a. Convenient methods for patterning the adhesion of mammalian cells to surfaces using self-assembled monolayers of alkanethiolates on gold. *Journal of the American Chemical Society* 115: 5877-78
- Lopez GP, Biebuyck HA, Harter R, Kumar A, Whitesides GM. 1993b. Fabrication and imaging of two-dimensional patterns of proteins adsorbed on self-assembled monolayers by scanning electron microscopy. *Journal of the American Chemical Society* 115: 10774-81
- Luk Y-Y, Kato M, Mrksich M. 2000. Self-assembled monolayers of alkanethiolates presenting mannitol groups are inert to protein adsorption and cell attachment. *Langmuir* 16: 9604-08
- Ma Y-Z, Cogdell RJ, Gillbro T. 1997. Energy transfer and exciton annihilation in the B800– 850 antenna complex of the photosynthetic purple bacterium *Rhodospseudomonas acidophila* (Strain 10050). A femtosecond transient absorption study. *Journal of Physical Chemistry B* 101: 1087-95
- Madigan M. 1988. Microbiology, physiology, and ecology of phototrophic bacteria. *Biology of anaerobic microorganisms*. Wiley, New York: 39-111
- Madigan MT, Gest H. 1979. Growth of the photosynthetic bacterium *Rhodospseudomonas capsulata* chemoautotrophically in darkness with H₂ as the energy source. *Journal of Bacteriology* 137: 524-30
- Magis GJ, den Hollander M-J, Onderwaater WG, Olsen JD, Hunter CN, et al. 2010. Light harvesting, energy transfer and electron cycling of a native photosynthetic membrane adsorbed onto a gold surface. *Biochimica et Biophysica Acta (BBA)- Biomembranes* 1798: 637-45
- Mancini JA, Kodali G, Jiang J, Reddy KR, Lindsey JS, et al. 2017. Multi-step excitation energy transfer engineered in genetic fusions of natural and synthetic light-harvesting proteins. *Journal of The Royal Society Interface* 14: 20160896
- Maniatis T, et al. Fritsch E, Sambrook J. 1982. Molecular cloning: a laboratory manual Cold Spring Harbor. NY: Cold Spring Harbor Laboratory
- Maoz R, Frydman, E. , Cohen, S. R. and Sagiv, J. 2000a. Constructive Nanolithography: Site-Defined Silver Self-Assembly on Nanoelectrochemically Patterned Monolayer Templates. *Advanced Materials* 12: 424-29
- Maoz R, Frydman, E. , Cohen, S. R. and Sagiv, J. 2000b. “Constructive Nanolithography”: Inert Monolayers as Patternable Templates for In-Situ Nanofabrication of Metal–Semiconductor–Organic Surface Structures—A Generic Approach. *Advanced Materials* 12: 725-31

- Martínez RV, Losilla NS, Martínez J, Huttel Y, García R. 2007. Patterning Polymeric Structures with 2 nm Resolution at 3 nm Half Pitch in Ambient Conditions. *Nano Letters* 7: 1846-50
- Mateo C, Abian O, Fernández - Lorente G, Pedroche J, Fernández - Lafuente R, Guisan JM. 2002. Epoxy sepabeads: a novel epoxy support for stabilization of industrial enzymes via very intense multipoint covalent attachment. *Biotechnology Progress* 18: 629-34
- Matthew Montague, Robert E. Ducker, Karen S. L. Chong, Robert J. Manning, Frank J. M. Rutten, et al. 2007. Fabrication of Biomolecular Nanostructures by Scanning Near-Field Photolithography of Oligo(ethylene glycol)-Terminated Self-Assembled Monolayers. *Langmuir* 23 (13): 7328–37
- Maury P, Escalante M, Péter M, Reinhoudt DN, Subramaniam V, Huskens J. 2007. Creating Nanopatterns of His-Tagged Proteins on Surfaces by Nanoimprint Lithography Using Specific NiNTA-Histidine Interactions. *Small* 3: 1584-92
- McDermott G, Prince S, Freer A, Hawthornthwaite-Lawless A, Papiz M, et al. 1995. Crystal structure of an integral membrane light-harvesting complex from photosynthetic bacteria. *Nature* 374: 517-21
- McEvoy JP, Brudvig GW. 2006. Water-splitting chemistry of photosystem II. *Chemical Reviews* 106: 4455-83
- Meadows KA, Iida K, Tsuda K, Recchia PA, Heller BA, et al. 1995. Enzymic and chemical cleavage of the core light-harvesting polypeptides of photosynthetic bacteria: Determination of the minimal polypeptide size and structure required for subunit and light-harvesting complex formation. *Biochemistry* 34: 1559-74
- Menglong Yang DW, Marcel Giesbers, Ulrich S. Schubert and Han Zuilhof. 2009. Local Probe Oxidation of Self-Assembled Monolayers on Hydrogen-Terminated Silicon. *ACS Nano* 3: 2887–900
- Möller C, Allen M, Elings V, Engel A, Müller DJ. 1999. Tapping-mode atomic force microscopy produces faithful high-resolution images of protein surfaces. *Biophysical Journal* 77: 1150-58
- Monshouwer R, de Zarate IO, van Mourik F, van Grondelle R. 1995. Low-intensity pump-probe spectroscopy on the B800 to B850 transfer in the light harvesting 2 complex of *Rhodobacter sphaeroides*. *Chemical Physics Letters* 246: 341-46
- Mothersole DJ. 2013. *Assembly, structure and organisation of photosynthetic membranes*. Phd Thesis, University of Sheffield
- Moxey M, Johnson A, El-Zubir O, Cartron M, Dinachali SS, et al. 2015. Fabrication of Self-Cleaning, Reusable Titania Templates for Nanometer and Micrometer Scale Protein Patterning. *ACS Nano* 9: 6262-70
- Nagarajan V, Parson W. 1997. Excitation energy transfer between the B850 and B875 antenna complexes of *Rhodobacter sphaeroides*. *Biochemistry* 36: 2300-06

- Nagata M, Amano M, Joke T, Fujii K, Okuda A, et al. 2012. Immobilization and photocurrent activity of a light-harvesting antenna complex II, LHCII, isolated from a plant on electrodes. *ACS Macro Letters* 1: 296-99
- Nath N, Hyun J, Ma H, Chilkoti A. 2004. Surface engineering strategies for control of protein and cell interactions. *Surface Science* 570: 98-110
- Ng IW, Adams PG, Mothersole DJ, Vasilev C, Martin EC, et al. 2011. Carotenoids are essential for normal levels of dimerisation of the RC-LH1-PufX core complex of *Rhodobacter sphaeroides*: characterisation of R-26 as a crtB (phytoene synthase) mutant. *Biochimica et Biophysica Acta (BBA)-Bioenergetics* 1807: 1056-63
- Nicholas P. Reynolds, Jaimey D. Tucker, Paul A. Davison, John A. Timney, C. Neil Hunter, Leggett GJ. 2009. Site-specific immobilization and micrometer and nanometer scale photopatterning of yellow fluorescent protein on glass surfaces. *Journal of the American Chemical Society* 131: 896-97
- Niederman RA, Mallon DE, Langan JJ. 1976. Membranes of *Rhodospseudomonas sphaeroides*. IV. Assembly of chromatophores in low-aeration cell suspensions. *Biochimica et Biophysica Acta (BBA) - Bioenergetics* 440: 429-47
- Novoderezhkin V, Marin A, van Grondelle R. 2011. Intra-and inter-monomeric transfers in the light harvesting LHCII complex: the Redfield-Förster picture. *Physical Chemistry Chemical Physics* 13: 17093-103
- Noy D, Moser CC, Dutton PL. 2006. Design and engineering of photosynthetic light-harvesting and electron transfer using length, time, and energy scales. *Biochimica et Biophysica Acta (BBA)-Bioenergetics* 1757: 90-105
- Nuzzo RG, Allara DL. 1983. Adsorption of bifunctional organic disulfides on gold surfaces. *Journal of the American Chemical Society* 105: 4481-83
- Olsen JD, Adams PG, Jackson PJ, Dickman MJ, Qian P, Hunter CN. 2014. Aberrant assembly complexes of the reaction center light-harvesting 1 PufX (RC-LH1-PufX) core complex of *Rhodobacter sphaeroides* imaged by atomic force microscopy. *Journal of Biological Chemistry* 289: 29927-36
- Olsen JD, Tucker JD, Timney JA, Qian P, Vassilev C, Hunter CN. 2008. The organization of LH2 complexes in membranes from *Rhodobacter sphaeroides*. *Journal of Biological Chemistry* 283: 30772-79
- Ostuni E, Chapman RG, Holmlin RE, Takayama S, Whitesides GM. 2001. A survey of structure-property relationships of surfaces that resist the adsorption of protein. *Langmuir* 17: 5605-20
- Otte SC, Kleinherenbrink FA, Amesz J. 1993. Energy transfer between the reaction center and the antenna in purple bacteria. *Biochimica et Biophysica Acta (BBA)-Bioenergetics* 1143: 84-90
- Padan E. 1979. Facultative anoxygenic photosynthesis in cyanobacteria. *Annual Review of Plant Physiology* 30: 27-40

- Pale-Grosdemange C, Simon ES, Prime KL, Whitesides GM. 1991. Formation of self-assembled monolayers by chemisorption of derivatives of oligo (ethylene glycol) of structure HS (CH₂)₁₁ (OCH₂CH₂) mOH on gold. *Journal of the American Chemical Society* 113: 12-20
- Papiz MZ, Prince SM, Howard T, Cogdell RJ, Isaacs NW. 2003. The structure and thermal motion of the B800–850 LH2 complex from *Rps. acidophila* at 2.0 Å resolution and 100 K: new structural features and functionally relevant motions. *Journal of Molecular Biology* 326: 1523-38
- Patel N, Davies MC, Hartshorne M, Heaton RJ, Roberts CJ, et al. 1997. Immobilization of protein molecules onto homogeneous and mixed carboxylate-terminated self-assembled monolayers. *Langmuir* 13: 6485-90
- Patole S, Vasilev C, El-Zubir O, Wang L, Johnson MP, et al. 2015. Interference lithographic nanopatterning of plant and bacterial light-harvesting complexes on gold substrates. *Interface Focus* 5: 20150005
- Perl A, Reinhoudt DN, Huskens J. 2009. Microcontact printing: limitations and achievements. *Advanced Materials* 21: 2257-68
- Pfennig N. 1978. Ch. I, General physiology and ecology of photosynthetic bacteria In *The Photosynthetic Bacteria*, ed. R.K. Clayton, WR Sistrom, pp. 1-18. New York: Plenum Press
- Pflock T, Dezi M, Venturoli G, Cogdell RJ, Köhler J, Oellerich S. 2008. Comparison of the fluorescence kinetics of detergent-solubilized and membrane-reconstituted LH2 complexes from *Rps. acidophila* and *Rb. sphaeroides*. *Photosynthesis Research* 95: 291-98
- Pflock TJ, Oellerich S, Krapf L, Southall J, Cogdell RJ, et al. 2011a. The Electronically Excited States of LH2 Complexes from *Rhodopseudomonas acidophila* Strain 10050 Studied by Time-Resolved Spectroscopy and Dynamic Monte Carlo Simulations. II. Homo-Arrays Of LH2 Complexes Reconstituted Into Phospholipid Model Membranes. *Journal of Physical Chemistry B* 115: 8821-31
- Pflock TJ, Oellerich S, Southall J, Cogdell RJ, Ullmann GM, Köhler Jr. 2011b. The electronically excited states of LH2 complexes from *Rhodopseudomonas acidophila* strain 10050 studied by time-resolved spectroscopy and dynamic Monte Carlo simulations. I. Isolated, non-interacting LH2 complexes. *Journal of Physical Chemistry B* 115: 8813-20
- Piner RD, Zhu J, Xu F, Hong S, Mirkin CA. 1999. 'Dip-pen' nanolithography. *Science* 283: 661-63
- Pisignano D, Persano L, Mele E, Visconti P, Anni M, et al. 2005. First-order imprinted organic distributed feedback lasers. *Synthetic Metals* 153: 237-40
- Prime KL, Whitesides GM. 1991. Self-assembled organic monolayers: model systems for studying adsorption of proteins at surfaces. *Science*: 1164-67

- Qian P, Bullough PA, Hunter CN. 2008. Three-dimensional reconstruction of a membrane-bending complex the RC-LH1-PufX core dimer of *Rhodobacter sphaeroides*. *Journal of Biological Chemistry* 283: 14002-11
- Qian P, Hunter CN, Bullough PA. 2005. The 8.5 Å projection structure of the core RC-LH1-PufX dimer of *Rhodobacter sphaeroides*. *Journal of Molecular Biology* 349: 948-60
- Qian P, Papiz MZ, Jackson PJ, Brindley AA, Ng IW, et al. 2013. Three-dimensional structure of the *Rhodobacter sphaeroides* RC-LH1-PufX complex: dimerization and quinone channels promoted by PufX. *Biochemistry* 52: 7575-85
- Qian P, Siebert CA, Wang P, Canniffe DP, Hunter CN. 2018. Cryo-EM structure of the *Blastochloris viridis* LH1-RC complex at 2.9 Å. *Nature*: 1
- Rao SV, Anderson KW, Bachas LG. 1999. Controlled layer-by-layer immobilization of horseradish peroxidase. *Biotechnology and Bioengineering* 65: 389-96
- Ratcliffe EC, Tunnicliffe RB, Ng IW, Adams PG, Qian P, et al. 2011. Experimental evidence that the membrane-spanning helix of PufX adopts a bent conformation that facilitates dimerisation of the *Rhodobacter sphaeroides* RC-LH1 complex through N-terminal interactions. *Biochimica et Biophysica Acta (BBA)-Bioenergetics* 1807: 95-107
- Reynolds NP, Janusz S, Ducker RE, Leggett GJ, Escalante-Marun M, et al. 2007. Directed formation of micro- and nanoscale patterns of functional light-harvesting LH2 complexes. *Journal of the American Chemical Society* 129: 14625-31
- Reynolds NP, Tucker JD, Davison PA, Timney JA, Hunter CN, Leggett GJ. 2009. Site-specific immobilization and micrometer and nanometer scale photopatterning of yellow fluorescent protein on glass surfaces. *J Am Chem Soc* 131: 896-7
- Roca-Cusachs P, Rico F, Martinez E, Toset J, Farré R, Navajas D. 2005. Stability of microfabricated high aspect ratio structures in poly (dimethylsiloxane). *Langmuir* 21: 5542-48
- Rozsak AW, Isaacs NW, Howard TD, Southall J, Gardiner AT, et al. 2003. Crystal Structure of the RC- LH1 Core Complex from *Rhodospseudomonas palustris*. *Science* 302: 1969-72
- Rozkiewicz DI, Brugman W, Kerkhoven RM, Ravoo BJ, Reinhoudt DN. 2007. Dendrimer-mediated transfer printing of DNA and RNA microarrays. *Journal of the American Chemical Society* 129: 11593-99
- Ruban AV, Young AJ, Pascal AA, Horton P. 1994. The Effects of Illumination on the Xanthophyll Composition of the Photosystem II Light-Harvesting Complexes of Spinach Thylakoid Membranes. *Plant Physiology* 104: 227-34
- Rusmini F, Zhong Z, Feijen J. 2007. Protein immobilization strategies for protein biochips. *Biomacromolecules* 8: 1775-89

- Ryan D, Parviz BA, Linder V, Semetey V, Sia SK, et al. 2004. Patterning multiple aligned self-assembled monolayers using light. *Langmuir* 20: 9080-88
- Sackmann E. 1996. Supported membranes: scientific and practical applications. *Science* 271: 43-48
- Saer RG, Blankenship RE. 2017. Light harvesting in phototrophic bacteria: structure and function. *Biochemical Journal* 474: 2107-31
- Salaita K, Wang Y, Fragala J, Vega RA, Liu C, Mirkin CA. 2006. Massively Parallel Dip-Pen Nanolithography with 55 000-Pen Two-Dimensional Arrays. *Angewandte Chemie* 118: 7378-81
- Schachman HK, Pardee AB, Stanier RY. 1952. Studies on the macromolecular organization of microbial cells. *Archives of Biochemistry and Biophysics* 38: 245-60
- Scheuring S, Busselez J, Lévy D. 2005. Structure of the dimeric PufX-containing core complex of *Rhodobacter blasticus* by in situ atomic force microscopy. *Journal of Biological Chemistry* 280: 1426-31
- Scheuring S, Seguin J, Marco S, Levy D, Breyton C, et al. 2003. AFM characterization of tilt and intrinsic flexibility of *Rhodobacter sphaeroides* light harvesting complex 2 (LH2). *Journal of Molecular Biology* 325: 569-80
- Şener M, Hsin J, Trabuco LG, Villa E, Qian P, et al. 2009. Structural model and excitonic properties of the dimeric RC-LH1-PufX complex from *Rhodobacter sphaeroides*. *Chemical Physics* 357: 188-97
- Sener M, Strumpfer J, Singharoy A, Hunter CN, Schulten K. 2016. Overall energy conversion efficiency of a photosynthetic vesicle. *Elife* 5
- Şener M, Strümpfer J, Timney JA, Freiberg A, Hunter CN, Schulten K. 2010. Photosynthetic vesicle architecture and constraints on efficient energy harvesting. *Biophysical Journal* 99: 67-75
- Şener MK, Olsen JD, Hunter CN, Schulten K. 2007a. Atomic-level structural and functional model of a bacterial photosynthetic membrane vesicle. *Proceedings of the National Academy of Sciences USA* 104: 15723-28
- Şener MK, Olsen JD, Hunter CN, Schulten K. 2007b. Atomic-level structural and functional model of a bacterial photosynthetic membrane vesicle. *Proceedings of the National Academy of Sciences* 104: 15723-28
- Şener MK, Schulten K. 2009. From Atomic-Level Structure to Supramolecular Organization in the Photosynthetic Unit of Purple Bacteria In *The Purple Phototrophic Bacteria*, ed. CN Hunter, F Daldal, MC Thurnauer, JT Beatty, pp. 275-94. Dordrecht: Springer Netherlands
- Sharp KG, Blackman GS, Glassmaker NJ, Jagota A, Hui C-Y. 2004. Effect of stamp deformation on the quality of microcontact printing: theory and experiment. *Langmuir* 20: 6430-38

- Shim H-W, Lee J-H, Hwang T-S, Rhee YW, Bae YM, et al. 2007. Patterning of proteins and cells on functionalized surfaces prepared by polyelectrolyte multilayers and micromolding in capillaries. *Biosensors and Bioelectronics* 22: 3188-95
- Siebert CA, Qian P, Fotiadis D, Engel A, Hunter CN, Bullough PA. 2004. Molecular architecture of photosynthetic membranes in *Rhodobacter sphaeroides*: the role of PufX. *EMBO journal* 23: 690-700
- Siefert E, Irgens R, Pfennig N. 1978. Phototrophic purple and green bacteria in a sewage treatment plant. *Applied and Environmental Microbiology* 35: 38-44
- Sirevåg R. 1995. Carbon metabolism in green bacteria. In *Anoxygenic Photosynthetic Bacteria*, ed. R.E. Blankenship, M. T. Madigan, CE Bauer, pp. 871-83: Kluwer
- Sorribas H, Padeste C, Tiefenauer L. 2002. Photolithographic generation of protein micropatterns for neuron culture applications. *Biomaterials* 23: 893-900
- Springer JW, Parkes-Loach PS, Reddy KR, Krayner M, Jiao J, et al. 2012. Biohybrid photosynthetic antenna complexes for enhanced light-harvesting. *Journal of the American Chemical Society* 134: 4589-99
- Standfuss J, van Scheltinga ACT, Lamborghini M, Kühlbrandt W. 2005. Mechanisms of photoprotection and nonphotochemical quenching in pea light-harvesting complex at 2.5 Å resolution. *EMBO journal* 24: 919-28
- Sturgis JN, Tucker JD, Olsen JD, Hunter CN, Niederman RA. 2009. Atomic force microscopy studies of native photosynthetic membranes. *Biochemistry* 48: 3679-98
- Suemori Y, Nagata M, Nakamura Y, Nakagawa K, Okuda A, et al. 2006. Self-assembled monolayer of light-harvesting core complexes of photosynthetic bacteria on an amino-terminated ITO electrode. *Photosynthesis Research* 90: 17-21
- Sugawara T, Matsuda T. 1995. Photochemical surface derivatization of a peptide containing Arg-Gly-Asp (RGD). *Journal of Biomedical Materials Research Part A* 29: 1047-52
- Sumino A, Dewa T, Kondo M, Morii T, Hashimoto H, et al. 2011a. Selective assembly of photosynthetic antenna proteins into a domain-structured lipid bilayer for the construction of artificial photosynthetic antenna systems: structural analysis of the assembly using surface plasmon resonance and atomic force microscopy. *Langmuir* 27: 1092-99
- Sumino A, Dewa T, Noji T, Nakano Y, Watanabe N, et al. 2013. Influence of Phospholipid Composition on Self-Assembly and Energy-Transfer Efficiency in Networks of Light-Harvesting 2 Complexes. *Journal of Physical Chemistry B* 117: 10395-404
- Sumino A, Dewa T, Sasaki N, Watanabe N, Kondo M, et al. 2011b. Reconstitution and AFM Observation of Photosynthetic Membrane Protein Assembly in Planar Lipid Bilayers. *e-Journal of Surface Science and Nanotechnology* 9: 15-20

- Sun S, Leggett GJ. 2004. Matching the Resolution of Electron Beam Lithography by Scanning Near-Field Photolithography. *Nano Letters* 4: 1381-84
- Sun S, Montague M, Critchley K, Chen M-S, Dressick WJ, et al. 2006. Fabrication of biological nanostructures by scanning near-field photolithography of chloromethylphenylsiloxane monolayers. *Nano Letters* 6: 29-33
- Swainsbury DJK, Proctor MS, Hitchcock A, Cartron ML, Qian P, et al. 2018. Probing the local lipid environment of the *Rhodobacter sphaeroides* cytochrome bc1 and *Synechocystis* sp. PCC 6803 cytochrome b6f complexes with styrene maleic acid. *Biochimica et Biophysica Acta (BBA) - Bioenergetics* 1859: 215-25
- Swoboda M, Henig Jr, Cheng H-M, Brugger D, Haltrich D, et al. 2012. Enzymatic oxygen scavenging for photostability without pH drop in single-molecule experiments. *ACS Nano* 6: 6364-69
- Sznee K, Dekker JP, Dame RT, van Roon H, Wuite GJ, Frese RN. 2011. Jumping mode atomic force microscopy on grana membranes from spinach. *Journal of Biological Chemistry* 286: 39164-71
- Tabita FR. 1995. The biochemistry and metabolic regulation of carbon metabolism and CO₂ fixation in purple bacteria In *Anoxygenic Photosynthetic Bacteria*, ed. R.E. Blankenship, M. T. Madigan, CE Bauer, pp. 885-914: Kluwer
- Tan SC, Crouch LI, Mahajan S, Jones MR, Welland ME. 2012. Increasing the open-circuit voltage of photoprotein-based photoelectrochemical cells by manipulation of the vacuum potential of the electrolytes. *ACS Nano* 6: 9103-09
- Tanaka M, Sackmann E. 2005. Polymer-supported membranes as models of the cell surface. *Nature* 437: 656-63
- Terasaki N, Iwai M, Yamamoto N, Hiraga T, Yamada S, Inoue Y. 2008. Photocurrent generation properties of His₆-tag-photosystem II immobilized on nanostructured gold electrode. *Thin Solid Films* 516: 2553-57
- Timpmann K, Chenchiliyan M, Jalviste E, Timney JA, Hunter CN, Freiberg A. 2014. Efficiency of light harvesting in a photosynthetic bacterium adapted to different levels of light. *Biochimica et Biophysica Acta (BBA)-Bioenergetics* 1837: 1835-46
- Trammell SA, Griva I, Spano A, Tsoi S, Tender LM, et al. 2007. Effects of distance and driving force on photoinduced electron transfer between photosynthetic reaction centers and gold electrodes. *Journal of Physical Chemistry C* 111: 17122-30
- Truskett VN, Watts MP. 2006. Trends in imprint lithography for biological applications. *Trends in Biotechnology* 24: 312-17
- Tsibouklis J, Nevell TG. 2003. Ultra-Low Surface Energy Polymers: The Molecular Design Requirements. *Advanced Materials* 15: 647-50
- Tucker JD, Siebert CA, Escalante M, Adams PG, Olsen JD, et al. 2010. Membrane invagination in *Rhodobacter sphaeroides* is initiated at curved regions of the

cytoplasmic membrane, then forms both budded and fully detached spherical vesicles. *Molecular Microbiology* 76: 833-47

Turchanin A, El-Desawy M, Götzhäuser A. 2007. High thermal stability of cross-linked aromatic self-assembled monolayers: Nanopatterning via selective thermal desorption. *Applied Physics Letters* 90: 053102

ul Haq E, Liu Z, Zhang Y, Ahmad SA, Wong LS, et al. 2010. Parallel scanning near-field photolithography: the snomipede. *Nano Letters* 10: 4375-80

Ulman A. 1996. Formation and Structure of Self-Assembled Monolayers. *Chemical Reviews* 96: 1533-54

Uragami C, Sugai Y, Hanjo K, Sumino A, Fujii R, et al. 2015. Observation of hybrid artificial photosynthetic membranes using peripheral and core antennae from two different species of photosynthetic bacteria by AFM and fluorescence microspectroscopy. *Journal of Photochemistry and Photobiology A: Chemistry* 313: 60-71

van Grondelle R. 1985. Excitation energy transfer, trapping and annihilation in photosynthetic systems. *Biochimica et Biophysica Acta (BBA)-Reviews on Bioenergetics* 811: 147-95

van Niel C. 1944. The culture, general physiology, morphology, and classification of the non-sulfur purple and brown bacteria. *Bacteriological Reviews* 8: 1

VanBeek DB, Zwier MC, Shorb JM, Krueger BP. 2007. Fretting about FRET: Correlation between κ and R . *Biophysical Journal* 92: 4168-78

Vasilev C, Brindley AA, Olsen JD, Saer RG, Beatty JT, Hunter CN. 2014a. Nano-mechanical mapping of the interactions between surface-bound RC-LH1-PufX core complexes and cytochrome c_2 attached to an AFM probe. *Photosynthesis Research* 120: 169-80

Vasilev C, Johnson MP, Gonzales E, Wang L, Ruban AV, et al. 2014b. Reversible switching between nonquenched and quenched states in nanoscale linear arrays of plant light-harvesting antenna complexes. *Langmuir* 30: 8481-90

Visscher K, Bergström H, Sundström V, Hunter C, Van Grondelle R. 1989. Temperature dependence of energy transfer from the long wavelength antenna BChl-896 to the reaction center in *Rhodospirillum rubrum*, *Rhodobacter sphaeroides* (wt and M21 mutant) from 77 to 177K, studied by picosecond absorption spectroscopy. *Photosynthesis Research* 22: 211-17

Wacker R, Schröder H, Niemeyer CM. 2004. Performance of antibody microarrays fabricated by either DNA-directed immobilization, direct spotting, or streptavidin-biotin attachment: a comparative study. *Analytical Biochemistry* 330: 281-87

Wadu-Mesthrige K, Amro NA, Garno JC, Xu S, Liu G-y. 2001. Fabrication of nanometer-sized protein patterns using atomic force microscopy and selective immobilization. *Biophysical Journal* 80: 1891-99

- Walz T, Jamieson SJ, Bowers CM, Bullough PA, Hunter CN. 1998. Projection structures of three photosynthetic complexes from *Rhodobacter sphaeroides*: LH2 at 6 Å, LH1 and RC-LH1 at 25 Å. *Journal of Molecular Biology* 282: 833-45
- Wei X, Su X, Cao P, Liu X, Chang W, et al. 2016. Structure of spinach photosystem II–LHCII supercomplex at 3.2 Å resolution. *Nature* 534: 69
- Wen K, Maoz R, Cohen H, Sagiv J, Gibaud A, et al. 2008. Postassembly Chemical Modification of a Highly Ordered Organosilane Multilayer: New Insights into the Structure, Bonding, and Dynamics of Self-Assembling Silane Monolayers. *ACS Nano* 2: 579-99
- Werwie M, Dworak L, Bottin A, Mayer L, Basché T, et al. 2018. Light-harvesting chlorophyll protein (LHCII) drives electron transfer in semiconductor nanocrystals. *Biochimica et Biophysica Acta (BBA)-Bioenergetics* 1859: 174-81
- Wilbur JL, Kumar A, Biebuyck HA, Kim E, Whitesides GM. 1996. Microcontact printing of self-assembled monolayers: applications in microfabrication. *Nanotechnology* 7: 452
- Wood WH, MacGregor-Chatwin C, Barnett SF, Mayneord GE, Huang X, et al. 2018. Dynamic thylakoid stacking regulates the balance between linear and cyclic photosynthetic electron transfer. *Nature Plants*: 1
- Xia S, Cartron M, Morby J, Bryant DA, Hunter CN, Leggett GJ. 2016. Fabrication of Nanometer- and Micrometer-Scale Protein Structures by Site-Specific Immobilization of Histidine-Tagged Proteins to Aminosiloxane Films with Photoremovable Protein-Resistant Protecting Groups. *Langmuir* 32: 1818-27
- Xia Y, Kim E, Zhao X-M, Rogers JA, Prentiss M, Whitesides GM. 1996. Complex optical surfaces formed by replica molding against elastomeric masters. *Science* 273: 347-49
- Xia Y, McClelland JJ, Gupta R, Qin D, Zhao XM, et al. 1997. Replica molding using polymeric materials: A practical step toward nanomanufacturing. *Advanced Materials* 9: 147-49
- Xia Y, Whitesides GM. 1998. Soft lithography. *Annual Review of Materials Science* 28: 153-84
- Yang M, Zheng Z, Liu Y, Zhang B. 2005. Scanned probe oxidation on an octadecyl-terminated silicon (111) surface with an atomic force microscope: kinetic investigations in line patterning. *Nanotechnology* 17: 330
- Yang M, Zheng Z, Liu Y, Zhang B. 2006. Kinetics of atomic force microscope-based scanned probe oxidation on an octadecylated silicon (111) surface. *Journal of Physical Chemistry B* 110: 10365-73
- Yeates TO, Komiya H, Rees DC, Allen JP, Feher G. 1987. Structure of the reaction center from *Rhodobacter sphaeroides* R-26: membrane-protein interactions. *Proceedings of the National Academy of Sciences USA* 84: 6438-42

- Yehezkeili O, Wilner OI, Tel-Vered R, Roizman-Sade D, Nechushtai R, Willner I. 2010. Generation of photocurrents by bis-aniline-cross-linked Pt nanoparticle/photosystem I composites on electrodes. *Journal of Physical Chemistry B* 114: 14383-88
- Yoneda Y, Noji T, Katayama T, Mizutani N, Komori D, et al. 2015. Extension of light-harvesting ability of photosynthetic light-harvesting complex 2 (LH2) through ultrafast energy transfer from covalently attached artificial chromophores. *Journal of the American Chemical Society* 137: 13121-29
- Yu L-J, Suga M, Wang-Otomo Z-Y, Shen J-R. 2018. Structure of photosynthetic LH1-RC supercomplex at 1.9 Å resolution. *Nature* 556: 209
- Zhao J, Zou Y, Liu B, Xu C, Kong J. 2002. Differentiating the orientations of photosynthetic reaction centers on Au electrodes linked by different bifunctional reagents. *Biosensors and Bioelectronics* 17: 711-18
- Zhao X-M, Xia Y, Whitesides GM. 1997. Soft lithographic methods for nanofabrication. *Journal of Materials Chemistry* 7: 1069-74
- Zhong Q, Inniss D, Kjoller K, Elings V. 1993. Fractured polymer/silica fiber surface studied by tapping mode atomic force microscopy. *Surface Science Letters* 290: L688-L92
- Zhou D, Sinniah K, Abell C, Rayment T. 2003. Label-Free Detection of DNA Hybridization at the Nanoscale: A Highly Sensitive and Selective Approach Using Atomic-Force Microscopy. *Angewandte Chemie International Edition* 42: 4934-37
- Zimorski V, Ku C, Martin WF, Gould SB. 2014. Endosymbiotic theory for organelle origins. *Current Opinion in Microbiology* 22: 38-48